

Modelling carbon exchange in the air, sea, and ice of the Arctic Ocean

Eric Mortenson

B. Sc. Hendrix College, 2000

M. Sc. Florida State University, 2013

A Dissertation Submitted in Partial Fulfillment of the
Requirements for the Degree of

DOCTOR OF PHILOSOPHY

in the School of Earth and Ocean Sciences

© Eric Mortenson, 2019

University of Victoria

All rights reserved. This dissertation may not be reproduced in whole or in part, by photocopying or other means, without the permission of the author.

Modelling carbon exchange in the air, sea, and ice of the Arctic Ocean

by

Eric Mortenson

B. Sc. Hendrix College, 2000

M. Sc. Florida State University, 2013

Supervisory Committee

Dr. Nadja Steiner, Co-Supervisor
(School of Earth and Ocean Sciences)

Dr. Adam H. Monahan, Co-Supervisor
(School of Earth and Ocean Sciences)

Dr. Lisa A. Miller, Departmental Member
(Centre for Ocean Climate Chemistry, Institute of Ocean Sciences)

Dr. Debby Ianson, Departmental Member
(School of Earth and Ocean Sciences)

Abstract

The purpose of this study is to investigate the evolution of the Arctic Ocean's carbon uptake capacity and impacts on ocean acidification with the changing sea-ice scape. In particular, I study the influence on air-ice-sea fluxes of carbon with two major updates to commonly-used carbon cycle models I have included. One, incorporation of sea ice algae to the ecosystem, and two, modification of the sea-ice carbon pump, to transport brine-associated Dissolved Inorganic Carbon (DIC) and Total Alkalinity (TA) to the depth of the bottom of the mixed layer (as opposed to releasing it in the surface model layer). I developed the ice algal ecosystem model by adding a sympagic (ice-associated) ecosystem into a 1D coupled sea ice-ocean model. The 1D model was applied to Resolute Passage in the Canadian Arctic Archipelago and evaluated with observations from a field campaign during the spring of 2010. I then implemented an inorganic carbon system into the model. The carbon system includes effects on both DIC and TA due to the coupled ice-ocean ecosystem, ikaite precipitation and dissolution, ice-air and air-sea carbon exchange, and ice-sea DIC and TA exchange through a formulation for brine rejection to depth and freshwater dilution associated with ice growth and melt. The 1D simulated ecosystem was found to compare reasonably well with observations in terms of bloom onset and seasonal progression for both the sympagic and pelagic algae. In addition, the inorganic carbon system showed reasonable agreement between observations of upper water column DIC and TA content. The simulated average ocean carbon uptake during the period of open water was $10.2 \text{ mmol C m}^{-2} \text{ day}^{-1}$ ($\sim 11 \text{ g C m}^{-2}$ over the entire open-water season).

Using the developments from the 1D model, a 3D biogeochemical model of the Arctic Ocean incorporating both sea ice and the water column was developed and tested, with a focus on the pan-Arctic oceanic uptake of carbon in the recent era of Arctic sea ice decline (1980 – 2015). The model suggests the total uptake of carbon for the Arctic Ocean (north of 66.5°N) increases from $\sim 110 \text{ Tg C yr}^{-1}$ in the early eighties (1980 – 1985) to $\sim 140 \text{ Tg C yr}^{-1}$ for 2010 – 2015, an increase of $\sim 30\%$. The rise in SST accounts for $\sim 10\%$ of the increase in simulated pan-Arctic sea surface $p\text{CO}_2$. A regional analysis indicated large variability between regions, with the Laptev Sea exhibiting low sea surface pH relative to the pan-Arctic domain mean and seasonal undersaturation of Ω_{arag} by the end of the standard run.

Two sensitivity studies were performed to assess the effects of sea-ice algae and the sea-ice carbon pump in the pan-Arctic, with a focus on sea surface inorganic carbon properties. Excluding the sea ice-carbon-pump showed a marked decrease in seasonal variability of sea-surface DIC and TA averaged over the Arctic Ocean compared to the standard run, but only a small change in the net total carbon uptake (of $\sim 1\%$ by the end of the no ice-carbon-pump run). Neglecting the sea ice algae, on the other hand, exhibits only a small change in sea-surface DIC and TA averaged over the pan-Arctic Ocean, but a cumulative effect on the net total carbon uptake of the Arctic Ocean (reaching $\sim 5\%$ less than that of the standard run by the end of the no-ice-algae run).

Contents

Supervisory Committee	ii
Abstract	iii
Table of Contents	v
List of Tables	viii
List of Figures	x
Acknowledgements	xvi
1 Introduction	1
1.1 Introduction	1
1.1.1 Objectives	4
1.2 Carbon exchange processes related to ice	4
1.2.1 Ice-ocean carbon exchange due to ice growth/melt	4
1.2.2 Sympagic biological productivity	5
1.3 Methodology/Methods	5
1.4 Layout	6
1.5 Attribution of work	7
2 A model-based analysis of physical and biological controls on ice algal and pelagic primary production in Resolute Passage	8
2.1 Introduction	9
2.2 Methods	11
2.2.1 Model description	11
2.2.2 Observations	16
2.3 Results	16
2.3.1 Model evaluation	17
2.3.2 Sympagic-pelagic ecosystem coupling	26

2.3.3	Sensitivity analyses for ice algae	31
2.4	Discussion	36
2.5	Conclusions	38
3	A model-based analysis of physical and biogeochemical controls on carbon exchange in the upper water column, sea ice, and atmosphere in a seasonally ice-covered Arctic strait	40
3.1	Introduction	41
3.2	Methods	43
3.2.1	Site description	43
3.2.2	Model description	43
3.3	Results and Discussion	53
3.3.1	Standard Run and Inorganic Carbon Module Validation	53
3.3.2	Sensitivity Analysis	61
3.4	Conclusions	72
4	Evaluating the evolution of the inorganic carbon system in the Arctic Ocean from 1980 to 2015	75
4.1	Introduction	76
4.2	Methods	78
4.2.1	Ocean and sea ice physics models	78
4.2.2	Ocean biogeochemical model	78
4.2.3	Model domain	80
4.2.4	Atmospheric forcing	81
4.2.5	Initial and boundary conditions	82
4.3	Results	83
4.3.1	Evolution of the Arctic Ocean model through the sea ice transition period, 1980 – 2015	83
4.3.2	A regional perspective on carbon uptake in Arctic seas	93
4.4	Discussion	103
4.4.1	No ice-carbon-pump run	103
4.4.2	No ice-algae run	105
4.5	Conclusions	106
5	Conclusion	111
	Appendices	116

A Additional Information	117
A.1 Additional information for Chapter 2	117
A.1.1 Parameterizations for subgrid-scale snow depth distribution and light penetration through snow, sea ice, and melt ponds	117
A.1.2 Ecosystem model equations	120
A.2 Additional information for Chapter 4	134
A.2.1 CanOE documentation	134
A.2.2 Meteorological forcing and ocean boundary conditions	153
A.2.3 Regional trends in carbonate system surface properties/fluxes	154
Bibliography	156

List of Tables

2.1	Extinction and transmissivity coefficients, as well as surface albedos used in this study	12
3.1	List of parameters values for the standard run (SR), which will be varied in the sensitivity studies.	53
3.2	List of model runs (standard and sensitivity analyses). Runs 1 increase/decrease initial water column DIC_0 and TA_0 ; runs 2 suppress some or all of the modelled biological productivity; runs 3 vary the amount of carbon converted into ikaite, DIC_{ikaite}^{ref} ; runs 4 vary the depth of the brine release layer; and runs 5 vary the proportion of carbon rejected during ice growth into the atmosphere, instead of the seawater.	62
3.3	Analyses and resulting net ocean carbon uptake sensitivity to initial DIC and TA concentrations. Runs 1a-1d increase/decrease initial water column concentrations for either DIC_0 or TA_0 by 10 mmol C m^{-3} ; runs 1e and 1f increase/decrease initial water column concentrations for both DIC_0 and TA_0 such that their effects on pCO_2 are counteractive.	62
3.4	Sensitivity of net ocean carbon uptake to primary production. Runs analyze the effect of biological productivity on the net ocean uptake of carbon, including a run with the suppression of only ice algae (2a), with the suppression of both ice algae and phytoplankton (2b), and with the suppression of only phytoplankton (2c).	65
3.5	Sensitivity of net ocean carbon uptake to changes to ikaite concentration in ice ($\Delta DIC:\Delta TA=1:2$) and equal changes to DIC and TA concentrations in the ice ($\Delta DIC:\Delta TA=1:1$). Runs vary in the amount of DIC and TA deposited in the ice. They include a run with no ikaite (3a) and with an order of magnitude more ikaite in the ice than in the standard run (3b). . .	67
3.6	Sensitivity of net ocean carbon uptake to changes in depth of brine deposition. In run 4a, brine-associated DIC and TA is deposited evenly throughout the upper 40 m, and in run 4b, the brine-associated DIC and TA are released in the 1 m surface layer (4b).	69
3.7	Sensitivity of net ocean and ice inorganic carbon uptake to the proportion of sea-ice carbon exchange with the atmosphere vs. the ocean. Runs include 95 and 90% of inorganic carbon released by growing ice into the ocean (5a, 5b) and 95 and 90% of the inorganic carbon taken up by melting ice coming from the ocean (5c, 5d).	71

4.1	List of studies that have analyzed the Arctic Ocean carbon uptake, along with a brief description of the method used and an identification of what the range indicates.	89
A.1	List of state variables in the coupled sea ice-ocean biogeochemical model. .	132
A.2	Parameters for the sea ice biogeochemical model.	132
A.3	Parameters for the ocean biogeochemical model.	133
A.4	Prescribed annual-mean river-flow concentrations of biogeochemical variables at the 6 major Arctic rivers in the model simulation.	153
A.5	Changes to pH over the standard run. The initial value is the mean of the first half-decade (1981 – 1985), the final value is the mean of the last half-decade (2010 – 2015), the difference, percent difference, and difference/decade are between initial and final decadal means.	154
A.6	Changes to sea surface pCO ₂ (μ atm) over the standard run. Headings are the same as in Table A.5	154
A.7	Changes to air-sea flux of CO ₂ (mg C m ⁻² year ⁻¹ , positive is into the ocean) over the standard run. Headings are the same as in Table A.5	154
A.8	Changes to sea surface Ω_{arag} over the standard run. Headings are the same as in Table A.5	155
A.9	Changes to sea surface Ω_{calc} over the standard run. Headings are the same as in Table A.5	155
A.10	Changes to ice coverage (% of total area) over the standard run. Headings are the same as in Table A.5	155

List of Figures

- 1.1 Bjerrum plot illustrates the relative proportions of bicarbonate (HCO_3^-), carbonate (CO_3^{2-}) and carbonic acid, or aqueous CO_2 (CO_{2aq}) under typical seawater conditions. The vertical bar represents the variability, and the arrow conveys the projected shift due to ocean acidification. Figure from wikipedia commons. 2

- 2.1 Schematic diagram of the coupled sea ice-ocean biogeochemical model. Circles represent the model state variables: nitrate (NO_3), ammonium (NH_4), silicate (Si), ice algae (IA), small phytoplankton (P1), large phytoplankton (P2), microzooplankton (Z1), mesozooplankton (Z2), small detritus (D1), large detritus (D2), and biogenic silica (BSi). Sinking variables are bounded by yellow circles. Black and red arrows represent paths of nitrogen and silicon transfers between the variables, respectively: photosynthesis (PH), nitrification (NI), diffusive mixing (DI), flushing (FL), seeding (SE), linear mortality (LM), quadratic mortality (QM), remineralization (RE), grazing (GR), ingestion (IN), sloppy feeding (SL, for inefficient grazing that leaves unconsumed but dead prey), and excretion (EX). 14

- 2.2 Simulated and observed snow depth, melt-pond depth, and ice thickness. Time series of (a) simulated daily-mean snow (solid line) and melt pond (dashed line) depths, observed snow/melt pond depth (circles), and (b) simulated daily-mean (line) and observed (circles) ice thickness. Circles represent the site-average values with one standard deviations indicated by vertical bars. 18

- 2.3 Simulated snow, melt-pond depth, and bare ice area, and simulated and observed PAR. Time series of (a) surface area fraction of simulated snow (red), melt ponds (green), and bare ice (blue) and (b) simulated daily-mean (line) and observed (circles) under-ice PAR during the Arctic-ICE 2010 study period. In (b), the units for the simulated PAR values were converted from W m^{-2} to $\mu\text{mol photons m}^{-2} \text{s}^{-1}$ by a conversion factor of 4.56 following *Lavoie et al.* [2005a]. Vertical bars associated with the solid line represent the diurnal range of simulated under-ice PAR. Red and blue circles represent the daily-mean values measured using tethers deployed over high (HSC) and low (LSC) snow cover sites, respectively. Yellow circles are the instantaneous values based on CTD casts (CTD). 19

2.4	Simulated and observed ice algal biomass, nutrients, growth limitations, and simulated sympagic and pelagic production. Time series of (a) simulated (line) and observed (circles) Chl <i>a</i> concentrations in the bottom 3 cm of the sea ice, (b) simulated nitrate (solid black), ammonium (dashed black) and silicate (red) concentrations in the bottom 3 cm of sea ice, (c) simulated daily-mean growth limitation index for light (yellow), nitrogen (black), silicate (red), and ice melting (green), and (d) primary production rates of simulated ice algae (solid line) and phytoplankton (dashed line). In (a), circles represent the site-average values with one standard deviations indicated by vertical bars.	21
2.5	Simulated and observed Chl <i>a</i> concentration. Time series of (a) simulated and (b) observed Chl <i>a</i> concentrations in the upper 80 m of the water column.	23
2.6	Simulated water column concentrations of nutrients and biological uptake and drawdown of nitrate. Simulated time series of (a) nitrate, (b) ammonium, and (c) silicate concentrations in the upper 80 m of the water column (depth of entire water column is 141 m). (d) Simulated time series of cumulative depth-integrated nitrate uptake and drawdown. In (d), areas filled in red represent the cumulative uptake by ice algae integrated over the bottom 3 cm of the ice skeletal layer, areas filled in blue represent the cumulative uptake by phytoplankton (P1 and P2) integrated over the upper 80 m of the water column, and the black line represents the cumulative amount of nitrate drawn down from the upper 80 m of the water column. Note that the sum of the two uptake terms (red+blue) does not balance with the drawdown during the ice-free period; the mismatch represents the uptake of nitrate entrained from the layer below 80 m.	25
2.7	Water column Chl <i>a</i> concentration when ice algae are present, absent, and the difference. Simulated phytoplankton bloom in the upper 50 m of the water column when ice algae are present (a), absent (b), and the difference (c). Phytoplankton are sum of large and small (P1 and P2) groups.	27
2.8	Water column nitrate when ice algae are present, absent, and the difference. Simulated NO ₃ concentration in the upper 50 m of the water column when ice algae are present (a), absent (b), and the difference (c).	29
2.9	Phytoplankton in the water column with fast-sinking detritus. Simulated phytoplankton in the upper 50 m of the water column, with fast-sinking detritus (D2) set at 50 m d ⁻¹ (a), 15 m d ⁻¹ (b), and 5 m d ⁻¹ (c). First bloom is dominated by large phytoplankton (P2, diatoms) and the later bloom in (c) is dominated by small phytoplankton (P1, flagellates).	30

2.10	Snow and ice thickness and ice algal biomass, varying pre-bloom biomass. Snow and ice thickness (cm) and ice algal biomass during sensitivity analyses of the simulated ice algal bloom to variation of pre-bloom biomass (b), prescribed at 10, 2, 1/2, and 1/10 times that in the standard simulation (solid black line).	32
2.11	Snow and ice thickness, ice algal biomass varying mortality function, and onset of the bloom. Snow and ice thickness (cm) (a) and ice algal biomass (mg Chl <i>a</i> m ⁻³) differing linear and quadratic dependencies on mortality (b). The black solid line in (b) is the standard run, the dashed red (blue) line is the simulated bloom with both linear and quadratic dependencies decreased (increased) by 25%. The solid colored lines are for blooms with linear and quadratic dependencies changed in opposite directions, e.g., increased for linear and decreased for quadratic. The onset of the bloom in the red box in (b) is expanded in (c).	35
3.1	Schematic of the carbon system during the seasonal ice growth and melt cycle. Processes included in the model, and described in Section 4.2, are: 1. ice-air outgassing of CO ₂ during ice growth; 2. air-sea CO ₂ exchange during the open-water season; 3. brine-associated rejection of DIC and TA during ice growth; 4a. ikaite precipitation in ice during growth; 4b. ikaite dissolution in the water during ice melt; 5. ice algal growth; 6. dilution due to low-DIC, -TA meltwater during ice melt; 7. pelagic primary production; and 8. pelagic remineralization of phytoplankton (PP) and zooplankton (ZP) detritus.	45
3.2	Simulated and observed water column profiles for a) DIC and b) TA. The black dashed lines are initial conditions for the model. Simulated bi-weekly results (solid lines) are from May and June 2010, and observations (dots) are in/near Resolute Passage from May 2010 (dark blue, <i>Brown et al.</i> [2015]), June 2012 (light blue, <i>Geilfus et al.</i> [2015]), and August 2015 (brown, A. Mucci, personal communication, from GEOTRACES, 2015). One surface measurement from 2012 was identified as a clear outlier and excluded from the figure (DIC and TA values of 560 and 603 $\mu\text{mol kg}^{-1}$, respectively) in order to focus on the majority of data.	55
3.3	Simulated (a) ice/snow thickness and cumulative open-water exchange of carbon, (b) <i>p</i> CO ₂ , TA, and DIC at the sea surface, (c) phytoplankton biomass (expressed in units of carbon), (d) DIC, and (e) TA in the upper 80 m of the water column.	57

3.4	Simulated (a) salinity (ppt) and (b) temperature ($^{\circ}\text{C}$) in the upper 80 m of the water column.	58
3.5	Simulated sea surface DIC (top) and TA (bottom) versus salinity over the period of ice growth (left) and ice melt and open water (right) over the standard simulation. The colors indicate time periods listed in the legends, and are the same for DIC and TA.	59
3.6	Time series of daily- and weekly-mean ocean carbon uptake over the open-water season.	60
3.7	Simulated ice thickness in blue (a and b) and net ocean carbon uptake in the standard run (solid black lines) and with DIC_0 and TA_0 increased/decreased a) independently and b) together (dashed lines).	63
3.8	Simulated ice depth and net ocean carbon uptake: (a); surface seawater NO_3 concentration (b); and surface phytoplankton biomass (c) in the standard run (solid black) and with ice algae (IA) and pelagic algae (P) blooms suppressed. Note that a small amount of phytoplankton are present (but do not grow) in the top 1 m in the run with ice algae, but with pelagic algae suppressed, due to seeding from ice algae (blue dashed line in c).	65
3.9	Simulated ice depth (blue) and net ocean carbon uptake in the standard run (solid black) and a) with $\text{DIC}_{ikaite}^{ref}$ and TA_{ikaite}^{ref} varied in a 1:2 ratio (a); and with DIC_{ice}^{ref} and TA_{ice}^{ref} varied by the same amount (b).	67
3.10	Simulated ice depth and net ocean carbon uptake in the standard run (solid black) and with brine-associated DIC and TA deposited in the upper 1 m (red) and in the upper 40m (green) (a) and TA and DIC in the standard run minus the run with surface 1 m deposition of brine-associated DIC and TA (b and c, respectively).	70
4.1	Model bathymetry (left) and grid cell resolution (right) for the Arctic Ocean.	81
4.2	Simulated monthly- (dashed lines) and annually-averaged (solid lines) sea ice area (top) and sea ice volume (bottom) for the Arctic Ocean. The dotted lines indicate the maximum and minimum monthly values of sea ice area from NSIDC and of sea ice volume from PIOMAS. The domain of the modelled sea ice area calculations is the entire model domain, and north of 31° N for NSIDC. The domain for both the sea ice volume in this study and for the PIOMAS data are the region north of 66.5° N.	85

4.3	For the standard run, monthly (dashed line) and annual (solid) simulated sea surface temperature, simulated sea surface salinity, DFS-forced wind speed, and simulated total ice area (black) and simulated total ice volume (red). All variables are averaged for the region north of 66.5° N.	86
4.4	As in Figure 4.3, showing only the annually-averaged values.	87
4.5	Comparison of the climatological sea surface salinity in the Arctic based on observations compiled for the Polar science center Hydrographic Climatology (PHC) and from the model mean over the period 1981 – 2015.	88
4.6	Top panel: net annual CO ₂ uptake over the Arctic Ocean (solid black line); net seasonal CO ₂ uptake (solid color lines) over spring (cyan), summer (red), fall (orange), and winter (blue), all scaled to match the annual uptake (multiplied by 4); and net monthly CO ₂ uptake (dashed line) scaled to match the annual uptake (multiplied by 12). Middle panel: annual (solid black line) and monthly mean (dashed black line) sea surface <i>p</i> CO ₂ and atmospheric <i>p</i> CO ₂ (red line). Bottom panel: annual (solid) and monthly mean (dashed) sea surface pH. All variables are analyzed over the region north of 66.5° N.	91
4.7	Annual (solid) and monthly-averaged (dashed line) sea surface DIC, sea surface TA, and sea surface aragonite calcite saturation states. All variables are averaged over the region north of 66.5° N.	92
4.8	Top panel: Total annual (solid) and monthly (dashed) phytoplankton carbon content in the upper 50 m of the Arctic Ocean north of 66.5° N (Tg C). The lower panels display the same for NO ₃ and NH ₄ content in the upper 50 m.	94
4.9	As in Figure 4.8, but including the spinup period (1970 – 1979).	95
4.10	Regions that exhibit distinctive differences in carbon system properties from the pan-Arctic mean. Colors match those of the regions in Figures 4.11 and 4.12. The regions are the Canadian Polar Shelf, the South and North Beaufort Seas, Laptev Sea, Barents Sea, and Norwegian Sea.	96
4.11	Annual averaged sea surface (and atmospheric, dashed black line) <i>p</i> CO ₂ , mean carbon flux, pH, and ice cover for the region north of 66.5° N (black), and for selected regions identified in Figure 4.1. Line colors match those of the regions in Figure 4.10. Different linestyles (solid/dashed/dotted) are to aide in differentiating similar colors.	98
4.12	Annual averaged sea surface DIC, TA, Ω_{arag} , Ω_{calc} for the region north of 66.5° N, and for same regions as in Figure 4.11.	99

4.13	Hovmoeller plot of annually averaged DIC content (left) and Ω_{arag} (right) through the upper 300 m of the water column for the North (top) and South (bottom) Beaufort Seas over the standard run period.	101
4.14	As in Figure 4.13, but averaged over the summer months (July, August, and September).	102
4.15	As in Figure 4.13, from measurements for the off-shelf region of the Beaufort Sea (similar, but not exactly the same, as the domain defined in this study as the North Beaufort Sea) presented in <i>Bellerby et al.</i> [2018].	102
4.16	Top panel: Total annual (black) and seasonal (colors, scaled to match the annual total; summer=red, fall=orange, winter=blue, and spring=cyan) ocean carbon uptake of the Arctic Ocean north of 66.5° N (Tg C). The dashed lines indicate the no ice-carbon-pump run and the dotted lines indicate the no ice-algae run. The lower panels are pan-Arctic averaged sea surface DIC, TA, and Ω_{arag} averaged monthly (dashed) and yearly (solid), all for the standard run (black) and the sensitivity runs with the ice-carbon-pump suppressed (red) and the ice algae suppressed (cyan).	104
4.17	Total annual (solid) and monthly (dashed) phytoplankton carbon content in the upper 50 m and of the ice algae for the pan-Arctic (Tg C). The black lines indicate the standard run and the cyan lines indicate the no ice-algae run. The lower panels display the same for NO_3 and NH_4 content in the upper 50 m over the same area.	107
A.1	P1, P2, and their light and nutrient limitations. Time series of simulated biomass of (a) P1 and (b) P2, light limitation index of (c) P1 and (d) P2, (e) nitrogen limitation index of P1 and P2, and (f) silicate limitation index of P2.	131

Acknowledgements

I would like to thank Dr. Nadja Steiner and Dr. Adam H. Monahan, my supervisors, who have been incredibly supportive on multiple levels. I would not have been able to do this without your help, and I owe you more than can briefly expressed here.

I would also be very remiss if I did not thank my colleague Dr. Hakase Hayashida (Hakase Hakase), with whom I have sat many hours in front of computers learning the ropes.

I also thank my committee members, Dr. Lisa A. Miller and Dr. Debby Ianson, as well as the external member Dr. Frédéric Maps (Université Laval), for their guidance, advice, and criticism.

I would like to acknowledge Allison Rose and Kalisa Valenzuela in the School of Earth and Ocean Sciences main office for all the help, support, organizing, and friendliness through my time here.

Thanks to Arlan Dirkson for providing PIOMAS ice volume for the subdomain north of 66.5° N.

Finally, I am grateful to Kristina Brown, Odile Crabeck, Nix Geilfus, Jerry Henderson, Lisa Miller, Sebastien Moreau, CJ Mundy, Tim Papakyriakou, Andrew Shao, Tessa Sou, Martin Vancopenolle, and Liz Williams for useful discussions and ideas along the way. In particular, Tessa and Andrew gave much needed help and support in identifying problems with the almost final iterations of the model runs through careful analysis of model results and model code.

I would like to thank ArcticNet, NETCARE, CSIRO, and the University of Victoria for financial support.

1 Introduction

1.1 Introduction

Anthropogenic carbon production has led to a steady rise in the atmospheric concentration of CO_2 , and this process has been recorded continuously since the middle of the 20th century. Observations have shown that, so far, the fate of the anthropogenic carbon released can be divided roughly into the following: of the 375 ± 30 petagrams carbon (PgC) of anthropogenic origin, two thirds remain in the atmosphere (240 ± 10 PgC), and one third has been taken up by the global oceans (-155 ± 30 PgC) [Ciais *et al.*, 2013]. However, the ability for the global ocean to maintain the present rate of carbon uptake is uncertain. The rate of oceanic carbon uptake is sensitive to sea surface properties, with sea ice, which is a common feature of polar oceans, providing an obvious example. Although it is clear the presence of sea ice affects air-sea exchange, the effects on carbon exchange are multifaceted and subtler than general treatment by global ocean models (as an inert barrier to air-sea carbon exchange). Furthermore, the sea-ice scape, particularly in the Arctic, is in the process of undergoing remarkable changes to seasonal ice cover, extent, and depth [Barber *et al.*, 2015]. The proper treatment of sea ice, with respect to a modelled carbon system, is the major focus of this work.

The uptake capacity of the global oceans is directly related to the size of the oceanic carbon reservoir, which is roughly two orders of magnitude larger than the atmospheric and terrestrial reservoirs [Cubasch *et al.*, 2013]. The magnitude of the oceanic carbon reservoir is partly due to sea water's carbonate chemistry. Given the temperature, salinity and pressure of a parcel of seawater, the complete carbonate chemistry of the parcel can be determined by knowing any 2 of the four inorganic carbon quantities: $p\text{CO}_{2sw}$, pH, Dissolved Inorganic Carbon (DIC), and Total Alkalinity (TA). These quantities are briefly introduced here:

- Dissolved inorganic carbon, or DIC, is the sum of all carbonate species in a solution. Neglecting less common carbonate species, $[\text{DIC}] \cong [\text{CO}_2]_{aq} + [\text{HCO}_3^-] + [\text{CO}_3^{2-}]$, as in

Eq. 1.1. In typical seawater conditions, this approximation is quite accurate. In seawater under historical conditions, bicarbonate (HCO_3^-) comprises the largest proportion of DIC (at $\sim 95\%$), followed by carbonate (CO_3^{2-} , at just under 5%), and lastly carbonic acid, or aqueous CO_2 (CO_{2aq}), as shown in Figure 1.1,. However, changes happening in the present and projected into the near future include a shift to the left in the Bjerrum plot due to acidification through the increase in the uptake of atmospheric CO_2 , leading to a decrease in the capacity for further carbon uptake by surface oceans. Another way to describe this is that the following stoichiometric equation will shift towards the left due to ongoing ocean acidification:

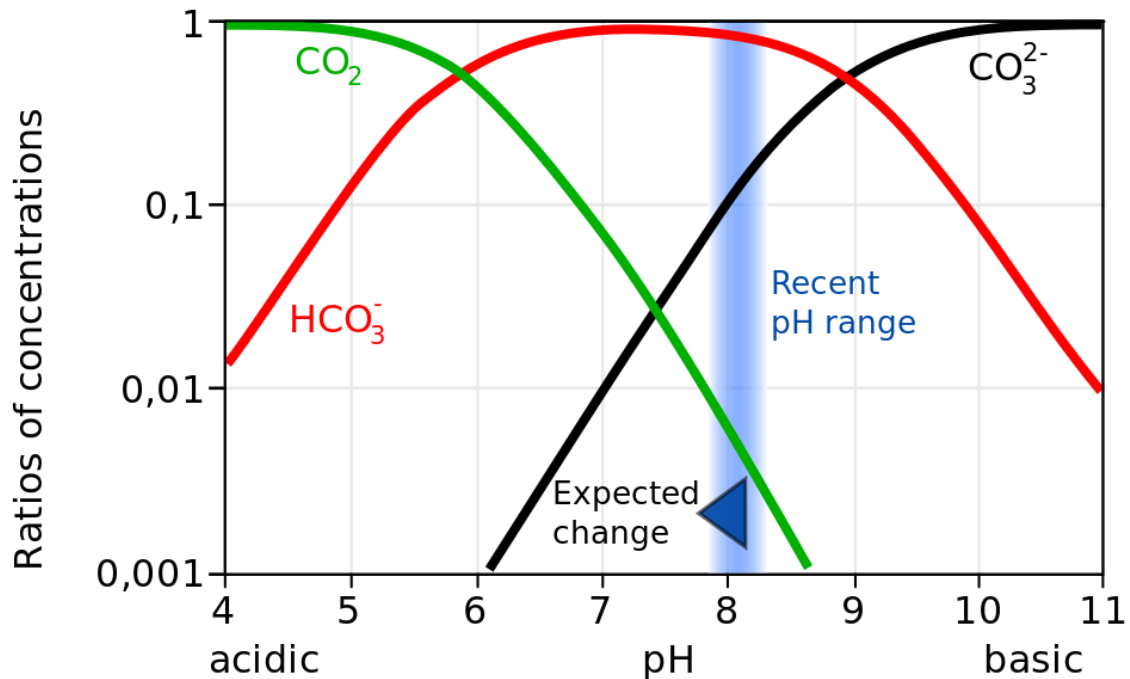
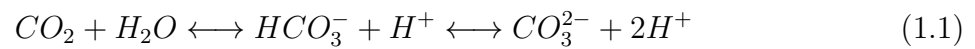


Figure 1.1: Bjerrum plot illustrates the relative proportions of bicarbonate (HCO_3^-), carbonate (CO_3^{2-}) and carbonic acid, or aqueous CO_2 (CO_{2aq}) under typical seawater conditions. The vertical bar represents the variability, and the arrow conveys the projected shift due to ocean acidification. Figure from wikipedia commons.

- Total alkalinity, or TA, is defined as the buffering capacity of a solution, or the excess of proton acceptors to proton donors ($\text{TA} \cong [\text{HCO}_3^-] + 2*[\text{CO}_3^{2-}]$, where the 2 retained terms on the right hand side account for 96.6% of TA [*Sarmiento and Gruber, 2006*], and

smaller terms have been neglected).

- At the surface, the fugacity of CO₂ for seawater, $f\text{CO}_2$, is a major component in the determination of air-sea exchange. In the form $p\text{CO}_{2sw}$ (which can be equated with the atmospheric partial pressure of CO₂, or $p\text{CO}_{2atm}$), it determines the water side of $\Delta p\text{CO}_2 = p\text{CO}_{2sw} - p\text{CO}_{2atm}$.

- The negative log of the free protons concentration [H⁺] in the solution, pH, is the quantity that conventionally used to discuss ocean acidification.

Two related quantities of importance, that are also closely related to the sea water carbon system, are the saturation states for aragonite and calcite (Ω_{arag} and Ω_{calc}). The calcium carbonate saturation state for sea water is defined as

$$\Omega = ([Ca^{2+}][CO_3^{2-}])/[CaCO_3], \quad (1.2)$$

where CaCO₃ is calcium carbonate in either the form of aragonite or calcite, with a distinction due to different dissociation constants, aragonite being the less stable of the two. When $\Omega = 1$, the seawater is in equilibrium, and with $\Omega > (<) 1$, the seawater is super-(under-)saturated. Many biological materials (e.g., shells of molluscs, crustacean exoskeletons) are comprised largely of calcium carbonate in the form of aragonite or calcite. In the case of calcium carbonate undersaturation, organisms with calcite or aragonite in part(s) of their bodies find it energetically more expensive to grow or maintain those parts.

The reduction of pH, Ω_{arag} , and Ω_{calc} , defined as ocean acidification, is accelerating due to increasing uptake of atmospheric CO₂, and is a second major focus of this study. Of the world's oceans, the Arctic Ocean is particularly vulnerable to a decrease in pH due to its cold temperatures, extensive shallow continental shelves (increasing the proportion of surface area to volume), high river inflow (typically high in dissolved organic carbon), and low biological productivity. Observations are showing substantial decreases in ocean pH and/or in calcium carbonate saturation states in regions across the Arctic Ocean. These regions include the Chukchi and Beaufort Seas [Evans *et al.*, 2015; Cross *et al.*, 2018], along the shelf of the Laptev and East Siberian Seas [Semiletov *et al.*, 2016], as well as on the Atlantic side of the Arctic Ocean, in the Western European Arctic shelves [Wallhead *et al.*, 2017].

1.1.1 Objectives

Process-based numerical models are an important tool in understanding the complex drivers of the Earth's climate system with the ongoing production of anthropogenic carbon. Coupled ice-ocean models commonly neglect the role of sea ice in carbon exchange, effectively treating sea ice cover as an impermeable cap preventing any exchange of carbon. Observations indicate that this treatment of sea ice in ocean models may not be sufficient. Not only is the sea ice permeable through openings in the form of leads and polynyas, but it also actively participates in carbon exchange through the growth and melt of sea ice.

This work is aimed at evaluating two fundamental questions about the carbonate system in the Arctic:

- 1., What are the dominant mechanisms of carbon exchange in the air-sea-ice system of the marine Arctic?
- 2., How will carbon exchange be affected in a changing Arctic environment?

1.2 Carbon exchange processes related to ice

Carbon exchange in the air-ice-ocean system of the Arctic is influenced by many different processes. These processes occur in different seasons and can interact with one another (*e.g.*, both sea ice melt and ice algae blooms can serve to lower near-surface [DIC], which in turn influences the air-sea exchange during the subsequent open-water season by enhancing oceanic uptake of atmospheric carbon.) The following sections describe the mechanisms behind the main processes in this system. All of these different processes are known to influence carbon exchange, and an assessment of their relative importance is a key goal of this study.

1.2.1 Ice-ocean carbon exchange due to ice growth/melt

Observations indicate that ice (in bulk) is depleted in both DIC and TA relative to the seawater from which it formed [*Brown et al.*, 2015]. This is a result of brine rejection during ice growth, in which seawater solutes are rejected from the relatively pure ice matrix as it forms. When the ice is close to the melting point, brine channels can interconnect [*Golden et al.*, 1998], and the DIC-rich brine can drain gravitationally out of the ice into the mixed layer.

Because the DIC content of underlying waters is subject to changes due to multiple processes (*e.g.*, air-sea exchange at ice leads, horizontal advection, in and under-ice net primary production), separating out the variation in upper ocean DIC content due solely to ice growth and melt is difficult through observation. Because of this, ice-ocean exchange of carbon is not well constrained.

1.2.2 Sympagic biological productivity

Net primary production is associated with changes to DIC and TA, proportional to nutrient uptake. During ice melt, the organic carbon associated with ice-algae remains (detritus) is released and is transported away from the sea surface via sinking through the water column.

The ice-algae community in the Arctic typically resides in the lower, permeable layer of the ice (known as the skeletal layer, about 2 to 4 cm thick) and is largely comprised of *Nitzshia frigida*, a pennate diatom which is relatively large in comparison to pelagic algae [Campbell *et al.*, 2017]. The ice algae bloom when there is sufficient light penetration during the early summer thawing of snow on the surface of the ice, which occurs before the under-ice pelagic bloom. The ice-algae bloom typically lasts about six weeks and can reach a maximum biomass of bulk concentrations usually within the range of 40-100 mg chl-a/m² in coastal and landfast sea ice at polar latitudes up to 65° N, and much lower values farther north and/or farther from continental shelves [Leu *et al.*, 2015]. The evolution of the bloom is strongly dependent on snow cover, with longer, flatter blooms associated with more snow cover [Campbell *et al.*, 2015]. Typically, the ice algae bloom is limited by light at the beginning of the bloom and by nutrients in the latter half [Lavoie *et al.*, 2005b].

1.3 Methodology/Methods

Findings described in this dissertation span work from the conceptual development of an ice ecosystem in a biogeochemical model and implementation of a carbon cycle. In the 1-D configuration, a physical model (General Ocean Turbulence Model, or GOTM) simulates both the ice and ocean and is coupled to a biogeochemical model (Framework for Aquatic Biological Model, or FABM). Both sympagic and pelagic ecosystems are implemented (N3P3Z2D2), based on, respectively, Lavoie *et al.* [2005b] and Fasham *et al.* [1990]. In addition, an ice carbon pump, associated with the growth and melt of sea ice,

was implemented in the existing ocean carbon system. Both (eco- and carbon) systems were compared with available observations. These observations include 2 years recording the progression of the ice algae biomass through the progression of the bloom. We varied parameters associated with different aspects of the ice algae bloom (*e.g.*, over-wintering biomass, photosynthetic efficiency, rate mortality) in order to determine how sensitive the model output (*i.e.*, the ice algae biomass through the bloom period) is to changes to these parameters. These tests of model sensitivity were then compared in order to ascertain where/what/when observations might be most useful to better constrain model parameters.

The conceptual framework applied in the 1-D configuration was then applied to a 3-D model of the Arctic Ocean and surrounding seas. The physical ocean model was the Nucleus for European Modelling of the Oceans, version 3.4 (NEMO3.4), which was coupled to the Louvain-la-Neuve sea Ice Model, version 2 (LIM2). A biogeochemical and ecosystem model (Canadian Ocean Ecosystem, or CanOE) was implemented and modified to include both the ice carbon pump and sympagic ecosystem developed and tested in the 1-D study. The 3-D model standard run was forced by meteorological observations (described in detail in Chapter 4) from initial conditions starting in 1969 and continuing up to 2015. Model results were compared to observations of ice extent and volume, to known biological dataset (with again the caveat of sparse sampling), as well as general ocean properties, both physical and biogeochemical.

Finally, two sensitivity tests, on the two independent implementations (sympagic ecosystem and ice carbon pump), were set up. In the two experiments, each of the implementations were independently suppressed, branching from the standard run in 1990 and running to 2010. The results were analyzed with foci on how the implementations affect (1) the sea surface carbon properties and the subsequent changes to total carbon uptake of the Arctic Ocean and (2) water column carbon properties as they relate to ocean acidity and aragonite saturation.

1.4 Layout

The following sections includes the implementation and testing of the ice algal ecosystem in a coupled ice-ocean 1-D biogeochemical model (Chap. 2) and the development and testing of the inorganic carbon system in the same coupled ice-ocean biogeochemical 1-D model (Chap. 3). Chapter 4 describes the incorporation of sea-ice algae in a 3-D regional

model for the Arctic Ocean, along with implementation of the DIC system. Last, Chapter 5 is a summary of the findings in this compilation of work.

1.5 Attribution of work

Chapter 2 of this dissertation involved extensive collaboration with the co-author Hakase Hayashida. The model development described in Chapter 2 included incorporation of a pelagic ecosystem (by Hakase Hayashida) and a sympagic ecosystem (by Eric Mortenson) into the 1-D biogeochemical model. Both co-authors contributed equally to writing the manuscript published as *Mortenson et al.* [2017], with inputs from the rest of the co-authors.

Chapter 3 of this dissertation is published as *Mortenson et al.* [2018] and describes the implementation of DIC and TA effects due to both sympagic and pelagic ecosystems described in Chapter 2, as well as the implementation of DIC and TA fluxes due to ice melt and growth. Both of these modifications were implemented by the first author (Eric Mortenson). Conceptual development of these modifications involved discussions with Nadja Steiner, Adam Monahan, Lisa Miller, Kristina Brown, and Hakase Hayashida. Observations used to compare water column and ice DIC and TA content were made by Kristina Brown, Nicolas-Xavier Geilfus, and Alfonso Mucci. I wrote the manuscript published as *Mortenson et al.* [2018] along with inputs from the rest of the co-authors.

In Chapter 4, I implemented DIC and TA effects due to sympagic and pelagic ecosystems as well as ice growth and melt in the same conceptual framework as in Chapter 3 in a 3-D regional model of the Arctic Ocean. Tessa Sou, Andrew Shao, and Xianmin Hu provided assistance with the setup of the model as well as analysis of model output, and the implementation of the ecosystem was done largely by Hakase Hayashida. Conceptual development of these modifications involved discussions with Nadja Steiner, Adam Monahan, Hakase Hayashida, Tessa Sou, Andrew Shao, and Xianmin Hu.

2 A model-based analysis of physical and biological controls on ice algal and pelagic primary production in Resolute Passage

The following chapter is a manuscript published as:

Mortenson, E., Hayashida, H., Steiner, N., Monahan, A., Blais, M., Gale, M., Galindo, V., Gosselin, M., Hu, X., Lavoie, D., and Mundy, C-J. (2017): A model-based analysis of physical and biological controls on ice algal and pelagic primary production in Resolute Passage, *Elementa*, <https://doi.org/10.1525/elementa.229>

The manuscript is repeated here with some adjustments to fit the format of the dissertation and to address comments from the PhD committee.

Chapter Abstract

A coupled 1-D sea ice-ocean physical-biogeochemical model was developed to investigate the processes governing ice algal and phytoplankton blooms in the seasonally ice-covered Arctic Ocean. The 1-D column is representative of one grid cell in 3-D model applications and provides a tool for parameterization development. The model was applied to Resolute Passage in the Canadian Arctic Archipelago and assessed with observations from a field campaign during spring of 2010. The factors considered to limit the growth of simulated ice algae and phytoplankton were light, nutrients, and in the case of ice algae, ice melt. In addition to the standard simulation, several model experiments were conducted to determine the sensitivity of the simulated ice algal bloom to parameterizations of light, mortality, and pre-bloom biomass. Model results indicated that: (1) ice algae limit subsequent pelagic productivity in the upper 10 m by depleting nutrients to limiting levels; (2) light availability and pre-bloom biomass determine the onset timing of the ice algal bloom; (3) the maximum biomass is relatively insensitive to the pre-bloom biomass, but is limited by nutrient availability; (4)

a combination of linear and quadratic parameterizations of mortality rate is required to adequately simulate the evolution of the ice algal bloom; and (5) a sinking rate for large detritus greater than a threshold of $\sim 10 \text{ m d}^{-1}$ effectively strips the surface waters of the limiting nutrient (silicate) after the ice algal bloom, supporting the development of a deep chlorophyll maximum.

2.1 Introduction

Satellite records indicate that the minimum annual sea ice extent in the Arctic has been decreasing by more than 10% per decade over the last half century [Vaughan *et al.*, 2013], which results in a longer and more widespread open-water season [Barber *et al.*, 2015]. In addition to the loss of sea ice, there has been a general shift in ice type, from thicker multiyear ice to younger and thinner first-year ice [Lindsay and Schweiger, 2015]. These trends in ice type, cover, and timing have significant consequences on marine and sea-ice ecosystems and air-sea exchange, as well as broader implications for the global climate. To reproduce recent changes and project future changes of sea ice related primary production in models we need to be able to understand the driving processes and develop adequate model parameterisations. 1-D models are excellent tools to develop such parameterisations and test the system sensitivity to parameter variations.

In the Arctic, ice algae live in a relatively sheltered environment concentrated within the bottom few centimeters of the sea ice [Smith *et al.*, 1990; Galindo *et al.*, 2014; Brown *et al.*, 2015-1]. Ice algal blooms occur at high polar latitudes where snow and ice-cover substantially reduce incident light to the bottom of the ice column. This environment, and the timing of ice algal blooms, suggest that they are shade-acclimated to low-light conditions [Kirst and Wiencke, 1995]. The algae within the ice can reach very high biomass (exceeding $1000 \text{ mg Chl } a \text{ m}^{-3}$) that is up to two orders of magnitude greater than the underlying phytoplankton biomass [Galindo *et al.*, 2014; Leu *et al.*, 2015]. Previous observational studies indicate that primary production by ice algae can make a substantial contribution to the total (sea ice and pelagic) primary production at various locations in the Arctic Ocean [Legendre *et al.*, 1992; Gosselin *et al.*, 1997]. Ice algae are dependent on the ice as a habitat and also affect the ice through light absorption and its subsequent conversion to heat, and through production of extracellular polymeric substances [Riedel *et al.*, 2006; Krembs *et al.*, 2011]. In addition, the termination of the ice algal bloom translates to nutrient release to, and possible seeding of, the phytoplankton bloom [Galindo *et al.*, 2014] in the surface ocean.

One challenge for model studies of Arctic sea ice is that observations from the field are sparse due to the remote location and harsh environment. As a result, many parameters required to simulate biogeochemical processes in ice-covered regions are poorly constrained. In this modeling study, we have been able to take advantage of observations of ice algal blooms and environmental variables from several recent field campaigns at one location in order to better understand the processes constraining the simulation. To address the impact of remaining uncertainties, the modelled ice algal growth can be tested against variations in relevant parameters, with ranges based on measured or inferred uncertainty. Sensitivity analyses are a common way to assess the impact of specific processes or parameters on the whole system and evaluate the variables to which the system is most sensitive. Testing the model's sensitivity over a certain parameter range, based on observations, allows for an estimate of the importance of a given process, compared to others, and identification of parameters that need to receive focused observational attention to reduce the overall uncertainty of the system [Steiner *et al.*, 2016a]. Several 1-D sea ice algal models have been developed in order to reproduce observations at particular locations [Lavoie *et al.*, 2005a; Pogson *et al.*, 2011]. Some include focused sensitivity studies, e.g., Arrigo and Sullivan [1994], show that adjustments lowering the ice algal nutrient supply (via a nutrient transport coefficient) can cause the ice algal system to become nutrient-limited, and identify a high sensitivity to the ice algal growth rate. Jin *et al.* [2006] identified a strong correlation between net primary production of ice algae and the initial nutrient concentration in the water column. Steiner *et al.* [2016a] highlighted several components and parameters that lack either full understanding or observational constraints. Based on these previous studies, the following parameters were selected for testing in this study: the amount of algae in the ice during the winter (pre-bloom biomass), photosynthetic efficiency of the ice algae in low light conditions, the strength of nutrient flushing during the ice algal bloom period, and the magnitude and form of specific mortality of the ice algae. While model studies suggest that ice algal seeding of an ice-associated pelagic bloom mainly affects the timing rather than the magnitude of the pelagic bloom [Jin *et al.*, 2007; Tedesco *et al.*, 2012] the link between ice algal and pelagic production remains an area of uncertainty and that we also address here.

Another challenge for both 1-D and 3-D modelling of sea ice ecosystems is the treatment of (subgrid-scale) heterogeneous snow cover and how this heterogeneity affects the light penetration to the bottom of the ice (where Arctic ice algae are most prominent). In order to represent a grid cell average over multiple square kilometers, this heterogeneity needs to be taken into account in the model. This challenge has been the focus of Abraham *et al.* [2015]. They compare light penetration through a Rayleigh-distributed snow cover to a

uniformly distributed snow cover, identifying substantial improvement to the grid-cell mean light transmission compared to observations. Light transmission to the bottom of the sea ice has been identified as a major problem in simulating ice algal growth particularly during the period of snow decline [Arrigo and Sullivan, 1994; Lavoie et al., 2005a; Pogson et al., 2011]. In the present study, we test the impact of the newly-developed parameterization for light transmission through sea ice [Abraham et al., 2015] on ice algal growth.

With the broader objective of establishing a set of parameterizations that can be transferred into a 3-D regional Arctic model (coupling sea-ice and the ocean along with associated ecosystems), this study uses a 1-D coupled sea ice-ocean physical-biogeochemical model to analyze the physical and biological controls on simulated ice algae and phytoplankton blooms. The analysis contains three distinct components: 1) Investigation of the impacts of subgrid-scale non-uniform snow depth distributions on the growth of ice algae by applying a new parameterization for light transmission through sea ice [Abraham et al., 2015]; 2) assessment of the influences of ice algae on the simulated phytoplankton bloom by coupling and decoupling the sympagic and pelagic ecosystems; and 3) evaluating the sensitivity of the simulated ice algal bloom to a set of selected parameters and parameterizations following recommendations by Steiner et al. [2016a]. The test location for our model study is set in Resolute Passage in the Canadian Arctic Archipelago, based on the availability of a comparatively rich observational dataset at this location. Observations are described in detail in the Experimental Design and Observation Subsections below.

2.2 Methods

2.2.1 Model description

Physical model

The sea ice component of the coupled sea ice-ocean physical model is the 1-D thermodynamic model of Flato and Brown [1996] with most recent updates from Abraham et al. [2015]. These updates include new parameterizations for the light fields and heat fluxes through sea ice by accounting for a subgrid-scale snow depth distribution, melt ponds, and temperature-dependent extinction and transmissivity coefficients (see Appendix A1 for a synopsis of these updates). These new parameterizations improved the evolution of the simulated light fields under the landfast ice in Resolute Passage during the melt period of 2002 [Abraham et al., 2015]. In the present study, some of the optical parameters of the

sea ice model were modified to improve the fit of the simulated results to observations. A set of retuned optical parameters is provided with references for justification in Table 2.1. Although seasonal changes to the properties of snowfall have not been included in the present study, the snowfall rate has been varied with time based on specified precipitation data, in contrast to a prescribed constant rate as in earlier studies [Flato and Brown, 1996; Abraham et al., 2015]. An alternative approach to that of Abraham et al. [2015] for the treatment of subgrid scale variability of snow/ice depth, not attempted in this study, is described in Long et al. [2015]. Long et al. [2015] treat subgrid scale variability of ice thickness by altering the default model formulation, in which photosynthesis is subject to grid-cell averaged light penetration, to a formulation where the photosynthesis is subject to differing light conditions under the ice due to different ice conditions within a given grid scale. The modifications in Long et al. [2015] indicate that the mean grid-cell primary productivity is over-estimated in the default formulation.

Table 2.1: Extinction and transmissivity coefficients, as well as surface albedos used in this study

Symbol	Quantity	Value	Reference
$\kappa_{s,f}$	Extinction coefficient for freezing snow	14 m ⁻¹	Grenfell and Maykut [1977]
$\kappa_{s,m}$	Extinction coefficient for melting snow	7.5 m ⁻¹	Grenfell and Maykut [1977]
$\kappa_{i,f}$	Extinction coefficient for freezing sea ice	1.2 m ⁻¹	Smith [1988]
$\kappa_{i,m}$	Extinction coefficient for melting sea ice	0.8 m ⁻¹	Light et al. [2008]
κ_m	Extinction coefficient for melt ponds	0.5 m ⁻¹	Abraham et al. [2015]
κ_{ia}	Extinction coefficient for ice algae	0.017 (mmol N m ⁻³) ⁻¹ m ⁻¹	McDonald et al. [2015]
κ_{pd}	Extinction coefficient for phytoplankton and detritus	0.03 (mmol N) ⁻³) ⁻¹ m ⁻¹	Lavoie et al. [2009]
$i_{0,s,f}$	Transmissivity coefficient for freezing snow	0.15	Vancoppenolle et al. [2010]
$i_{0,s,m}$	Transmissivity coefficient for melting snow	0.15	Vancoppenolle et al. [2010]
$i_{0,i,f}$	Transmissivity coefficient for freezing sea ice	0.5	Lavoie et al. [2005a]
$i_{0,i,m}$	Transmissivity coefficient for melting sea ice	0.5	Lavoie et al. [2005a]
$i_{0,m}$	Transmissivity coefficient for melt ponds	0.5	Abraham et al. [2015]
$\alpha_{s,f}$	Surface albedo of freezing snow	0.8	Vancoppenolle et al. [2010]
$\alpha_{s,m}$	Surface albedo of melting snow	0.7	Lavoie et al. [2005a]
$\alpha_{i,f}$	Surface albedo of freezing sea ice	0.6	Within the range between Vancoppenolle et al. [2010] and Perovich et al. [2002]
$\alpha_{i,m}$	Surface albedo of melting sea ice	0.5	Vancoppenolle et al. [2010]
α_m	Surface albedo of melt ponds	0.3	Light et al. [2008]

The physical processes in the water column are simulated by the General Ocean Turbulence Model (GOTM) of Burchard et al. [2006]. GOTM provides the physical quantities required for computation of biogeochemical variables in the water column, such as horizontal velocity fields, turbulent transports, photosynthetically active radiation (PAR), and temperature. Details of model parameterizations for these quantities are provided in the GOTM website (<http://www.gotm.net>).

Biogeochemical model

A biogeochemical model representing the lower-trophic level of sea ice and pelagic ecosystems in the Arctic was developed within the Framework for Aquatic Biogeochemical Models [Bruggeman and Bolding, 2014] to facilitate the coupling with the physical model described above. The schematic diagram of the biogeochemical model is shown in Figure 2.1. The sea ice component of the biogeochemical model simulates the temporal evolution of four state variables (ice algae, nitrate, ammonium, and silicate) in the sea ice skeletal layer. The ice algae module is based on Lavoie *et al.* [2005a]. It was updated in this study by incorporating nitrate to account for potential algal growth reduction due to nitrogen limitation, as well as including ammonium to represent the biogeochemical processes within sea ice more realistically. At any given time, the growth of simulated ice algae is limited by one of the four limiting factors: light, ice melt, silicate, or nitrate. A limitation index for each factor is determined as a non-dimensional index that varies between 0 and 1 as in Lavoie *et al.* [2005a]. The ice algal growth rate is then determined by the minimum of the four indices multiplied by the specific growth rate at a given temperature of the ice skeletal layer (A2).

We used a series of sensitivity analyses, carefully planned as a progression from most-to least-known variables, to determine parameters for unknown/unmeasured quantities or processes (e.g., over-wintering biomass or ice-algae mortality) based on more easily obtained observations (i.e. phenology of the ice algae bloom). In the 1D ice algae/pelagic ecosystem development paper, the first step was setting our model parameters to documented/known parameters (e.g. temperature-, light-, and nutrient-dependence). The next step was intended to fit the onset of the bloom (defined arbitrarily at when the ice-algae biomass becomes greater than 100 mg chl-a/m³) close to that of observations, and minimum/over-wintering biomass was used as the primary tuning mechanism for matching the observation-model for bloom onset. For the next step, maximum biomass was determined through the coincident tuning of linear and quadratic mortality (but countering effects to keep the bloom onset at the same time).

To study the sympagic-pelagic ecological interactions at the lower-trophic level, the sea ice biogeochemical model was coupled to a ten-compartment (small and large phytoplankton, microzooplankton, mesozooplankton, small and large detritus, biogenic silica, nitrate, ammonium, and silicate) pelagic biogeochemical module based on Steiner *et al.* [2006a]. This module was updated by including mesozooplankton as a prognostic variable and by partitioning detritus into small and large size classes. At the ice-water interface dissolved nutrients are exchanged through molecular diffusion. Ice algae released into the water

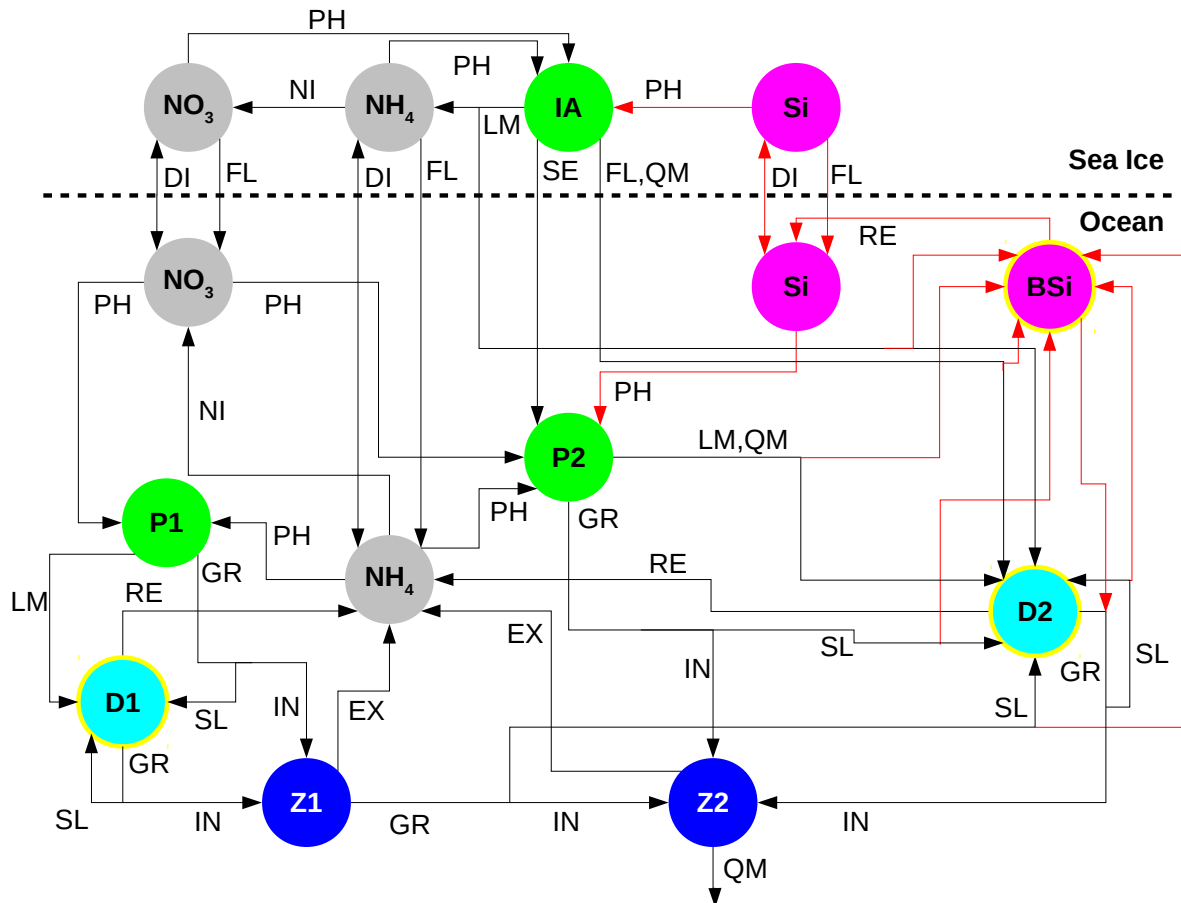


Figure 2.1: Schematic diagram of the coupled sea ice-ocean biogeochemical model. Circles represent the model state variables: nitrate (NO_3), ammonium (NH_4), silicate (Si), ice algae (IA), small phytoplankton (P1), large phytoplankton (P2), microzooplankton (Z1), mesozooplankton (Z2), small detritus (D1), large detritus (D2), and biogenic silica (BSi). Sinking variables are bounded by yellow circles. Black and red arrows represent paths of nitrogen and silicon transfers between the variables, respectively: photosynthesis (PH), nitrification (NI), diffusive mixing (DI), flushing (FL), seeding (SE), linear mortality (LM), quadratic mortality (QM), remineralization (RE), grazing (GR), ingestion (IN), sloppy feeding (SL, for inefficient grazing that leaves unconsumed but dead prey), and excretion (EX).

column are treated similarly as in the coupled model of *Lavoie et al.* [2009]: sloughed ice algae enter either the large phytoplankton pool in which they continue to grow or the large detritus pool in which they sink rapidly as aggregate products. The equations and parameters for the coupled biogeochemical model are provided in Appendix A2.

Experimental design

The 1-D model was applied to simulate ice algae and pelagic primary production within and under the landfast first-year sea ice in Resolute Passage, at a location with a water depth of 141 m. Resolute Passage was chosen for the study site because extensive field research has been conducted in the area [*Cota et al.*, 1987; *Lavoie et al.*, 2005a; *Papakyr-iakou and Miller*, 2011; *Galindo et al.*, 2014; *Brown et al.*, 2015-1; *Geilfus et al.*, 2015a]. Specifically, model simulations were conducted for a location representative of the Arctic Ice Covered Ecosystem (Arctic-ICE) field campaign (74.71°N, 95.25°W). This field campaign took place during the spring of 2010 in order to study the physical and biological processes controlling the timing of ice algae and under-ice phytoplankton blooms [*Mundy et al.*, 2014a]. The model was divided into 10 uniformly-spaced layers for sea ice and 100 layers for the upper 100 m of the water column. With the ultimate goal of implementing the parameterizations considered into coarser-resolution regional or global ocean circulation models, we do not attempt to resolve small-scale under-ice processes finer than 1 m. In order to limit the ultimate computational burden, we compared the 10-layer model to 5- and 2-layer simulations, deciding that the minor differences (1–2%) in output did not justify curtailing the effort at this stage.

The model was integrated for 8 months (1 February – 30 September, 2010) with a timestep of 10 minutes, and forced with Environment Canada’s hourly weather data (including surface air temperature, zonal and meridional wind at 10 m above the sea surface, surface air pressure, relative humidity, cloud cover, and precipitation) collected at the Resolute airport, located within 10 km of the study site. Temperature, salinity, and horizontal velocity fields of the ocean were restored over the entire water column with restoring timescale of 1 day (temperature and salinity) and 10 minutes (horizontal velocity) to the output of a 3-D regional model simulation (NEMO-LIM2) used in *Dukhovskoy et al.* [2016a]. We chose to restore the model this often in order to tightly constrain the physical water column properties and thus focus on comparing biogeochemical components of the model. The initial snow and melt pond depths and ice thickness were set to 5, 0, and 55 cm, respectively. The initial concentration of ice algae was set to 1.0 mmol N m⁻³ (ca. 3.5 mg Chl *a* m⁻³; the observed range of C:N:Chl *a* ratios is described in Appendix

A2). The initial concentration of nitrate (silicate) was set to a constant value of $7.2 \text{ mmol N m}^{-3}$ ($14.7 \text{ mmol Si m}^{-3}$) throughout the bottom ice and the water column, based on the measurements of these nutrients during the Arctic-ICE 2010 field campaign [Mundy *et al.*, 2014a; Galindo *et al.*, 2014]. The initial concentrations of ammonium both in the sea ice and the water column were assumed to be small [e.g., Harrison *et al.*, 1990], and hence, set to $0.01 \text{ mmol N m}^{-3}$. Similarly, the initial concentrations of all other pelagic biogeochemical state variables were set to $0.01 \text{ mmol N m}^{-3}$ (mmol Si m^{-3} for biogenic silica) throughout the water column.

2.2.2 Observations

Observational data used to evaluate the model results include snow and melt pond depths, ice thickness, under-ice PAR, and chlorophyll *a* (Chl *a*). Measurements of these variables were conducted during May and June of 2010 as part of the Arctic-ICE field campaign. Observed snow and melt pond depths, ice thickness, and Chl *a* in the bottom 3 cm of sea ice were sampled at various sites of high, medium, and low snow covers. The mean value of Chl *a* is therefore an estimate of the site average, as presented in Galindo *et al.* [2014], and is comparable to a grid cell average in a regional or global model. Concentrations of Chl *a* in the water column were determined by collecting samples at five depths (2, 5, 10, 25, and 50 m below the sea surface) using 5 L Niskin bottles and following the procedures outlined in Galindo *et al.* [2014]. *In situ* time series data for daily-mean under-ice (2 m below sea surface) PAR were collected using two independent tethers moored to the sea ice below high (> 40 cm prior to snowmelt onset) and low (< 20 cm prior to snowmelt onset) snow cover sites (within 4 – 6 m of the CTD casts). Technical details of these PAR measurements are provided in Mundy *et al.* [2014a]. In addition to the tether measurements, instantaneous under-ice PAR was estimated by extrapolating the 20 m depth CTD-based PAR measurement to the surface following Frey *et al.* [2011]. Casts of CTD and a biospherical 4 pi sensor were obtained daily through the main sampling hole within a heated tent on the sea ice. Details of the CTD-based under-ice PAR estimates are described in Gale [2014].

2.3 Results

Results are divided into three parts based on the types of model simulations conducted. The first subsection evaluates the performance of the standard run. The second subsection

compares the result of the standard run with a simulation that excludes ice algae. The third subsection provides the results of parameter sensitivity experiments. Specific setups of these runs are described in each of these subsections.

2.3.1 Model evaluation

The standard run was conducted with the setup outlined in the previous section (Experimental design) and by applying the Rayleigh distribution for representing the subgrid-scale snow depth variability (see Appendix A1). *Abraham et al.* [2015] indicated a better fit for the Rayleigh distribution than gamma probability distribution based on observations from the Arctic-ICE 2010 study (not shown).

Snow and melt pond depths and ice thickness

In many previous 1-D model studies, the temporal evolution of snow depth was either prescribed to observed snow depth data [e.g., *Lavoie et al.*, 2005a; *Pogson et al.*, 2011; *Palmer et al.*, 2014a] or simulated by prescribing a constant snowfall rate [*Flato and Brown*, 1996; *Abraham et al.*, 2015]. In this study, snow depth was simulated by prescribing a variable snowfall rate based on observed precipitation data. The simulated and observed time series of snow and melt pond depths are shown in Figure 2.2a. The simulated snow depth increased occasionally as a result of snowfall events until the maximum depth (ca. 20 cm) was reached by mid-May. In the standard run, the simulated snow started melting toward the end of May and completely vanished within 3 weeks. Snowmelt resulted in the formation of melt ponds which reached a maximum depth of 5 cm shortly after the snow disappearance. In comparison with the field measurements presented in Figure 2.2a, the timing of melt events was simulated reasonably with the distributed snow case.

Figure 2.2b shows the simulated and observed time series of ice thickness. In the standard run, simulated ice grew gradually to a maximum thickness of about 150 cm by early June and then started melting following the initial snowmelt. In the standard case, the distributed snow parameterization represents snow-free areas, which allows the ice to start melting before all the snow has disappeared. The simulated ice vanished completely in early July after which the sea surface remained ice-free until late September. The simulated ice thickness agreed well with the observations throughout the sampling period (Figure 2.2b), whereas the ice break up in the simulation occurred a week earlier than in the observations [*Galindo et al.*, 2014]. This difference could be attributed to dynamic processes of sea ice (e.g., wind-driven ridging and rafting) which are not accounted for in our 1-D model.

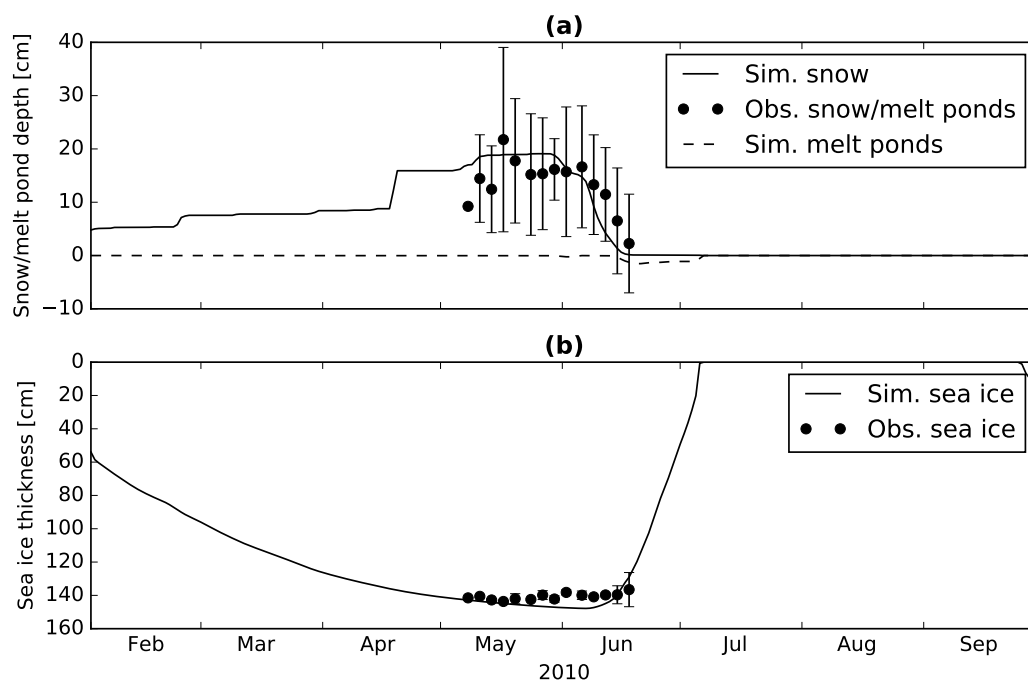


Figure 2.2: Simulated and observed snow depth, melt-pond depth, and ice thickness. Time series of (a) simulated daily-mean snow (solid line) and melt-pond (dashed line) depths, observed snow/melt pond depth (circles), and (b) simulated daily-mean (line) and observed (circles) ice thickness. Circles represent the site-average values with one standard deviations indicated by vertical bars.

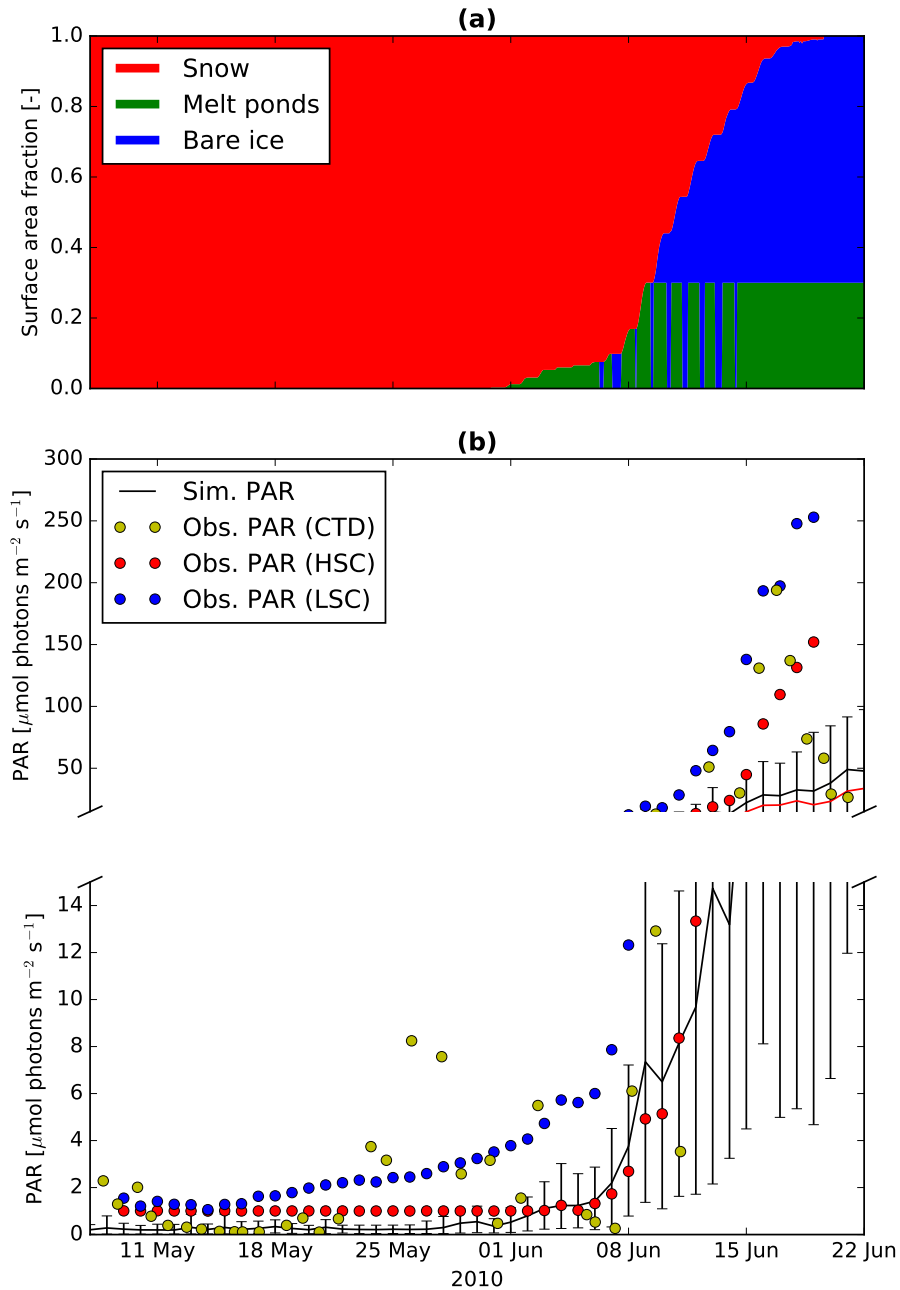


Figure 2.3: Simulated snow, melt-pond depth, and bare ice area, and simulated and observed PAR. Time series of (a) surface area fraction of simulated snow (red), melt ponds (green), and bare ice (blue) and (b) simulated daily-mean (line) and observed (circles) under-ice PAR during the Arctic-ICE 2010 study period. In (b), the units for the simulated PAR values were converted from W m^{-2} to $\mu\text{mol photons m}^{-2} \text{s}^{-1}$ by a conversion factor of 4.56 following *Lavoie et al.* [2005a]. Vertical bars associated with the solid line represent the diurnal range of simulated under-ice PAR. Red and blue circles represent the daily-mean values measured using tethers deployed over high (HSC) and low (LSC) snow cover sites, respectively. Yellow circles are the instantaneous values based on CTD casts (CTD).

Surface area fractions and under-ice PAR

Simulation of the light penetration through snow and sea ice is crucial for simulating a reasonable ice algal bloom, as the initial phase of the bloom is typically limited by light [Gosselin *et al.*, 1990; Lavoie *et al.*, 2005a; Leu *et al.*, 2015]. During the melt period, surface area fractions of simulated snow, melt ponds, and bare ice undergo changes that affect the amount of light reaching the ice base as indicated in Figure 2.3. In the standard simulation, the surface of the simulated ice was fully snow-covered prior to the snowmelt onset. Consequently, the simulated daily-mean under-ice PAR during this period was less than $1 \mu\text{mol photons m}^{-2} \text{ s}^{-1}$. This value is lower than either of the tether measurements, but in good agreement with most of the CTD-based estimates. In the model, about 10% of the snow surface was replaced with melt ponds due to snowmelt during the first week of June, resulting in an increase of the daily-mean under-ice PAR to more than $1 \mu\text{mol photons m}^{-2} \text{ s}^{-1}$. This value is comparable to the tether measurements at high snow cover station, as well as to the CTD-based estimates. By June 9, the surface area coverage of simulated melt ponds extended to 30% (the maximum value prescribed by the model). Further areal loss of simulated snow resulted in an emergence of bare ice, which covered 70% of the ice surface following the snow disappearance. The pulsed effect in melt pond area in mid-June (Figure 2.3a) reflects daily signals associated with daytime melting and overnight freezing (causing surface bare ice). The simulated under-ice PAR during this period exceeded $10 \mu\text{mol photons m}^{-2} \text{ s}^{-1}$ (Figure 2.3b), which is comparable to both the tether and the CTD-based observations. As expected, the simulated gridbox-mean under-ice PAR was quantitatively closer to the CTD-based (site-average) estimates than the tether (point) measurements. Furthermore, the standard simulation successfully reproduced the smooth seasonal transition of under-ice PAR that is evident in the tether measurements during the melt period.

Sea ice ecosystem

Figure 2.4 shows the simulated time series of sea ice ecosystem variables. The standard run simulated an ice algal bloom that is comparable to the observations in terms of both the magnitude and timing of the bloom (Figure 2.4a). In the following, we discuss the dynamics of simulated sea ice ecosystem by partitioning into growth and decline phases.

The growth phase of simulated ice algal bloom lasted from late March to mid-May, while the bloom decline phase is from mid-May to late June. During the growth phase of the ice algal bloom, the simulated ice algal biomass in the standard run increased up to 1050

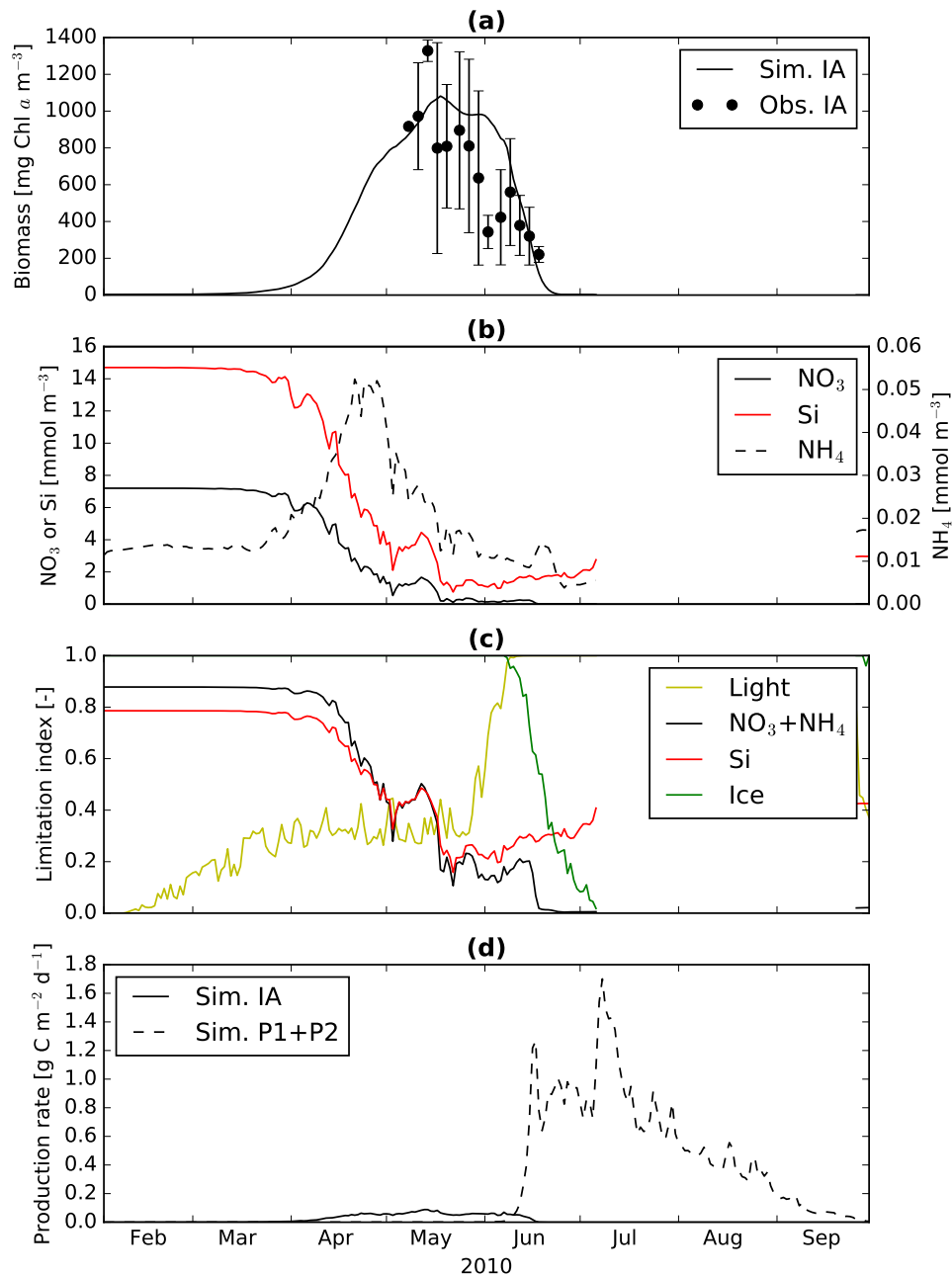


Figure 2.4: Simulated and observed ice algal biomass, nutrients, growth limitations, and simulated sympagic and pelagic production. Time series of (a) simulated (line) and observed (circles) Chl a concentrations in the bottom 3 cm of the sea ice, (b) simulated nitrate (solid black), ammonium (dashed black) and silicate (red) concentrations in the bottom 3 cm of sea ice, (c) simulated daily-mean growth limitation index for light (yellow), nitrogen (black), silicate (red), and ice melting (green), and (d) primary production rates of simulated ice algae (solid line) and phytoplankton (dashed line). In (a), circles represent the site-average values with one standard deviations indicated by vertical bars.

mg Chl *a* m⁻³ (Figure 2.4a). This maximum value in the bloom is within the range of observed values during the peak of the ice algal biomass (800 – 1300 mg Chl *a* m⁻³). Note that this wide range in the observed peak is due to sampling over different snow depth conditions, and that the model succeeded in simulating a bloom that falls near the center of the observed range. Up until the end of April, concentrations of simulated nitrate and silicate in the ice decreased rapidly due to uptake by ice algae, while the simulated ammonium concentration increased as a result of remineralization of dead ice algal cells (Figure 2.4b). During this time, the ice algal growth rate declined slightly even though nutrients are not yet limiting, likely due to the quadratic term in the parameterization of mortality. Consequently, both nitrate and silicate concentrations recovered slightly until they were drawn down further by ice algae during their bloom peak in mid-May. The ice algal growth was generally light-limited during the growth phase (Figure 2.4c), except for a day in the beginning of May when the nitrate concentration reached nearly 0.5 mmol m⁻³ (Figure 2.4b).

At the peak of the ice algal bloom, simulated nutrients became extremely low, nearly 0 mmol m⁻³ for nitrate and ammonium and 1 mmol m⁻³ for silicate (Figure 2.4b). Consequently, the ice algal growth became nitrogen-limited following the peak (Figure 2.4c), and remained so until the end of the bloom in late June (Figure 2.4a). The simulated range of nitrate concentration (0 – 8 mmol m⁻³; Figure 2.4b) matches with the observed range reported in *Galindo et al.* [2014]. In contrast, the simulated range of ammonium concentration (0 – 0.05 mmol N m⁻³) is much smaller than the range typically observed in the bottom ice [e.g., *Vancoppenolle et al.*, 2013a]. This discrepancy is most likely due to the fact that much of the ammonium found in the bottom ice is trapped in the ice matrix and therefore not accessible to ice algae residing in the brine phase of the ice [*Vancoppenolle et al.*, 2013a]. The model simulates the remaining fraction of ammonium available for ice algae which is low in abundance due to rapid turnover of ammonium production and removal processes. Figure 2.4d presents the time series of depth-integrated production rates by simulated ice algae and phytoplankton (i.e., sum of P1 and P2). The production rate of simulated ice algae was around 0.1 g C m⁻² d⁻¹ during its bloom peak in mid-May. The time-integrated production by ice algae and phytoplankton over the simulation period was about 4 and 60 g C m⁻², respectively. Hence, the primary production by simulated ice algae accounted for 6% of the entire sea ice and water column primary production. This fraction is within the range of the observational and model estimates for first-year Arctic sea ice [2 – 33%; *Legendre et al.*, 1992; *Gosselin et al.*, 1997; *Lavoie et al.*, 2009].

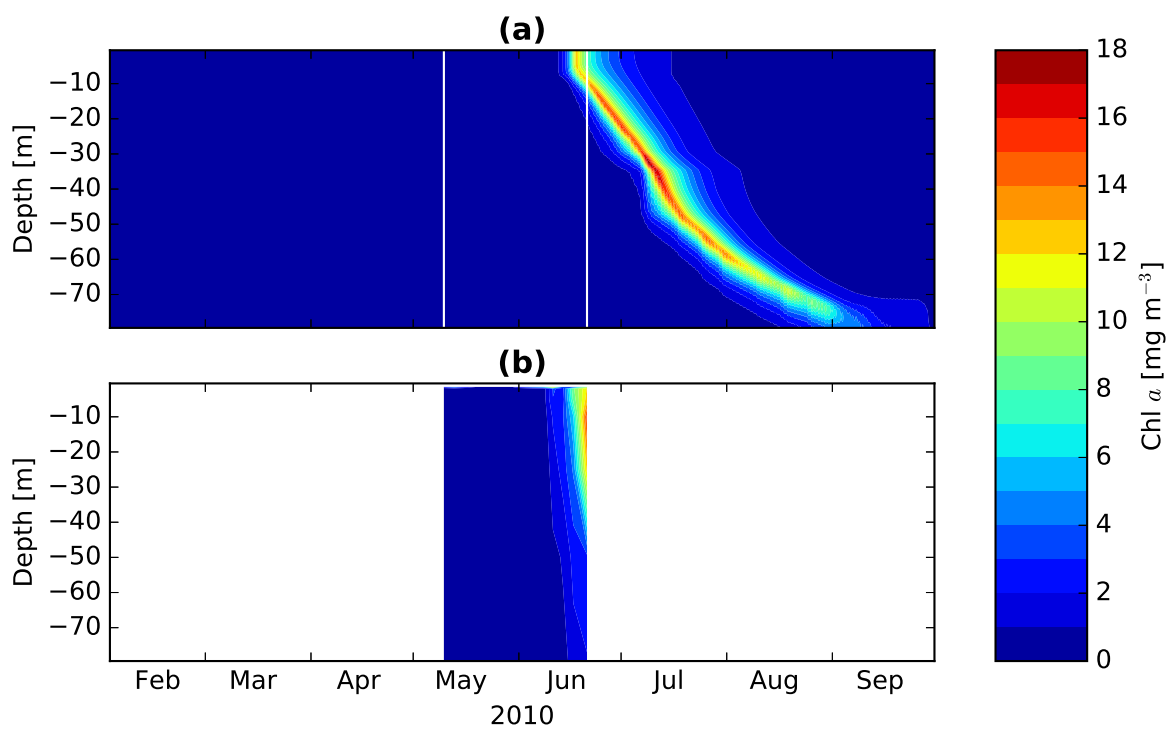


Figure 2.5: Simulated and observed Chl a concentration. Time series of (a) simulated and (b) observed Chl a concentrations in the upper 80 m of the water column.

Pelagic ecosystem

Figure 2.5 shows the comparison of simulated and observed time series of chlorophyll *a* concentrations in the upper 80 m of the water column. In mid-June, the model simulated an under-ice phytoplankton bloom in the upper 10 m of the water column (Figure 2.5a). This bloom was dominated by large phytoplankton (Figure S1b), and reached a peak concentration of $13 \text{ mg Chl } a \text{ m}^{-3}$ in late June. The timing, magnitude, and vertical extent of the simulated under-ice phytoplankton bloom are consistent with the observed bloom (Figure 2.5b), which was also dominated by large cells [Mundy *et al.*, 2014a]. The simulated bloom migrated downward and formed a subsurface chlorophyll maximum of $18 \text{ mg Chl } a \text{ m}^{-3}$ at 15 – 40 m between late June and early July. During the ice-free period, increased light penetration allowed the deepening of the simulated subsurface chlorophyll maximum to a depth of 75 m where it maintained fairly large concentrations (above $6 \text{ mg Chl } a \text{ m}^{-3}$) until the end of August. The formation and subsequent deepening of a deep chlorophyll-maximum is a typical feature in the Arctic where surface nutrients are low (the chlorophyll maximum typically follows the nitricline). No direct observations are available for this particular time period near Resolute to evaluate the deepening of the subsurface chlorophyll maximum simulated by the model. However, observations taken during the last decade in the Beaufort Sea and Canadian Archipelago show the subsurface chlorophyll maxima with depths ranging from 35 and close to 100 m depending on time and location measured [Tremblay *et al.*, 2008; Carmack *et al.*, 2010; McLaughlin and Carmack, 2010; Carmack and McLaughlin, 2011] which is also represented in model results [Steiner *et al.*, 2015b]. The chlorophyll maximum in the Chukchi Sea tends to be much shallower [Brown *et al.*, 2015-2], while the deepest maxima have been observed in the Beaufort Sea. A maximum depth of 75 m for the deep chlorophyll maximum in the Canadian Arctic Archipelago is within the range of observations. The daily production rates corresponding to the under-ice phytoplankton bloom ($1.2 \text{ g C m}^{-2} \text{ d}^{-1}$) and the subsurface chlorophyll maximum (up to $1.6 \text{ g C m}^{-2} \text{ d}^{-1}$) simulated by the model (Figure 2.4d) are comparable to the observed rates in Resolute Passage [$1.1 \text{ g C m}^{-2} \text{ d}^{-1}$; Mundy *et al.*, 2014a] and in the Beaufort Sea [$1.4 \text{ g C m}^{-2} \text{ d}^{-1}$; Mundy *et al.*, 2009], respectively.

Figure 2.6a-c illustrates the temporal evolution of simulated dissolved nutrients in the upper 80 m of the water column. Prior to the development of the under-ice phytoplankton bloom in mid-June (Figure 2.5a), the concentrations of simulated nitrate (Figure 2.6a) and silicate in the upper 15 m (Figure 2.6c) were reduced as a result of the uptake by ice algae. In contrast to nitrate and silicate, concentrations of simulated ammonium increased slightly below the nitracline due to the remineralization of dead ice algal cells released into

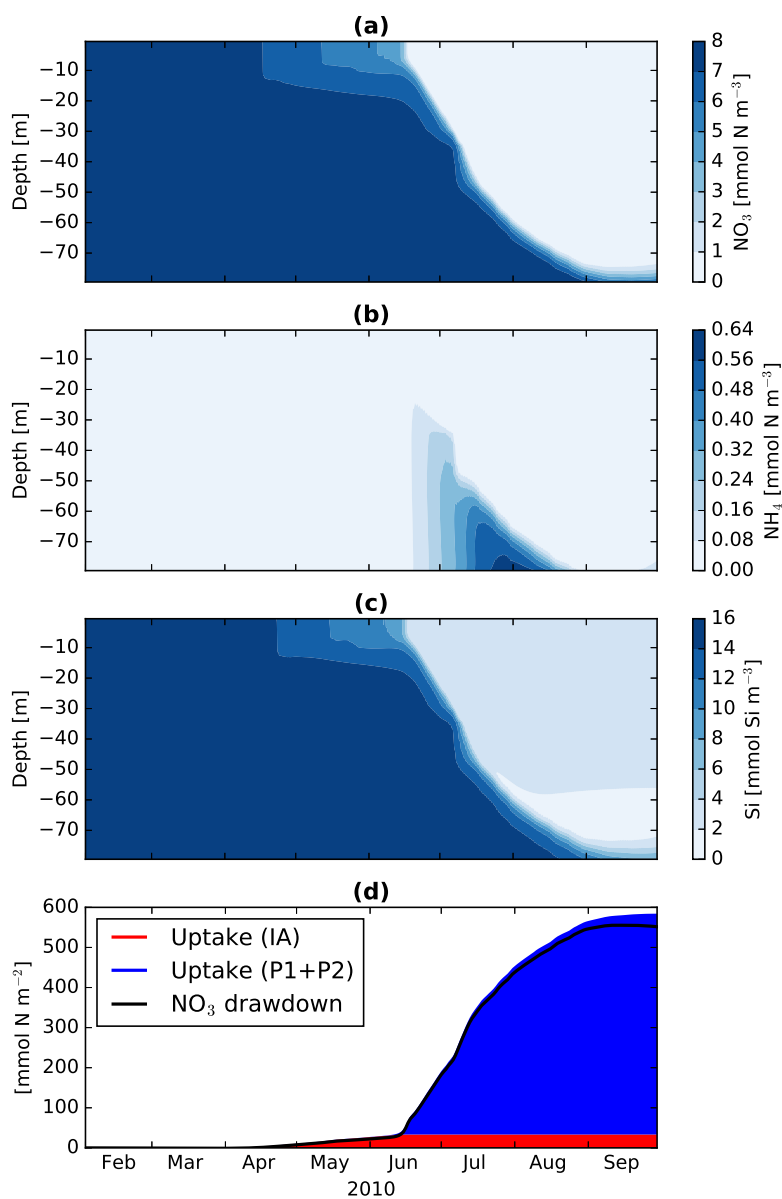


Figure 2.6: Simulated water column concentrations of nutrients and biological uptake and drawdown of nitrate. Simulated time series of (a) nitrate, (b) ammonium, and (c) silicate concentrations in the upper 80 m of the water column (depth of entire water column is 141 m). (d) Simulated time series of cumulative depth-integrated nitrate uptake and drawdown. In (d), areas filled in red represent the cumulative uptake by ice algae integrated over the bottom 3 cm of the ice skeletal layer, areas filled in blue represent the cumulative uptake by phytoplankton (P1 and P2) integrated over the upper 80 m of the water column, and the black line represents the cumulative amount of nitrate drawn down from the upper 80 m of the water column. Note that the sum of the two uptake terms (red+blue) does not balance with the drawdown during the ice-free period; the mismatch represents the uptake of nitrate entrained from the layer below 80 m.

the water column (Figure 2.6b). In late June, these nutrients were drawn down by large phytoplankton, and decreased to $< 1 \text{ mmol m}^{-3}$ (nitrate; Figure 2.6a), $< 0.04 \text{ mmol m}^{-3}$ (ammonium; Figure 2.6b), and $< 4 \text{ mmol m}^{-3}$ (silicate; Figure 2.6c) in the upper 10 m of the water column. These values of simulated nitrate and silicate concentrations are close to the values (0.2 mmol m^{-3} for nitrate+nitrite and 2.8 mmol m^{-3} for silicate) reported at the end of the sampling period (21 June) in Resolute Passage [*Mundy et al.*, 2014a]. The concentrations of simulated nutrients remained below these levels until the end of the simulation period (Figure 2.6a-c) because large detritus, which consists of dead cells of ice algae and large phytoplankton and fecal pellets, sank quickly (50 m d^{-1} as specified in the model, following *Lavoie et al.*, 2009) into the deeper water column before they could be remineralized in the upper water column. The rapid sinking of large detritus resulted in the accumulation of ammonium at depth below the nitracline in late June onwards (Figure 2.6b).

To demonstrate that the ice algal uptake and the nutrient removal in the water column are balanced in the model, the time series of depth-integrated (3 cm) cumulative nitrate uptake by ice algae is displayed with the depth-integrated cumulative nitrate drawdown and total uptake by phytoplankton in the upper 80 m of the water column (Figure 2.6d). Clearly, the total amount of nitrate consumed by ice algae is equivalent to the amount removed from the water column until the onset of the pelagic bloom in mid-June. The result demonstrates an important role of ice algae in reducing the ambient nutrients in the upper water column. This important aspect of sympagic-pelagic ecological coupling will be examined further in a later section. The decreasing trend of simulated nitrate in the water column during May and June (Figure 2.6a) is generally in good agreement with the observed nitrogen time series in the ice and underlying water column as reported in *Galindo et al.* [2014].

2.3.2 Sympagic-pelagic ecosystem coupling

In order to assess the impact of the simulated ice algal bloom on the underlying pelagic ecosystem, we conducted an additional simulation that turned off the ice algal bloom (referred to as the exclusion run). This scenario was established by setting the initial biomass of ice algae to zero, while all other setups are identical to the standard run. Hence, the difference in the results between the standard and the exclusion runs represents the impact of ice algae on the pelagic ecosystem.

Figure 2.7 displays the comparison of the two runs in terms of Chl *a* concentrations in the

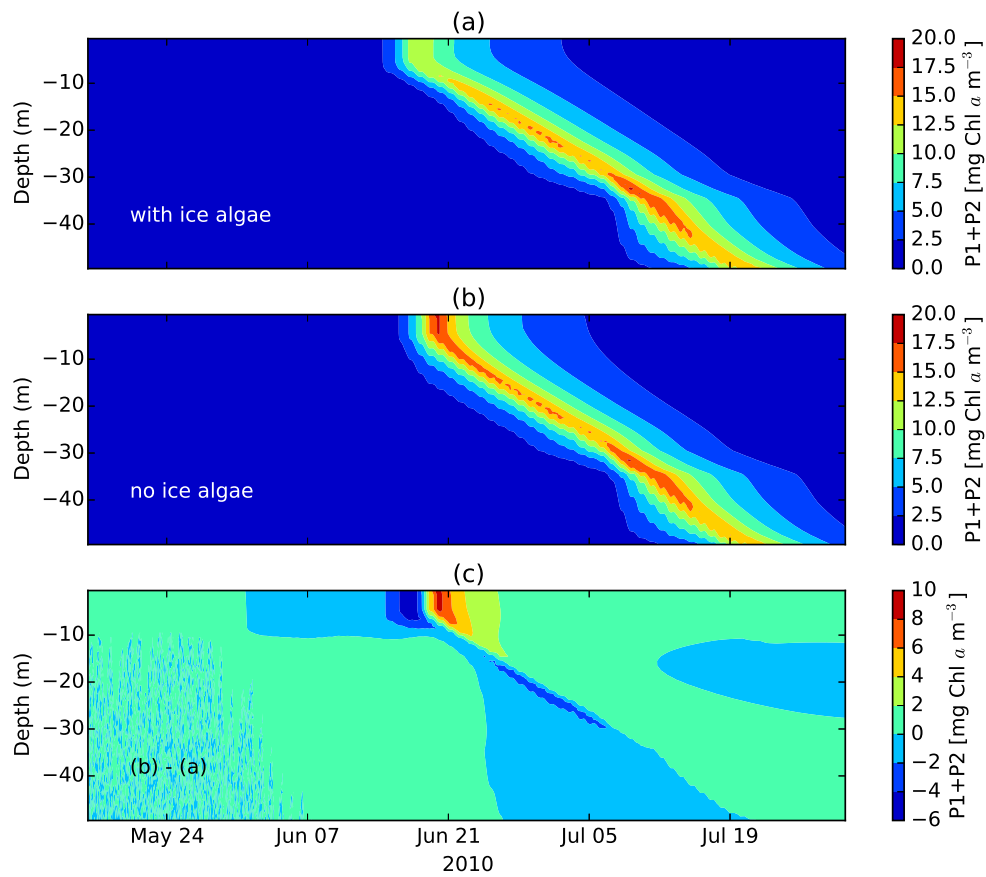


Figure 2.7: Water column Chl *a* concentration when ice algae are present, absent, and the difference. Simulated phytoplankton bloom in the upper 50 m of the water column when ice algae are present (a), absent (b), and the difference (c). Phytoplankton are sum of large and small (P1 and P2) groups.

upper 50 m of the water column. The differences between the two runs are most evident in late June, which correspond to the under-ice bloom in the upper 10 m of the water column (Figure 2.7c). Both the timing and magnitude of the bloom were affected by the presence/absence of ice algae. When ice algae were excluded from the simulation (Figure 2.7b), the onset of the under-ice bloom was delayed by a few days. This delay in the bloom onset is due to the lack of seeding by ice algae in the exclusion run [Hayashida *et al.*, 2016]. Despite the delay in the development of the under-ice bloom, the exclusion run simulated a higher peak in Chl *a* (with a concentration difference of about 7 mg Chl *a* m⁻³) than the standard run. The enhanced peak in the exclusion run is due to the absence of nutrient drawdown by ice algae (Figure 2.8), which makes a concentration difference of about 3 mmol N m⁻³ in the upper 10 m of the water column at the onset of the under-ice bloom. (It is not due to the absence of light-shading by the ice algae, as the pelagic bloom does not begin in the standard run until after the ice algal bloom has ended.). The effects of ice algae in the pelagic ecosystem appear to be relatively small below the upper 10 m of the water column, as there is no substantial difference in either Chl *a* or nitrate concentrations between the standard and the exclusion runs.

Sinking rate of large detritus

In the model, large detritus (D2) represents the non-living particulate matter originating mainly from ice algal and large phytoplankton cells. The simulated large detritus is assumed to sink at a constant rate (w_{d2} ; Appendix A2) which is presumably faster than the sinking rate of small detritus, another form of detritus considered in the model. In the standard run, a sinking rate of 50 m d⁻¹ was prescribed for large detritus following Lavoie *et al.* [2009]. However, observations of this rate span a range of values. Onodera *et al.* [2015] observed sinking rates from 37 to more than 85 m d⁻¹ for diatoms in the western Arctic Ocean. Higher and lower rates have also been measured, with sinking rates well over 100 m d⁻¹ among Antarctic ice algal aggregates [Sibert *et al.*, 2010] and near 20 m d⁻¹ in lab tests with the common Arctic ice algae diatom *Nitzschia frigida* [Aumack and Juhl, 2015].

In this sensitivity analysis, we assessed the simulated phytoplankton response to a change in the fast sinking rate. Runs with a slower sinking rate do not show much difference in the pelagic ecosystem until the sinking rate is lowered below a threshold of approximately 10 m d⁻¹. Above this threshold, large detritus is effectively removed from the euphotic layer and transported to depth before it can be remineralized (Figure 2.9 a and b). Below that

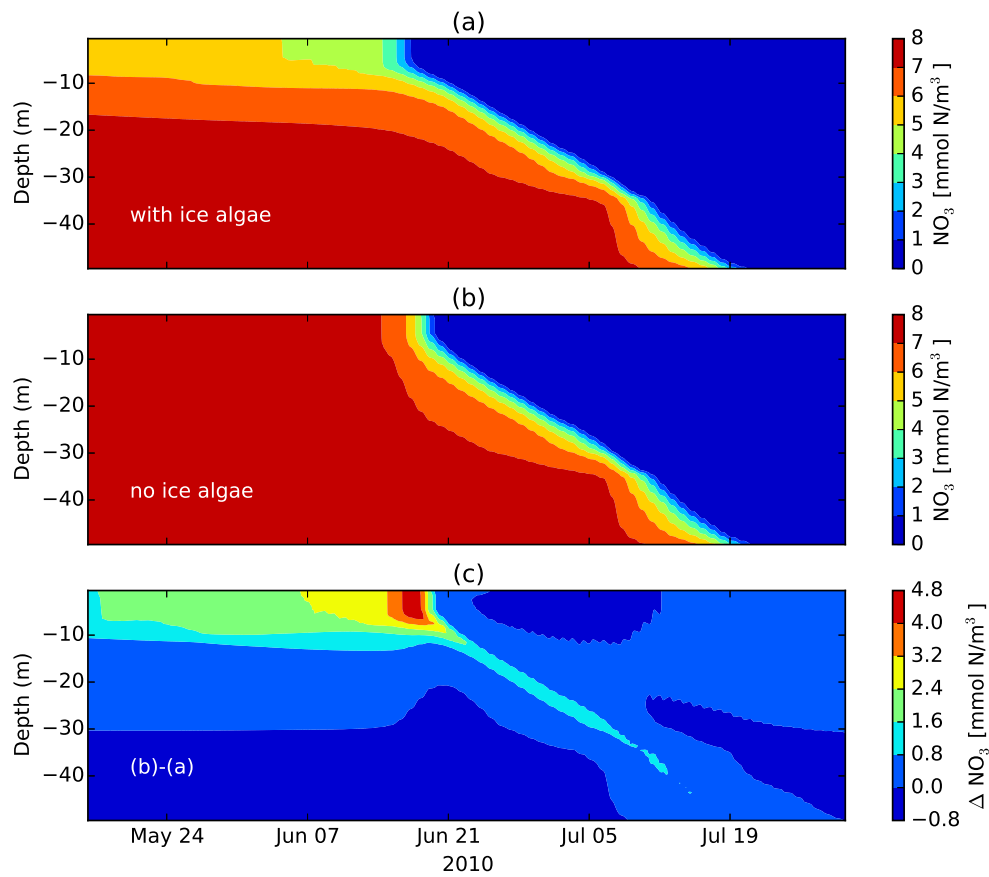


Figure 2.8: Water column nitrate when ice algae are present, absent, and the difference. Simulated NO_3 concentration in the upper 50 m of the water column when ice algae are present (a), absent (b), and the difference (c).

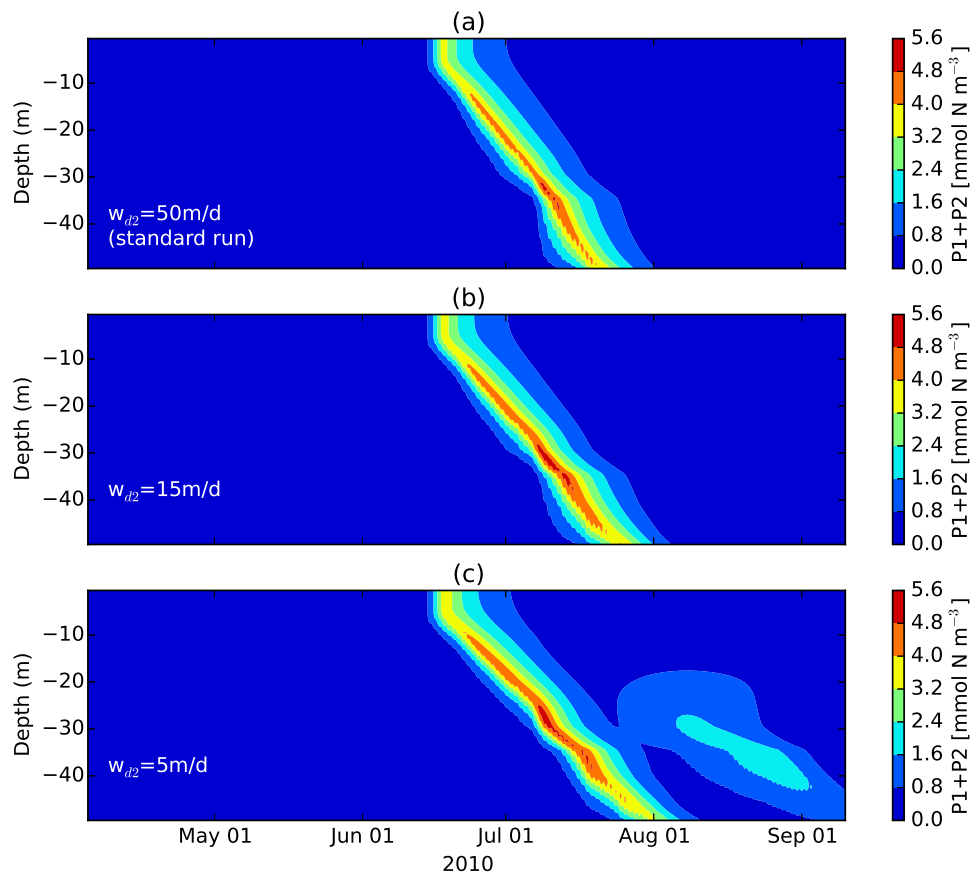


Figure 2.9: Phytoplankton in the water column with fast-sinking detritus. Simulated phytoplankton in the upper 50 m of the water column, with fast-sinking detritus (D_2) set at 50 m d^{-1} (a), 15 m d^{-1} (b), and 5 m d^{-1} (c). First bloom is dominated by large phytoplankton (P2, diatoms) and the later bloom in (c) is dominated by small phytoplankton (P1, flagellates).

threshold, e.g., at $w_{d2} = 5 \text{ m d}^{-1}$, a secondary sub-surface bloom, comprised of small phytoplankton (P1), forms after the first bloom (Figure 2.9c). This secondary bloom results from an increased supply of nitrogen. The remineralization rate from biogenic silica is an order of magnitude slower than that from D2 (0.01 d^{-1} , and 0.3 d^{-1} , respectively, Table S2), and hence the second bloom does not allow for silicate-dependent large phytoplankton.

2.3.3 Sensitivity analyses for ice algae

Given the influence of simulated ice algae on the underlying pelagic ecosystem, it is of utmost interest to investigate the physical and biological controls on the simulated ice algal bloom (and subsequently on the underlying ecosystem). The shape of these control functions is set via parameter values which are often not measured directly, but inferred from concentrations of observed variables that are also not well constrained. Sensitivity analyses focus on parameters that represent key uncertainties in the observational record. By varying each parameter over the range of observed (or estimated if not constrained by observations) uncertainty and determining which parameters have the strongest impact on properties of the simulated ice algal bloom, we can identify which observations would be most beneficial to improve our understanding of the system.

The growth of the ice algal bloom is dependent on both physical and biogeochemical processes. In the simulated ice algal bloom, several key parameters determine the strength of these influences. In the standard simulation, parameters controlling the onset, growth, maximum biomass, and termination of the modelled ice algae have been adjusted to result in good agreement with observations. In this section, key parameters associated with overwintering (pre-bloom) ice algal biomass, mortality, photosynthetic sensitivity, and nutrient limitation, are varied independently in order to determine the sensitivity of the simulated bloom.

The experiments testing photosynthetic efficiency (not shown) demonstrated that increasing photosynthetic efficiency does not increase the maximum biomass substantially, because of nutrient limitation. The experiments varying the ratio of intracellular silicate to nitrogen (also not shown) indicated that increasing the intracellular ratio Si:N by $\sim 20\%$ was enough for the ice algal growth to become silicate-limited instead of nitrogen-limited.

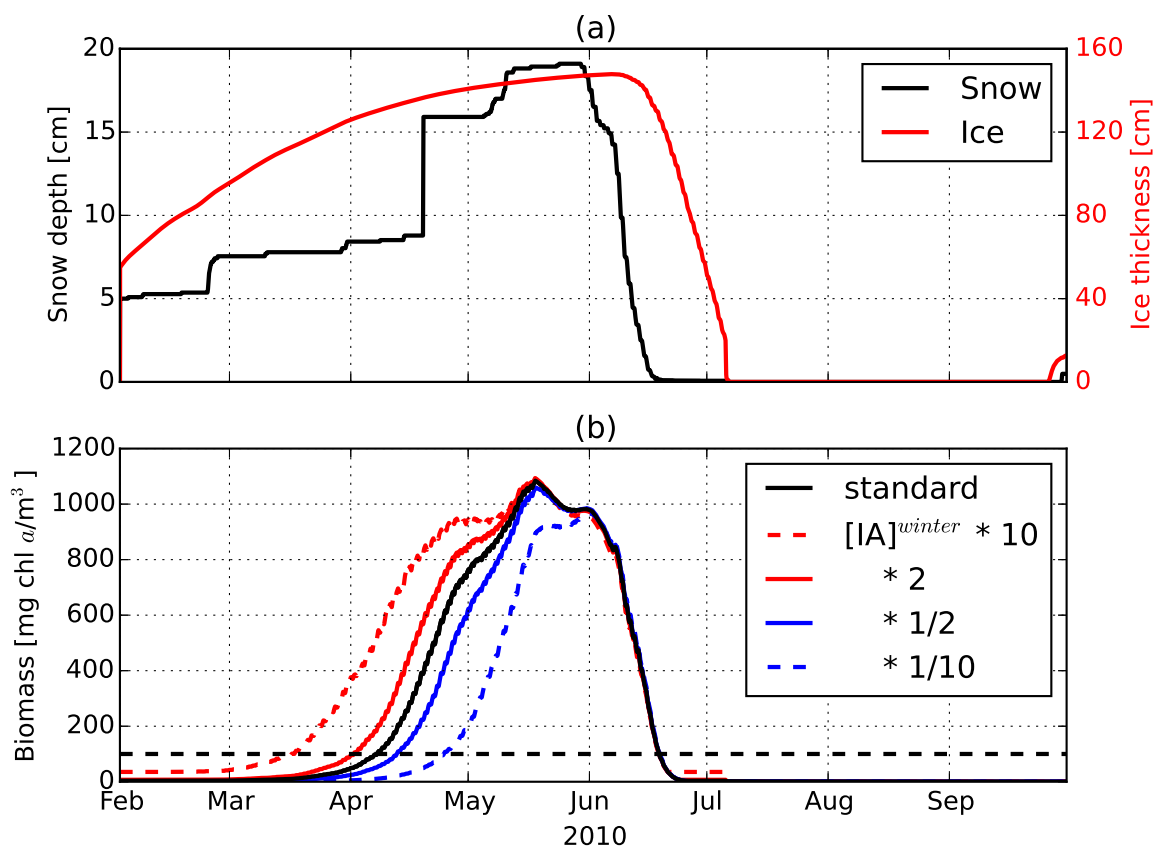


Figure 2.10: Snow and ice thickness and ice algal biomass, varying pre-bloom biomass. Snow and ice thickness (cm) and ice algal biomass during sensitivity analyses of the simulated ice algal bloom to variation of pre-bloom biomass (b), prescribed at 10, 2, 1/2, and 1/10 times that in the standard simulation (solid black line).

Pre-bloom algal biomass in the ice

In previous work, the pre-bloom ice algal biomass in simulations has been estimated based on water column measurements during ice formation [Steiner *et al.*, 2016a], or from early bloom measurements [Lavoie *et al.*, 2005a; Pogson *et al.*, 2011]. It is possible that processes involved in ice formation can preferentially pick up certain marine particles, such as algal cells, and ice algal biomass concentrations up to 2 orders of magnitude higher than the underlying water column have been observed in sea ice in fall and winter [Róžańska *et al.*, 2008; Niemi *et al.*, 2011].

The year-to-year variability in the amount of ice algae before the bloom may have a strong effect on the timing of the bloom onset. The timing of the onset of the simulated ice

algal bloom (defined as when the biomass surpasses $100 \text{ mg Chl } a \text{ m}^{-3}$) depends on the pre-bloom, or over-wintering, concentration (Figure 2.10b). The pre-bloom concentration is implemented in the model as a minimum ice algal biomass. In the standard run, the pre-bloom concentration was set at 1 mmol N m^{-3} (or $3.533 \text{ mg Chl } a \text{ m}^{-3}$) to match the observed bloom onset. This value is approximately 20% of the value used in *Lavoie et al.* [2009] of $0.5 \text{ mg Chl } a \text{ m}^{-2}$ ($16.7 \text{ mg Chl } a \text{ m}^{-3}$, assuming a 3 cm ice algal layer). This value was set for the more productive Beaufort Sea, but is an order of magnitude larger than that observed by *Niemi et al.* [2011] ($0.1 \text{ mg Chl } a \text{ m}^{-3}$ for first-year ice in the Beaufort Sea). Because of the large difference between these estimates of the pre-bloom concentration, the simulation was run with pre-bloom concentrations at 200%, 150%, 50%, and 10% of the standard value in order to test the importance of this value on the onset and maximum concentration of the ice algal bloom. With pre-bloom concentrations of 50% (200%) of the standard value, the subsequent ice algal blooms are slightly later (earlier), with the biomass reaching $100 \text{ mg Chl } a \text{ m}^{-3}$ approximately 4 days later (earlier). It is evident that a multiplicative change in the pre-bloom biomass results in an additive offset in the time needed to reach a specified biomass (consistent with exponential growth through the earlier parts of the bloom).

Modelled ice algal blooms for runs with the pre-bloom ice algal biomass values an order of magnitude larger or smaller than the standard value (Figure 2.10b) indicate that, at higher pre-bloom biomass, the bloom occurs earlier, but the maximum biomass is not much greater than in the standard run because the growth is terminated by nutrient limitation. When the pre-bloom ice algal biomass is one-tenth of that in the standard run, the timing of the bloom onset is delayed and the bloom levels off (at the time of the maximum biomass in the standard run). This is because the NO_3 limitation in that time period is approximately 0.2 day^{-1} (not shown). In an idealized 12 hour day, and no other limitation, the daily averaged minimum limitation would be half of that (0.1 day^{-1}), which is roughly equal to the grazing rate.

These results are in agreement with those of *Jin et al.* [2006], who found that doubling the initial ice algal biomass does not affect the maximum biomass of the bloom, and results in an onset 3 – 5 days earlier. In addition, *Pogson et al.* [2011] find that using the observed low initial biomass under high snow cover causes underestimation of the simulated maximum biomass when compared to the observations.

Mortality

The mortality rate for marine algae is commonly parameterized as some combination of linear and quadratic dependencies on biomass. To our knowledge mortality rates have not been directly measured for ice algae and the contribution of linear and quadratic contributions needs to be tested. Here, the mortality rate for ice algae (M ; Appendix A2) is defined as a function of biomass:

$$M = m_{lia} \exp(b_{ia}[T]_{ia}) + m_{qia}[IA] \quad (2.1)$$

where b_{ia} , $[T]_{ia}$, and $[IA]$ represent the temperature sensitivity coefficient, temperature in the ice skeletal layer, and ice algal biomass, respectively (see the Appendix for details). m_{lia} represents the rate constant for the temperature-dependent linear mortality and m_{qia} is the rate constant for the quadratic mortality. The linear term represents ice algal biomass-independent processes, in which a specified fraction of the population is lost per unit time. *Lavoie et al.* [2005a] defined this term as the grazing rate on ice algae, and prescribed it at 10% of the growth rate. The quadratic term represents crowding effects, in that the fraction of biomass lost per unit time increases with higher biomass. (Although the quadratic formulation is a commonly used approach in representing the crowding effect of large phytoplankton cells (i.e., diatoms) in marine ecosystem models [e.g., *Steiner et al.*, 2006a; *Aumont et al.*, 2015], we do not implement it in the case of small plankton because they do not reach high enough densities.) Based on the model tuning to match observations, m_{lia} and m_{qia} are respectively set to 0.03 d^{-1} and 0.00015 d^{-1} in the standard run. As the simulated bloom grows, the population will have a quasi-exponential growth if the linear contribution to mortality varies slowly with time, and the biomass is small enough that the quadratic contribution to mortality is small.

Figure 2.11b presents the standard run along with multiple runs in which the linear and quadratic mortality parameters have been increased or decreased. As expected, when both parameters are increased (decreased), the simulated ice algae has a lower (higher) maximum biomass than the standard run. When the two are changed in opposite directions, the magnitude of the maximum biomass does not vary substantially, but the onset timing is earlier or later. In Figure 2.11c, the red box from Figure 2.11b is enlarged in order to show when the simulated ice algal bloom crosses the $100 \text{ mg Chl } a \text{ m}^{-3}$ threshold. With a 25% decrease (increase) to this parameter, the bloom reaches the $100 \text{ mg Chl } a \text{ m}^{-3}$ threshold 2 days earlier (later).

Dashed lines correspond to simulations in which the linear and quadratic mortality param-

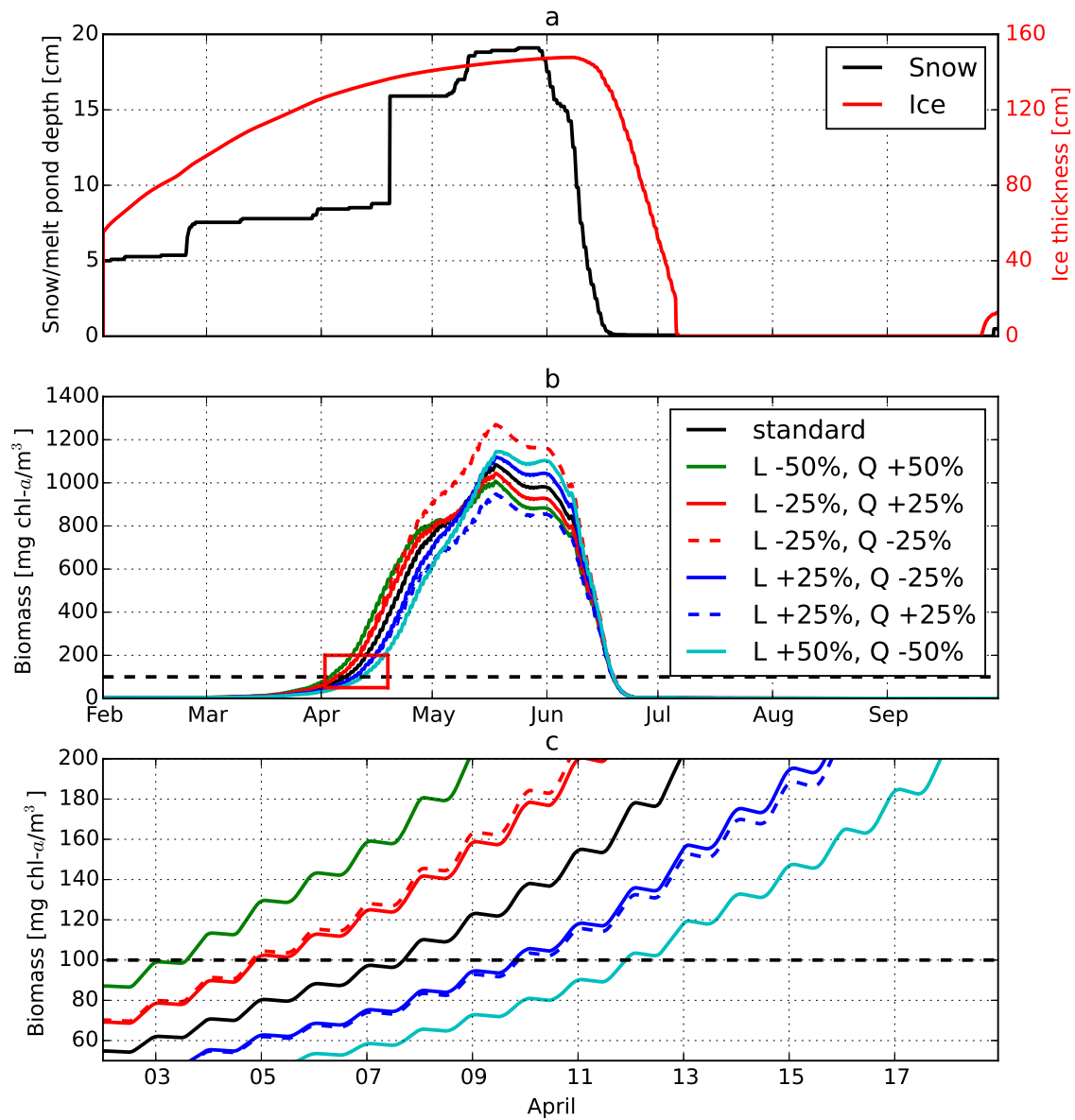


Figure 2.11: Snow and ice thickness, ice algal biomass varying mortality function, and onset of the bloom. Snow and ice thickness (cm) (a) and ice algal biomass ($\text{mg Chl } a \text{ m}^{-3}$) differing linear and quadratic dependencies on mortality (b). The black solid line in (b) is the standard run, the dashed red (blue) line is the simulated bloom with both linear and quadratic dependencies decreased (increased) by 25%. The solid colored lines are for blooms with linear and quadratic dependencies changed in opposite directions, e.g., increased for linear and decreased for quadratic. The onset of the bloom in the red box in (b) is expanded in (c).

eters have been changed in the same way. These different runs cross the $100 \text{ mg Chl } a \text{ m}^{-3}$ threshold at almost the same time, indicating that the bloom onset (when ice algal biomass is small) is relatively insensitive to the quadratic mortality dependency. Therefore, these two mortality parameters can be adjusted to best fit observations for the timing of the bloom onset and magnitude of maximum biomass.

2.4 Discussion

The recent model study by *Abraham et al.* [2015] showed that grid-cell mean simulations of light and heat fluxes through sea ice could be improved by parameterizing the subgrid-scale snow depth variability, relative to simulations with spatially uniform snow depth distribution. These authors pointed out the need to examine biological responses to this new parameterization. In the first part of the present study, we investigated the impact of the new parameterization on simulated ice algae. The results indicate an improvement in simulating the ice algal bloom especially during the melt period, owing to an improvement in simulating the gradual increase in light availability to the ice algae. However, in this study, we are unable to further assess the impact of the new light parameterization on earlier stages of the bloom because the observed time series of ice algal biomass are confined mostly to the decline phase of the bloom. Measurements focusing on ice algal biomass during the onset and early growth of blooms are needed for assessing this impact.

As discussed in *Arrigo* [2014], the presence of ice algae affects several important processes in the underlying water column ecosystem. However, it is logistically difficult to isolate the contribution of ice algae from that of phytoplankton in terms of observed nutrient drawdown and biomass production. It is similarly difficult to observationally assess the seeding of the phytoplankton bloom by ice algae. Hence, process models become important tools to address questions like: *What if ice algae were excluded from a given environment?* In particular, the absence of advective processes in 1-D models allows focus on the *in situ* sympagic-pelagic ecosystem coupling. The present analysis demonstrated some of the influences of ice algae on the pelagic ecosystem. The results indicate that both the timing and magnitude of the simulated under-ice phytoplankton bloom are affected by the presence of ice algae. The timing of the bloom is affected due to seeding as a result of ice algal flushing, whereas the magnitude is affected due to the nutrient drawdown by the earlier ice algal bloom. These impacts of ice algae further influence other important biogeochemical processes, such as the production of dimethylsulfide [*Hayashida et al.*, 2016]. Previous model studies also indicated the timing and magnitude of the ice-associated

pelagic bloom as an important response to ice algal seeding *Jin et al.* [2007]; *Tedesco et al.* [2012]. However *Jin et al.* [2007] highlighted the importance of stratification on the response suggesting that sudden mixing events following ice melt would disrupt the ice-associated pelagic bloom. More quantitative estimates for the effects of ice algae on the underlying ecosystem can be achieved by conducting simulations (including the exclusion run) in a full 3-D model using the parameterizations considered in this study. *Deal et al.* [2011] and *Jin et al.* [2012] 3-D model applications highlight both high regional variability as well as the seasonal importance of ice algal primary production.

The model applies several simplified assumptions due to lack of observations in the ice. For instance, the simulated ice algal nitrogen uptake preference (p_{no3}^{ia} in Equation A.25) is constant throughout the simulation. However, *Harrison et al.* [1990] observed that nitrogen utilization by ice algal communities of Barrow Strait shift from a nitrate- to an ammonium-dominated metabolism. In addition, the nitrification rate (NH_4 to NO_3) in sea ice is set to a constant rate, even though bacteria in the ice that facilitate the process [*Fripiat et al.*, 2014] may experience variations due to environmental fluctuations.

In both the modelled ice and water column, nutrient depletion due to phytoplankton uptake leads to near-zero concentrations in the limiting nutrient. Observations of post-bloom nutrient concentrations in an area with little horizontal transport could allow assessment of this result. The influence of horizontal advection on the nutrient drawdown below the ice could be assessed in 3-D model simulations.

The model results indicate that a combination of linear and quadratic mortality terms is required to adequately represent the development and decline of the ice algal bloom. The application of a quadratic mortality term implies a larger specific mortality at higher ice algal concentrations, representing lysis due to viral infection and other overcrowding processes that occur at higher ice algal concentrations. Additional field observations during the height of the bloom could help to constrain this term.

In the standard simulation, the growth of ice algae was initially limited by light, and then by nutrients (nitrate) during the peak and the decline of the bloom, which is consistent with the findings of previous studies [*Mundy et al.*, 2014a]. The simulated under-ice bloom was similar to the observed bloom in terms of the magnitude, timing, and the species composition (dominated by diatoms, *Galindo et al.* [2014]). During the ice-free period, the simulated under-ice bloom was succeeded by the formation of a subsurface chlorophyll maximum. While this is a common feature in low-nutrient Arctic waters, observations are lacking for this particular time and location. It is possible that high tidal and/or horizontal mixing could prevent a deep chlorophyll maximum from developing in particular regions.

The parameters were adjusted to this specific dataset (particular year, particular place). Applications for different years and locations, and subsequent implementation in a 3-D model, will indicate if some retuning may be necessary. A need for retuning would hint at processes that are incompletely understood and indicate whether further measurements to constrain the process are required.

2.5 Conclusions

This 1-D study is intended as a step in the development of a 3-D model, one of a growing number that incorporate biogeochemical processes in order to represent the sympagic ecosystem and its coupling to the underlying pelagic ecosystem.

In order to establish a set of parameterizations which can be transferred into a 3-D regional Arctic model which couples sea-ice, ocean and associated ecosystems, this 1-D model study investigates the physical and biological controls on sympagic and pelagic primary production using observations from Resolute Passage. Results of the standard simulation, including a snow distribution function allowing for a slow evolution towards bare ice and melt ponds, were generally in good agreement with the variability of snow/melt pond depths, ice thickness, under-ice PAR, and bottom-ice and seawater Chl *a* observed during the melt season in 2010. The simulated ice algal and under-ice phytoplankton blooms in the standard run were in reasonable agreement with the observations in terms of timing and magnitude.

Several findings can be taken from the sensitivity analyses. (1) Ice algal growth limits subsequent pelagic biomass in the upper water column by removing nutrients and limiting their availability to the phytoplankton, with a decrease of $\sim 50\%$ of the maximum phytoplankton concentration in the upper 10 m in the standard run relative to the run without ice algae. (2) Photosynthetic sensitivity and pre-bloom biomass determine the onset timing of the ice algal bloom. (3) The maximum biomass is relatively insensitive to the pre-bloom ice algal biomass. (4) A combination of linear and quadratic parameterizations of mortality rate is required to adequately simulate the evolution of the ice algal bloom, indicating that processes associated with each of these functional forms are occurring within the ice algal bloom phase. And (5), a large detrital (D2) sinking rate greater than a threshold of $\sim 10 \text{ m d}^{-1}$ effectively strips the upper water column of the potential to regenerate the limiting nutrient after the bloom by transporting it to depth. For this scenario a deep chlorophyll maximum develops, as is characteristic for low nutrient Arctic waters. A D2 sinking rate slower than this threshold allows for a subsequent subsurface

P1 bloom due to availability of remineralized ammonium (from detritus) after the initial (P2 dominated) pelagic bloom.

Measurements needed to better constrain the simulated ice algal bloom include ice algal concentration in the winter, in situ mortality rate, and sinking rates for ice algal aggregates. This 1-D study is part of two subsequent 1-D studies, implementing sulfur (dimethyl sulfide, or DMS) and inorganic carbon cycles. The work in all three of these studies will be used as a basis for the implementation of ice algae, DMS, and carbon cycles into a 3-D coupled ice-ocean biogeochemical regional model of the Canadian marine Arctic.

One interesting path of future development in this 1-D study could involve testing of the efficiency of nutrient exchange across the ice-ocean interface. Sea-ice algae are located near the bottom of the sea ice, and their rate of growth and maximum biomass is largely dependent on the replenishment of nutrients from the water column. Conversely, a higher exchange of nutrients across the ice-ocean interface could also potentially serve to create a nutrient deficit for the subsequent near surface phytoplankton bloom, thereby tipping the competitive balance between pelagic and sympagic productivity and nutrient uptake in favor of ice algae.

3 A model-based analysis of physical and biogeochemical controls on carbon exchange in the upper water column, sea ice, and atmosphere in a seasonally ice-covered Arctic strait

The following chapter is a manuscript published as:

Mortenson, E., N. Steiner, A.H. Monahan, L.A. Miller, N.-X. Geilfus, and K. Brown (2018): A Model-Based Analysis of Physical and Biogeochemical Controls on Carbon Exchange in the Upper Water Column, Sea Ice, and Atmosphere in a Seasonally Ice-Covered Arctic Strait, *Journal of Geophysical Research: Oceans*. doi:10.1029/2018JC014376

The manuscript is repeated here with some adjustments to fit the format of the dissertation.

Chapter Abstract

In this study, we consider a 1D model incorporating both sea ice and pelagic systems in order to assess the importance of various processes on the vertical transport and exchange of carbon in the seasonally ice covered marine Arctic. The model includes a coupled ice-ocean ecosystem, a parameterization of ikaite precipitation and dissolution, a formulation for ice-air carbon exchange, and a formulation for brine rejection and freshwater dilution of dissolved inorganic carbon (DIC) and total alkalinity (TA) associated with ice growth and melt. Sensitivity analyses illustrate that: 1. the pelagic ecosystem accounts for more than half of the net ocean carbon uptake, but ice algae have little effect on the air-sea exchange in the standard run; 2. inclusion of ikaite precipitation and dissolution do not strongly affect the net ocean carbon uptake for concentrations within the observed range, but can become important for

larger concentrations; 3. varying DIC and TA in the ice by equal amounts, or varying brine deposition depth, does not affect the net ocean carbon uptake, because the coincident changes in TA and DIC concentrations at the sea surface serve to counteract one another with respect to sea surface $p\text{CO}_2$; and 4. the proportions of carbon released to the water column (versus to the atmosphere) during ice growth and melt are important quantities to constrain in order to determine the contribution of the combined ice-ocean system to oceanic uptake of atmospheric carbon.

3.1 Introduction

Carbon dioxide is continually being exchanged between the ocean and atmosphere at the sea surface. The amount and direction of the net carbon exchange depends on the $p\text{CO}_2$ difference between the ocean and atmosphere as well as physical and biogeochemical properties across the air-sea interface.

In the polar oceans, ice cover further complicates the exchanges. Modellers have conventionally treated ice as an inert barrier to the exchange of CO_2 , but recent field work has shown that the growth and melt of sea ice can have a substantial impact on the transport of dissolved inorganic carbon (DIC) and total alkalinity (TA) in the surface polar oceans (e.g., *Miller et al.* [2011a,b]; *Nomura et al.* [2013]; *Delille et al.* [2014]; *Brown et al.* [2015]; *Geilfus et al.* [2015]).

The Arctic Ocean is changing rapidly, with a transition from multiyear to first year ice, a lengthening of the open-water season [*Barber et al.*, 2015; *Galley et al.*, 2016], and a loss in September sea ice extent of more than 10% per decade over the last 70 years [*Overland and Wang*, 2013]. The change in CO_2 uptake in a future Arctic Ocean with less ice-cover is not well-constrained. Estimates of the change have ranged from an increase [*Bates and Mathis*, 2009] to a decrease [*Cai et al.*, 2010; *Else et al.*, 2013; *Steiner et al.*, 2013] in the net CO_2 uptake by the present and future Arctic Ocean relative to the recent past. *Rysgaard et al.* [2011] discuss the potential importance of sea ice as a carbon pump, as a result of the rejection of high-DIC brine during ice growth and the release of low-DIC meltwater at ice melt. Only very recently have model studies quantitatively examined the effects of sea ice on the ocean carbon system [*Moreau et al.*, 2016; *Grimm et al.*, 2016]. Both of those studies found that the contribution of the sea-ice carbon pump could have a substantial regional effect on air-sea exchange, as well as on carbon distribution in the polar oceans, but that the sea-ice pump contributes a small proportion of the global air-sea

carbon exchange. Neither study included the effect of sympagic biological processes on the ocean carbon system.

During ice growth, TA- and DIC-rich brine is rejected from the ice and sinks as negatively buoyant plumes into the mixed layer beneath the ice (e.g., *Vancoppenolle et al.* [2013b]). Later during ice melt, low-salinity, low-TA, and low-DIC meltwater creates a freshwater lens at the surface. Freshening, cooling, and changes to the DIC:TA ratio all contribute to lowering the $p\text{CO}_2$ in the freshwater lens, and hence increase ocean uptake of atmospheric CO_2 . Another process associated with sea ice is the precipitation of ikaite (an abiogenic phase of calcium carbonate) in the highly saline brine pockets within the ice [*Rysgaard et al.*, 2014]. Some ikaite may be flushed through the connecting brine channels as the ice warms, transferring both DIC and TA to the water column from the melting ice in a 1:2 molar ratio (DIC:TA) [*Geilfus et al.*, 2016]. The differential DIC:TA ratio will affect the $p\text{CO}_2$ of seawater. In addition, sea ice provides a habitat for microorganisms. During the spring bloom ice algae take up CO_2 and nutrients, whereas heterotrophic bacteria may release CO_2 throughout much of the year. Detrital release provides a source of organic matter and nutrients (through remineralization) to the underlying pelagic ecosystem [*Arrigo*, 2017], which in turn affects the biological uptake of CO_2 and water column carbonate chemistry. These processes vary spatially and temporally, with rates that are poorly constrained. Model studies can help determine the relative impacts of these different processes on net CO_2 exchange between the atmosphere and the seasonally ice-covered ocean in the Arctic.

This study considers air-ice-ocean carbon fluxes using an ice-ocean coupled physical and biogeochemical 1D model. The ecosystem component, described in *Mortenson et al.* [2017], includes a coupling of the sea ice and water column and is tuned to match observations representative of a seasonally ice-covered marine Arctic environment. A representation of the inorganic carbon system has been added to the model to assess the overall importance of sea-ice growth and melt to net CO_2 exchange, as well as to quantify the relative importance of individual processes. The carbon system includes a parameterization for sea-ice carbonate dynamics, air-sea CO_2 exchange, and biological primary productivity, including both sea-ice algae and a pelagic ecosystem (two phytoplankton and two zooplankton functional groups). To determine model parameters and assess performance, we use observations near Resolute Passage in the Canadian Arctic Archipelago (CAA). The location was chosen for this 1D study because it has been the site of multiple field campaigns to measure inorganic carbon fluxes and carbonate chemical properties above, in, and below the sea ice in the area (notably *Brown et al.* [2015], and *Geilfus et al.* [2015]). This location also has a nearby meteorological station from which atmospheric forcing data were

obtained (Environment Canada, <http://climate.weather.gc.ca/>).

The ocean-ice coupled ecosystem developed by *Mortenson et al.* [2017] and the carbon system developed in this study represent conditions in seasonally ice-covered waters. Ultimately, a biogeochemical model with parameterizations based on this 1D model study are to be implemented in a 3D regional model of the Arctic Ocean.

3.2 Methods

3.2.1 Site description

Resolute Passage is located near Barrow Strait in the CAA on the south side of Cornwallis Island at 74°N, 94°W. It is normally covered with landfast ice from late September to early July. The ice algae bloom generally begins in mid-May [*Mundy et al.*, 2014b], and the biomass is relatively high compared to other Arctic locations that have been measured [*Leu et al.*, 2015]. A meteorological station is at Resolute airport, maintained by Environment Canada, approximately 3 km from Resolute Bay.

3.2.2 Model description

The 1D sea ice-ocean biogeochemical model, including coupled ice and water column ecosystems, is described in detail in *Mortenson et al.* [2017]. Specifically, the development of the simulated ice algae is described in detail in *Mortenson et al.* [2017] and has been utilized in analysis of the Arctic sulfur cycle [*Hayashida et al.*, 2017]. Development of the pelagic ecosystem has been validated in *Steiner et al.* [2006b]; *Steiner and Denman* [2008]; *Steiner et al.* [2012]. The modeled ecosystem is comprised of three algal functional groups (one sympagic and two pelagic), two zooplankton functional groups, and three nutrients (NO_3 , NH_4 , and Si). The model domain covers the upper 100 m of the ocean with a resolution of 1 m. The physical model GOTM (General Ocean Turbulence Model) was forced by meteorological observations (precipitation, winds, temperature, humidity, and cloudiness) from the Environment Canada meteorological station at Resolute Airport. Atmospheric $p\text{CO}_2$ was set at a constant value of 400 μatm . Water column temperature, salinity, and velocity were restored to 3D NEMO regional model output near Resolute Bay in the CAA (*Dukhovskoy et al.* [2016b]; with respective time scales of one day, one day, and ten minutes). In both *Mortenson et al.* [2017] and the present study, we have chosen

to tightly constrain the physical oceanographic variables in order to focus on the biogeochemical component of the model. The biogeochemical model parameters were tuned to match observations of ice algal and phytoplankton biomass when initialized with observed concentration profiles of NO_3 , NH_4 , and Si. Simulated under-ice light is in good agreement with observations [Abraham *et al.*, 2015; Mortenson *et al.*, 2017].

We have added a representation of the inorganic carbon cycle to the model above. Following a similar conceptual framework to that presented in Rysgaard *et al.* [2011] and Miller *et al.* [2011b], Figure 3.1 shows a schematic of the DIC transport processes, sinks, and sources represented in the model: air-sea exchange, sympagic and pelagic net primary production, remineralization of detritus, precipitation of ikaite in ice during ice growth and its subsequent dissolution in the water column during ice melt, brine rejection, and meltwater dilution. The last of these processes is a virtual flux of DIC, analogous to the virtual salt flux described in Roulet and Madec [2000]. The transport, sinks, and sources of inorganic carbon through the water column are represented as

$$\frac{\partial}{\partial t} \text{DIC}(z) = \Phi^{\text{DIC}}(z) + S_{\text{bio}}^{\text{DIC}}(z) + \frac{\partial}{\partial z} \left(K_z \frac{\partial \text{DIC}(z)}{\partial z} \right) \quad (3.1)$$

where $\Phi^{\text{DIC}}(z)$ represents exchange of inorganic carbon at the ice-sea or air-sea interface, $S_{\text{bio}}^{\text{DIC}}(z)$ represents sinks and sources of DIC within the pelagic ecosystem (including the remineralization of dead ice algae which have been released into the pelagic large detritus pool), and K_z is the eddy diffusivity computed by GOTM. Note that, although $\Phi^{\text{DIC}}(z)$ is a surface flux to the water column, it is included in Eqn. 3.1 as a function of z because we represent transport by brine plumes as an instantaneous nonlocal transport of material from the ice-water interface to within the water column.

The exchange of inorganic carbon at the top of the water column is subject to different processes at different times of the year, so $\Phi^{\text{DIC}}(z)$ is represented differently under three different conditions, two for ice-covered water and one for open water:

$$\Phi^{\text{DIC}}(z) = \begin{cases} \phi_{IG}^{\text{DIC}}(z) + \phi_{\text{ice-algae}}^{\text{DIC}}, & \text{for freezing ice;} \\ \phi_{IM}^{\text{DIC}} + \phi_{\text{ice-algae}}^{\text{DIC}}, & \text{for melting ice;} \\ \phi_{\text{air-sea}}^{\text{DIC}}, & \text{for open water;} \end{cases} \quad (3.2)$$

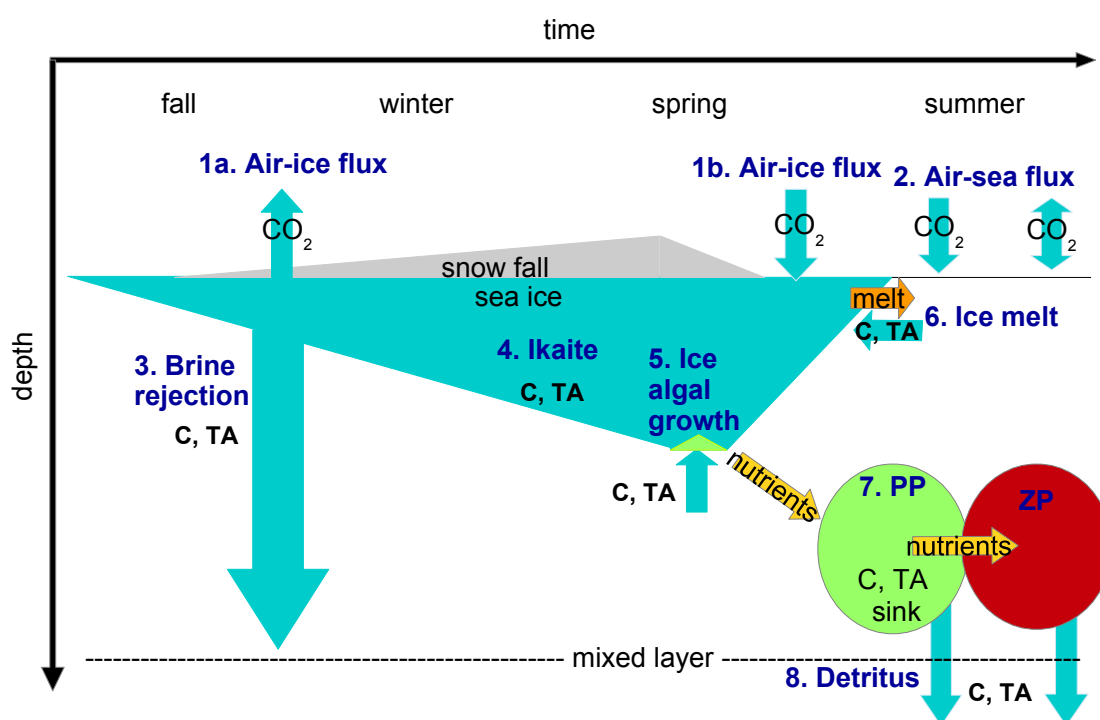


Figure 3.1: Schematic of the carbon system during the seasonal ice growth and melt cycle. Processes included in the model, and described in Section 4.2, are: 1. ice-air outgassing of CO_2 during ice growth; 2. air-sea CO_2 exchange during the open-water season; 3. brine-associated rejection of DIC and TA during ice growth; 4a. ikaite precipitation in ice during growth; 4b. ikaite dissolution in the water during ice melt; 5. ice algal growth; 6. dilution due to low-DIC, -TA meltwater during ice melt; 7. pelagic primary production; and 8. pelagic remineralization of phytoplankton (PP) and zooplankton (ZP) detritus.

where $\phi_{IG}^{DIC}(z)$ and ϕ_{IM}^{DIC} are, respectively, the effective fluxes of DIC due to ice growth and melt; $\phi_{ice-algae}^{DIC}$ represents the uptake of DIC due to ice algal growth; and $\phi_{air-sea}^{DIC}$ is the air-sea flux of CO_2 . The inorganic carbon flux due to ice growth, $\phi_{IG}^{DIC}(z)$, directly affects the carbon budgets of subsurface layers of the simulated water column, while all of the other terms on the right hand side of Eqn. 3.2 act on the uppermost model layer (corresponding to an upper boundary flux). Each of these terms, along with the reasoning for the subsurface effect of ice growth, are described in more detail in subsections 3.2.2 - 3.2.2.

The transport, sinks, and sources of total alkalinity (TA) are modelled similarly to those of DIC:

$$\frac{\partial}{\partial t}TA(z) = S_{bio}^{TA}(z) + \frac{\partial}{\partial z} \left(K_z \frac{\partial TA(z)}{\partial z} \right) \quad (3.3)$$

but with the air-sea flux set to zero, as TA is not exchanged with the atmosphere:

$$\Phi^{TA}(z) = \begin{cases} \phi_{IG}^{TA}(z) + \phi_{ice-algae}^{TA}, & \text{for freezing ice.} \\ \phi_{IM}^{TA} + \phi_{ice-algae}^{TA}, & \text{for melting ice;} \\ 0, & \text{for open water;} \end{cases} \quad (3.4)$$

where $\phi_{IG}^{TA}(z)$ and ϕ_{IM}^{TA} are the effective ice-ocean fluxes of TA due to ice growth and melt, and $\phi_{ice-algae}^{TA}$ represents the effect of ice algal growth on TA. The exchange of TA during ice growth and melt and the effect of biological processes will be described in further detail in subsections 3.2.2 to 3.2.2.

For the 1D carbon system development, the initial steps involved setting some parameters based on relatively well-known observations (e.g., DIC and TA fluxes were based on observed sea ice and water concentrations of DIC and TA). Other parameterizations, based on less well-known observations, (e.g. ikaite precipitation, ice-air CO_2 exchange as a proportion of total import/export of carbon from the ice, and depth of brine-associated DIC/TA deposition), were based on ad hoc best-guess estimates, and then varied around those values in order to compare the subsequent effect on the better-known/-measured air-sea exchange during the open-water season.

Surface Flux Due to Ice Growth and Melt

When the ocean is covered by ice, we have chosen two distinct representations for the ice-ocean inorganic carbon exchange associated with ice growth and melt. This is because the transfer of inorganic carbon to or from the ice in the growth and melt phases is subject to different physical processes. During ice growth, the concentration of solutes, including DIC and TA, in constricting brine channels/pockets leads to the rejection of dense, high-DIC brine into the water column (as well as an ice-to-air flux of CO_2 at the ice surface). The inorganic carbon taken up by the ice during ice melt, however, is associated with a dilution of the brine channels and an increase in porosity of the warming ice, which leads to a release of buoyant, low-DIC meltwater (and an air-to-ice flux of CO_2).

In the case of ice growth, the DIC released from ice is distributed across depths as a parameterization of nonlocal transport by negatively buoyant plumes of rejected brine. This parameterization is based on the results of *Jin et al.* [2015], which showed that a simulated salinity distribution in an idealized ice- and lead-covered model domain has best agreement with observations when dissolved substances carried by brine are deposited predominantly at the bottom of the mixed layer (as opposed to into the surface layer). Our simplified representation models this transport as instantaneous.

We parameterize the ice-water inorganic carbon exchange during ice growth as:

$$\phi_{IG}^{DIC} = \begin{cases} \frac{\partial h_{ice}}{\partial t} \Delta DIC^{eff} \delta P_{SW}, & \text{if } z_{bot} < z < z_{top} \\ 0, & \text{if } z < z^{top} \text{ or } z > z^{bot} \end{cases} \quad (3.5)$$

where $\frac{\partial h_{ice}}{\partial t}$ is the rate of change of ice thickness, ΔDIC^{eff} is the effective ice-water difference in DIC concentration, z^{top} and z^{bot} define the depth range within which DIC- and TA-rich brine is modelled to settle during ice growth, $\delta = \frac{1}{z_{top} - z_{bot}}$ is a depth-distribution weight factor, and P_{SW} is a parameter that represents the percent of inorganic carbon rejected from the growing ice into the seawater (as opposed to into the atmosphere). In the standard run, the proportion of inorganic carbon that is released to the ocean (atmosphere) from ice is set at 99% (1%) during ice growth, based on estimates of *Sejr et al.* [2011] and *Geilfus et al.* [2016]. We set the brine deposition depths in the standard run to 30-40m. This depth range was chosen because it is close to the simulated halocline depth (of about 35m). The sensitivity of the results to both the proportion of inorganic carbon released to the ocean and the depth of brine deposition are presented in Section 3.3.

The effective ice-water difference in DIC (ΔDIC^{eff}) is the DIC concentration difference between seawater and ice, including ikaite precipitation within the ice:

$$\Delta DIC^{eff} = DIC_{SW}^{ref} - (DIC_{ice}^{ref} + DIC_{ikaite}^{ref}) \quad (3.6)$$

The terms DIC_{SW}^{ref} and DIC_{ice}^{ref} are reference concentrations of DIC in the seawater and ice, and DIC_{ikaite}^{ref} represents DIC trapped in ikaite within the ice. The reference ice concentration is set at 400 mmol C m⁻³, based on observed values of DIC for first-year landfast sea ice near Resolute (generally in the range of 300-500 mmol C m⁻³, *cf.*, *Brown et al.* [2015]; *Geilfus et al.* [2015]). During ice formation, the average DIC concentration of sea water from which the ice is formed is near 2100 mmol C m⁻³ [*Brown et al.*, 2015], and hence DIC_{SW}^{ref} is set at 2100 mmol C m⁻³. Inorganic carbon trapped in ikaite within the ice that is released during ice melt (DIC_{ikaite}^{ref}) is set at 50 mmol C m⁻³ in the standard run, an estimate based on observed ice-ocean transport of ikaite [*Geilfus et al.*, 2016]. Ikaite that both precipitates and dissolves within the sea-ice is not accounted for because it does not contribute to ice-ocean fluxes of DIC (or TA).

The reference concentrations DIC_{SW}^{ref} , DIC_{ice}^{ref} , and DIC_{ikaite}^{ref} are held constant to ensure that the inorganic carbon in the system is conserved through an entire sea-ice growth and melt cycle. For example, in an idealized case where sea-water DIC concentration is higher during freeze-up than during ice-melt (and air-ice exchange is suppressed), using a variable DIC_{SW} in place of DIC_{SW}^{ref} in the parameterized flux would lead to a stronger flux during ice freeze than during ice melt, because ΔDIC^{eff} would be higher during freezing than during melting. While this treatment of the inorganic ice carbon pump only has a small effect in this single-season 1D study, in a regional or global 3D model, spuriously large or small ice-ocean fluxes could occur in areas of markedly high or low DIC_{SW} if these reference concentrations are not held constant, as described by *Roulet and Madec* [2000] in detail with respect to salinity and by *Moreau et al.* [2016] with respect to DIC and TA.

During ice melt, low-DIC meltwater is released into the model surface layer (the upper 1 m) of the ocean, diluting the concentration of DIC at the surface:

$$\phi_{IM}^{DIC} = \frac{\partial h_{ice}}{\partial t} \Delta DIC^{eff} P_{SW}^* \quad (3.7)$$

where P_{SW}^* represents the proportion of the virtual (negative) inorganic carbon flux released into the ocean. Values of P_{SW}^* less than one result from the uptake of atmospheric

CO₂ by melting sea ice (resulting in higher-DIC meltwater and therefore a smaller virtual inorganic carbon flux than in the standard run). The default setting for P_{SW}^* of 97.5% corresponds to an ice-seawater inorganic carbon flux during ice melt. The ice-air flux, proportional to $1-P_{SW}^*$ (equal to 2.5% of the total inorganic carbon flux), is chosen such that uptake of CO₂ during ice melt is within the range of observations [Delille *et al.*, 2014; Geilfus *et al.*, 2016]. The air-ice fluxes during both ice growth and melt are taken into account in the computation of net flux of carbon between the combined ice-ocean system and the atmosphere. In our parameterization, air-ice CO₂ fluxes during ice melt are modelled as instantaneously affecting the ice-water flux. The slight delay in this low-DIC meltwater entering the water column, because it has to pass through the ice, is neglected in the model.

The ice flux of TA during ice formation is parameterized in the same way as DIC, except without air-ice exchange:

$$\phi^{TA} = \begin{cases} \frac{\partial h_{ice}}{\partial t} \Delta TA_{IG}^{eff} \delta, & \text{if } z_{bot} < z < z_{top} \\ 0, & \text{if } z > z^{bot} \text{ or } z < z^{top} \end{cases} \quad (3.8)$$

where the effective TA flux during ice growth and melt is:

$$\Delta TA^{eff} = TA_{SW}^{ref} - (TA_{ice}^{ref} + TA_{ikaite}^{ref}) \quad (3.9)$$

TA_{SW}^{ref} is set to 2200 mmol m⁻³ and TA_{ice}^{ref} to 500 mmol m⁻³ based on observations [Brown *et al.*, 2015; Geilfus *et al.*, 2015]. The ikaite contribution to TA in ice, TA_{ikaite}^{ref} , is twice that of DIC_{ikaite}^{ref} because precipitation (dissolution) of ikaite removes (contributes) 2 moles of TA to 1 mole of DIC.

Pelagic Ecosystem Component

The simulated pelagic ecosystem uses nitrogen as a currency and consists of two photosynthesizing functional groups and two zooplankton groups (described in detail in Mortenson *et al.* [2017]). The DIC in the water column is affected by pelagic primary production and remineralization of detritus:

$$S_{bio}^{DIC} = S_P(z) + S_D(z) \quad (3.10)$$

The first term on the right hand side of Eqn. 3.10 represents primary production of phytoplankton:

$$S_P(z) = -\mu_P P(z) r_1^{C:N} \quad (3.11)$$

where μ_P is the phytoplankton specific growth rate (in s^{-1}), P is concentration of phytoplankton (in $mmol-N\ m^{-3}$) and $r_1^{C:N}$ is the molar carbon:nitrogen Redfield ratio (106:16) [Redfield *et al.*, 1963a]. The detrital remineralization rate is given by:

$$S_D(z) = (D1(z)R_{D1} + D2(z)R_{D2}) r_1^{C:N} \quad (3.12)$$

where $D1$, $D2$ are the concentrations of small and large detritus and R_{D1} , R_{D2} are the specific remineralization rates for small and large detritus.

Changes in TA due to phytoplankton growth and pelagic remineralization are modelled as

$$S_{bio}^{TA} = S_P^{TA}(z) + S_D^{TA}(z) + S_N^{TA}(z) \quad (3.13)$$

where S_P^{TA} , S_D^{TA} and S_N^{TA} respectively denote changes due to phytoplankton growth, detrital remineralization, and nitrification. Following *Wolf-Gladrow et al.* [2007], we model TA changes associated with nitrogen flows in the following way:

(1a) 1 mole of NO_3 uptake (new primary production) is associated with a source of 1 mole TA,

(2a) 1 mole of NH_4 uptake (recycled primary production) is associated with a sink of 1 mole TA,

(3a) 1 mole of NH_4 production from detrital remineralization is associated with a source of 1 mole TA, and

(4a) 1 mole of NH_4 transformed to NO_3 (nitrification) is associated with a sink of 2 moles TA.

Wolf-Gladrow et al. [2007] also describe a change in TA associated with phosphate and sulfate uptake and remineralization. Although phosphate and sulfate are not explicitly represented in the model, we can calculate a Redfield ratio-linked change in TA due to phosphate (1P:16N) and sulfate (2 moles times 2.4S:1P) uptake. The net change is 5.8/16 moles TA per mole nitrogen uptake (both NO_3 and NH_4) and a loss of the same amount for each mole of NH_4 produced by remineralization. We therefore obtain the following expressions for the biologically-mediated TA sources and sinks linked to phosphate and sulfate:

(1b) 1 mole of NO_3 uptake is associated with a source of 5.8/16 mole TA,

(2b) 1 mole of NH_4 uptake is associated with a source of 5.8/16 mole TA, and

(3b) 1 mole of NH_4 from detritus (remineralization) is associated with a sink of 5.8/16 mole TA.

The terms in Eqn.3.13 are therefore expressed as

$$S_P^{TA}(z) = \mu_P^{NH_4} P(z)(1 + 5.8/16) + \mu_P^{NO_3} P(z)(-1 + 5.8/16) \quad (3.14)$$

$$S_D^{TA}(z) = (D1(z)R_{D1} + D2(z)R_{D2})(1 - 5.8/16) \quad (3.15)$$

$$S_N^{TA}(z) = -2NH_4(z)R_{NH_4 \rightarrow NO_3} \quad (3.16)$$

where $\mu_P^{NH_4}$ and $\mu_P^{NO_3}$ represent specific rates of NH_4 and NO_3 uptake by phytoplankton, $[NH_4](z)$ is the depth-dependent ammonium concentration, and $R_{NH_4 \rightarrow NO_3}$ is the light-dependent specific rate of nitrification (described in *Mortenson et al.* [2017]).

DIC and TA Flux Due to Ice Algae

Sea-ice algae production during ice covered periods results in a flux of DIC:

$$\phi_{IA}^{DIC} = -\mu_{IA} I A r_2^{C:N} d_{IA} \quad (3.17)$$

where d_{IA} is the depth of the ice algal layer (set at 3 cm), $[IA]$ is concentration of ice algae (in units of mmol-N m^{-3}), and μ_{IA} is the specific growth rate of ice algae (in units of s^{-1}). This rate is converted into $\text{mmol C m}^{-3} \text{ s}^{-1}$ by multiplying by the molar carbon:nitrogen (non-Redfield) ratio, $r_2^{C:N}$, of 106/12 as in *Palmer et al.* [2014b]. This value is in the middle of the range of 4.8 to 17 found by *Niemi and Michel* [2015] for the C:N ratio of sea-ice algae in the CAA. Sea-ice algal primary production also results in an ice-water flux of TA:

$$\phi_{IA}^{TA} = \mu_{IA}^{NH_4} [IA] (1 + 5.8/16) + \mu_{IA}^{NO_3} [IA] (-1 + 5.8/16) \quad (3.18)$$

where $\mu_{IA}^{NH_4}$ ($\mu_{IA}^{NO_3}$) is the specific growth rate due to ammonium (nitrate) uptake.

Carbon Flux Due to Air-Sea Exchange

During the open-water season, the simulated air-sea exchange of CO_2 depends on wind speed and the difference in $p\text{CO}_2$ between the atmosphere and the surface water :

$$\phi_{air-sea}^{DIC} = \alpha (p\text{CO}_2^{atm} - p\text{CO}_2^{sw}) k_{gasex} \quad (3.19)$$

where α is the solubility coefficient for CO_2 in seawater [*Weiss*, 1974], $p\text{CO}_2^{atm}$ is the atmospheric partial pressure of CO_2 , $p\text{CO}_2^{sw}$ is the sea surface fugacity of CO_2 following *Lueker et al.* [2000], and k_{gasex} is the gas transfer velocity

$$k_{gasex} = k_o v_{10}^2 (S_c/660)^{-1/2} \quad (3.20)$$

[*Wanninkhof*, 1992], where $k_o = 0.39$, v_{10} is the wind speed at 10 m, and S_c is the temperature-dependent Schmidt number for CO_2 . This formulation of the gas exchange is used assuming open water with little ice coverage throughout the open-water season.

Parameter	SR setting	Description
DIC_0	2200 mmol C m ⁻³	Initial DIC concentration for the upper 100m of the water column.
TA_0	2285 mmol m ⁻³	Initial TA concentration for the upper 100m water column.
DIC_{SW}^{ref}	2100 mmol C m ⁻³	Reference seawater concentration of DIC for calculating inorganic carbon ice pump.
DIC_{ice}^{ref}	400 mmol C m ⁻³	Reference ice concentration of DIC for calculating inorganic carbon ice pump.
DIC_{ikaite}^{ref}	50 mmol C m ⁻³	Reference ikaite DIC concentration in ice, to be transported to water column.
TA_{SW}^{ref}	2200 mmol m ⁻³	Reference seawater concentration of TA for calculating inorganic carbon ice pump.
TA_{ice}^{ref}	500 mmol m ⁻³	Reference ice concentration of TA for calculating inorganic carbon ice pump.
TA_{ikaite}^{ref}	100 mmol m ⁻³	Reference ikaite TA concentration in ice, to be transported to 50-100m depth.
P_{SW}	99%	Percent of inorganic carbon released to the ocean during ice growth.
P_{SW}^*	97.5%	Percent of virtual inorganic carbon removed from the ocean during ice melt.
d_{brine}	30-40m	Depth range for the release of brine.
IA_{min}	1 mmol-N m ⁻³	Background (minimum) ice algal concentration.
P_{min}	0.01 mmol-N m ⁻³	Background (minimum) phytoplankton concentration.

Table 3.1: List of parameters values for the standard run (SR), which will be varied in the sensitivity studies.

3.3 Results and Discussion

3.3.1 Standard Run and Inorganic Carbon Module Validation

All simulations used atmospheric forcing from observations for the year 2010, starting early in the ice growth season (1 February) and continuing through the end of the open-water season (end of November) as in *Mortenson et al.* [2017]. Table 3.1 provides a list of parameters tested in the sensitivity analyses, along with their respective values set in the standard run.

Biological and physical variables were initialized as described in *Mortenson et al.* [2017]. Observations of water- and ice-column DIC and TA are available from two time series from the beginning of May to early June of 2010 [*Brown et al.*, 2015] and over the month of June 2012 [*Geilfus et al.*, 2015]. We use these observations to choose initial (1 February

2010) water column profiles such that the modelled DIC and TA would best match the observations near Resolute Bay through the period of sea-ice decline from May to June. In addition, we also consider observations from August 2015 in Barrow Strait, outside of Resolute Bay, for comparison. This latter data set is interesting because it comes from a different (physically proximate, but oceanographically distinct) location, where horizontal advection is expected to be more important than in Resolute Bay. The observed water column DIC and TA during the ice-cover to open-water transition period in the region (May to August) is shown in Figure 3.2, along with bi-weekly simulated output from May to June 2010. An important caveat to this observation-model comparison is that the available observations are from three different years and two distinct regions, whereas the simulated values only show the progression from May to August of 2010 at one place, subject to 2010 meteorological forcing. Limitations due to inaccessibility and harsh environmental conditions for the marine Arctic contribute to a dearth of observations available for comparison to the model output. Due to sparsity of observations, quantitative comparison between model data and observations are only possible in limited circumstances, hence qualitative comparisons are necessary. As more observations become available, further analysis of the model output will be possible and can be applied. However, under-ice observations of water-column DIC and TA are especially difficult to obtain and hence scarce, and the comparison has value in interpretation, but with reservation. Here we highlight noteworthy similarities and differences between observations and model output. In the upper 10m, simulated values are largely within the range of variability of observations for the months of May and June. In particular, the model captures the observed reductions in surface DIC and TA that begin with the onset of sea ice melt. Observations of DIC and TA in August 2015 in the upper 40m of the water column in Barrow Strait (Figure 3.2, brown) are markedly different from observations earlier in the season near Resolute Bay, and from the 2010 August model results (not shown). This difference may result from interannual variability (e.g. in meteorological forcing) that is absent in the single-year simulation, and/or from spatial variability and horizontal advection not captured by the single column model.

Figure 3.3a shows the simulated ice growth and snow accumulation in the standard run, along with the net carbon uptake by the ocean over the open-water season. Changes in TA and DIC that occur under the sea ice persist into the open-water season and can have a substantial impact on the air-sea exchange of carbon. The net uptake of carbon by the ocean during the open-water season is therefore a focus of observation-model comparison, as well as for the sensitivity analyses (section 3.3.2). Uptake of carbon by ice algae in May results in a reduction in sea surface $p\text{CO}_2$ in the upper 1 m of the water column of ~ 50

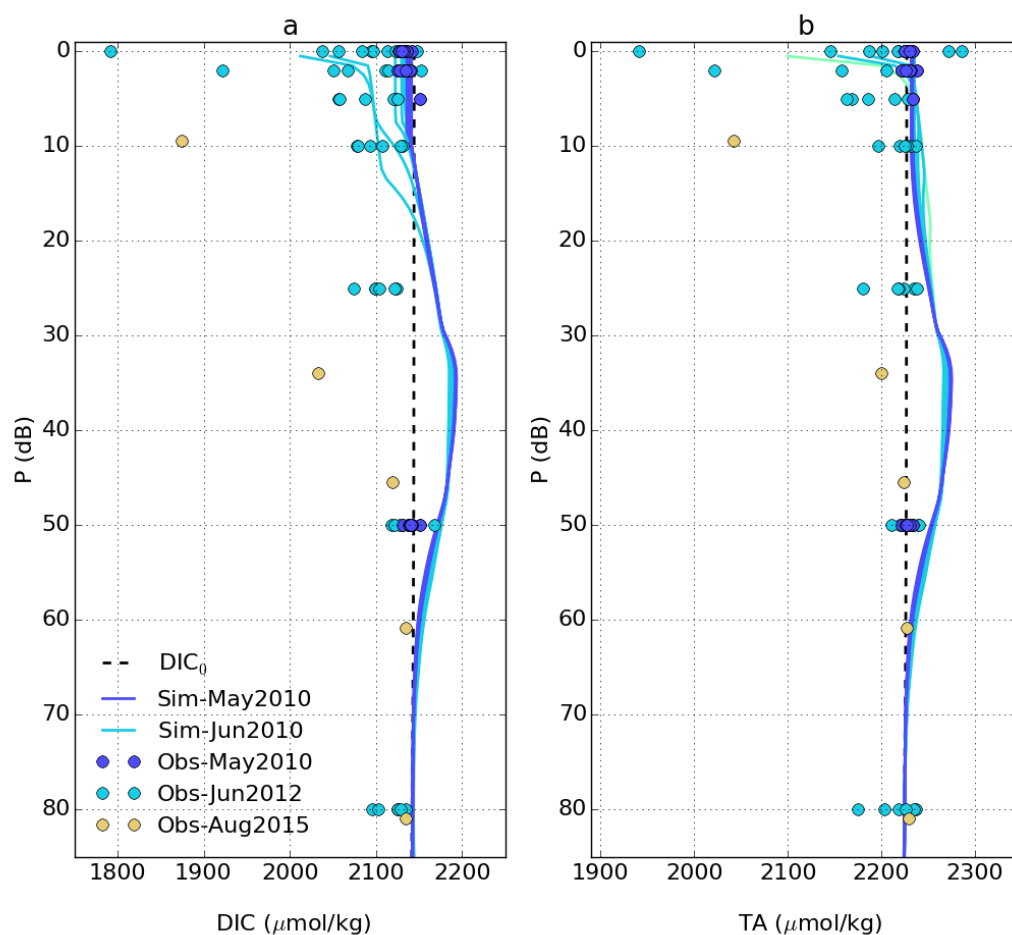


Figure 3.2: Simulated and observed water column profiles for a) DIC and b) TA. The black dashed lines are initial conditions for the model. Simulated bi-weekly results (solid lines) are from May and June 2010, and observations (dots) are in/near Resolute Passage from May 2010 (dark blue, *Brown et al.* [2015]), June 2012 (light blue, *Geilfus et al.* [2015]), and August 2015 (brown, A. Mucci, personal communication, from GEOTRACES, 2015). One surface measurement from 2012 was identified as a clear outlier and excluded from the figure (DIC and TA values of 560 and 603 $\mu\text{mol kg}^{-1}$, respectively) in order to focus on the majority of data.

μatm (Figure 3.3b). The release of low DIC and low TA meltwater contributes to the drop in surface water concentrations through dilution (by $\sim 525 \text{ mmol C m}^{-3}$ for DIC and $\sim 475 \text{ mmol m}^{-3}$ for TA) from June to early July (Figures 3.3b, d, and e). While the coincident phytoplankton bloom (Figure 3.3c) reduces DIC through biological uptake, the bloom may increase or decrease the TA, depending on whether the nitrogen taken up is NH_4 or NO_3 . This "one-way" effect of phytoplankton growth on DIC, vs. the "two-way" effect on TA, is evident in the $\sim 50 \text{ mmol m}^{-3}$ larger drop in surface seawater DIC than TA during the ice melt period (Figure 3.3b). The simulated evolution of DIC in the water column shows an increase at 30-40 m during ice growth due to the brine release to these model layers (Figure 3.3d). A drop in water column DIC of $\sim 50 \text{ mmol C m}^{-3}$ follows the descending phytoplankton bloom. The simulated phytoplankton bloom first occurs at the surface in mid-June, just after the start of ice melt, and then descends through the upper 80 m due to persistent nutrient depletion in the water column above the bloom. Figure 3.3e shows simulated TA in the water column. As with DIC, notable features include the increase in TA during ice growth at 30-40m due to brine release and the decrease in TA at the surface due to dilution during ice melt. There is also a descending drop in water column TA following the phytoplankton bloom which is less pronounced than that for DIC.

Figures 3.4a and b show the simulated salinity and temperature distribution throughout the water column. As discussed earlier, salinity and temperature are constrained to follow output from a 3D regional model. This regional model does not take into account nonlocal transport of salt by brine plumes. The time-evolution of the salinity profile shows that the halocline at approximately 35m persists through the simulation (Figure 3.4b). Sea surface temperature is close to freezing except over the majority of the open-water season (early July to the end of August, Figure 3.4c). The higher temperature during this period serves to increase the surface seawater $p\text{CO}_2$, and hence reduces the carbon uptake capacity of the ocean.

To first order, changes to DIC and TA are generally dependent on changes to salinity. As a test of the DIC-salinity and TA-salinity coupling, Figure 3.5 tracks the salinity vs. DIC and TA at the surface (upper 5 m of the water column) through the ice growth and ice melt and open water periods. During the ice growth period, both DIC and TA show little variability with a slight decrease in DIC and a small increase in TA, and salinity stays between 31.9 and 32.5 ppt. During the sea-ice melt and open water periods, DIC and TA both show a substantial drop by the end of the first time period (17 July) then return to the previous range ($\sim 2150 \text{ mmol m}^{-3}$ for DIC and $\sim 2250 \text{ mmol m}^{-3}$ for TA) for the remainder of the run. The drop in DIC and TA that occurs around 17 July is due to the release of meltwater, and the return to the previous range is due to mixing with underlying

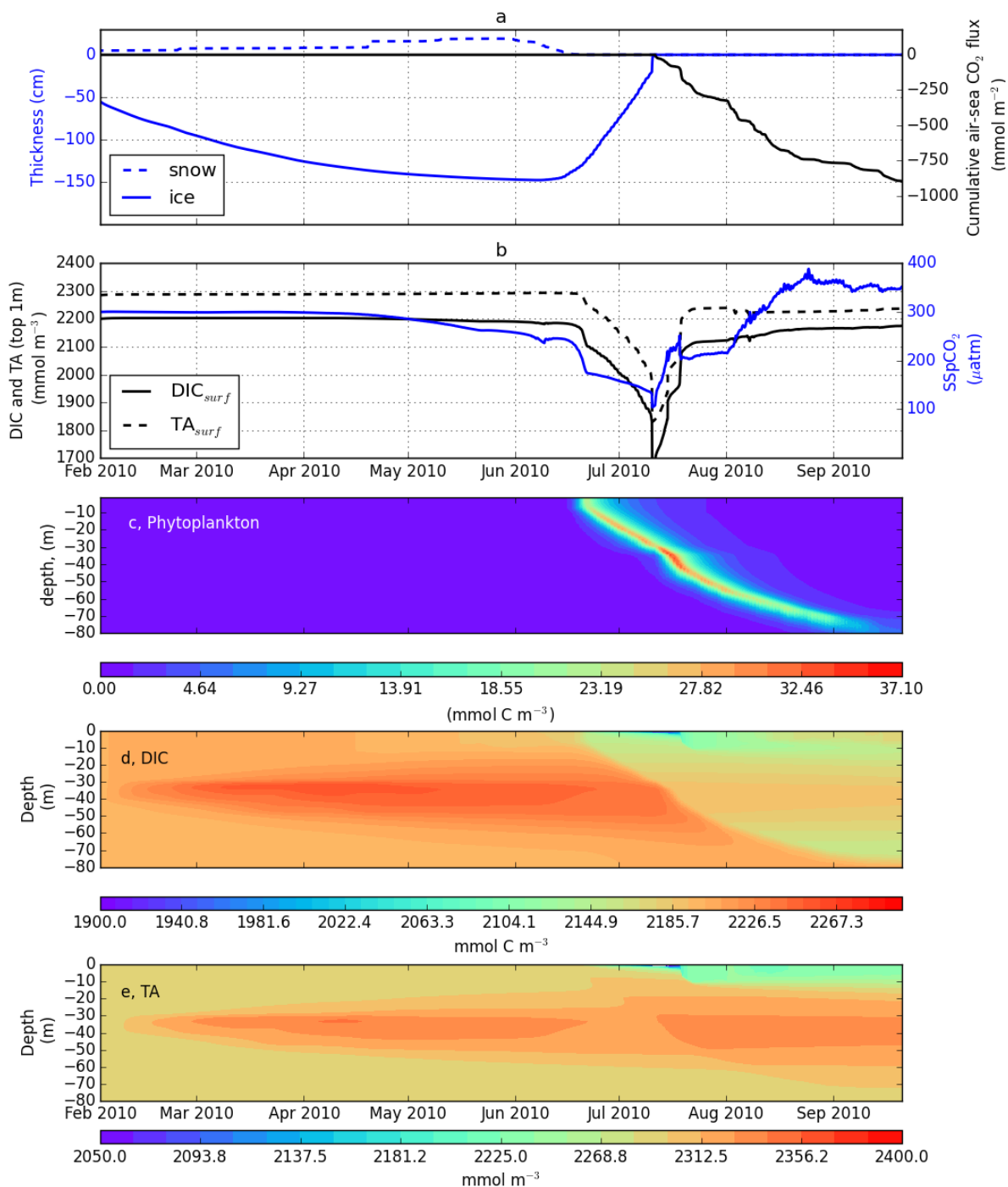


Figure 3.3: Simulated (a) ice/snow thickness and cumulative open-water exchange of carbon, (b) $p\text{CO}_2$, TA, and DIC at the sea surface, (c) phytoplankton biomass (expressed in units of carbon), (d) DIC, and (e) TA in the upper 80 m of the water column.

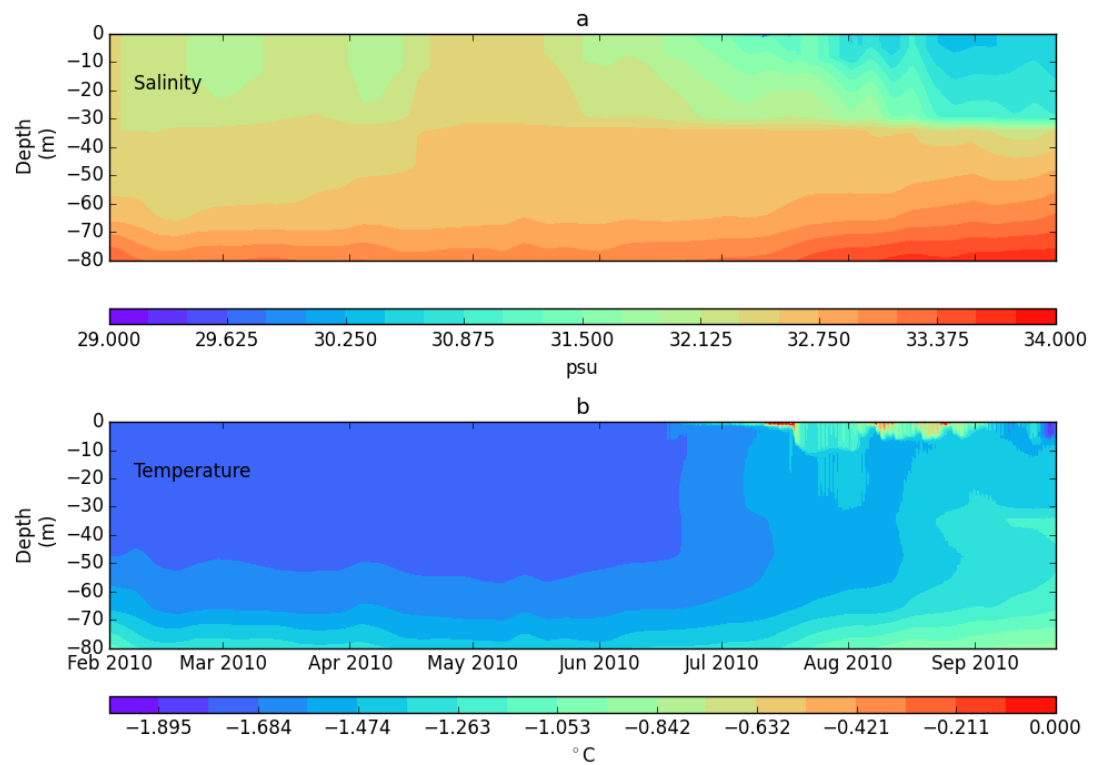


Figure 3.4: Simulated (a) salinity (ppt) and (b) temperature ($^{\circ}\text{C}$) in the upper 80 m of the water column.

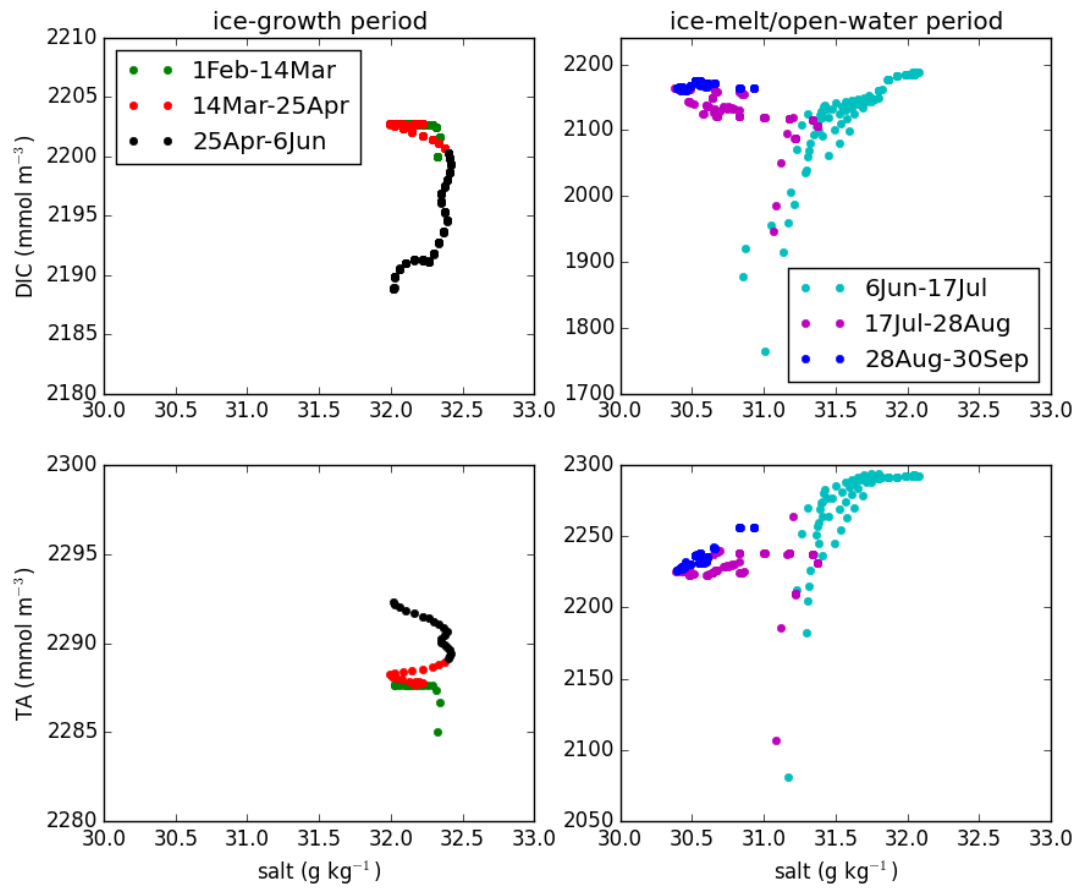


Figure 3.5: Simulated sea surface DIC (top) and TA (bottom) versus salinity over the period of ice growth (left) and ice melt and open water (right) over the standard simulation. The colors indicate time periods listed in the legends, and are the same for DIC and TA.

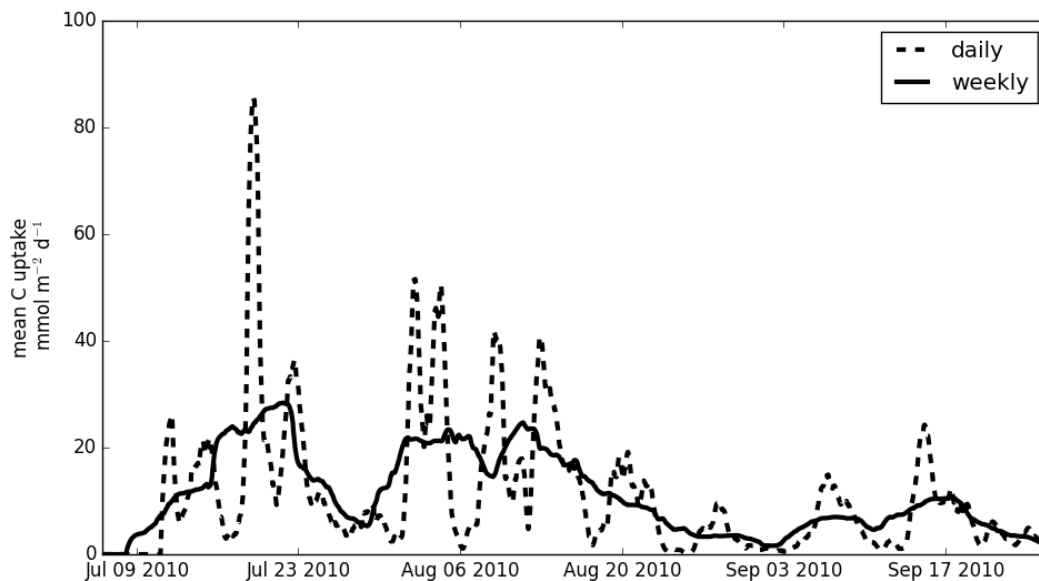


Figure 3.6: Time series of daily- and weekly-mean ocean carbon uptake over the open-water season.

water. The sea surface progressively freshens during the period of ice-melt and open-water, but does not experience the large drop apparent in DIC and TA. The mismatch between the reaction of sea surface salinity and both DIC and TA during the meltwater pulse is due to the fact that the salinity is constrained to an independent 3D regional model. The timing and intensity of ice melt is likely not the same as in this 1D model, and hence the salinity does not exhibit the same reaction to sea ice melt. With the exception of the melt-water pulse, however, TA and salinity generally follow a linear positive correlation, corresponding to seawater end members of, respectively, $TA=2225 \text{ mmol m}^{-3}$ and $S=30.25$ ppt at the lower end, and $TA=2300 \text{ mmol m}^{-3}$ and $S=31.75$ ppt at the upper end. The correlation between DIC and salinity at the sea surface is not as clear, but this can be attributed to the other processes affecting DIC but not salinity (e.g., primary production and air sea CO_2 exchange).

The simulated daily-averaged ocean carbon uptake rate in the standard run over the open-water season (Figure 3.6, dashed line) ranges from $5 \text{ mmol C m}^{-2} \text{ day}^{-1}$ to a one-time extreme of $95 \text{ mmol C m}^{-2} \text{ day}^{-1}$. The corresponding average of $10.2 \text{ mmol C m}^{-2} \text{ day}^{-1}$ over the 90-day open-water season is at the upper end of the carbon uptake rate observed in *Burgers et al. [2017]* of $3\text{-}12 \text{ mmol C m}^{-2} \text{ day}^{-1}$ (into the ocean) in the CAA and Baffin Bay during the late summers of 2013 and 2014. The simulated ocean carbon uptake rate is highest in the first half of the open-water season due to low sea surface $p\text{CO}_2$, which

increases from just under 100 to $\sim 250 \mu\text{atm}$ from the start of the open-water season on July 9 to the beginning of August (Figure 3.3b). *Fransson et al.* [2009] observed sea surface $p\text{CO}_2$ within this range ($200 \pm 19 \mu\text{atm}$) while transiting the region from 17-19 July of 2005. The latter half of the open-water season has lower uptake, maintaining a higher sea surface $p\text{CO}_2$ of around $340 \mu\text{atm}$ (still undersaturated relative to the atmosphere).

In summary, water- and ice-column DIC and TA were constrained by direct observations just before the beginning of the open-water season. The subsequent changes to simulated DIC and TA, dependent on processes including ice melt and ecosystem productivity, were used to compute air-sea exchange and $p\text{CO}_2$ during the open-water season. These fell within the range of independent observations of sea surface $p\text{CO}_2$ and oceanic carbon uptake in the region at similar times of year.

3.3.2 Sensitivity Analysis

The biogeochemical model developed in this study can be used to understand the relative importance of the different processes affecting the air-sea-ice exchange of inorganic carbon in the seasonally ice-covered Arctic Ocean. By changing relevant parameters and comparing model output between the standard and sensitivity runs, we learn what parameters and processes are most important to quantify inorganic carbon flows (and therefore what observations are most important for this purpose). While in general the above argument concerning model-observation collaboration holds, it is particularly relevant for sea ice biogeochemistry, in which observations are difficult and expensive to obtain [*Steiner et al.*, 2016b]. For most of the sensitivity analyses, we focus on net carbon uptake over the open-water season, as it is a commonly-considered integrated measure that is affected by processes both during the ice-covered and ice-free seasons. Table 3.2 lists the sensitivity tests along with their descriptions. Tables 3.3 through 3.7 list the standard run and all the runs for each respective sensitivity test, along with the resultant net ocean (or ocean and ice) carbon uptake for each run.

Initial concentrations of DIC, TA

The initial DIC and TA profiles, DIC_0 and TA_0 , were chosen based on two series of measurements over the ice-melt seasons in 2010 and 2012 [*Brown et al.*, 2015; *Geilfus et al.*, 2015]. The May 2010 observations of water-column DIC and TA in the upper 10 m showed

Run no.	Description
0	Standard run
1	Variation of the initial water column DIC and/or TA
2	Suppression of biological activity
3	Ikaite concentration in the ice
4	Depth of brine deposition
5	Ice-air CO ₂ flux

Table 3.2: List of model runs (standard and sensitivity analyses). Runs 1 increase/decrease initial water column DIC₀ and TA₀; runs 2 suppress some or all of the modelled biological productivity; runs 3 vary the amount of carbon converted into ikaite, DIC_{ikaite}^{ref}; runs 4 vary the depth of the brine release layer; and runs 5 vary the proportion of carbon rejected during ice growth into the atmosphere, instead of the seawater.

Run no.	Description	Net oceanic carbon uptake
0	standard run	916 mmol C m ⁻²
1a	DIC ₀ +10 mmol C m ⁻³	823 mmol C m ⁻²
1b	DIC ₀ -10 mmol C m ⁻³	1008 mmol C m ⁻²
1c	TA ₀ +10 mmol m ⁻³	1001 mmol C m ⁻²
1d	TA ₀ -10 mmol m ⁻³	830 mmol C m ⁻²
1e	DIC ₀ +50 mmol C m ⁻³	880 mmol C m ⁻²
	TA ₀ +50 mmol m ⁻³	
1f	DIC ₀ -50 mmol C m ⁻³	951 mmol C m ⁻²
	TA ₀ -50 mmol m ⁻³	
1g	DIC ₀ +100 mmol C m ⁻³	844 mmol C m ⁻²
	TA ₀ +100 mmol m ⁻³	
1h	DIC ₀ -100 mmol C m ⁻³	987 mmol C m ⁻²
	TA ₀ -100 mmol m ⁻³	

Table 3.3: Analyses and resulting net ocean carbon uptake sensitivity to initial DIC and TA concentrations. Runs 1a-1d increase/decrease initial water column concentrations for either DIC₀ or TA₀ by 10 mmol C m⁻³; runs 1e and 1f increase/decrease initial water column concentrations for both DIC₀ and TA₀ such that their effects on pCO₂ are counteractive.

small variability around the mean ($\sim 10 \text{ mmol m}^{-3}$, Figure 3.2), but the June 2010 observations had a higher variability (attributable to the influence of melt-water dilution and the onset of the sympagic and pelagic blooms). In this sensitivity analysis, we individually vary the initial water column values of DIC and TA by ± 10 and vary them together by $\pm 50 \text{ mmol m}^{-3}$.

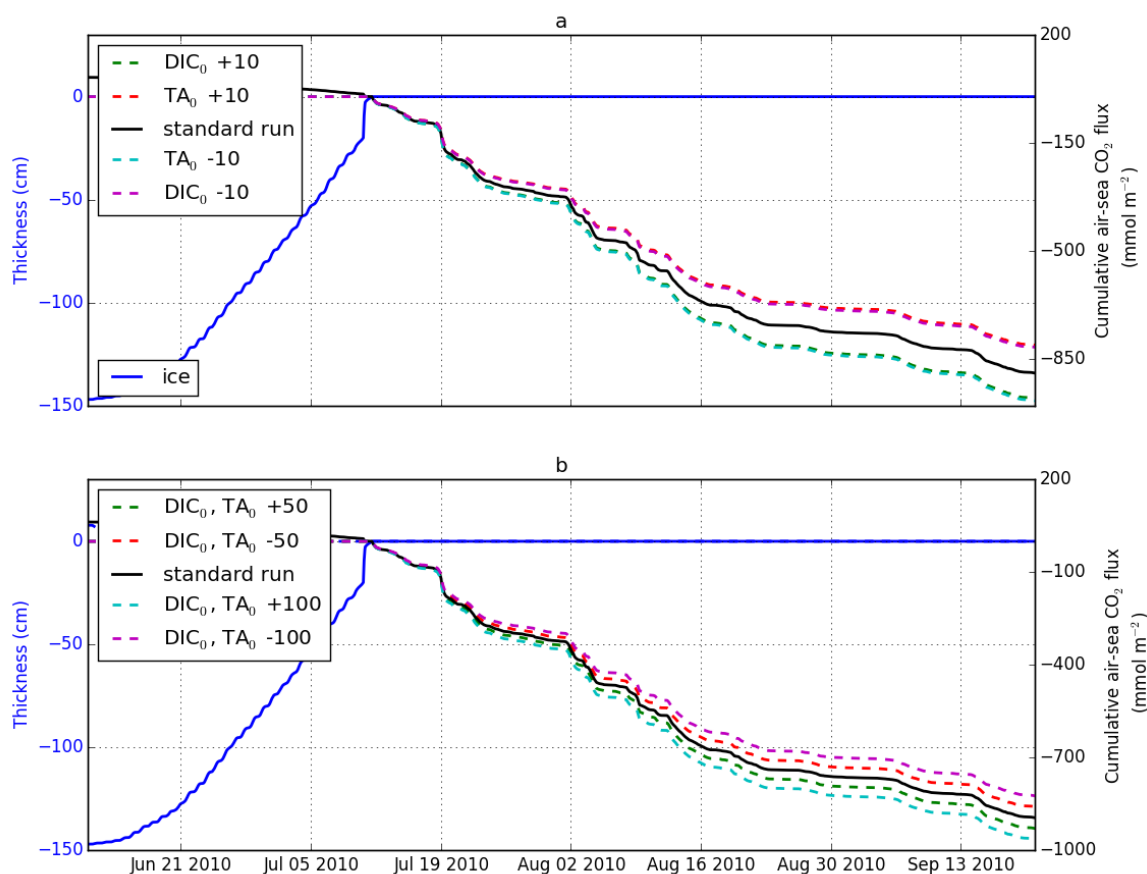


Figure 3.7: Simulated ice thickness in blue (a and b) and net ocean carbon uptake in the standard run (solid black lines) and with DIC_0 and TA_0 increased/decreased a) independently and b) together (dashed lines).

Figure 3.7 shows the cumulative carbon uptake for the standard run, compared with the CO_2 uptake in runs with different DIC_0 and TA_0 . Figure 3.7a shows results with DIC_0 and TA_0 increased/decreased independently by 10 mmol m^{-3} . Increasing (decreasing) DIC_0 reduces (enhances) the uptake capacity of the water column. Increasing DIC_0 by 10 mmol m^{-3} results in a 10% ($\sim 90 \text{ mmol C m}^{-2}$) reduction in the net ocean carbon uptake during

the open-water season, and decreasing DIC_0 by 10 mmol m^{-3} results in a 10% higher uptake. Increasing TA_0 by a given amount has an almost equal and opposite effect to an increase in DIC_0 by the same amount, and similarly for decreasing both. The net carbon uptake in sensitivity runs with TA_0 changed by $\pm 10 \text{ mmol m}^{-3}$ overlies those with DIC_0 changed by $\mp 10 \text{ mmol m}^{-3}$ (Figure 3.7a.).

In runs with DIC_0 and TA_0 increased/decreased together by the same amount, their combined effect on the net CO_2 uptake are all within 9% of the standard run. An increase (or decrease) in both DIC_0 and TA_0 of 50 mmol m^{-3} leads to a change in the net oceanic carbon uptake of $\sim 35 \text{ mmol C m}^{-2}$ over the open-water season. When both DIC_0 and TA_0 are increased (or decreased) by 100 mmol m^{-3} , the resulting change in the net oceanic carbon uptake is $\sim 70 \text{ mmol C m}^{-2}$, which is less than the effect of changing either DIC_0 or TA_0 independently by 10 mmol m^{-3} .

These results indicate that the net carbon uptake is highly sensitive to the values of DIC_0 and TA_0 . Varying either by a small amount, e.g., changing DIC_0 by 10 mmol m^{-3} from the standard run setting of 2200 mmol m^{-3} , leads to a 10% change in the simulated net carbon uptake during the open-water season. In light of this high sensitivity, we note that the standard run values for DIC_0 and TA_0 (based on water column measurements late in the sea-ice season) result in an air-sea exchange of carbon during the open-water season that is close to observations of sea surface $p\text{CO}_2$ and air-sea carbon exchange in the same region during the open-water season (Subsection 3.3.1).

In addition, these results indicate that similar changes in DIC_0 and TA_0 (in sign and magnitude) result in a small change in net carbon uptake in the open-water season, because the changes in DIC and TA have about an equal and opposite effect on the sea surface $p\text{CO}_2$. Necessarily, brine-associated DIC and TA fluxes due to ice growth occur at the same time, as do DIC and TA dilution due to ice melt. If perturbations to both DIC and TA due to ice growth (or melt) are of similar magnitude, then the effects on seawater $p\text{CO}_2$ will be largely counteractive, as will the effects on net carbon uptake during the subsequent open-water season.

Biological contribution: Ice algae and phytoplankton blooms

The simulated sympagic-pelagic ecosystem were set up to closely match observed biological productivity [Mortenson *et al.*, 2017]. The ecosystem has a substantial impact on both the DIC and TA in the upper water column through primary productivity and through the production of detrital organic matter which remineralizes as it sinks. In this sensitivity

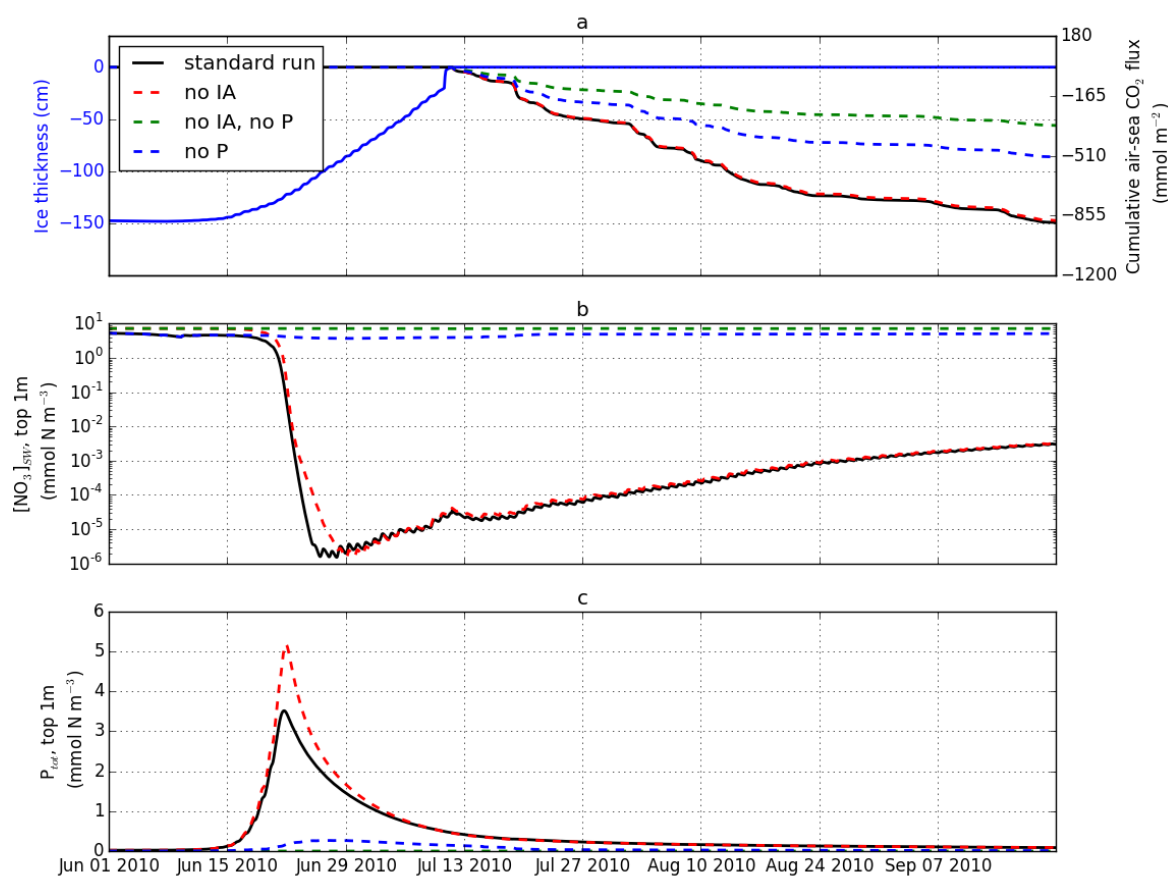


Figure 3.8: Simulated ice depth and net ocean carbon uptake: (a); surface seawater NO_3 concentration (b); and surface phytoplankton biomass (c) in the standard run (solid black) and with ice algae (IA) and pelagic algae (P) blooms suppressed. Note that a small amount of phytoplankton are present (but do not grow) in the top 1 m in the run with ice algae, but with pelagic algae suppressed, due to seeding from ice algae (blue dashed line in c).

Run no.	Description	Net oceanic carbon uptake
0	standard run	916 mmol C m^{-2}
2a	ice algal biomass = 0	904 mmol C m^{-2}
2b	ice and pelagic algal biomass = 0	342 mmol C m^{-2}
2c	pelagic algal biomass = 0	526 mmol C m^{-2}

Table 3.4: Sensitivity of net ocean carbon uptake to primary production. Runs analyze the effect of biological productivity on the net ocean uptake of carbon, including a run with the suppression of only ice algae (2a), with the suppression of both ice algae and phytoplankton (2b), and with the suppression of only phytoplankton (2c).

analysis, we suppress the sympagic and pelagic components of the simulated ecosystem (independently and together) to quantify their respective influences on the air-sea carbon exchange.

A model simulation in which the ice algal biomass is set to zero decreases the net ocean carbon uptake by 12 mmol C m^{-2} , or about 1%, relative to the standard run (Figure 3.8a). In the run with ice algae suppressed, the nutrient concentrations near the surface are higher at the start of the ice melt than in the standard run (Figure 3.8b), which leads to a larger surface phytoplankton bloom at the beginning of the open-water season (Figure 3.8c, and in addition, *Mortenson et al.* [2017]). In the run without ice algae, the reduction in DIC near the sea surface due to the larger pelagic bloom largely (but not completely) compensates for the loss of surface carbon by sinking detrital ice algae in the standard run.

In a simulation with both ice algae and the pelagic primary production set equal to zero, the uptake of carbon over the ice-free period is 37% of that in the standard run. However, when only pelagic primary production is suppressed and ice algae are allowed to bloom, the uptake is 57% of that in the standard run. In the standard run, when both the sympagic and pelagic ecosystems are included, the modelled ice algal bloom is terminated by nutrient limitation (*cf.* Figure 4 of *Mortenson et al.* [2017]). The two runs with pelagic primary production suppressed indicate that ice algae have a stronger influence on air-sea carbon fluxes in the absence of a large under-ice bloom, because the underlying water column would not be as depleted of nutrients.

In our model, almost two thirds of the simulated net ocean uptake of carbon at Resolute is biologically mediated, with pelagic primary production being the dominant process. Primary production by ice algae only slightly increases the drawdown in the standard run, as a result of their competition with phytoplankton for nutrients. In the absence of phytoplankton (as in the central Arctic Ocean), however, the presence of ice algae would have a stronger effect on the net ocean uptake of carbon because more nutrients would be available. In order for a model of the Arctic domain to accurately represent seasonally ice-covered air-sea carbon exchange, it must take biological activity in the water column into account.

Ikaite and ice carbon and TA concentrations

The abiogenic calcium carbonate phase $\text{CaCO}_3 \cdot 6(\text{H}_2\text{O})$, or ikaite, has been detected in Arctic, Antarctic, and experimental sea ice [*Dieckmann et al.*, 2008, 2010; *Rysgaard et al.*,

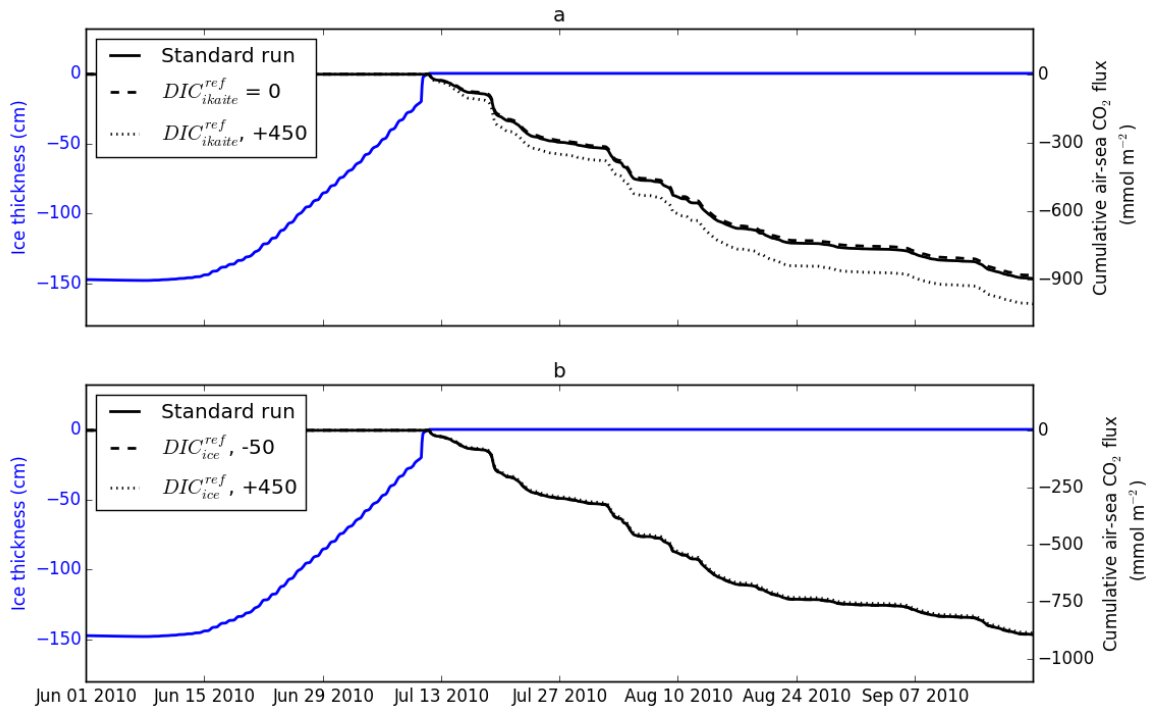


Figure 3.9: Simulated ice depth (blue) and net ocean carbon uptake in the standard run (solid black) and a) with DIC_{ikaite}^{ref} and TA_{ikaite}^{ref} varied in a 1:2 ratio (a); and with DIC_{ice}^{ref} and TA_{ice}^{ref} varied by the same amount (b).

Run no.	Description	Net oceanic carbon uptake
0	standard run	916 mmol C m ⁻²
3a	$DIC_{ikaite}^{ref} = 0$ $TA_{ikaite}^{ref} = 0$	903 mmol C m ⁻²
3b	$DIC_{ikaite}^{ref} = 500 \text{ mmol C m}^{-3}$ $TA_{ikaite}^{ref} = 1000$	1028 mmol C m ⁻²
3c	$DIC_{ice}^{ref} = 350 \text{ mmol C m}^{-3}$ $TA_{ice}^{ref} = 450 \text{ mmol m}^{-3}$	917 mmol C m ⁻²
3d	$DIC_{ice}^{ref} = 850 \text{ mmol C m}^{-3}$ $TA_{ice}^{ref} = 950 \text{ mmol m}^{-3}$	909 mmol C m ⁻²

Table 3.5: Sensitivity of net ocean carbon uptake to changes to ikaite concentration in ice ($\Delta DIC:\Delta TA=1:2$) and equal changes to DIC and TA concentrations in the ice ($\Delta DIC:\Delta TA=1:1$). Runs vary in the amount of DIC and TA deposited in the ice. They include a run with no ikaite (3a) and with an order of magnitude more ikaite in the ice than in the standard run (3b).

2014]. Ikaite will have an impact on both DIC and TA in the ice and underlying water, based on where it precipitates and dissolves. We have represented ikaite in the model as a sea-ice DIC and TA reservoir which is released into the water during ice melt. The concentration of ikaite in ice, $\text{DIC}_{\text{ikaite}}^{\text{ref}}$, is set to 50 mmol C m^{-3} , based on *Geilfus et al.* [2015]. The value of $\text{DIC}_{\text{ikaite}}^{\text{ref}}$ for sea ice is not well constrained, however, and is likely to be dependent on environmental conditions, such as the speed of ice formation and growth [*Papadimitriou et al.*, 2014], and a wide range of ikaite concentrations have been observed, even within a single ice column. In an outdoor laboratory experiment, *Rysgaard et al.* [2013] measured $900 \mu\text{mol ikaite kg}^{-1}$ in the upper ice ($810 \text{ mmol C m}^{-3}$, assuming sea ice density of 0.9 kg m^{-3}), ranging down to $100 \mu\text{mol kg}^{-1}$ (90 mmol C m^{-3}) at the bottom of the sea ice.

We examined the effect of ikaite on net ocean carbon uptake by varying the ikaite parameters $\text{DIC}_{\text{ikaite}}^{\text{ref}}$ and $\text{TA}_{\text{ikaite}}^{\text{ref}}$ from minimum possible values = 0 mmol m^{-3} up to maxima corresponding to a factor of 10 times the standard run values (respectively $500 \text{ mmol C m}^{-3}$ and $1000 \text{ mmol TA m}^{-3}$). We ran two further simulations where both $\text{DIC}_{\text{ice}}^{\text{ref}}$ and $\text{TA}_{\text{ice}}^{\text{ref}}$ are offset by an equal amount (as opposed to the 1:2 DIC:TA ratio inherent in ikaite precipitation and dissolution), relative to the standard run. In these latter two simulations, $\text{DIC}_{\text{ice}}^{\text{ref}}$ and $\text{TA}_{\text{ice}}^{\text{ref}}$ were both offset by negative 50 mmol m^{-3} and positive 450 mmol m^{-3} more than in the standard run (Table 3.5, c and d). We did this in order to compare the effect of differentially changing DIC and TA due to ikaite precipitation in the ice (as in 3a and 3b) to the effect of changing the DIC and TA in the ice by equal amounts (as in 3c and 3d).

In case 3a ($\text{DIC}_{\text{ikaite}}^{\text{ref}} = 0 \text{ mmol C m}^{-3}$), net ocean carbon uptake is reduced by 1%, and in case 3b ($\text{DIC}_{\text{ikaite}}^{\text{ref}} = 500 \text{ mmol C m}^{-3}$), the ocean carbon uptake increased by 12% relative to the standard run (Figure 3.9a). A simulation with $\text{DIC}_{\text{ikaite}}^{\text{ref}}$ twice that in the standard run (not shown) increases the net ocean carbon uptake by 1% (roughly equal and opposite to that in case 3a). The simulations with both $\text{DIC}_{\text{ice}}^{\text{ref}}$ and $\text{TA}_{\text{ice}}^{\text{ref}}$ offset by an equal amount relative to the standard run show a change in the net ocean carbon uptake of less than 1% (Table 3.5c and d, Figure 3.9b).

This model analysis of ikaite precipitation in the sea ice indicates that, within a range in ikaite concentration between 0 and $100 \text{ mmol C m}^{-3}$, there is only a small (1%) change in the net ocean uptake of carbon. However, an order of magnitude increase in ikaite concentration relative to the standard run (from 50 to $500 \text{ mmol C m}^{-3}$) in the simulated ice plays a more important role, accounting for a change of $>10\%$ in the simulated net ocean uptake of carbon in the subsequent open-water season. In contrast, cases 3c and d,

Run no.	Description	Net oceanic carbon uptake
0	standard run	916 mmol C m ⁻²
4a	$d_{brine} = 0 - 40$ m	889 mmol C m ⁻²
4b	$d_{brine} = 0 - 1$ m	864 mmol C m ⁻²

Table 3.6: Sensitivity of net ocean carbon uptake to changes in depth of brine deposition. In run 4a, brine-associated DIC and TA is deposited evenly throughout the upper 40 m, and in run 4b, the brine-associated DIC and TA are released in the 1 m surface layer (4b).

with the ikaite concentration held constant but both DIC and TA within the ice (DIC_{ice}^{ref} and TA_{ice}^{ref}) changed by an equal amount, result in small changes to the simulated air-sea exchange (<1%). This holds even in the case with a near doubling of both DIC_{ice}^{ref} and TA_{ice}^{ref} by an offset of 450 mmol m⁻³ for each (Table 3.5d). Comparing cases 3b and 3d emphasizes that the differential DIC:TA concentration ratio of ikaite, rather than a 1:1 DIC:TA molar offset in the ice, is needed to affect changes to the simulated net ocean carbon uptake.

Depth of brine deposition

As mentioned in Section 4.2, the deposition layer for DIC and TA rich brine in the standard run is set near the simulated halocline, between 30 and 40 m. As this is a physically motivated, but otherwise *ad hoc*, parameterization, we assess model sensitivity to its formulation with regards to both surface carbon flux in the open-water season and to the transport of carbon to depth over a seasonal ice cycle. Figure 3.10a shows the cumulative air-sea carbon exchange over the open-water season for three different representations of the depth range of brine deposition: between 30-40 m (standard run), within the top 1 m, and mixed throughout the top 40 m. Comparison of DIC and TA in the standard run with those in the run with deposition at 0-1 m are shown in Figures 3.10b and c. Although there is a large increase in the DIC near the surface in the surface deposition run, relative to the standard run, the coincident increase in TA in the 1 m run changes the pCO_2 of surface water by an approximately equal and opposite amount, leading to a decrease of less than 6% in the net ocean carbon uptake over the open-water season relative to the standard run. For the run with brine distributed evenly over the top 40m, the decrease in net ocean uptake relative to the standard run was 3% (Figure 3.10a).

The results of this analysis again emphasize that, although the net ocean uptake of carbon during the open-water season is an important and physically relevant output, it is not the only important metric when considering changes to the surface ocean inorganic carbon

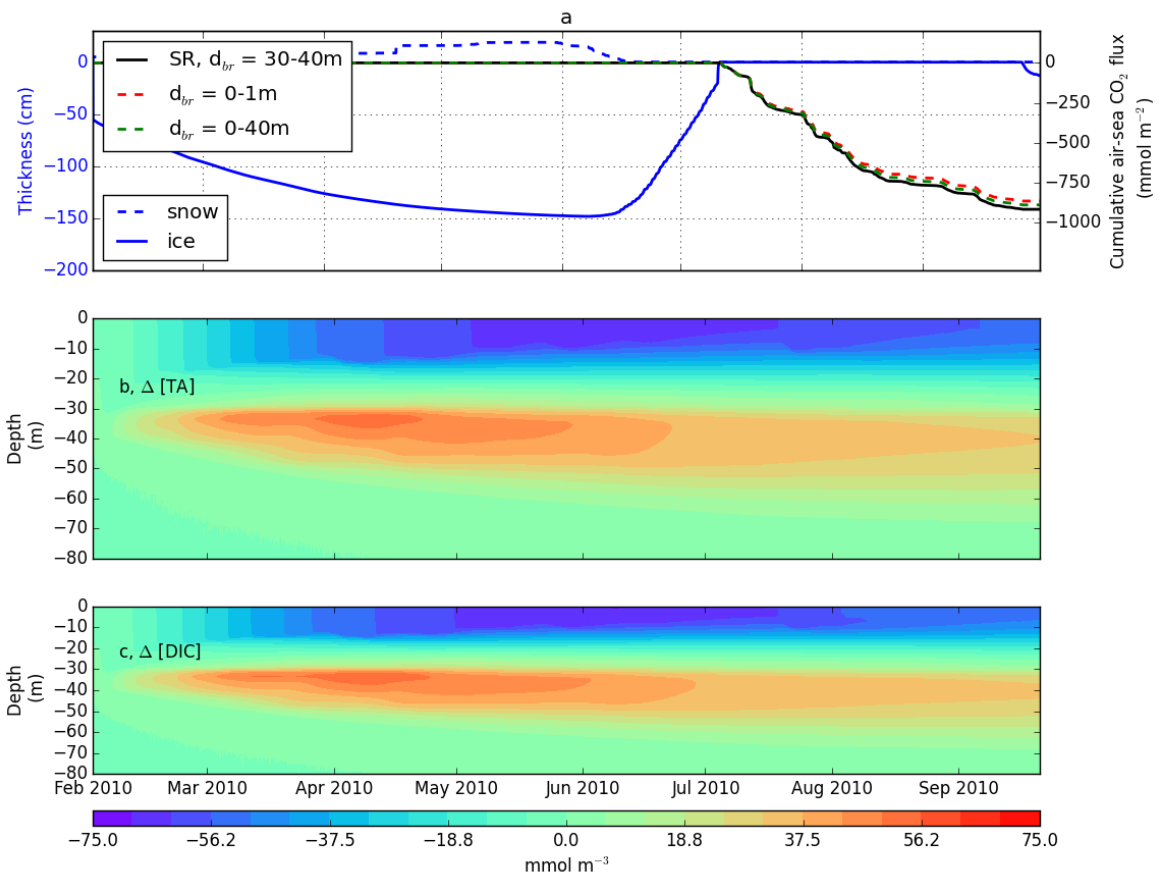


Figure 3.10: Simulated ice depth and net ocean carbon uptake in the standard run (solid black) and with brine-associated DIC and TA deposited in the upper 1 m (red) and in the upper 40m (green) (a) and TA and DIC in the standard run minus the run with surface 1 m deposition of brine-associated DIC and TA (b and c, respectively).

Run no.	Description	Net oceanic + ice (total) carbon uptake
0	standard run	916 + 50 (966) mmol C m ⁻²
5a	$P_{SW} = 95\%$	916 - 20 (896) mmol C m ⁻²
5b	$P_{SW} = 90\%$	916 - 103 (813) mmol C m ⁻²
5c	$P_{SW}^* = 95\%$	902 + 107 (1009) mmol C m ⁻²
5d	$P_{SW}^* = 90\%$	873 + 231 (1104) mmol C m ⁻²

Table 3.7: Sensitivity of net ocean and ice inorganic carbon uptake to the proportion of sea-ice carbon exchange with the atmosphere vs. the ocean. Runs include 95 and 90% of inorganic carbon released by growing ice into the ocean (5a, 5b) and 95 and 90% of the inorganic carbon taken up by melting ice coming from the ocean (5c, 5d).

system. Even if there is a large change in DIC at or near the surface, a similar change in TA would counter the effect on $p\text{CO}_2$ of the surface water, reducing any change in net ocean uptake of carbon. Despite the fact that sea surface $p\text{CO}_2$ is relatively insensitive to changes to the parameterized brine-injection depth, there are substantial differences in the vertical transport of inorganic carbon (Figure 3.10c). This experiment illustrates that there can be local vertical fluxes and enrichment of deep DIC without having local air-sea fluxes. Over multiple years in the CAA, as water travels from west to east, the vertical transport of carbon as parameterized in the standard run would result in an accumulation of carbon at depth over several ice seasons. This process could cause DIC to accumulate at depth in CAA outflow water (and potentially other Arctic sea shelf waters) and enhance the deep convective transport of carbon in downstream regions of deep water formation such as the North Atlantic seas [Melling and Moore, 1995].

Proportions of inorganic carbon released to seawater and air during ice growth and melt

The parameterizations for air-ice CO_2 exchange were chosen in order that the outgassing during ice growth and uptake during ice melt match observations. In the standard run, the proportion of inorganic carbon that is released to the ocean (atmosphere) from the growing ice is set at $P_{SW} = 99\%$ (1%), based on estimates of *Sejr et al.* [2011] and *Geilfus et al.* [2016]. During ice melt, the ice is parameterized as a carbon sink, with $P_{SW}^* = 97.5\%$ (2.5%) of the total, negative virtual flux of inorganic carbon into the ice from the ocean (atmosphere), in order to match CO_2 uptake rate of melting sea ice observed by *Delille et al.* [2014] and *Geilfus et al.* [2016]. The simulated ice is thus parameterized to outgas carbon during ice growth and take up atmospheric CO_2 during ice melt, resulting in a net air-to-ice uptake of 50 mmol C m⁻² over the length of the standard run (or 5% of the net ocean uptake of carbon during the open-water season). However, the values of P_{SW}

and P_{SW}^* are poorly constrained, due to the difficulty and scarcity of direct measurements of ice-air and ice-water carbon fluxes. Observations of ice-air CO_2 exchange are difficult to measure, and measurements have varied over an order of magnitude between chamber and eddy-covariance techniques [Nomura *et al.*, 2018]. Discussion of the reason(s) for different measured exchange rates between the 2 methods is beyond the scope of this paper, but if either the release during freezing, or the uptake during melt, is an order of magnitude larger, the net uptake by the ice-ocean system would change substantially. In this sensitivity analysis, we increase the air-ice exchange of CO_2 during ice growth and melt (by decreasing, independently, each of P_{SW} and P_{SW}^* to 95% and 90%).

The inorganic carbon released to the water column during ice growth (proportional to P_{SW}) is associated with brine deposition at the bottom of the mixed layer. Hence a change in P_{SW} results in a change to the DIC at 30-40m depth during ice growth, but this change does not mix up to the surface by the end of the open-water season. Therefore, the air-sea flux in the single open-water season we model is unchanged (Table 3.7). Varying P_{SW} does, however, affect the parameterized net air-ice carbon flux, a component of the net carbon flux from the combined ice-ocean system to the atmosphere. In the run with $P_{SW} = 95\%$ (90%) during ice growth, ice acts as a net source of carbon to the atmosphere, outgassing 20 (103) mmol C m^{-2} . These values correspond to 2% (11%) of the net ocean carbon uptake during the open-water season.

When P_{SW}^* is decreased, the parameterized air-to-ice carbon uptake is increased, but the surface ocean is a weaker sink of atmospheric carbon during the subsequent open-water season because the surface DIC concentrations are higher when P_{SW}^* is smaller. In terms of the combined ice-ocean uptake of atmospheric carbon, these two effects offset one another, but do not cancel. Sensitivity runs with P_{SW}^* equal to 95 and 90%, respectively, result in an increase of the combined ice-ocean uptake of carbon of 4.5% and 14%.

This analysis emphasizes and quantifies the importance of air-ice carbon fluxes for carbon exchange in seasonally ice-covered areas. Further work in constraining these proportions would be beneficial for understanding the air-sea-ice carbonate system and ocean carbon uptake in polar marine environments.

3.4 Conclusions

In this study, a 1D biogeochemical model incorporating both sea-ice and pelagic systems is used to assess the importance of various processes to the vertical transport and exchange

of inorganic carbon in a seasonally ice covered marine Arctic environment (specifically near Resolute, Nunavut, Canada). These processes include primary production, remineralization, and nitrification; ice-water and ice-air fluxes of carbon due to ice growth and melt (including transport by brine plumes); ikaite precipitation and dissolution; and direct air-sea exchange. Physical, chemical, and biological properties for the water column and ice were initialized based on observations. The resultant simulated outputs for net ocean carbon uptake during the open-water season are within the range of independent summer time observations of air-sea carbon flux in the region, with a mean value of $10.2 \text{ mmol C m}^{-2} \text{ day}^{-1}$ over the open-water season.

The carbon cycle we have implemented provides insight into the ocean carbon uptake and exchanges during ice growth, ice melt, and in the open-water season. Varying either the initial water column DIC or TA by a small percentage ($\pm 1\%$) leads to a relatively large change in the net ocean carbon uptake ($\pm 10\%$). This fact implies that we could expect large interannual variability in air-sea carbon exchange for the region. However, when both DIC and TA have similar changes in both sign and magnitude, as occurs during ice growth and melt (via concentration and dilution, respectively), the changes in sea surface $p\text{CO}_2$ largely cancel one another.

Sensitivity analyses indicate that sympagic and total (sympagic and pelagic) biological activity respectively account for 1% and more than 50% of the net ocean carbon uptake. Ice algae have a larger absolute impact when pelagic primary production is suppressed, because of reduced competition for nutrients. Brine rejection during ice growth impacts the carbon export to depth, but varying this depth does not substantially impact air-sea carbon exchange in the subsequent open-water season, because the changes to sea surface $p\text{CO}_2$ are effectively canceled out by the countering effects of changes to TA and DIC. Inclusion of ikaite precipitation within sea ice, and subsequent dissolution in the water column during ice melt, results in only a small change ($\sim 1\%$ for ikaite concentrations of 50 mmol C m^{-3}) to the net ocean carbon uptake. However, an order of magnitude larger ice-ocean transfer of ikaite could have a larger impact on the subsequent open-water season ($>10\%$) because of the inherent differential contribution of DIC and TA to the water column.

Lastly, the proportions of carbon exchanged between the ice and the atmosphere during growth and melt, respectively set in the standard run at 1% and 2.5% of the total fluxes from the ice, are not well constrained. In the case of enhanced release by growing ice, a tenfold increase in the ice-air outgassing of carbon during ice growth would amount to a decrease in the net annual uptake by the combined ocean-ice system of about 10%. In the

case of a similarly enhanced uptake by melting ice, the resulting higher DIC concentration in the melt-influenced surface waters leads to a reduction in the ocean uptake during the open-water season (which partially compensates for the increased carbon uptake by melting ice), but there is still an increase in the net uptake of the combined ocean-ice system of $\sim 20\%$.

Seasonal ice cover occurs over a large region of the Arctic Ocean. This 1D model study implements both physical and biogeochemical effects in the ice and water column and sheds some light on vertical carbon exchange processes in areas with both ice-covered and open-water seasons. Specifically in the CAA, where water is transported eastward towards Baffin Bay and ultimately the Labrador Sea, waters can experience the seasonal freeze and melt cycle 1-3 times during the transit across the CAA shelf (based on transport estimates presented in *Curry et al.* [2014]). The processes described in this study can lead to DIC, TA, and salt being preferentially deposited in the lower water column before entering deeper channels at the eastern edge of the CAA shelf. This may serve to enhance deep water convective transport of carbon in the Labrador Sea and North Atlantic Ocean.

This 1D study is the basis for further work with a sea-ice biogeochemical inorganic carbon cycle implemented in a 3D Arctic regional model. The purpose of the 3D study is to investigate how the present marine Arctic environment contributes to global air-sea CO_2 exchange. In addition, the regional model will be used to study how the changing sea-ice cover over the past recent decades, and into the near future, has affected, and will continue to affect, Arctic Ocean CO_2 uptake.

4 Evaluating the evolution of the inorganic carbon system in the Arctic Ocean from 1980 to 2015

Chapter Abstract

I present a biogeochemical model of the Arctic Ocean incorporating both sea ice and water column processes coupled to a 3D regional ice-ocean model, with a focus on the pan-Arctic oceanic uptake of carbon in the recent era of Arctic sea ice decline (1980 – 2015). The purpose of this study was to simulate the evolution of the Arctic Ocean’s carbon uptake capacity and impacts on ocean acidification with the changing sea ice-scape. Two major updates to commonly-used carbon cycle models implemented in this study are, one, incorporation of sea ice algae to the ecosystem, and two, modification of the sea-ice carbon pump to transport brine-associated Dissolved Inorganic Carbon (DIC) and Total Alkalinity (TA) to the depth of the bottom of the mixed layer (as opposed to releasing it in the surface model layer). The model suggests the total uptake of carbon for the Arctic Ocean (north of 66.5°N) increases from $\sim 115 \text{ Tg C yr}^{-1}$ in 1980 – 1985 to $\sim 135 \text{ Tg C yr}^{-1}$ for 2010 – 2015, an increase of $\sim 20\%$, and the mean pan-Arctic sea surface $p\text{CO}_2$ increases from 300 to 340 μatm over that time. The rise in SST accounts for $\sim 10\%$ of the increase in simulated pan-Arctic sea surface $p\text{CO}_2$. A regional analysis indicated large variability between regions, with the Laptev Sea in particular exhibiting low sea surface pH relative to the pan-Arctic mean and seasonal undersaturation of aragonite by the end of the standard run. Two sensitivity studies have been performed to assess the effects of sea-ice algae and the sea-ice carbon pump in the pan-Arctic, with a focus on sea surface inorganic carbon properties. Excluding the sea ice-carbon-pump results in a marked decrease in seasonal variability of sea-surface DIC and TA averaged over the Arctic Ocean, but only a small change in the net total carbon uptake (of $\sim 1\%$ by the end of the no-ice-algae run). Neglecting the sea

ice algae, on the other hand, exhibits only a small change in sea-surface DIC and TA averaged over the pan-Arctic Ocean, but a slightly stronger effect on the net total carbon uptake of the Arctic Ocean (increasing to $\sim 4\%$ by the end of the no-ice-algae run).

4.1 Introduction

Atmospheric $p\text{CO}_2$, and its oceanic counterpart, dissolved inorganic carbon (DIC), can be seen as a system of two reservoirs, coupled through the air-sea exchange of carbon. It can be argued that this coupled system is largely oceanic-driven, given that the carbon reservoir of the ocean is two orders of magnitude larger than that of the atmosphere [Ciais *et al.*, 2013].

In the last half-century, the Arctic Ocean has undergone dramatic shifts, particularly at the sea surface and along coastal shelves. In addition to the loss of sea ice immediately apparent from the satellite record (*e.g.*, Stroeve *et al.* [2012]; Barber *et al.* [2015]), the physical attributes of the Arctic Ocean have exhibited accelerated changes including warming and freshening [Carmack *et al.*, 2016]. The Arctic is also undergoing biogeochemical changes. In particular, it is becoming lower in pH and decreasing in calcium carbonate saturation state (of the biologically relevant forms of aragonite and calcite: Ω_{arag} and Ω_{calc}) faster than the global ocean-averaged trends [Miller *et al.*, 2014; Steiner *et al.*, 2015a; Wallhead *et al.*, 2017; Bellerby *et al.*, 2018].

The polar regions comprise a large proportion of the global ocean's carbon uptake. In the Arctic (as well as the Antarctic), sea ice provides a unique interface that both directly and indirectly affects the air-sea exchange of carbon. This study describes the development and application of a 3D coupled physical-biogeochemical model for the Arctic to analyze carbon fluxes in the Arctic Ocean. Many of the carbon-related mechanisms associated with sea ice are often neglected or over-simplified in current ocean and climate models. For example, observations describe a marked difference between the DIC concentration of sea ice and that of the seawater from which it formed (and similarly for TA). From a budgetary view, this necessitates a flux of carbon out of the forming ice, due to the transition from seawater to sea ice, as well as the dilution of near-surface seawater as ice melts. This two-part process is called the sea ice-carbon pump [Rysgaard *et al.*, 2011]. In this study, the sea-ice carbon pump is implemented as a parameterized carbon flux in order to represent the release of high-DIC, high-TA brine during ice growth, and of low-DIC, low-TA meltwater during ice melt. During ice growth, I implement a nonlocal

transport of the DIC and TA, associated with (dense) brine rejection, by depositing both DIC and TA at the bottom of the mixed layer rather than at the surface. The development and analysis of this parameterized ice-carbon pump in a 1-D model study are described in detail in Chapter 3. In the present chapter, the parameterized sea-ice carbon pump is implemented into a regional coupled sea-ice and ocean biogeochemical model of the Arctic Ocean.

In addition to the existing pelagic ecosystem previously developed for the model (Chapter A.2.1), I have added a sea-ice associated (sympagic) ecosystem to represent the Arctic spring bloom of sea ice algae, dominated by pennate diatoms, as an additional photosynthetic functional group. The sympagic ecosystem model is described in detail in Chapter 2. The simulated sea ice algae have a higher sensitivity to low-light conditions relative to the simulated pelagic phytoplankton, which represents the ice-algal acclimation to low-light conditions. The ice algae, along with the simulated pelagic ecosystem, serve as a sink of DIC associated with primary production, and a source of DIC associated with remineralization of detritus. Likewise, both the simulated ice-carbon pump and the sympagic and pelagic ecosystems affect the ocean TA at the surface and throughout the water column (although the effect on TA is not entirely analogous to that of DIC, Chapter 3).

With these implementations, which are described in detail in Section 4.2, I ran a coupled ice-ocean biogeochemical and physical simulation driven by atmospheric observations over the satellite record (1980 – 2015, including a spinup period from 1969 – 1979). I chose this period because it spans the recent retreat of Arctic sea ice. This regional model provides a new tool to analyze trends and changes in the carbon system during the recent changes in Arctic sea ice. This model study is the first to represent the ice carbon pump as a non-local transport mechanism for DIC and TA, and also the first to include both a pelagic and sympagic ecosystem in a model of the Arctic Ocean in order to assess the Arctic Ocean's carbon uptake capacity. I assess the results of the standard run in Section 4.3 and then describe regions that deviate from the pan-Arctic mean in the standard run. Furthermore, I assess the importance of representing the sea ice-carbon pump and sympagic ecosystem through two sensitivity studies in Section 4.4 in which each is independently suppressed. In the final section, I summarize results of this model study, implications, and potential future directions.

4.2 Methods

In this study, I have applied the Nucleus for European Modelling of the Oceans, version 3.4 (NEMO; *Madec and the NEMO team* [2008]) to a domain encompassing the Arctic Ocean. The model is broadly divided into three separate components representing, respectively, a physical ocean model, a biogeochemical ocean and sea ice model, and a physical sea ice model. The period of the standard run is 1980 – 2015, with a spinup period from 1969 – 1979. The period 1980 – 2015 was chosen based on available forcing, initialization, and lateral boundary datasets, and because it spans the period of substantial qualitative and quantitative changes in the Arctic Ocean sea ice-scape. Detailed sensitivity analyses regarding various model settings related to the Arctic sea ice and forcing were carried out in *Hayashida et al.* [2018].

4.2.1 Ocean and sea ice physics models

The ice-ocean physics in NEMO is simulated using Océan Parallélisé (OPA), coupled to the Louvain-la-Neuve sea Ice Model, version 2 (LIM2). The physical ocean model, OPA, represents ocean dynamics and thermodynamics through the primitive equations along with the nonlinear seawater equation of state and a free surface formulation for sea-surface height [*Madec and the NEMO team*, 2008]. The ice model, LIM2, is comprised of 2 ice layers and 1 snow layer, and represents dynamics and thermodynamics within the ice [*Bouillon et al.*, 2009]. The default setting for LIM2 does not allow any light penetration when there is snow cover. In order to provide adequate light penetration at the time of observed ice algae blooms, the default setting for LIM2 was modified to allow some light penetration through a thin snow cover, as described in *Hayashida et al.* [2018]. Documentation and source files for both sea-ice and ocean physical models (OPA and LIM2) can be found at <https://www.nemo-ocean.eu>.

4.2.2 Ocean biogeochemical model

In addition to the physical models for the ice and ocean, NEMO admits coupling to different biogeochemical models. In this study, a biogeochemical model including a pelagic ecosystem (Canadian Ocean Ecosystem, or CanOE) was implemented. The biogeochemical model CanOE was developed at the Canadian Centre for Climate Modelling and Analysis for implementation in the Canadian Earth System Model version 5 (CanESM5) (Christian

et al., in preparation, Appendix A.2). CanOE was implemented following the architecture provided for the Pelagic Interactions Scheme for Carbon and Ecosystem Studies, v2 (PISCES [Aumont et al., 2015]) model, one of two default options for the biogeochemical model in NEMO. CanOE includes a pelagic ecosystem comprised of four functional groups: two phytoplankton groups, representing small dinoflagellates (P1) and large diatoms (P2), and small and large zooplankton grazers (Z1 and Z2). Nutrients in CanOE include both nitrogen components (NH_4 and NO_3) as well as an inorganic carbon system with a sink of DIC associated with primary productivity and a source of DIC associated with remineralization of detritus. For the present study, CanOE is modified to include both a sympagic ecosystem and a sea-ice carbon pump.

Sea-ice ecosystem and sea-ice carbon pump

The sea-ice ecosystem is represented via the addition of a bottom ice-associated (sympagic) ice algae functional group. The ice algae, located in the lower ice column denoted the skeletal layer, is coupled to the pelagic ecosystem through the release of ice-algae detritus and to water column nutrients via transfer of nutrients at the ice-water interface. The growth rate for ice algae is dependent on temperature and the availability of light and nutrients. The ice algae take up nutrients within the ice skeletal layer during photosynthetic growth, and release both nutrients and organic carbon into the water column during senescence in the form of sinking detritus. Also, consistent with the 1D model described in Chapters 2 and 3, ice-algae detritus contributes to the pelagic large phytoplankton through seeding. The organic carbon is converted to DIC through remineralization as the detritus sinks through the water column. At the same time, NH_4 is converted to NO_3 by nitrification.

Modifications to the model’s inorganic carbon system are due directly and indirectly to the sea ice directly by changing the mechanism for DIC and TA fluxes via the seasonal growth and melt cycle, as described above, and indirectly as a base for the sympagic ecosystem. CanOE has been modified to include an ice carbon pump with nonlocal transport of brine (high in DIC and TA relative to *in situ* sea water concentrations) during ice growth, and the dilution of near-surface waters during ice melt. The DIC and TA fluxes (respectively, ϕ_{ice}^{DIC} and ϕ_{ice}^{TA}) due to brine rejection into the water column during ice growth, and due to the dilution of DIC and TA in the surface water during ice melt, are parameterized through a constant ice-ocean concentration difference, similar to the (salt-normalized) default setting in PISCES, multiplied by the change in ice volume in a given timestep:

$$\phi_{ice}^{DIC} = P_{SW} \frac{(DIC_{ice}^{ref} - DIC_{SW}^{ref}) \Delta V_{ice}}{A_{ice} \Delta t}, \quad (4.1)$$

where P_{SW} is the proportion of DIC released to the water column (as opposed to the atmosphere, as in the 1D study described in Chapter 2), $\frac{\Delta V_{ice}}{\Delta t}$ is the change in the volume of the ice over a model timestep, A_{ice} is the ice area within the grid cell, and DIC_{ice}^{ref} and DIC_{SW}^{ref} are the reference concentrations of DIC in the ice and seawater (Table 3.1 in Chapter 3). Similarly, for TA,

$$\phi_{ice}^{TA} = \frac{(TA_{ice}^{ref} - TA_{SW}^{ref}) \Delta V_{ice}}{A_{ice} \Delta t}, \quad (4.2)$$

where TA_{ice}^{ref} and TA_{SW}^{ref} are the reference concentrations of total alkalinity in the ice and seawater. The inclusion of ikaite precipitation in the ice and dilution in the water discussed in Chapter 3 were not treated explicitly in the DIC and TA budgets of the 3D formulation. They are implicit in the reference concentration differences for each between ice and seawater. It is also worthwhile to note that in Chapter 3, ikaite was shown to have little effect on air-sea carbon exchange within the range of observations.

The major difference between the sea ice-carbon pump in the default framework of PISCES and the modified sea ice-carbon pump in the present study is the depth of release of brine-associated DIC and TA during ice growth. In PISCES the brine-associated TA and DIC fluxes are released into the surface layer of the model, while in the present study they are released at the bottom of the mixed layer as a representation of the non-local transport of brines (as described in Chapter 3, based on *Jin et al.* [2015]).

The carbon system properties of pH, pCO_2 , Ω_{arag} , and Ω_{calc} presented in this study were calculated offline from model output of DIC, TA, temperature and salinity, following *Dickson et al.* [2007], with equilibrium constants of *Lueker et al.* [2000]. The saturation states were based on *Mucci* [1983] with the pressure correction of *Millero* [1995]. When spatially or temporally averaged carbon system quantities are shown, these are computed at each point in time and space first, and then averaged.

4.2.3 Model domain

I apply NEMO on the North Atlantic and Arctic (NAA) grid developed at the University of Alberta and available at http://knossos.eas.ualberta.ca/xianmin/anha/model_

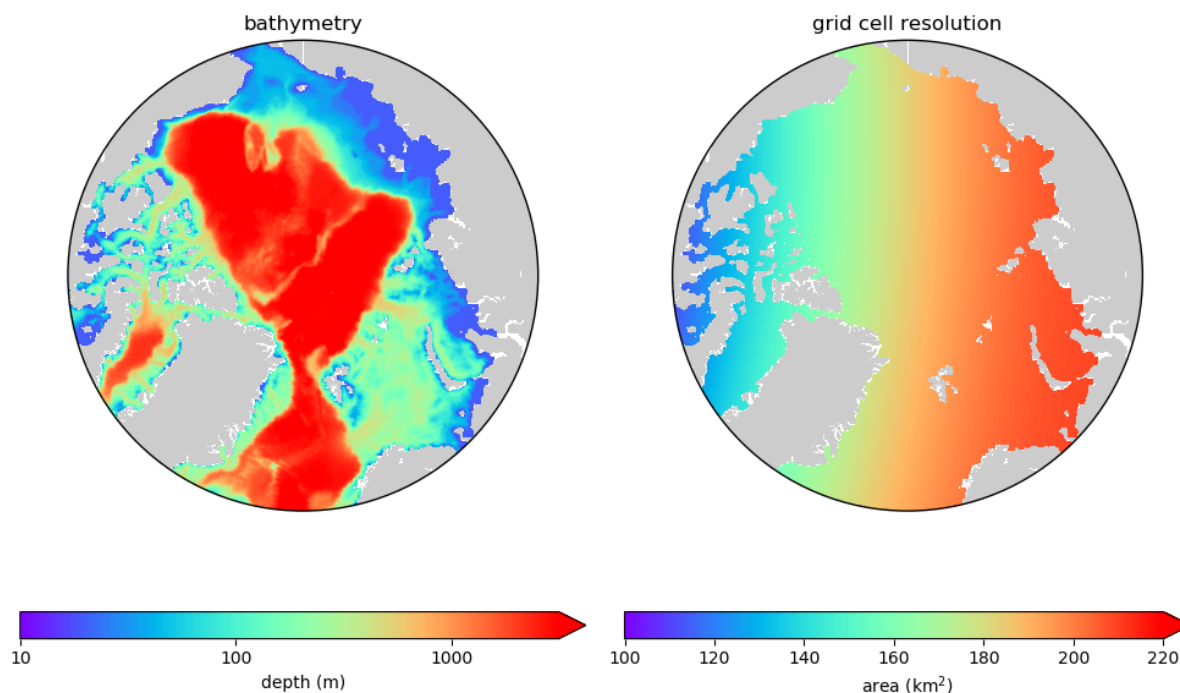


Figure 4.1: Model bathymetry (left) and grid cell resolution (right) for the Arctic Ocean.

configuration.pspl#naa. The domain of the NAA grid in the present study does not follow lines of latitude and longitude, but has 3 major boundaries: at approximately 60° N or 100 km south of Bering Strait in the North Pacific, across the North Atlantic at about 50° N, and at the mouth of Hudson Bay. The horizontal grid resolution ranges from 11 km near the North American coastline to 15 km along the northern Eurasian coastline (Figure 4.1). The vertical resolution is modified from the original NAA configuration in order to have higher vertical resolution near the ocean surface (from ~ 6 m for the upper surface layer to 1 m), as described in *Hayashida et al.* [2018]. The time resolution of the model is set to 20 minutes.

4.2.4 Atmospheric forcing

The 3D simulation is forced by meteorological data for the Arctic Ocean from 1969 to 2015, from the Drakkar Forcing Set (DFS), version 5.2 (<https://www.drakkar-ocean.eu/>). The DFS dataset provides atmospheric information on a 0.7 degree resolution grid, with temporal resolution of 3 hours for winds at 10 m above the surface and air temperature and humidity at 2 m; and daily resolution for incoming shortwave and longwave radiation,

snowfall and total precipitation (rain plus snow). Note that the period 1969 – 1979 is used as a spin up period and not included in the model evaluation.

4.2.5 Initial and boundary conditions

The model is initialized with physical variables (temperature and salinity) from data fields in the Ocean Reanalysis System 4 (ORAS4) [Balmaseda and Weaver, 2013]. Initial conditions for biogeochemical variables (NO_3 , DIC and TA) were based on the GLObal Ocean Data Analysis Project version 2 (GLODAP) [Lauvset et al., 2016]. For grid cells with initial ocean temperature within 2°C of freezing, sea ice thickness and concentration were respectively set to 2.5 m and 95%, with 10 cm of snow cover; otherwise these were set to 0.

In the model, the ocean surface is subject to air-sea gas exchange as well as dilution (concentration) due to river runoff and precipitation (evaporation). The atmospheric $p\text{CO}_2$ is set to monthly-mean values from observations at Mauna Loa (<http://scrippsco2.ucsd.edu>), which increase from $\sim 320 \mu\text{atm}$ in 1970 to more than $400 \mu\text{atm}$ by 2015. It should be noted that the seasonal variability in atmospheric $p\text{CO}_2$ is more pronounced in the Arctic than in the lower latitudes as measured at Mauna Loa. A more accurate representation of atmospheric $p\text{CO}_2$ over the Arctic Ocean would be the time series of observations from Point Barrow, Alaska. The trends for both Mauna Loa and Point Barrow and annual average largely overlap, but the seasonal variability is $\sim 15 \mu\text{atm}$ for Point Barrow while the range at Mauna Loa is about half of that in the Arctic.

River flow input at the six major Arctic rivers (MacKenzie and Yukon Rivers in North America, and Kolyma, Lena, Yenisey, and Ob in Eurasia) is based on the climatological monthly means of Dai et al. [2009]. Each of the rivers was assigned a particular concentration for DIC, TA, and nitrate based on the studies of Tank et al. [2012], Cooper et al. [2008], and McClelland et al. [2012]. Organic matter, in the form of dissolved organic carbon (DOC) and dissolved organic nitrate (DON), for each river was based on the studies of Cooper et al. [2008], Holmes et al. [2012], and McClelland et al. [2012]. The riverine input of DOC and DON are added directly to the respective inorganic pools of DIC and nitrate.

Open-ocean boundaries of the model domain are located in the North Pacific south of Bering Strait, and in the North Atlantic south of Greenland. The boundary conditions for physical variables (temperature, salinity and velocity) were based on climatological monthly-mean fields of ORAS4, and interpolated to the NAA grid's open ocean boundaries.

Relaxation time scales were set to 1 day for inflow and 15 days for outflow, consistent with *Dupont et al.* [2015]. For inorganic carbon system variables, the open-ocean boundary conditions were held constant at the initial values. The constant value at the open ocean boundary may lead to an inaccurate representation, especially for DIC, in that there is likely to be a drift in the surface concentration linked to the positive trend in atmospheric $p\text{CO}_2$ over the time period of the model simulation. This misrepresentation should be examined in future work, but it should also be noted that the model domain at the largest boundary (in the North Atlantic at $\sim 45^\circ\text{N}$) is relatively far from the domain analyzed and defined as the pan-Arctic (at 66.5°N). The distance between the boundary and the region of analysis could ameliorate the inaccuracy due to the lack of DIC trend at the boundary, because any surface water mass reaching the pan-Arctic from the boundary would have time to equilibrate with the atmosphere (the observed trend in $p\text{CO}_2^{atm}$ is implemented as described above) during the transit.

4.3 Results

To fully analyze the Pan-Arctic carbon system and the impacts of specific parameterisations, the following simulations are performed: the standard run (1980 – 2015, with a spinup period from 1969 – 1979) in which both the sea-ice algae and the sea-ice carbon pump implementations are included; the no ice-carbon pump run (1991 – 2010, starting from year 1990 of the standard run) in which the sea ice algae implementation is included, but the dilution/concentration due to ice growth/melt is suppressed; and the no ice-algae run (1991 – 2010, starting from year 1990 of the standard run) in which the sea-ice carbon pump implementation is included, but the sea ice algae are suppressed. This section focuses on analysis of the standard run, and the following Section 4.4 considers the two sensitivity runs.

4.3.1 Evolution of the Arctic Ocean model through the sea ice transition period, 1980 – 2015

The standard run encompasses the recent epoch in which the Arctic Ocean has transitioned from a largely sea-ice covered ocean (in both area and time) to a seasonally open-water dominated ocean. Among other relevant aspects, this transitional period is important because of the potential effect the loss of sea ice may have on the annual uptake of atmospheric carbon by the Arctic Ocean. The simulated sea ice area generally has slightly

lower maxima when compared to the sea ice extent of the National Snow and Ice Data Center (NSIDC, *Fetterer et al.* [2017], based on satellite observations of the domain north of 31° N) (Figure 4.2, upper panel). The difference in maxima is likely due to the larger domain used for NSIDC sea ice area data.

The simulated sea ice volume shows generally good agreement when compared to the sea ice volume of the Pan-Arctic Ice Ocean Modelling and Assimilation System (PIOMAS, *Zhang and Rothrock* [2003]), as illustrated in Figure 4.2, lower panel. One exception is the slight offset in ice volume extrema between the two model products for a ~ 5 -year period centered around the year 2000 and from 2011 – 2012. That being said, it is important to note that both quantities being compared are model products, and the maximum deviation between extrema is less than 4000 km^3 (or $< 20\%$ of the mean annual ice volume). In general, both PIOMAS and the present study show similar ranges around the annual mean and a consistent decline in simulated ice volume with time.

Simulated physical sea surface, atmospheric, and sea ice variables, averaged over the domain north of 66.5° N, are presented in Figure 4.3 (both monthly and annual averages in order to illustrate seasonal variability) and in Figure 4.4 (annual averages alone in order to emphasize interannual variability and trends). Time series of the sea ice variables are repeated in Figures 4.3 and 4.4 to provide a reference for variability in the other physical variables. Simulated Arctic sea surface temperature shows a seasonal range of around 2°C (Figure 4.3) with an approximate increase of 0.3°C over the period of the standard run (from approximately -0.6°C in the decade 1980 – 1990 to -0.3°C in the decade 2005 – 2015, Figure 4.4). Simulated Arctic sea surface salinity shows a seasonal range between minima of around 2 PSU below the average to 1 PSU above the long-term average (of 30.75, psu Figure 4.3) with some interannual variability, but no substantial trend around the long-term average and with annual averages largely within ± 0.25 psu (Figure 4.4). Atmospheric windspeed averaged over the Arctic Ocean north of 66.5° N (a forcing variable, rather than a modelled quantity), shows a seasonal range of ± 1 m/s (Figure 4.3) around a mean for the standard run of 6.2 m/s, with an interannual variability generally within 0.2 m/s of the mean. Therefore, during the period of decrease in pan-Arctic sea ice area and volume (Figure 4.4) there is no marked pan-Arctic trend in sea surface salinity nor wind speed, in contrast to sea surface temperature.

A comparison of sea surface salinity between the model-mean over the standard run period (1981 – 2015) and a climatological mean based on observations from the Polar science center Hydrographic Climatology (PHC; *Steele et al.* [2001]) is presented in Figure 4.5. Both the modelled and observed sea surface salinities are highest in the Atlantic sector

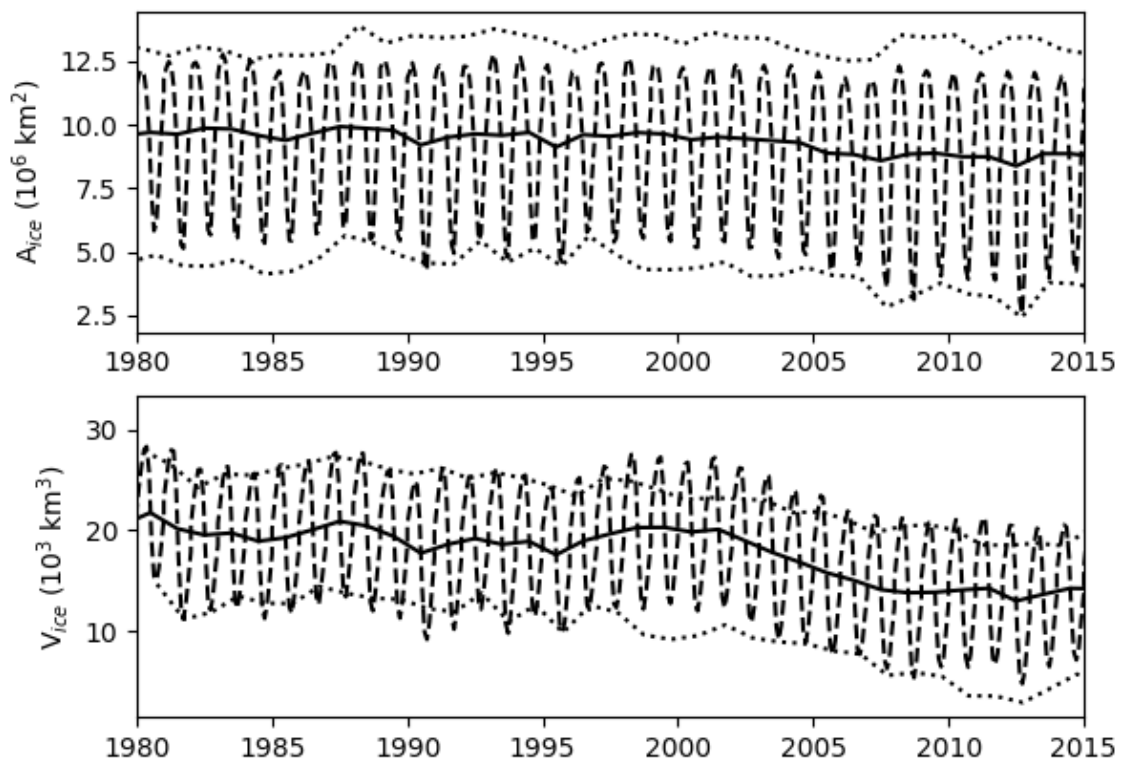


Figure 4.2: Simulated monthly- (dashed lines) and annually-averaged (solid lines) sea ice area (top) and sea ice volume (bottom) for the Arctic Ocean. The dotted lines indicate the maximum and minimum monthly values of sea ice area from NSIDC and of sea ice volume from PIOMAS. The domain of the modelled sea ice area calculations is the entire model domain, and north of 31° N for NSIDC. The domain for both the sea ice volume in this study and for the PIOMAS data are the region north of 66.5° N.

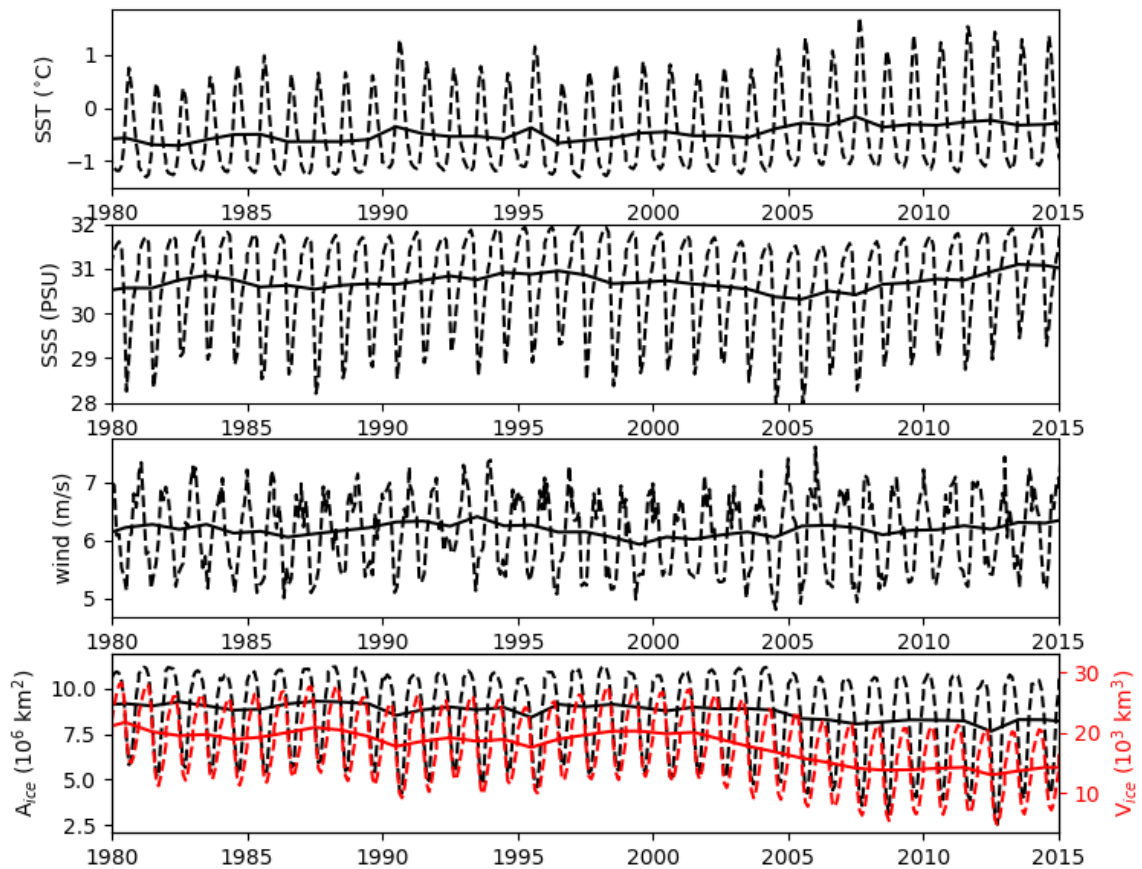


Figure 4.3: For the standard run, monthly (dashed line) and annual (solid) simulated sea surface temperature, simulated sea surface salinity, DFS-forced wind speed, and simulated total ice area (black) and simulated total ice volume (red). All variables are averaged for the region north of 66.5° N.

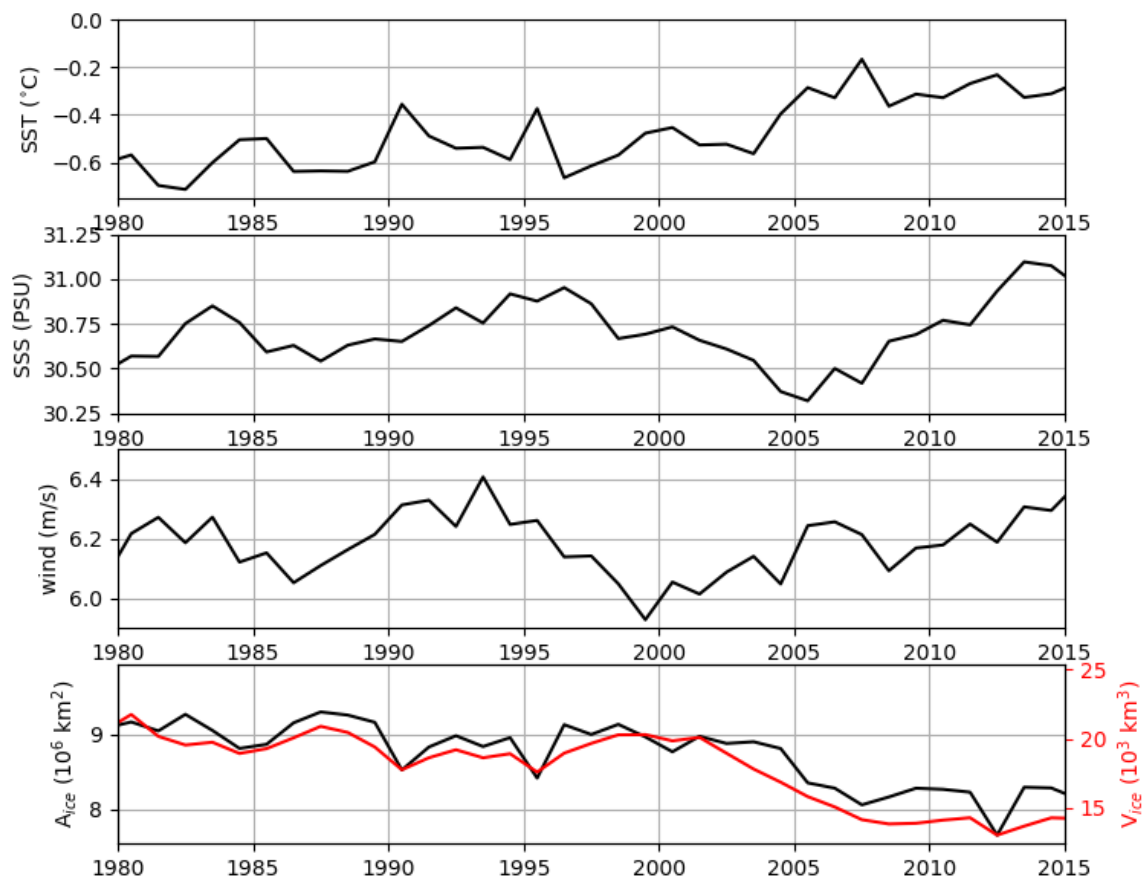


Figure 4.4: As in Figure 4.3, showing only the annually-averaged values.

of the Arctic, and low salinity values exist in both datasets along the Eurasian coast and Alaska. The most notable difference between the two is a lower salinity in the model-mean through the Chukchi and Beaufort Seas and in the Canadian Polar Shelf. It is important to note, however, that the PHC data product is interpolated from observations, which are particularly sparse in the northern extent of both the Chukchi and Beaufort Seas and throughout the Canadian Polar Shelf (see *Steele et al.* [2001], Figure 1). In addition, the PHC data product is based on observations spanning only the first half (before 2000) of the standard run period in this study (1981 – 2015).

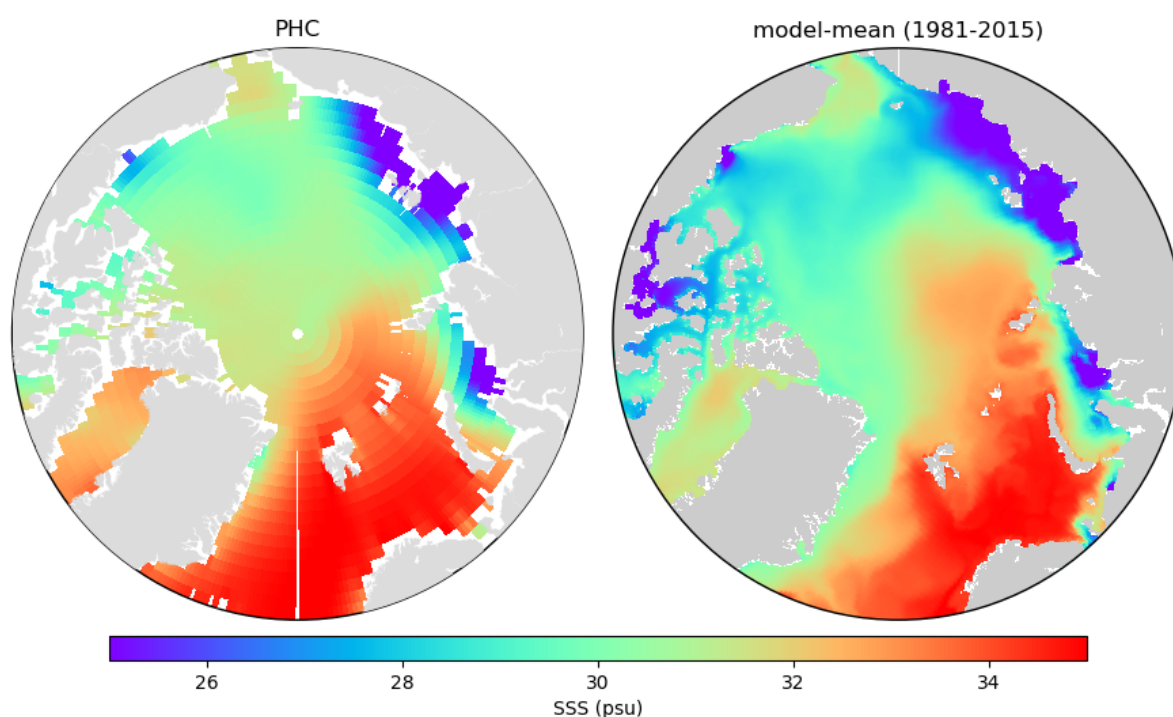


Figure 4.5: Comparison of the climatological sea surface salinity in the Arctic based on observations compiled for the Polar science center Hydrographic Climatology (PHC) and from the model mean over the period 1981 – 2015.

The annual carbon uptake of the Arctic Ocean north of 66.5° N (Figure 4.6) ranges from $115 \text{ Tg C year}^{-1}$ at the beginning of the standard run and increases to $135 \text{ Tg C year}^{-1}$ by the end of the standard run, an increase of $\sim 20\%$ over that period of time (1980-2015).

This simulated carbon uptake is within the range of several recent studies employing various distinct methods, including *Bates and Mathis* [2009], *Arrigo et al.* [2010], *Schuster et al.* [2013], *MacGilchrist et al.* [2014], and *Yasunaka et al.* [2016] (see Table 4.1 for details

Study	Carbon uptake	Method	Range
<i>Bates and Mathis</i> [2009]	66 – 199 Tg C year ⁻¹	literature review	uncertainty
<i>Arrigo et al.</i> [2010]	111 – 125 Tg C year ⁻¹	model study 1998 – 2003	trend
<i>Manizza et al.</i> [2013]	52 – 64 Tg C year ⁻¹	model study 1996 – 2007	trend
<i>Schuster et al.</i> [2013]	60 – 180 Tg C year ⁻¹	cross-method study 1990 – 2009	trend
<i>MacGilchrist et al.</i> [2014]	106 – 226 Tg C year ⁻¹	obs. and mass balance	uncertainty
<i>Yasunaka et al.</i> [2016]	180 (+/-210) Tg C year ⁻¹	obs. sea surf. <i>p</i> CO ₂	uncertainty
<i>Manizza et al.</i> [2019]	136 – 164 Tg C year ⁻¹	model study 2006 – 2013	trend

Table 4.1: List of studies that have analyzed the Arctic Ocean carbon uptake, along with a brief description of the method used and an identification of what the range indicates.

of these studies). Our results fall outside of the range estimated in *Manizza et al.* [2013] and are at the lower bound of the range estimated by *Manizza et al.* [2019]. The modelling study by *Manizza et al.* [2013] over the period 1996 – 2007 finds a smaller (relative to this study) uptake for the pan-Arctic of ~ 50 to 65 Tg C year⁻¹ from beginning to end of the model run. This difference can be attributed to their overestimation of sea-ice extent of $\sim 10\%$ over the entire run when compared to satellite data, as acknowledged in *Manizza et al.* [2019].

The top panel of Figure 4.6 also includes seasonal uptake for summer (red; July, August, September), fall (orange; October, November, December), winter (blue; January, February, March), and spring (cyan; April, May, June). The seasonal carbon uptake (scaled to allow better comparison with the annual total carbon uptake by multiplying by four) shows that the largest uptake rate occurs in summer and the weakest in winter, as expected. The summer carbon uptake rate represents the majority of the uptake with a rate ~ 2.5 times the annual average, and the winter carbon uptake is the lowest at ~ 0.5 times the annual average. Spring and autumn carbon uptake rates are intermediate between summer and winter rates. Over the standard run period, the increases in the spring and summer uptake (of $\sim 40\%$ and $\sim 35\%$) are slightly higher than the trend in the annually averaged carbon uptake over the standard run period. The fall exhibits the smallest increase in carbon uptake of $\sim 10\%$ over the standard run period.

The increase in carbon uptake from 1980 to 2015 is coincident with an increase in the (prescribed) atmospheric and (simulated) sea surface *p*CO₂ and a decrease in simulated sea surface pH (Figure 4.6, middle and lower panels). As mentioned above, the increase in

Arctic Ocean carbon uptake during this period is also coincident with an increase in sea surface temperature and a decrease in sea ice area and volume. For the pan-Arctic domain, the average sea surface $p\text{CO}_2$ increases from 300 μatm at the beginning of the standard run to 340 μatm by the end (Figure 4.6). The increased Arctic Ocean uptake of carbon can be attributed to increased atmospheric CO_2 over the model run and an increase in open water (which leads to increased surface ocean mixing as well as increased direct exposure to the atmosphere). Another influence is temperature-based solubility change to the surface waters, although warmer temperatures and more light exposure can also lead to increased primary production and associated carbon drawdown. Based on the the increase in pan-Arctic SST of 0.3°C and the relationship with $p\text{CO}_2$ as described in *Takahashi et al.* [1993] (their Equation 2: $\frac{\partial p\text{CO}_2}{\partial T} = 0.0423(^\circ\text{C})^{-1}$), $\sim 10\%$ of the total simulated increase in sea surface $p\text{CO}_2$ can be explained by the temperature-based solubility change. The annually-averaged pan-Arctic sea surface pH shows a steady decline from 8.1 to just over 8 in the standard run, with seasonal summer maxima approximately 0.1 above the annual mean, and with winter minima that are below 8 by the period 2010 – 2015.

Additional sea surface carbon variables averaged over the Arctic Ocean north of 66.5°N (sea surface DIC, TA, Ω_{arag} and Ω_{calc}) are shown in Figure 4.7. The variability in Arctic-wide sea surface DIC and TA is comparable, ranging from $\sim 100\text{ mmol m}^{-3}$ above to 150 mmol m^{-3} below the respective annual means of 1875 mmol m^{-3} and 1975 mmol m^{-3} . Neither DIC nor TA show trends apparent in many of the other carbon system variables. A fact sometimes overlooked in discussions about the ocean carbon system is that the relationship between sea-surface DIC and TA, rather than DIC alone, determines how the other carbon system properties act. To first order, the relationship between DIC and TA can be described as a reciprocal one, and the ratio of annually averaged pan-Arctic DIC/TA (not shown) does increase from 0.945 to 0.955 over the period 1980 – 2015.

The pan-Arctic annual average of Ω_{arag} shows a trend from just over 1.2 to just under 1.1 over the period under consideration, with seasonal minima in winter that approach the threshold of undersaturation by the end of the standard run. The annual averaged Ω_{calc} shows a general decline over the standard run from ~ 2 to 1.7, but neither the annual nor monthly-averaged pan-Arctic means approach undersaturation by the end of the standard run.

Lastly, the pan-Arctic simulated phytoplankton biomass integrated over the upper 50 m of the water column and ice algae biomass, both in units of carbon content, are presented in Figure 4.8 along with the pan-Arctic integrated values of NO_3 and NH_4 in the upper 50 m of the water column. Over the standard run period, the annually averaged phyto-

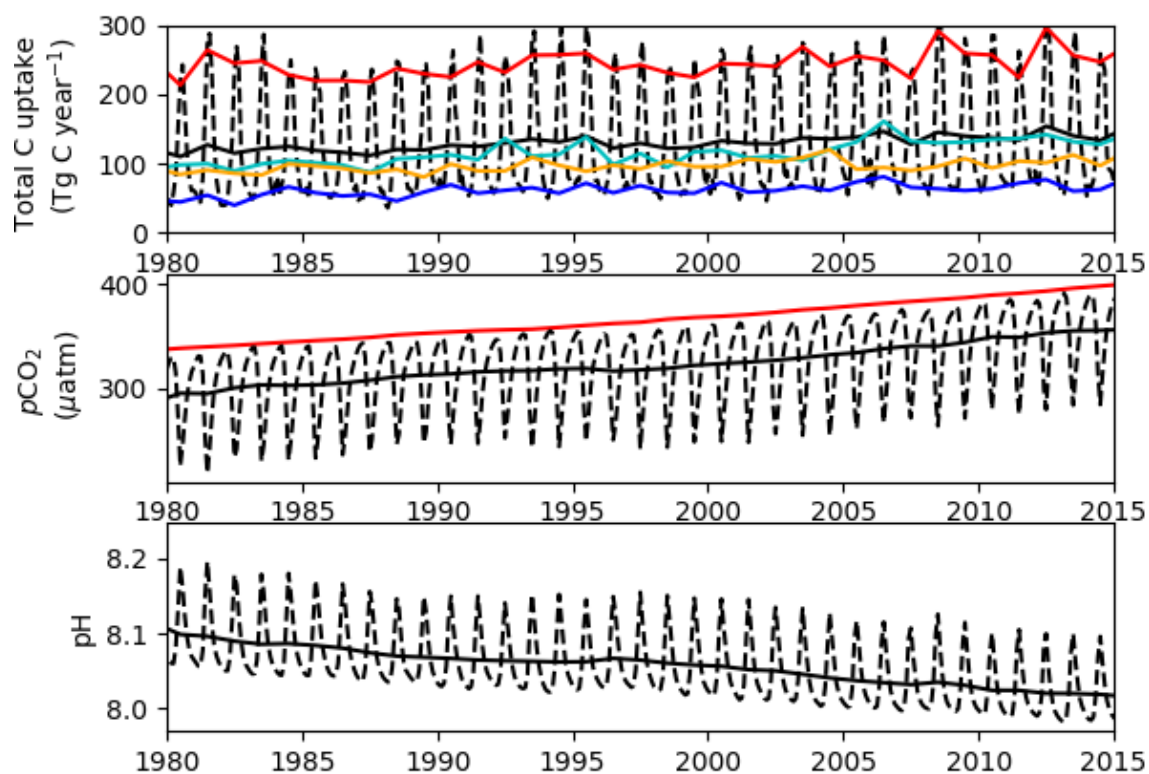


Figure 4.6: Top panel: net annual CO_2 uptake over the Arctic Ocean (solid black line); net seasonal CO_2 uptake (solid color lines) over spring (cyan), summer (red), fall (orange), and winter (blue), all scaled to match the annual uptake (multiplied by 4); and net monthly CO_2 uptake (dashed line) scaled to match the annual uptake (multiplied by 12). Middle panel: annual (solid black line) and monthly mean (dashed black line) sea surface $p\text{CO}_2$ and atmospheric $p\text{CO}_2$ (red line). Bottom panel: annual (solid) and monthly mean (dashed) sea surface pH. All variables are analyzed over the region north of 66.5°N .

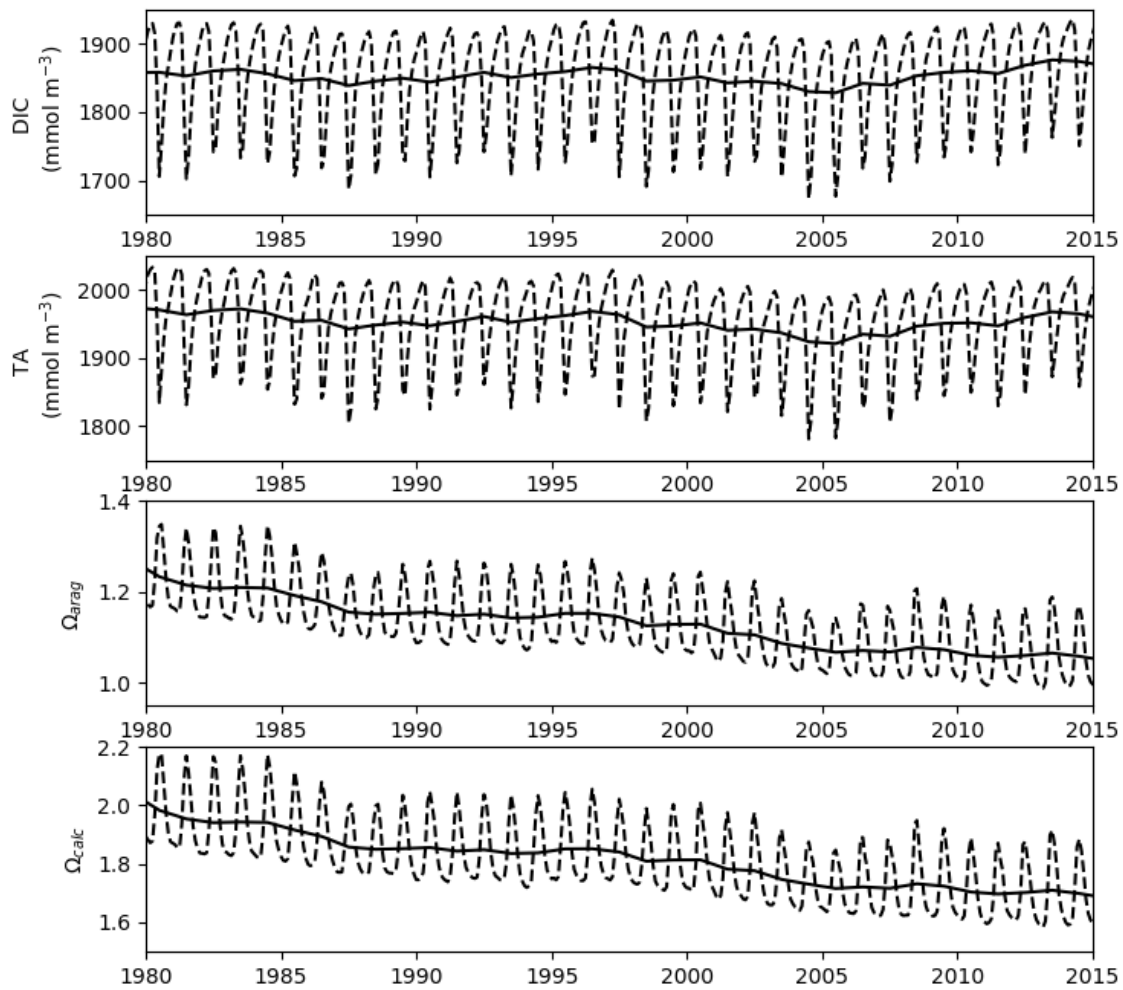


Figure 4.7: Annual (solid) and monthly-averaged (dashed line) sea surface DIC, sea surface TA, and sea surface aragonite calcite saturation states. All variables are averaged over the region north of 66.5° N.

plankton biomass increases by just over 10% (from 400 to 450 Tg C). The seasonal range in phytoplankton biomass is from near 0 in winter to a maximum of 1000 – 1200 Tg C. Ice algae biomass peaks in the spring, generally between 20 and 60 Tg C, or two orders of magnitude less than the maximum phytoplankton biomass. There is not an apparent loss of pan-Arctic sea ice algae coincident with the evident loss in sea ice area (Figure 4.2). The stability of the pan-Arctic sea ice algae bloom throughout the standard run, despite the apparent loss of habitat (sea ice area), can be attributed to the fact that the remaining sea ice is thinner, allowing for more light at the bottom of the ice and a larger ice algae bloom [Hayashida, 2018b].

The pan-Arctic annually averaged total NO_3 in the upper 50 m of the water column exhibits interdecadal variability superimposed on a negative trend from 4200 to 3500 Tg N over the standard run period, with the main loss occurring over the decade 1980 – 1990. The decrease in NO_3 content of the upper water column is likely due to river influence as opposed to spinup effects. Figure 4.9 shows the same variables as Figure 4.8, but also including the spinup period to illustrate that the decrease in NO_3 over the 1980 – 1990 period is not due to the effect of model spinup. In general, the rivers have higher nitrogen concentrations than does the pan-Arctic Ocean (Table A.4), and the decade 1980 – 1990 has relatively low river flow, which means that the pan-Arctic’s riverine NO_3 source is depleted during this time. The seasonal variability in NO_3 ranges from a maximum 15% above the annual mean to 20% below the annual mean. The NH_4 content of the upper 50 m pan-Arctic Ocean remains relatively stable at ~ 200 Tg N over the entire model run, with a seasonal range from near 0 in winter to a maximum at, or just above, 400 Tg N.

4.3.2 A regional perspective on carbon uptake in Arctic seas

The Arctic Ocean averages presented above illustrate a general pan-Arctic picture of how the physical and carbon system variables vary, however all variables may exhibit substantial regional variability. Regions that exhibit relatively large deviations from the pan-Arctic mean, with regards to the oceanic uptake of carbon and the oceanic carbon system, are the Laptev, Norwegian, and Barents Seas in the Atlantic sector, the Canadian Polar Shelf (CPS, a region also known by its terrestrial designation as the Canadian Arctic Archipelago) and the North and South Beaufort Seas in the sector adjacent to the Pacific (Figure 4.10). Figure 4.11 displays the annual average of sea surface $p\text{CO}_2$, mean carbon flux (normalized to the area of the respective region), pH, and sea ice cover for these regions. The corresponding pan-Arctic annual averages are indicated in black for

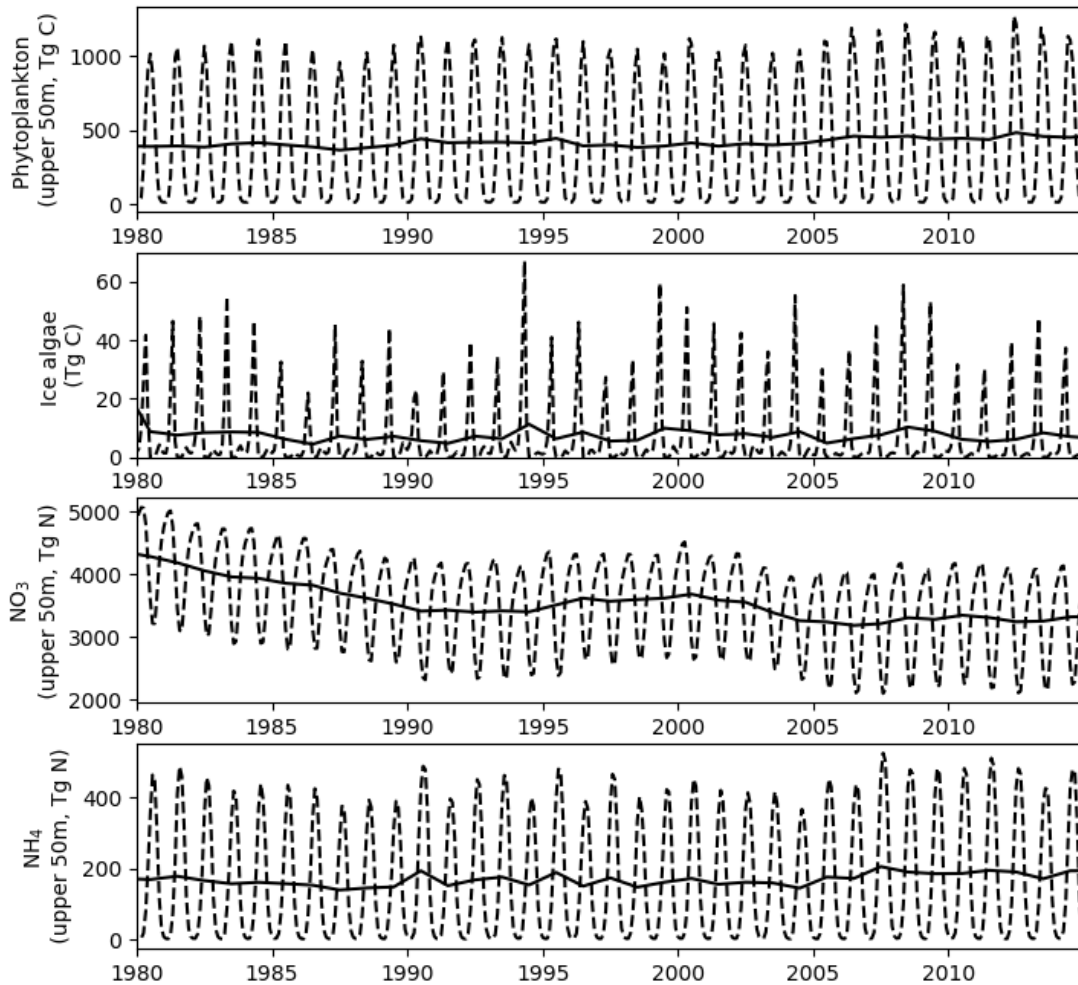


Figure 4.8: Top panel: Total annual (solid) and monthly (dashed) phytoplankton carbon content in the upper 50 m of the Arctic Ocean north of 66.5° N (Tg C). The lower panels display the same for NO₃ and NH₄ content in the upper 50 m.

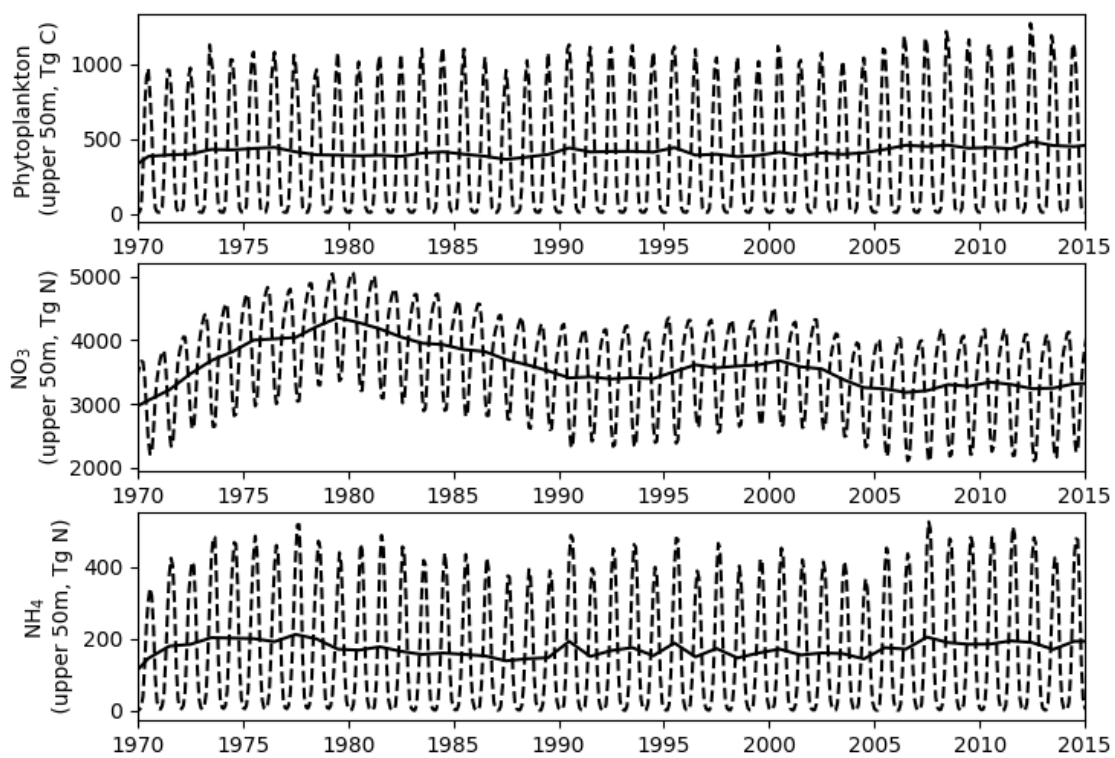


Figure 4.9: As in Figure 4.8, but including the spinup period (1970 – 1979).

comparison. The changes in the properties displayed in Figure 4.11, as well as Ω_{arag} and Ω_{calc} , are also provided in tabular format in Appendix Subection A.2.3.



Figure 4.10: Regions that exhibit distinctive differences in carbon system properties from the pan-Arctic mean. Colors match those of the regions in Figures 4.11 and 4.12. The regions are the Canadian Polar Shelf, the South and North Beaufort Seas, Laptev Sea, Barents Sea, and Norwegian Sea.

Regional differences are particularly pronounced in the annually-averaged mean carbon flux, with high annual uptake in the Barents and Norwegian Seas relative to the pan-Arctic mean, and low uptake in both the North and South Beaufort Seas and the Laptev Sea. Increases in carbon uptake in both the Norwegian and Barents Seas over the standard run time period (of approximately $5\text{ g C m}^{-2}\text{ year}^{-1}$ for each of these regions) account for a large proportion of the pan-Arctic increase in net annual oceanic carbon uptake described in Section 4.3.1 (each of the Barents and Norwegian Seas comprises roughly 10% of the entire Arctic Ocean surface area). The CPS exhibits an annual net carbon uptake of $\sim 15\text{ g C m}^{-2}\text{ year}^{-1}$, which is approximately one third the uptake found for the Resolute Bay

region in the 1D study in Chapter 3. Resolute Bay is in the southern part of the CPS region, and therefore is expected to have a longer open-water season and higher carbon uptake than the regional average. The 1D study in Resolute Bay also has a larger simulated phytoplankton bloom than in the CPS regional average, which would further contribute to a larger carbon uptake in the 1D study.

The trend in pH is negative in all regions displayed in Figure 4.11. The slope of the trend in pH for all regions is similar to that of the pan-Arctic average (a drop of ~ 0.1 in pH over the period of the standard run), with the exception of the CPS region which exhibits an accelerated decrease in pH (of 0.15 drop in pH over the standard run period).

Figure 4.12 shows DIC, TA, Ω_{arag} , Ω_{calc} for the same regions. As in the pan-Arctic analysis, neither DIC nor TA show trends that are as pronounced as the trends seen for $p\text{CO}_2$, CO_2 uptake, pH, Ω_{arag} , and Ω_{calc} . Regions with low pH (Laptev Sea and North and South Beaufort Seas, Figure 4.11) relative to the pan-Arctic mean are similarly low in both Ω_{arag} and Ω_{calc} . The Laptev Sea and North and South Beaufort Seas all exhibit annually averaged sea-surface undersaturation in aragonite over most of the standard run period. The low aragonite in the Laptev Sea is in line with observations [Semiletov *et al.*, 2016]. In the Beaufort Seas, however, observations indicate that aragonite undersaturation has been persistent only since around 2000, and was more sporadic before that [Bellerby *et al.*, 2018; Qi *et al.*, 2017].

The low uptake in the Laptev Sea can be attributed to the high sea surface $p\text{CO}_2$ in the region, largely at or above atmospheric $p\text{CO}_2$ throughout the model run. The high sea surface $p\text{CO}_2$ in the Laptev Sea is due to the high amount of river flow in the region, which reduces the sea surface TA (raising $p\text{CO}_2$) through dilution, but has a less pronounced dilution effect on sea surface DIC because the Lena River, which outflows into the Laptev Sea, has a relatively high DIC+DOC content of $1658 \text{ mmol C m}^{-3}$. In addition, the Laptev Sea region has the lowest pH of all the regions, consistent with observations described in Semiletov *et al.* [2016].

The North Beaufort Sea has the highest annual ice coverage ($\sim 90\%$), and the South Beaufort Sea has ice coverage of 80% in the first half of the standard run, dropping to 60% by the decade 2005 – 2015. The low carbon uptake in the North Beaufort Sea, despite the sea surface $p\text{CO}_2$ in the region being below atmospheric $p\text{CO}_2$ (Figure 4.11), can be attributed to the generally high ice coverage, as illustrated in Figure 4.11. For the South Beaufort Sea, the low carbon uptake may be due to a combination of the relatively high sea surface $p\text{CO}_2$ (but lower than that of the Laptev Sea) and the relatively high ice cover (but lower than that of the North Beaufort Sea). This result is at least partly consistent

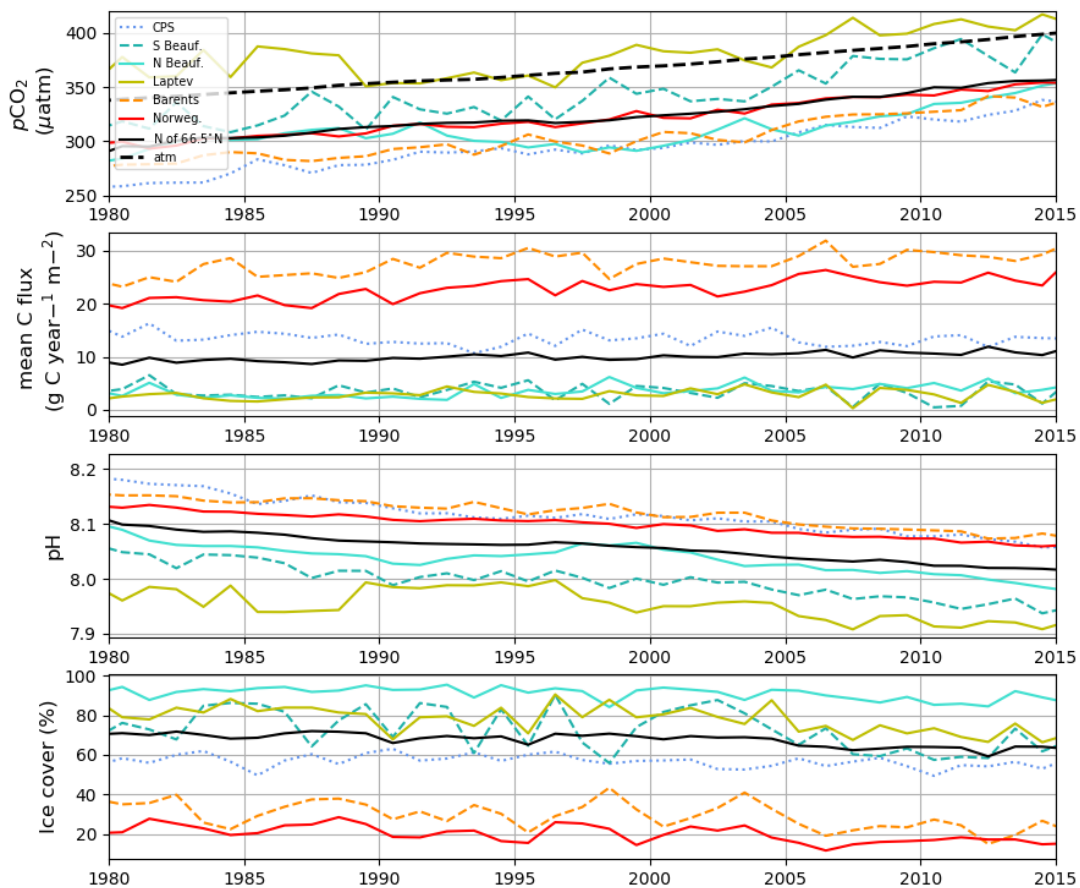


Figure 4.11: Annual averaged sea surface (and atmospheric, dashed black line) $p\text{CO}_2$, mean carbon flux, pH, and ice cover for the region north of 66.5°N (black), and for selected regions identified in Figure 4.1. Line colors match those of the regions in Figure 4.10. Different linestyles (solid/dashed/dotted) are to aide in differentiating similar colors.

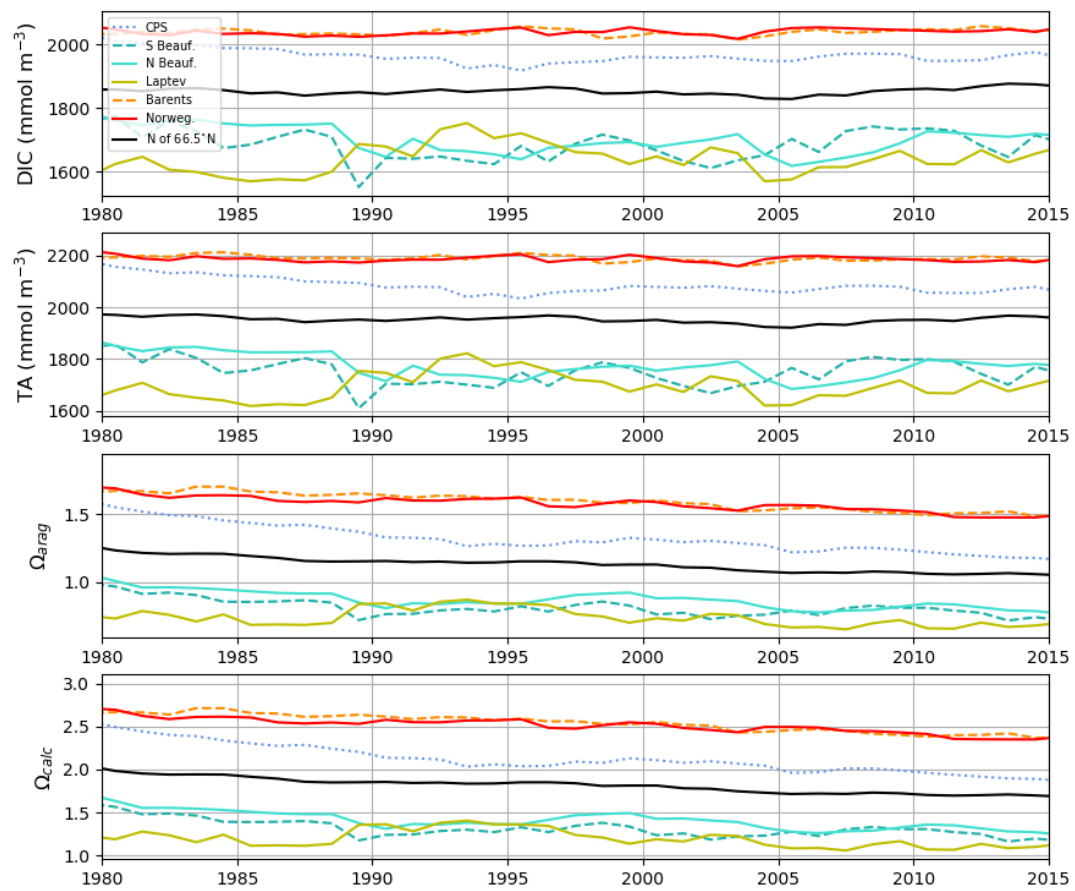


Figure 4.12: Annual averaged sea surface DIC, TA, Ω_{arag} , Ω_{calc} for the region north of 66.5° N, and for same regions as in Figure 4.11.

with *Cai et al.* [2010], who describe, through shipboard measurements in 1999 and 2008, a weak oceanic carbon uptake in the Beaufort Sea (both North and South) via an increase in sea surface $p\text{CO}_2$. The South Beaufort Sea exhibits an increase in average sea surface $p\text{CO}_2$ throughout the standard run, despite little or no increase in ocean carbon uptake over the period of the standard run. The result that $p\text{CO}_2$ is increasing in the South Beaufort Sea, despite minimal atmospheric carbon uptake in the region, indicates that the trend in sea surface $p\text{CO}_2$ is not due to air-sea exchange. The increase in $p\text{CO}_2$ in the South Beaufort Sea could be due to one or more of the following causes: vertical mixing, horizontal advection from other water masses, or the outflow of the MacKenzie River which is high in DIC+DOC and low in TA (Table A.4).

In Figure 4.13 we look at the South and North Beaufort Seas from a subsurface perspective by showing the progression of annual-averaged DIC and Ω_{arag} in the upper 300 m of the water column for both the North and South Beaufort over the period of the standard run. Horizontal layers from the surface to ~ 150 m depth in the North Beaufort Sea show a steady decrease with time in the DIC content up to about the year 2000. In contrast, the trend is only apparent in the South Beaufort in the first 10 years (1980 – 1990). The progression in water column DIC for the South Beaufort Sea looks similar to that observed by *Miller et al.* [2014]. Despite the low simulated surface Ω_{arag} , when compared to observations, the increase in subsurface undersaturation over time agrees with observations of both *Qi et al.* [2017] and *Bellerby et al.* [2018] (Figure 4.15). However, the undersaturation of simulated surface Ω_{arag} in the South Beaufort Sea (on the shelf) in this study is not apparent in either *Qi et al.* [2017] and *Bellerby et al.* [2018], which both show Ω_{arag} in the range of 1.5 – 2 for the Beaufort Sea shelf region (similar to the South Beaufort Sea region as defined in this study). As many of the observations described in *Miller et al.* [2014], *Qi et al.* [2017], and *Bellerby et al.* [2018] were taken in the summer months, Figure 4.14 displays the same variables as Figure 4.13, but over the summer period of July – September. Simulated summer-averaged Ω_{arag} are closer to observations than in the simulated annual averages, with higher values at the surface in both the North and South Beaufort, little or no aragonite undersaturation at the sea surface, and a more pronounced (lower in value) signal in the subsurface Ω_{arag} minimum for both regions. The seasonal variability in Ω_{arag} shown in this study, along with the sparsity of observations in winter due to inaccessibility of the region, highlights the use of model studies in filling in gaps in observable data sets.

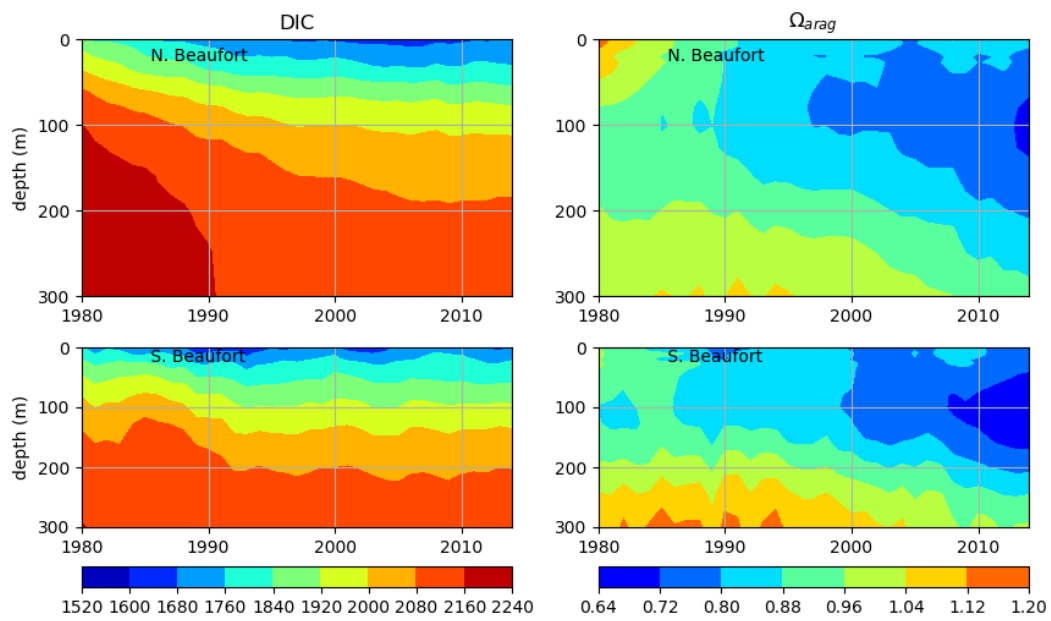


Figure 4.13: Hovmoeller plot of annually averaged DIC content (left) and Ω_{arag} (right) through the upper 300 m of the water column for the North (top) and South (bottom) Beaufort Seas over the standard run period.

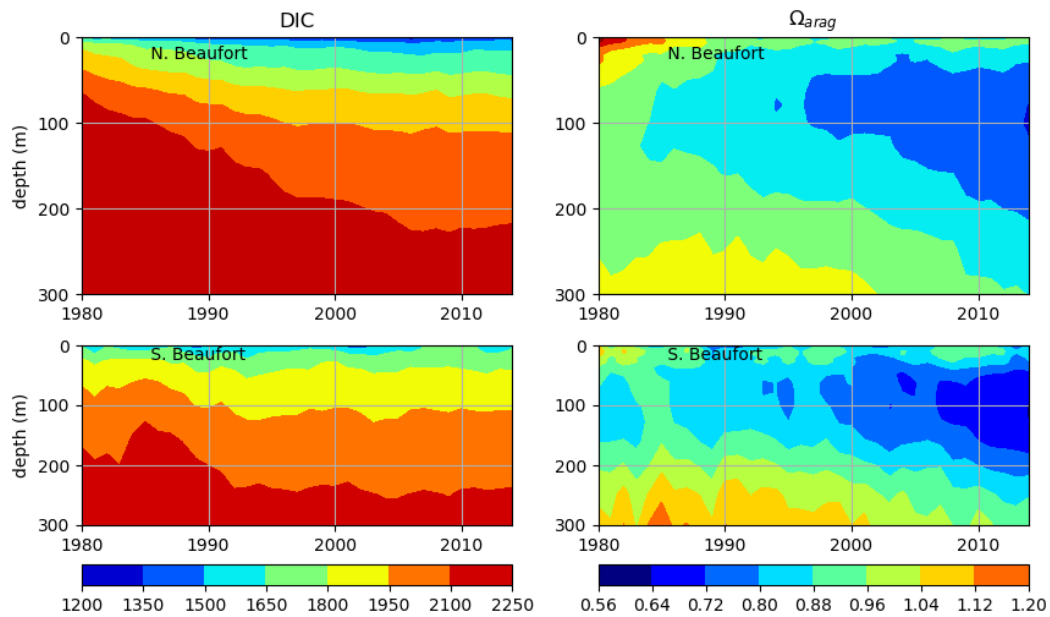


Figure 4.14: As in Figure 4.13, but averaged over the summer months (July, August, and September).

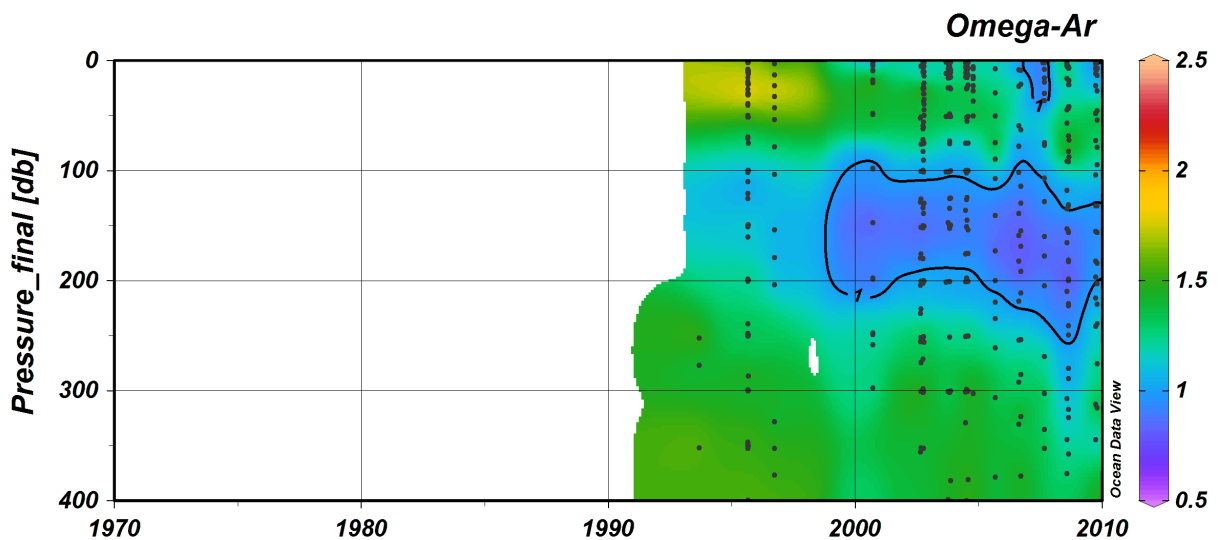


Figure 4.15: As in Figure 4.13, from measurements for the off-shelf region of the Beaufort Sea (similar, but not exactly the same, as the domain defined in this study as the North Beaufort Sea) presented in *Bellerby et al.* [2018].

4.4 Discussion

In addition to the standard run, two parallel simulations were carried out with initial conditions starting from the standard run's output at the end of model year 1990 and each spanning a 20-year time period from 1991 – 2010. The first sensitivity run has the ice-carbon pump (rejection of brine-associated DIC and TA due to ice growth and dilution due to ice melt) suppressed (denoted the "no ice-carbon-pump run"). The second sensitivity run has the ice algae production suppressed (denoted the "no ice-algae run"). The pan-Arctic total carbon uptake, sea surface DIC, and sea surface TA for the sensitivity and standard runs are presented in Figure 4.16.

4.4.1 No ice-carbon-pump run

In the no ice-carbon-pump, DIC and TA fluxes are suppressed by setting the reference sea-water and ice concentrations in equations 4.1 and 4.2 equal (i.e., $DIC_{ice}^{ref} = DIC_{SW}^{ref}$ and $TA_{ice}^{ref} = TA_{SW}^{ref}$), such that the fluxes associated with ice-growth and -melt become identically zero. In the initial year of the no ice-carbon-pump run, pan-Arctic net annual carbon uptake has a relatively large deviation from the standard run in comparison to subsequent years, due to the adjustment to the new scenario. After the adjustment, the pan-Arctic net annual carbon uptake stabilizes and there is very little difference between the run with the ice-carbon pump suppressed and the standard run.

In the no ice-carbon-pump run, both sea surface DIC and TA have a much diminished seasonal variability relative to the standard run (Figure 4.16). The magnitude of the seasonal range in pan-Arctic sea surface DIC (TA) is reduced to $\sim 25\%$ ($\sim 10\%$) of the seasonal range in the standard run. Despite the large decrease in seasonal variability in DIC and TA, the pan-Arctic annual ocean carbon uptake is relatively unchanged ($\sim 1\%$ difference from the standard run). The small change in pan-Arctic total annual carbon uptake can be explained in two different ways. First, the decrease in summer uptake (in the no ice-carbon-pump run) is largely counteracted by the increased uptake in winter and fall (Figure 4.16). Second, the synchronous addition (or removal) of both DIC and TA inherent in the ice-carbon pump has a counteractive effect on sea-water $p\text{CO}_2$, as described in Chapter 3.

The annual mean pan-Arctic saturation state Ω_{arag} follows a similar trend in the no-ice-carbon-pump as in the standard run, but offset slightly by ~ 0.02 . The offset is due largely to the difference in summer-time maxima, which are ~ 0.1 higher in the no ice-carbon-pump

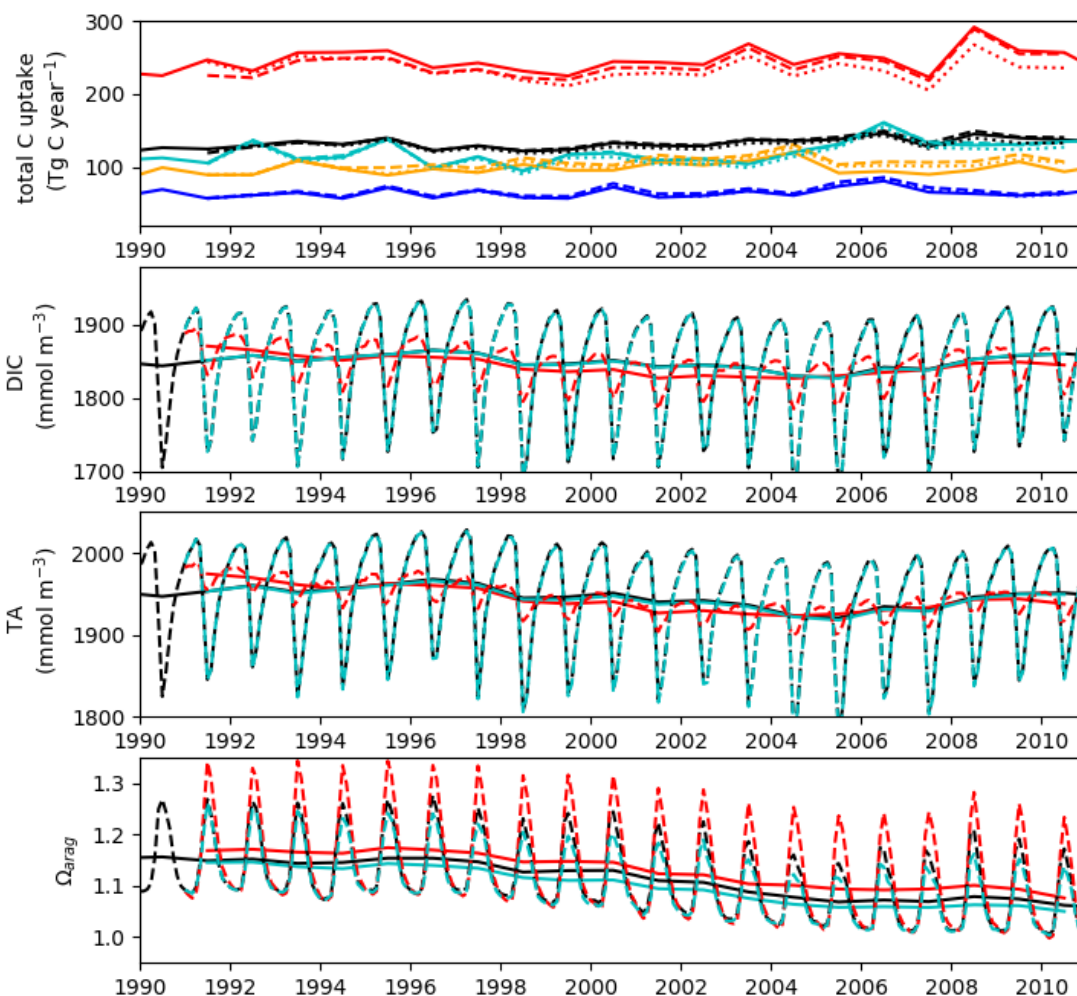


Figure 4.16: Top panel: Total annual (black) and seasonal (colors, scaled to match the annual total; summer=red, fall=orange, winter=blue, and spring=cyan) ocean carbon uptake of the Arctic Ocean north of 66.5° N (Tg C). The dashed lines indicate the no ice-carbon-pump run and the dotted lines indicate the no ice-algae run. The lower panels are pan-Arctic averaged sea surface DIC, TA, and Ω_{arag} averaged monthly (dashed) and yearly (solid), all for the standard run (black) and the sensitivity runs with the ice-carbon-pump suppressed (red) and the ice algae suppressed (cyan).

run relative to the standard run. In fact, differences in sea-surface carbon properties between the no ice-carbon-pump and standard runs do not appear to be cumulative, as the offsets between the runs do not exhibit trends over the 20 year period.

Despite the similarity in annual, pan-Arctic averaged Ω_{arag} between the standard and no ice-carbon-pump runs, there is a substantial difference in the seasonal variability. The annual (summer-time) maxima in the no ice-carbon-pump run are ~ 0.075 higher than in the standard run. This indicates that, when the ice carbon pump is not represented, there is an overestimation of the simulated annual maximum Ω_{arag} at the sea surface.

In summary, the ice-carbon pump does not appear to be of substantial importance for carbon fluxes, but does substantially influence seasonality of carbon system quantities.

4.4.2 No ice-algae run

The suppression of ice algae only has a small effect on the pan-Arctic monthly mean sea surface DIC and TA relative to the standard run (see Figure 4.16, middle panels). However, the net carbon uptake of the pan-Arctic does exhibit a disparity between the no ice-algae and standard runs, with a net reduction of 4% in the annual pan-Arctic ocean carbon uptake by the end of the sensitivity run, relative to the standard run. The reduction in pan-Arctic carbon uptake grows steadily throughout the sensitivity run, indicating that the effect of ice algae (or neglect thereof) on the pan-Arctic ocean carbon uptake is cumulative, and may be an important consideration in long-term simulations (Figure 4.16, top). Seasonally, the difference in the carbon uptake between the two runs is most pronounced in the summers. The saturation state Ω_{arag} shows an increasing difference in the summers between the standard and no ice-algae run, slightly lower in the no ice-algae run than in the standard run, approaching a difference between the runs of ~ 0.05 by the year 2010 (Figure 4.16, bottom).

As discussed in Chapter 3, ice algae have a two-fold impact on the inorganic carbon system of the water column. First, the growth of ice algae is associated with a reduction of inorganic carbon through the direct uptake of nutrients. Second, and partially offsetting the first effect, the ice algae reduce the pelagic bloom through surface nutrient depletion. In this 3D study, the integrated phytoplankton content of the upper 50 m of the water column, summed over the pan-Arctic, is largely unchanged between the standard run and the no ice-algae run (Figure 4.17, top). However, the nitrogen content of the upper 50 m of the water column is affected, with a net decrease of $\sim 10\%$ in both annually-averaged pan-Arctic NO_3 and NH_4 , in the no ice-algae run relative to the standard run, by the end of the

sensitivity run. The difference in both NO_3 and NH_4 between the two runs is cumulative. The result that nutrients are reduced in the no ice-algae run relative to the standard run is counterintuitive because detrital release of ice algae contributes to the fast-sinking large detritus pool, which mostly remineralizes below 50 m depth. It is difficult to ascertain the reason for the difference in upper-ocean nitrogen content between the standard and no ice-algae runs from a pan-Arctic average, but it is apparent that the difference in NO_3 occurs throughout the year, while for NH_4 , the difference between the two runs is largely in the summer (Figure 4.17). The seasonality of the differences in NO_3 and NH_4 between the runs is due to the light limitation on nitrification, which largely contributes to the conversion of NH_4 to NO_3 in the (darker) winter (Chapter A.2.1). From a transect through the Canadian Arctic (not shown) there are elevated (standard run relative to no ice-algae run) NO_3 and NH_4 contents in the upper 50 m in the CPS and for NH_4 on the South Beaufort Sea shelf, indicating that the difference may be largely located along shelf regions.

In summary, the inclusion of ice algae in a biogeochemical model for the Arctic Ocean leads to a more representative ecosystem, and has a cumulative, but relatively small, effect on the simulated ocean carbon system over a short time period (less than a decade). However, over longer time scales, the cumulative changes to simulated nutrients in the upper 50 m and net carbon uptake of the Arctic Ocean between the standard and no ice-algae runs indicate that neglecting the sympagic ecosystem leads to cumulative deviations of important biogeochemical ocean properties. This sensitivity analysis indicates that the sea ice ecosystem is a necessary component in the analysis of the Arctic Ocean inorganic carbon system in simulations longer than a decade.

4.5 Conclusions

In this study, a sea ice ecosystem and ice carbon pump were implemented in a biogeochemical model representing the Arctic Ocean in order to evaluate the impact on the inorganic carbon system, including CO_2 uptake, acidification, and the saturation states Ω_{arag} and Ω_{calc} , for the pan-Arctic domain and selected subregions. The model was forced by meteorological data for the recent period of observed sea ice loss (from 1980 – 2010, with a spinup period from 1969 – 1979). The simulated Arctic Ocean sea ice properties are in good agreement with observations of sea ice area and with a previous estimation of simulated sea ice volume, and the net pan-Arctic ocean carbon uptake is within the range of multiple previous studies. This study indicates that there is a $\sim 20\%$ increase in the pan-Arctic ocean uptake of carbon, from 115 to 135 Tg C yr⁻¹, during the simulated loss

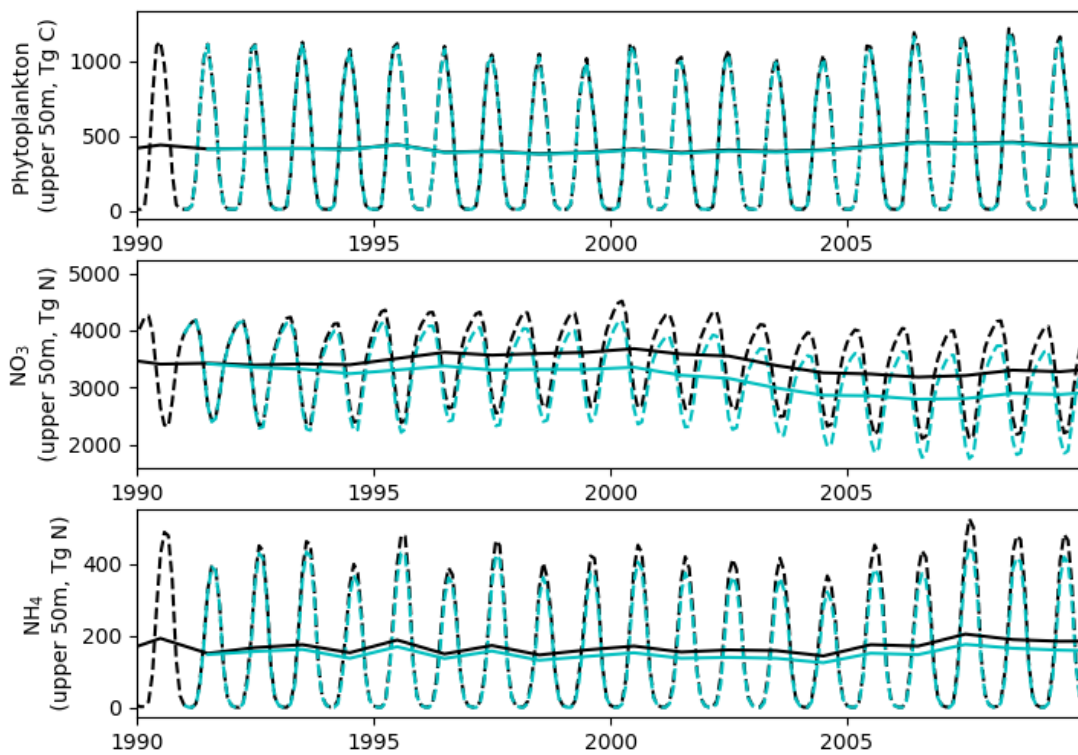


Figure 4.17: Total annual (solid) and monthly (dashed) phytoplankton carbon content in the upper 50 m and of the ice algae for the pan-Arctic (Tg C). The black lines indicate the standard run and the cyan lines indicate the no ice-algae run. The lower panels display the same for NO₃ and NH₄ content in the upper 50 m over the same area.

of sea ice over the period of the standard run. During the period 1980 – 2015, carbon uptake, area of open ocean, (imposed) atmospheric and (simulated) sea surface $p\text{CO}_2$, and temperature all increase coincident with decreases in saturation state (both Ω_{arag} and Ω_{calc}) and annually-averaged pH (from 8.1 to 8) over the pan-Arctic surface ocean. The increase in pan-Arctic sea surface temperature accounts for 10% of the pan-Arctic increase in sea surface $p\text{CO}_2$.

The simulated pan-Arctic sea surface salinity shows a fresh bias, relative to an interpolated observational dataset (PHC), centering on the regions of the Canadian Polar Shelf and the northern Beaufort and northern Chukchi Seas. These regions correspond to areas of sparse observations, so the low salinity simulated in these regions is not necessarily incorrect. However, given the influence of sea surface salinity on sea surface carbon properties, e.g., through the coincident influence on DIC and TA due to ice melt/growth as well as in regions of river inflow, it is important to determine whether the model accurately represents the sea surface salinity. The deviation between the model output and interpolated observations in these areas (the Canadian Polar Shelf and the northern Beaufort and northern Chukchi Seas) indicate that they are key regions of uncertainty, and hence there is a need for observations there in order to constrain the sea surface salinity.

Minima in Ω_{arag} and Ω_{calc} occur in winter, and regional and seasonal undersaturation of aragonite occurs in increasing frequency from the beginning to the end of the standard run. The timing and location of undersaturation events have a potential negative impact on (e.g.) pteropods in biologically important regions and seasons [Bednaršek *et al.*, 2014; Comeau *et al.*, 2012].

Regional analyses, with a focus on deviations from the pan-Arctic mean, indicate that the uptake of carbon is stronger in the seas adjacent to the Atlantic (Barents and Norwegian Seas) and accounts for a large proportion of the increase in net annual Arctic Ocean carbon uptake over the period of sea ice loss. The Laptev Sea has particularly low pH and high (sometimes supersaturated) $p\text{CO}_2$, relative to the pan-Arctic mean, in line with observations. The South (on-shelf) and North (off-shelf) Beaufort Seas exhibit distinct trends in both annual-averaged $p\text{CO}_2$, but similarly low total annual carbon uptake. For the North Beaufort, the low carbon uptake is attributed to the relatively high ice cover, but for the South Beaufort, the low carbon uptake is attributed to a combination of, 1) sea surface $p\text{CO}_2$ close to (but still undersaturated relative to) atmospheric $p\text{CO}_2$ and, 2) a relatively high (but not as high as the North Beaufort) sea ice cover. Lastly, the Canadian Polar Shelf does not exhibit a strong trend in ice cover or net annual carbon uptake, but does show an accelerated increase in $p\text{CO}_2$ and decrease in pH, relative to the pan-Arctic

mean.

Two sensitivity studies were performed to address the long term (two decades) effect of two parameterizations implemented in this study. The first study tests the sea-ice carbon pump of DIC and TA. In the standard run, the ice-carbon-pump during ice growth was altered to release both DIC and TA at the bottom of the mixed layer rather than the surface in order to represent brine-associated rejection of DIC and TA. A comparison run, with both DIC and TA fluxes associated with ice growth/melt suppressed, shows little effect on the total uptake of carbon by the Arctic Ocean (North of 66.5° N), but a substantial decrease in the seasonal variability in DIC and TA, as well as an increase in the summertime saturation state in the pan-Arctic sea surface. Neglecting the ice-carbon-pump results in an overestimation of the maximum simulated Ω_{arag} , and therefore underestimating the stress that aragonite-forming organisms will experience (or the period of low stress) in the future Arctic Ocean with the current trend in ocean acidification. Differences between the standard and no ice-carbon pump runs do not appear to increase with time.

A second sensitivity analysis tested the effect of simulated ice algae on the sea surface pCO_2 and ocean uptake of carbon with a comparison between the standard and no ice-algae runs. The no ice-algae run exhibited a cumulative decrease in the pan-Arctic uptake of carbon of 4%, relative to the standard run, by the end of this sensitivity run. This analysis indicates that the simulated ice algae have a small effect on the simulated Arctic Ocean over sub-decadal periods, but that the cumulative effect, namely on upper water column nutrients and the carbon uptake of the Arctic Ocean, suggests the sympagic ecosystem should be included in longer-term model runs.

In the Arctic Ocean, many measurement campaigns are focused on the summer months when the region is more accessible. Furthermore, proximity to research stations and/or accessible ports understandably influences decisions on where to make measurements. The strong seasonal and regional variability in the simulated inorganic carbon system properties presented in this study indicates that the interpretation of observational studies should take into account the seasonal and regional sampling bias when assessing the state of the inorganic carbon system, uptake capacity and $CaCO_2$ saturation states. Furthermore, the sparsity of winter-time observations due to the difficult conditions in Arctic winters emphasizes the importance of this type of model study, which can be compared to available observations and fill in the gaps where and when observations are not available. Another important fact emphasized by the results of this study is that changes to DIC alone are not sufficient to define changes to other carbon system properties. As an illustrative example, a coincident decrease in both the sea surface DIC and TA (as occurs with ice-melt) can

largely counter one another in terms of the sea surface $p\text{CO}_2$.

5 Conclusion

Over the last few decades and into the near future, the Arctic Ocean has experienced and will continue experiencing dramatic changes. The Arctic Ocean is undergoing a regime shift from a largely ice-covered ocean for most of the year to a largely ice-free ocean (especially) in the summers. Surface exchange of heat, momentum, and carbon between the Arctic atmosphere and ocean are likely to be strongly affected by the distribution and extent of sea ice. In this study, I developed a representation of the inorganic carbon system in a 1D and then 3D model incorporating an ice-associated ecosystem and inorganic biogeochemistry. The objectives were, first, to accurately represent the carbon system and analyze the relative importance of biological (both sympagic and pelagic) and inorganic (air-sea exchange, high-DIC brine transport associated with ice growth, and DIC dilution associated with ice melt) processes, and second, to estimate changes to the ocean uptake of carbon with an evolving ice-cover representing the changes over the recent past.

In order to establish a set of parameterizations which could be transferred into a 3D regional Arctic model, I used a 1D model as a tool to investigate the physical and biological controls on sympagic and pelagic primary production using observations from Resolute Passage. I implemented the sympagic ecosystem into the 1D model and ensured that physical variables agreed with measurements from observational studies during the spring bloom of 2010. Results of the standard simulation, including a snow distribution function allowing for a slow evolution towards bare ice and melt ponds, are generally in good agreement with the observations of snow/melt pond depths, ice thickness, under-ice PAR, and bottom-ice and seawater Chl *a* observed during the melt season in 2010. The simulated ice algal and under-ice phytoplankton blooms in the standard run agree well with the observations in terms of timing (for ice algae: onset, maximum, and senescence; for phytoplankton: onset only), and magnitude. I then implemented an inorganic carbon system into the 1D biogeochemical model incorporating a coupled sea-ice and pelagic ecosystem. The simulated inorganic carbon system depends on processes including primary production, remineralization, and nitrification; ice-water and ice-air fluxes of carbon due to ice growth and melt (including transport by brine plumes); ikaite precipitation and dissolution; and direct air-sea exchange. The simulated net ocean carbon uptake during the

open-water season is within the range of summer-time observations of air-sea carbon flux in the region found in other studies, with a mean value of $10.2 \text{ mmol C m}^{-2} \text{ day}^{-1}$ over the open-water season.

The carbon cycle I implemented in the 1D biogeochemical model provides insight into the ocean carbon uptake and exchanges during ice growth, ice melt, and in the open-water season. When both DIC and TA have similar changes in both sign and magnitude, as occurs during ice growth and melt (via concentration and dilution, respectively), the changes in sea surface $p\text{CO}_2$ largely cancel each other out. Sensitivity analyses indicate that sympagic and total (sympagic and pelagic) biological activity respectively account for 1% and more than 50% of the net ocean carbon uptake. Ice algae have a larger absolute impact when pelagic primary production is suppressed, because of reduced competition for nutrients. Inclusion of ikaite precipitation within sea ice, and subsequent dissolution in the water column during ice melt, results in only a small change ($\sim 1\%$ for ikaite concentrations of 50 mmol C m^{-3}) to the net ocean carbon uptake. However, an order of magnitude larger ice-ocean transfer of ikaite could have a larger impact on the subsequent open-water season ($>10\%$) because of the inherent differential contribution of DIC and TA to the water column.

Based on the results of the 1D model studies, I implemented the sympagic ecosystem and a modified ice carbon pump in an existing 3D regional biogeochemical model representing the entire Arctic Ocean. The model was forced by meteorological data over the recent period of observed sea ice loss (the satellite era from 1980 – 2015, with a spinup period from 1969 – 1979), in order to estimate changes to the Arctic Ocean's uptake of carbon and ocean acidification. The simulated Arctic Ocean sea ice properties are in good agreement with observations of sea ice area and with independently simulated sea ice volume, and the simulated net Arctic Ocean carbon uptake is in good agreement with multiple previous studies.

In the 3D standard run, there is a $\sim 20\%$ increase in the pan-Arctic ocean uptake of carbon, from 110 to 140 Tg C yr^{-1} (or an areal mean increase from 9.25 – 11.0402 $\text{mg C m}^{-2} \text{ year}^{-1}$), during the loss of simulated sea ice in the Arctic Ocean over the period 1980 – 2015. Coincident with the increases in carbon uptake, seasonal open-water area, sea surface temperature, and sea surface and (imposed) atmospheric $p\text{CO}_2$ are a decrease in the pan-Arctic annually-averaged saturation states (Ω_{arag} : from 1.22 to 1.06 and Ω_{calc} : from 1.95 to 1.7), and a decrease in annually-averaged pH, from 8.1 to 8, over the pan-Arctic surface ocean. The saturation states Ω_{arag} and Ω_{calc} are lowest in winter and occurrences of seasonal aragonite undersaturation occur regionally and become more frequent with

time over the standard run. In particular, the general decrease in Ω_{arag} has the potential to negatively impact sensitive biota in the marine Arctic. The increase in pan-Arctic, annually-averaged sea surface temperature accounts for $\sim 10\%$ of the increase in the pan-Arctic sea surface $p\text{CO}_2$ over the period 1980 – 2015.

Regional analyses indicate large spatial variability, and regions with pronounced sea surface characteristics, relative to the pan-Arctic mean, are as follows. The uptake of carbon is highest in the Barents and Norwegian Seas, which also account for a large proportion of the increase in Arctic Ocean carbon uptake over the period 1980 – 2015. The Laptev Sea has particularly low pH, Ω_{arag} , and Ω_{calc} and high $p\text{CO}_2$ at the sea surface, consistent with observations. The South and North Beaufort Seas exhibit increasing trends in annual-averaged $p\text{CO}_2$, despite relatively low total annual carbon uptake. For the North Beaufort, the low carbon uptake is due to the relatively high ice cover, but for the South Beaufort, the low carbon uptake is potentially due to a combination of low sea surface $p\text{CO}_2$, high (but not as high as the North Beaufort) sea ice cover, and high-DIC/low-TA river input. Lastly, the Canadian Polar Shelf is undergoing an accelerated increase in $p\text{CO}_2$ and decrease in pH, relative to the pan-Arctic mean.

I also tested the model sensitivity to two modifications implemented in this study. The first modification, which tested the effect of the (subsurface) sea-ice carbon pump, showed only a small change to the total uptake of carbon by the Arctic Ocean with the ice-carbon pump suppressed, consistent with the previous 1D study, but a marked decrease in the seasonal variability of both DIC and TA, as well as an offset in the summertime saturation state in the surface Arctic Ocean. The higher summertime maxima for simulated Ω_{arag} in the no ice-carbon-pump run indicate that neglecting the ice-carbon-pump leads to an underestimation of the stress to organisms that produce aragonite.

The second modification focused on the effect of the simulated ice algae on the sea surface $p\text{CO}_2$ and ocean uptake of carbon by comparing the standard and no ice-algae runs. In the no ice-algae run, pan-Arctic uptake of carbon was less than that in the standard run, and the difference between the runs increased to 4% at the end of 20 years. Comparison between the standard and no ice-algae runs indicates that the inclusion of simulated ice algae may not be necessary over shorter (sub-decadal) runs of a regional Arctic Ocean model, consistent with the 1D model study, but that the cumulative effects on upper water column nutrients and the carbon uptake imply that inclusion of the sympagic ecosystem has a growing importance for longer-term model runs.

In the Arctic Ocean, difficult winter conditions mean that many measurement campaigns are focused on the summer months when the region is more accessible. The strong sea-

sonal variability in the simulated inorganic carbon system properties presented in this study indicate that the interpretation of observational studies should take into account the seasonal sampling bias. Furthermore, the sparsity of winter-time observations due to the difficult conditions in Arctic winters emphasizes the importance of this type of model study, which can be compared to available observations and fill in the gaps when and where the observations are not available.

Sea ice algae are a functional group that occupy a unique niche in polar marine environments. They comprise a piece of a larger marine ecosystem and are linked to the underlying water column through exchange of nutrients and organic material (the latter can influence seeding of both sympagic and pelagic blooms). The extent and productivity of sea ice algae are limited to field observations, as they are undetectable via satellite measurements. An accurate model representation of sea ice algae can provide a valuable tool for expanding our understanding from point-wise measurements to a broader regional perspective. The 1D and 3D model developments in this study provide insight into how the sympagic and pelagic ecosystems interact and illustrate the relative importance of the two, with a focus on biomass and sea surface carbon system properties.

Another important general concept, evident in both the 1D and 3D studies, is the fact that changes to DIC alone are not sufficient to define changes to other carbon system properties. It is true that, at the air-sea interface, TA is not exchanged, such that air-sea exchange of carbon alone affects the sea surface $p\text{CO}_2$. As an illustrative counterexample, though, at the ice-ocean interface, the coincident decrease in both the sea surface DIC and TA (as occurs during ice melt) can largely counter one another in terms of the effect on the sea surface $p\text{CO}_2$.

This study is the first to couple simulated sympagic and pelagic ecosystems in order to analyze the effects of both sympagic and pelagic ecosystems on ocean carbon uptake in a 1D ocean model, and of ice algae in a regional 3D ocean model. Another novel aspect of the model in this study is the inclusion of a subsurface, non-local transport of DIC and TA during ice growth associated with brine deposition. This is also the first study to compare the relative effect of sea ice algae and the sea-ice carbon pump, with respect to inorganic carbon properties at the sea surface.

The sensitivity experiments for the no-ice-algae and no ice-carbon-pump runs are initialized with the output from the standard run for year 1990, when the system has already been spun-up with the inclusion of ice algae. Ignoring time/computational constraints, a better setup for these experiments would be to run them in parallel with the standard run with the same initial year for all runs (1969) and let the system evolve under the three different

runs. In particular for the no-ice-algae run, running the experiment from the same starting point as the standard run has the potential to shed some light on the decrease in pan-Arctic surface nitrogen concentration relative to the standard run, as the drift in surface nitrate may be due to the system readjustment to the loss of the sea ice from the period 1969 – 1990.

Other possible sensitivity experiments of the model could look at how the inorganic carbon system is affected by changes to river runoff, precipitation, or the representation of the pelagic ecosystem. Another future research direction could be further analysis of the simulated ice-carbon-pump through differentially varying the flux of DIC relative to TA (difference in ice and seawater reference concentrations) associated with ice growth and melt. Lastly, the two sensitivity analyses of the 3D model in this study could also include a third scenario, in which the ice carbon pump is confined to the surface layer during ice growth (the LIM-NEMO standard formulation) as an additional test.

Concerning the regional analysis, the present study employs a priori regions for comparison. One alternative suggestion is not to define the regions a priori, but to define them based on distinctive properties, e.g. sea-surface $p\text{CO}_2$ or pH, through a cluster analysis approach. Distinct subregions or overlap of regions defined in the present study might obscure areas that stand out in a cluster analysis. This alternative clustering approach to regional analysis has the potential advantage of identifying distinctive regions which might remain undiscovered by the "static region" approach in the present study.

Lastly, the Arctic Ocean biogeochemical sea-ice and ocean 3D model developed in this study lends itself to many potential future research questions. One of the clearest ways to move forward utilizing this model would be to apply it in a study of near-future projections in order to estimate the effect of continued sea ice loss on the pan-Arctic carbon uptake and to predict how the Arctic Ocean will evolve in terms of acidification and as a sink to anthropogenic carbon production. For the present study, the DIC boundary conditions imposed on the region are held constant, however in both the recent past and the near future the near-surface DIC at the boundaries should exhibit an increase reflecting the increase in atmospheric $p\text{CO}_2$. In addition, imposing atmospheric $p\text{CO}_2$ forcing conditions based on Arctic observations would be more appropriate for the Arctic Ocean (rather than tropical $p\text{CO}_2$ observations from in Mauna Loa).

Appendices

A Additional Information

A.1 Additional information for Chapter 2

A.1.1 Parameterizations for subgrid-scale snow depth distribution and light penetration through snow, sea ice, and melt ponds

To improve light and heat flux estimates through sea ice in regional and global models, *Abraham et al.* [2015] applied two kinds of one-parameter probability density functions for describing subgrid-scale snow depth variability: Rayleigh and gamma distributions. In this study, the Rayleigh distribution is used in model simulations since *Abraham et al.* [2015] indicated a better fit with observed snow depth evolution. The probability density function for the Rayleigh distributed snow ($pdf(h)$) is defined as

$$pdf(h) = \frac{\pi h}{2h_s^2} \exp\left(-\frac{\pi h^2}{4h_s^2}\right), \quad (\text{A.1})$$

where h is the snow depth (m) and h_s represents the gridbox-mean snow depth (m), which is simulated by the sea ice model. The light transmission through snow and sea ice is described by the Beer-Lambert law, which is defined in a generalized form as:

$$I(z) = I_0 \exp(-\kappa z), \quad (\text{A.2})$$

where $I(z)$ is the radiation at depth z (m) below the surface (W m^{-2}) and κ is the extinction coefficient of the medium (m^{-1}). I_0 represents the amount of incident light that penetrates into the snow/ice/melt ponds surface (W m^{-2}), which is defined in a generalized form as

$$I_0 = SWR(1 - \alpha)i_0, \quad (\text{A.3})$$

where SWR is the incident shortwave radiation (W m^{-2}), α is the surface albedo (dimensionless), and i_0 is the transmissivity coefficient (dimensionless). For a fully snow-covered surface of non-uniform snow depth, the gridbox-mean light intensity at the snow base is

obtained by averaging the Beer-Lambert law over all snow depths weighted by the relative probabilities:

$$\bar{I}_s = SWR(1 - \alpha_s) i_{0,s} \int_0^\infty pdf(h) \exp(-\kappa_s h) dh, \quad (\text{A.4})$$

where α_s , $i_{0,s}$, and κ_s respectively represent the albedo, the transmissivity coefficient, and the extinction coefficient for snow.

During melt periods, the ice surface may have different covers, such as snow, bare ice, and melt ponds. To account for different surface conditions in the parameterization of the gridbox-mean light intensity at the ice surface, *Abraham et al.* [2015] accounted for these different surface conditions within a grid box by introducing surface area fractions of snow (A_s), bare ice (A_i), and melt ponds (A_m), such that

$$A_s + A_i + A_m = 1. \quad (\text{A.5})$$

The parameterizations for A_s , A_i , and A_m are described in *Abraham et al.* [2015]. The gridbox-mean light intensity at the ice surface (\bar{I}_{top}) is then defined as a sum of the incident light that has: 1) penetrated through snow; 2) reached the bare ice; and 3) penetrated through melt ponds. Hence, \bar{I}_{top} is given by

$$\bar{I}_{top} = A_s \bar{I}_s + A_i I_{0,i} + A_m I_{0,m} \exp(-\kappa_m h_m) \quad (\text{A.6})$$

where \bar{I}_s is Equation A.4. κ_m and h_m are the extinction coefficient and the depth of melt ponds, respectively. $I_{0,i}$ and $I_{0,m}$ respectively represent the amounts of incident light that penetrates through the ice and melt ponds surface:

$$I_{0,i} = SWR(1 - \alpha_i) i_{0,i} \quad (\text{A.7})$$

$$I_{0,m} = SWR(1 - \alpha_m) i_{0,m} \quad (\text{A.8})$$

where α_i and α_m are the albedos and $i_{0,i}$ and $i_{0,m}$ are the transmissivity coefficients for sea ice and melt ponds, respectively. The optical parameters used in this study are listed in Table A.1. Note that different values for the extinction coefficients and albedos are set between the freezing and melting phases of snow and sea ice. To allow a smooth transition between the values under the freezing and melting phases, the extinction coefficients and

albedos of snow and sea are defined based on *Abraham et al.* [2015] as

$$\kappa_s = \frac{\kappa_{s,f} + \kappa_{s,m}}{2} + \frac{\kappa_{s,m} - \kappa_{s,f}}{2} \tanh(T - 273.15^\circ\text{C}) \quad (\text{A.9})$$

$$\kappa_i = \frac{\kappa_{i,f} + \kappa_{i,m}}{2} + \frac{\kappa_{i,m} - \kappa_{i,f}}{2} \tanh(T - 273.15^\circ\text{C}) \quad (\text{A.10})$$

$$\alpha_s = \frac{\alpha_{s,f} + \alpha_{s,m}}{2} + \frac{\alpha_{s,m} - \alpha_{s,f}}{2} \tanh(T - 273.15^\circ\text{C}) \quad (\text{A.11})$$

$$\alpha_i = \frac{\alpha_{i,f} + \alpha_{i,m}}{2} + \frac{\alpha_{i,m} - \alpha_{i,f}}{2} \tanh(T - 273.15^\circ\text{C}) \quad (\text{A.12})$$

Following *Zeebe et al.* [1996], it is assumed that only PAR penetrates into the ice interior, while the radiation outside of PAR bands is absorbed by the uppermost layer of snow, bare ice, or melt ponds. Therefore, the gridbox-mean PAR at the ice base (\overline{PAR}_{bot}) is defined as

$$\overline{PAR}_{bot} = \bar{I}_{top} \exp(-\kappa_i h_i) \quad (\text{A.13})$$

where h_i is the sea ice thickness. Finally, the gridbox-mean PAR in the water column under the ice ($\overline{PAR}_{ui}(z)$) is first attenuated by ice algae before it reaches the uppermost layer of the water column, and is further reduced as it penetrates through each model layer due to absorption and scattering by seawater itself, as well as by phytoplankton and detritus:

$$\overline{PAR}_{ui}(z) = \overline{PAR}_{bot} \exp(-\kappa_{ia}[IA]h_{ia} - \kappa_{ui}z_{sw}) \quad (\text{A.14})$$

where κ_{ia} is the extinction coefficient of ice algae, $[IA]$ is the ice algal biomass, and h_{ia} is the thickness of the ice skeletal layer, which are all defined in the next section. z_{sw} is the depth of seawater under the ice. κ_{ui} is the total extinction coefficient in the water column defined as

$$\kappa_{ui} = \kappa_{sw} + \kappa_{pd} \int_0^{z_{sw}} (P1 + P2 + D1 + D2) dz \quad (\text{A.15})$$

where κ_{sw} and κ_{pd} are the extinction coefficients for seawater and for both phytoplankton and detritus. κ_{sw} is computed by the GOTM model assuming the Jerlov type I [*Burchard et al.*, 2006]. The concentrations of phytoplankton ($P1$, $P2$) and detritus ($D1$, and $D2$) at the given model layer are defined in the next section.

A.1.2 Ecosystem model equations

The coupled sea ice-ocean biogeochemical model consists of 14 state variables (Figure 1 and Table A.1). Nitrogen is used as the currency for the model state variables other than $[Si]_{ia}$, $[Si]$, and $[BSi]$, which are expressed in silicon units. For comparison with observations, conversion from nitrogen (N) to Chl *a* and carbon (C) are required. For small phytoplankton (P1), the Redfield C:N ratio of 106:16 (mol:mol) following *Redfield et al.* [1963b] and a fixed C:Chl *a* ratio of 50:1 (wt:wt) following *Lavoie et al.* [2009] are used. For ice algae and large phytoplankton (IA and P2), a fixed C:N ratio of 106:12 (mol:mol) following *Palmer et al.* [2014a] and a fixed C:Chl *a* ratio of 28:1 (wt:wt) following *Lavoie et al.* [2009] were used. In *Lavoie et al.* [2009], the C:Chl *a* ratio of 28:1 (wt:wt) was used for ice algae, while 50:1 (wt:wt) was used for phytoplankton (corresponding to P2 in this study) assuming that ice algae was more acclimated to low light conditions. However, in this study, prescribing different C: Chl *a* ratios between IA and P2 would result in the violation of mass conservation of chlorophyll *a* in P2 because IA and P2 are coupled through the flushing of ice algae to enter the P2 pool, and also because chlorophyll *a* is not modeled explicitly. We represent the photoacclimation of IA relative to P2 by prescribing different values of photosynthetic parameters. The parameters for the ecosystem model are listed in Table A.3.

Sea ice component

The sea ice biogeochemical model consists of four state variables: ice algae, nitrate, ammonium, and silicate. The equation for ice algae is

$$\frac{\partial}{\partial t}[IA] = \mu_{ia}[IA] - M[IA] - \left(\frac{[R_{ice}] + f_{pond}r_{pond}}{z_{ia}} \right) [IA], \quad (\text{A.16})$$

where $[IA]$ is the ice algal biomass in the bottom 3 cm of the skeletal layer (mmol N m^{-3}). The first term in Equation A.16 represents the growth of ice algae due to primary production. The rate of ice algal growth (μ_{ia}) depends on the ambient temperature of the bottom ice ($[T]_{ia}$ in $^{\circ}\text{C}$) following *Eppley* [1972], as well as on the minimum value among the four limitation functions (L_{nit} , L_{sil} , L_{lig} , and L_{ice}):

$$\mu_{ia} = \mu_{ia}^{max} \ln(2) \exp(b_{ia}[T]_{ia}) \min(L_{nit}, L_{sil}, L_{lig}, L_{ice}), \quad (\text{A.17})$$

where μ_{ia}^{max} represents the specific growth rate and b_{ia} is the temperature sensitivity coefficient for the ice algal growth. Following *Lavoie et al.* [2005a], μ_{ia}^{max} and b_{ia} are set to

0.85 d⁻¹ and 0.0633 °C⁻¹. The nitrogen (L_{nit}) and silicon (L_{sil}) limitation functions are based on the Monod formulation [Monod, 1949]:

$$L_{nit} = \frac{[NO_3]_{ia} + [NH_4]_{ia}}{k_n + [NO_3]_{ia} + [NH_4]_{ia}} \quad (\text{A.18})$$

$$L_{sil} = \frac{[Si]_{ia}}{k_s + [Si]_{ia}} \quad (\text{A.19})$$

where $[NO_3]_{ia}$, $[NH_4]_{ia}$, and $[Si]_{ia}$ respectively represent the concentrations of nitrate (mmol N m⁻³), ammonium (mmol N m⁻³), and silicate (mmol Si m⁻³) in the bottom 3 cm of the ice skeletal layer. k_n and k_s are the half-saturation constants for nitrogen and silicon uptake, which are set to 1 mmol N m⁻³ and 4 mmol Si m⁻³ following Lavoie *et al.* [2005a], respectively. The light limitation function (L_{lig}) is formulated following Lavoie *et al.* [2005a]:

$$L_{lig} = \tanh \left(\frac{\alpha^{ia}}{P_m^{ia}} [PAR]_{ia} \right) \quad (\text{A.20})$$

where α^{ia} is the photosynthetic efficiency (mg C (mg Chl *a*)⁻¹ h⁻¹ (μmol photons m⁻² s⁻¹)⁻¹), P_m^{ia} is the maximum photosynthetic rate (mg C mg Chl *a*⁻¹ h⁻¹), and $[PAR]_{ia}$ is the PAR (in μmol photons m⁻² s⁻¹) penetrating the ice algae skeletal layer, which is computed by the sea ice thermodynamic model. Lavoie *et al.* [2005a] used various values (0.1-0.45) for the ratio of α^{ia} and P_m^{ia} depending on snow cover. We set the ratio of these two photosynthetic parameters (α^{ia}/P_m^{ia}) to 0.44, based on the results of our sensitivity studies.

The ice growth/melt limitation function (L_{ice}) is formulated similarly to Lavoie *et al.* [2005a]:

$$L_{ice} = \max \left(1 - \frac{[R_{ice}]}{C_m}, 0 \right) \quad (\text{A.21})$$

where $[R_{ice}]$ is the ice growth/melt rate at the ice base (m s⁻¹) computed by the physical model (see Flato and Brown [1996] for details) and C_m is the critical ice growth/melt rate, which is set to 0.015 m d⁻¹ following Lavoie *et al.* [2005a].

The second term in Equation A.16 represents the loss due to mortality. The mortality rate of ice algae (M) includes both linear and quadratic dependence on the ice algal biomass:

$$M = m_{lia} \exp(b_{ia}[T]_{ia}) + m_{qia}[IA] \quad (\text{A.22})$$

where m_{lia} is the rate constant for the temperature-dependent linear mortality and m_{qia} is the rate constant for the quadratic mortality. We set m_{lia} and m_{qia} to 0.03 d^{-1} and 0.00015 d^{-1} , based on the results of our sensitivity studies.

The last term in Equation A.16 represents the loss due to flushing. There are four sources of meltwater that contributes to flushing: ice meltwater originating from the 1) top, 2) interior, and 3) bottom of the sea ice; and 4) snow meltwater that drains out of melt ponds. The sum of the ice melt rates (R_{ice}) and the areal fraction of melt ponds (f_{pond}) are computed by the physical model (see *Flato and Brown [1996]* and *Abraham et al. [2015]* for details). r_{pond} represents the drainage rate of meltwater in the melt ponds, which is set to 0.0175 m d^{-1} following *Taylor and Feltham [2004]*. Finally, z_{ia} is the thickness of the ice skeletal layer, which is set to 0.03 m in this study.

The equations for nitrate ($[NO_3]_{ia}$) and ammonium ($[NH_4]_{ia}$) in the ice skeletal layer (mmol N m^{-3}) are defined as:

$$\begin{aligned} \frac{\partial}{\partial t}[NO_3]_{ia} = & -\mu_{ia}[IA]p_{no3}^{ia} \frac{[NO_3]_{ia}}{[NO_3]_{ia} + [NH_4]_{ia}} + r_{nit}[NH_4]_{ia} \\ & - \frac{f_{pond}r_{pond}}{z_{ia}}[NO_3]_{ia} + \frac{D}{h_\nu} \left(\frac{[NO_3] - [NO_3]_{ia}}{z_{ia}} \right) \end{aligned} \quad (\text{A.23})$$

$$\begin{aligned} \frac{\partial}{\partial t}[NH_4]_{ia} = & -\mu_{ia}[IA] \left(1 - p_{no3}^{ia} \right) \frac{[NO_3]_{ia}}{[NO_3]_{ia} + [NH_4]_{ia}} - r_{nit}[NH_4]_{ia} \\ & - \frac{f_{pond}r_{pond}}{z_{ia}}[NH_4]_{ia} + \frac{D}{h_\nu} \left(\frac{[NH_4] - [NH_4]_{ia}}{z_{ia}} \right) \\ & + f_{lia}m_{lia} \exp(b_{ia}[T]_{ia})[IA] \end{aligned} \quad (\text{A.24})$$

The first term in Equation A.23 and Equation A.24 represents the loss due to uptake by ice algae. To discriminate the uptake of nitrate from that of ammonium, the relative preference index (p_{no3}^{ia}) based on *Denman [2003]* is defined as:

$$p_{no3}^{ia} = \frac{\nu_n}{\nu_n + [NH_4]_{ia}}, \quad (\text{A.25})$$

where ν_n represents the half-saturation constant for preferential uptake of nitrate, which is set to $0.2 \text{ mmol N m}^{-3}$ following *Denman [2003]*. The second term in Equation A.23 and Equation A.24 represents the nitrification, which is a source for nitrate and a sink for ammonium. In this study, a first order reaction is assumed for this process in the sea ice with a rate constant of 0.01 d^{-1} . The third term in Equation A.23 and Equation A.24 represents the loss due to flushing, which is formulated in a similar manner as the flushing of ice algae. The fourth term in Equation A.23 and Equation A.24 represents the diffusive

exchange at the ice-ocean interface, where $[NO_3]$ and $[NH_4]$ are the concentrations (mmol N m^{-3}) of nitrate and ammonium in the uppermost layer of the water column. D is the molecular diffusion coefficient for dissolved nutrients at the ice-water interface, which is set to $4.7 \times 10^{-8} \text{ m}^2 \text{ s}^{-1}$ [Rebreanu *et al.*, 2008]. The exchange rate at the ice-water interface depends on the molecular sublayer thickness (h_ν) defined as:

$$h_\nu = \frac{\nu}{u_\tau}, \quad (\text{A.26})$$

where ν is the kinematic viscosity of seawater, which is set to $1.85 \times 10^{-6} \text{ m}^2 \text{ s}^{-1}$ [Lavoie *et al.*, 2005a]. u_τ represents the friction velocity, which is defined as

$$u_\tau = \left(\frac{|\tau|}{\rho_o} \right)^{1/2}, \quad (\text{A.27})$$

where τ is the ice-ocean stress and ρ_o is the seawater density. Following Goosse and Fichefet [1999], τ is defined as

$$\tau = \rho_o C_{io} |u_i - u_o| (u_i - u_o), \quad (\text{A.28})$$

where C_{io} is the drag coefficient at the ice-ocean interface, which is set to 0.0054 [Shirasawa and Ingram, 1997]. u_i and u_o are the magnitudes of horizontal velocity fields of ice and surface water, respectively. Substituting Equations A.27 and A.28 into Equation A.26 gives:

$$h_\nu = \frac{\nu}{|u_i - u_o|} C_{io}^{-\frac{1}{2}}, \quad (\text{A.29})$$

where u_o is computed by the physical ocean model, and we assume $u_i = 0$ for landfast ice considered in this study.

The fifth term in Equation A.24 represents the remineralization of dead ice algal cells. A direct transfer from ice algae to ammonium is implemented here due of lack of representation of detritus pool in the sea ice. It is assumed that only a fraction (f_{lia}) of linear mortality enters the ammonium pool, while the remaining fraction is released into the water column and enters the large detritus pool. In this study, f_{lia} is set to 0.3.

The equation for silicate ($[Si]_{ia}$) in the ice skeletal layer (mmol Si m^{-3}) is given by:

$$\frac{\partial}{\partial t} [Si]_{ia} = -q_{si2n} \mu_{ia} [IA] - \frac{f_{pond} r_{pond}}{z_{ia}} [Si]_{ia} + \frac{D}{h_\nu} \left(\frac{[Si] - [Si]_{ia}}{z_{ia}} \right) \quad (\text{A.30})$$

where the first term represents the uptake by ice algae, the second term represents the flushing, and the third term represents the diffusive mixing at the ice-ocean interface. The uptake rate is converted from nitrogen to silicon units by assuming a fixed nitrogen-to-silicon intracellular ratio (q_{si2n}) of 1.7 mol Si:mol N based on *Mundy et al.* [2014a]. $[Si]$ represents the concentration of silicate in the uppermost layer of the water column (mmol Si m⁻³).

Oceanic component

The ocean biogeochemical model consists of ten state variables: small and large classes of phytoplankton, zooplankton, and detritus, biogenic silica, nitrate, ammonium, and silicate. The equations for small and large phytoplankton are:

$$\frac{\partial}{\partial t}[P1] = \mu_{p1}[P1] - \Gamma_{z1} \frac{[P1]}{F_{z1}}[Z1] - M_{lp1}[P1] + \frac{\partial}{\partial z} \left(K_z \frac{\partial [P1]}{\partial z} \right) \quad (\text{A.31})$$

$$\begin{aligned} \frac{\partial}{\partial t}[P2] = & \mu_{p2}[P2] - \Gamma_{z2} \frac{[P2]}{F_{z2}}[Z2] - M_{lp2}[P2] + \frac{\partial}{\partial z} \left(K_z \frac{\partial [P2]}{\partial z} \right) \\ & - m_{qp2}[P2]^2 + f_{seed} ([R_{ice}] + r_{pond}) [IA] \frac{z_{ia}}{z_{oc}} \delta_{z,z1} \end{aligned} \quad (\text{A.32})$$

where $[P1]$ and $[P2]$ respectively represent the biomass of small and large phytoplankton (mmol N m⁻³). The first term in Equations A.31 and A.32 represent the growth due to primary production. The growth rates of phytoplankton (μ_{p1} and μ_{p2}) depend on the ambient temperature, nutrient and light conditions:

$$\mu_{p1} = \mu_{p1}^{max} Q_{10p}^{([T]-10)/10} \min(L_{nit}^{phy}, L_{lig}^{p1}) \quad (\text{A.33})$$

$$\mu_{p2} = \mu_{p2}^{max} Q_{10p}^{([T]-10)/10} \min(L_{nit}^{phy}, L_{lig}^{p2}, L_{sil}^{p2}) \quad (\text{A.34})$$

where μ_{p1}^{max} and μ_{p2}^{max} represent the maximum specific growth rates, which are set to 0.5 and 2.0 d⁻¹, respectively [Steiner et al., 2006a]. The temperature dependence is based on the Q10 formulation with a Q10 factor (Q_{10p}) of 1.55 [Suzuki and Takahashi, 1995]. $[T]$ is the ambient seawater temperature (°C), which is simulated by the physical model. The nutrient limitation functions are based on the Monod function [Monod, 1949]:

$$L_{nit}^{phy} = \frac{[NO_3] + [NH_4]}{k_n + ([NO_3] + [NH_4])} \quad (\text{A.35})$$

$$L_{sil}^{p2} = \frac{[Si]}{k_{si} + [Si]} \quad (\text{A.36})$$

where the same half-saturation constants are used between the sea ice and ocean biogeochemical modules. The light limitation functions are defined as

$$L_{lig}^{p1} = 1 - \exp\left(-\alpha^{p1}/P_m^{p1}[PAR]\right) \quad (\text{A.37})$$

$$L_{lig}^{p2} = 1 - \exp\left(-\alpha^{p2}/P_m^{p2}[PAR]\right) \quad (\text{A.38})$$

where α^{p1} and α^{p2} represent the photosynthetic efficiency and P_m^{p1} and P_m^{p2} represent the maximum photosynthetic rate. In this study, the ratios of photosynthetic parameters (i.e., α^{p1}/P_m^{p1} and α^{p2}/P_m^{p2}) are set to 0.07 for both phytoplankton groups. $[PAR]$ represents the photosynthetically active radiation in the water column ($\mu\text{mol photons m}^{-2} \text{ s}^{-1}$) which is defined in the previous section. The second term in Equations A.31 and A.32 represent the loss due to grazing by zooplankton. The rates of small and large zooplankton (Γ_{z1} and Γ_{z2}) are defined as

$$\Gamma_{z1} = \gamma_{z1} Q_{10z}^{([T]-10)/10} \frac{F_{z1}^2}{k_{z1}^2 + F_{z1}^2} \quad (\text{A.39})$$

$$\Gamma_{z2} = \gamma_{z2} Q_{10z}^{([T]-10)/10} \frac{F_{z2}^2}{k_{z2}^2 + F_{z2}^2} \quad (\text{A.40})$$

where γ_{z1} and γ_{z2} represent the maximum specific grazing rates, which are set to 1 d^{-1} for both zooplankton groups in this study. The Q10 factor for zooplankton (Q_{10z}) is set to 2.14 [Buitenhuis *et al.*, 2006]. k_{z1} and k_{z2} represent the half-saturation constants for grazing, which are set to 1 mmol N m^{-3} for both zooplankton groups in this study. F_{z1} and F_{z2} respectively represent the available food sources for small and large zooplankton, which are defined as

$$F_{z1} = [P1] + f_{d1}[D1] \quad (\text{A.41})$$

$$F_{z2} = [P2] + f_{d2}[D2] + f_{z1}[Z1] \quad (\text{A.42})$$

where f_{d1} represents the grazing preference of small zooplankton on small detritus. f_{d2} and f_{z1} represent the grazing preferences of large zooplankton on small and large detritus, respectively. f_{d1} , f_{d2} , and f_{z1} are all set to 0.5 following Steiner *et al.* [2006a].

The third terms in Equations A.31 and A.32 represent the linear mortality of small and large phytoplankton. Assuming a temperature dependence following the same Q10 formu-

lation, the rates of linear mortality are given by:

$$M_{lp1} = m_{lp1} Q_{10p}^{([T]-10)/10} \quad (\text{A.43})$$

$$M_{lp2} = m_{lp2} Q_{10p}^{([T]-10)/10} \quad (\text{A.44})$$

where m_{lp1} and m_{lp2} represent the rate constants for linear mortality of small and large phytoplankton, respectively. In this study, both of these rates are set to 0.03 d^{-1} .

The fourth terms in Equations A.31 and A.32 represent the vertical mixing of small and large phytoplankton at a given model layer with those in the adjacent (upper and/or lower) layers. K_z represents the vertical eddy diffusivity coefficient, which is calculated by the physical ocean model.

The fifth term in Equation A.32 represents the quadratic mortality of large phytoplankton, which depends on a rate constant, m_{qp2} . In this study, m_{qp2} is set to $0.05 \text{ d}^{-1} (\text{mmol N m}^{-3})^{-1}$. The sixth term in Equation A.32 represents the source for large phytoplankton due to seeding of ice algae. Following *Lavoie et al.* [2009], it is assumed that a certain fraction (f_{seed}) of ice algae flushed into the water column enters the large phytoplankton pool, while the remaining fraction ($1 - f_{seed}$) enters the large detritus pool. In this study, f_{seed} is set to 0.1, assuming that 10% of ice algae flushing results in large phytoplankton seeding. h_{oc} is the thickness of the uppermost layer of the ocean model (i.e., 1 m in this study), and δ_{z,z_1} is the Kronecker's delta which equals 1 in the uppermost layer of the ocean (z_1), while it is set to 0 elsewhere:

$$\delta_{z,z_1} = \begin{cases} 0 & \text{if } z \neq z_1 \\ 1 & \text{if } z = z_1 \end{cases} \quad (\text{A.45})$$

The equations for small and large zooplankton are defined as

$$\frac{\partial}{\partial t}[Z1] = a_1 \Gamma_{z1}[Z1] - M_{lz1}[Z1] - \Gamma_{z2} \frac{f_{z1}[Z1]}{F_{z2}}[Z2] + \frac{\partial}{\partial z} \left(K_z \frac{\partial [Z1]}{\partial z} \right) \quad (\text{A.46})$$

$$\frac{\partial}{\partial t}[Z2] = a_2 \Gamma_{z2}[Z2] - M_{lz2}[Z2] - m_{qz2}[Z2]^2 + \frac{\partial}{\partial z} \left(K_z \frac{\partial [Z2]}{\partial z} \right) \quad (\text{A.47})$$

where $[Z1]$ and $[Z2]$ respectively represent the biomass of small and zooplankton (mmol N m^{-3}).

The first terms in Equations A.46 and A.47 represent the sources due to ingestion, which are proportional to the zooplankton grazing. a_1 and a_2 respectively represent the assimilated

fractions of grazing by small and large zooplankton, both of which are set to 0.7 following *Lavoie et al.* [2009].

The second terms in Equations A.46 and A.47 represent the sinks due to linear mortality. The rates of zooplankton linear mortality (M_{lz1} and M_{lz2}) are parameterized in the same way as those of phytoplankton:

$$M_{lz1} = m_{lz1} Q_{10z}^{([T]-10)/10} \quad (\text{A.48})$$

$$M_{lz2} = m_{lz2} Q_{10z}^{([T]-10)/10} \quad (\text{A.49})$$

where the rate constants for linear mortality of small and large zooplankton (m_{lz1} and m_{lz2}) are both set to 0.03 d^{-1} [*Lavoie et al.*, 2009].

The third term in Equation A.46 represents the loss of small zooplankton due to (carnivorous) grazing by large zooplankton. The third term in Equation A.47 represents the loss of large zooplankton due to quadratic mortality which is parameterized in the same way as the quadratic mortality of large phytoplankton with a rate constant (m_{qz2}) of $0.1 \text{ d}^{-1} (\text{mmol N m}^{-3})^{-1}$ in this study.

The fourth terms in Equations A.46 and A.47 respectively represent the vertical mixing of small and large zooplankton. The equations for small and large detritus, as well as

biogenic silica are given by

$$\begin{aligned} \frac{\partial}{\partial t}[D1] &= (1 - a_1) \Gamma_{z1}[Z1] + M_{lp1}[P1] - \Gamma_{z1} \frac{f_{d1}[D1]}{F_{z1}}[Z1] \\ &\quad - R_{d1}[D1] - w_{d1} \frac{\partial[D1]}{\partial z} + \frac{\partial}{\partial z} \left(K_z \frac{\partial[D1]}{\partial z} \right) \end{aligned} \quad (\text{A.50})$$

$$\begin{aligned} \frac{\partial}{\partial t}[D2] &= (1 - a_2) \Gamma_{z2}[Z2] + M_{lp2}[P2] - \Gamma_{z2} \frac{f_{d2}[D2]}{F_{z2}}[Z2] \\ &\quad - R_{d2}[D2] - w_{d2} \frac{\partial[D2]}{\partial z} + \frac{\partial}{\partial z} \left(K_z \frac{\partial[D2]}{\partial z} \right) + m_{qp2}[P2]^2 \\ &\quad + (1 - f_{seed}) ([R_{ice}] + r_{pond}) [IA] \frac{z_{ia}}{z_{oc}} \delta_{z,z_1} \\ &\quad + (1 - f_{lia}) m_{lia} \exp(b_{ia}[T]_{ia}) [IA] \frac{z_{ia}}{z_{oc}} \delta_{z,z_1} \\ &\quad + m_{qia} [IA] \frac{z_{ia}}{z_{oc}} \delta_{z,z_0} \end{aligned} \quad (\text{A.51})$$

$$\begin{aligned} \frac{\partial}{\partial t}[BSi] &= q_{si2n} \left((1 - a_2) \Gamma_{z2}[Z2] + M_{lp2}[P2] - \Gamma_{z2} \frac{f_{d2}[D2]}{F_{z2}}[Z2] \right) \\ &\quad - R_{bsi}[BSi] - w_{d2} \frac{\partial[BSi]}{\partial z} + \frac{\partial}{\partial z} \left(K_z \frac{\partial[BSi]}{\partial z} \right) + q_{si2n} m_{qp2}[P2]^2 \\ &\quad + q_{si2n} (1 - f_{seed}) ([R_{ice}] + r_{pond}) [IA] \frac{z_{ia}}{z_{oc}} \delta_{z,z_1} \\ &\quad + q_{si2n} (1 - f_{lia}) m_{lia} \exp(b_{ia}[T]_{ia}) [IA] \frac{z_{ia}}{z_{oc}} \delta_{z,z_1} \\ &\quad + q_{si2n} m_{qia} [IA] \frac{z_{ia}}{z_{oc}} \delta_{z,z_0} \end{aligned} \quad (\text{A.52})$$

In each of Equations A.50, A.51, and A.52, the first term represents the unassimilated fraction of grazing that enter the detrital pool, the second term represents the source for detritus due to phytoplankton linear mortality, the third term represents the loss of detritus due to grazing, and the fourth term represents the remineralization of detrital materials. The rates of remineralization of small and large detritus and biogenic silica (R_{d1} , R_{d2} , R_{bsi}) depend on seawater temperature following the Q10 formulation:

$$R_{d1} = r_{d1} Q_{10b}^{([T]-10)/10} \quad (\text{A.53})$$

$$R_{d2} = r_{d2} Q_{10b}^{([T]-10)/10} \quad (\text{A.54})$$

$$R_{bsi} = r_{bsi} Q_{10b}^{([T]-10)/10} \quad (\text{A.55})$$

where r_{d1} , r_{d2} , and r_{bsi} represent the rate constants for remineralization, which are respectively set to 0.03 d^{-1} (this study), 0.3 d^{-1} [Lavoie *et al.*, 2009], and 0.01 d^{-1} [Steiner *et al.*,

2006a].

The fifth terms in Equations A.50, A.51, and A.52 represent the loss due to sinking. It is assumed that detritus sink at a fixed rate; a rate of 1 m d⁻¹ is given to small detritus, while a faster sinking rate of 50 m d⁻¹ is prescribed for large detritus and biogenic silica. Both of these rates are taken from *Lavoie et al.* [2009]. Detritus reaching the seafloor is accumulated in the deepest layer of the water column. The sixth terms in Equations A.50, A.51, and A.52 represent the vertical mixing of respective detrital materials.

The seventh terms in Equations A.50 and A.51 represent the sources for small and large detritus due to quadratic mortality of large phytoplankton. The last three terms in these equations represent the influxes of detrital materials from the ice skeletal layer due to flushing (the ninth terms), linear mortality (the tenth terms), and quadratic mortality (the eleventh terms) of ice algae. Note that the equation for biogenic silica is identical to the equation for large detritus except that the two state variables have different remineralization rates and that those terms expressed in nitrogen units are converted to silicon units by assuming a fixed intracellular nitrogen-to-silicon ratio of 1.7 mol N:mol Si [*Mundy et al.*, 2014a].

The equations for dissolved nutrients in the water column are defined as

$$\begin{aligned} \frac{\partial}{\partial t} [NO_3] = & -(\mu_{p1}[P1] + \mu_{p2}[P2]) p_{no3} \frac{[NO_3]}{[NO_3] + [NH_4]} + \eta[NH_4] \\ & - \frac{D}{h_\nu} ([NO_3] - [NO_3]_{ia}) \delta_{z,z_1} + \frac{\partial}{\partial z} \left(K_z \frac{\partial [NO_3]}{\partial z} \right) \end{aligned} \quad (A.56)$$

$$\begin{aligned} \frac{\partial}{\partial t} [NH_4] = & -(\mu_{p1}[P1] + \mu_{p2}[P2]) \left(1 - p_{no3} \frac{[NO_3]}{[NO_3] + [NH_4]} \right) - \eta[NH_4] \\ & + M_{lz1}[Z1] + M_{lz2}[Z2] + R_{d1}[D1] + R_{d2}[D2] \\ & - \frac{D}{h_\nu} ([NH_4] - [NH_4]_{ia}) \delta_{z,z_1} + \frac{\partial}{\partial z} \left(K_z \frac{\partial [NH_4]}{\partial z} \right) \end{aligned} \quad (A.57)$$

$$\begin{aligned} \frac{\partial}{\partial t} [Si] = & -q_{si2n} \mu_{p2}[P2] + R_{bsi}[BSi] \\ & - \frac{D}{h_\nu} ([Si] - [Si]_{ia}) \delta_{z,z_1} + \frac{\partial}{\partial z} \left(K_z \frac{\partial [Si]}{\partial z} \right) \end{aligned} \quad (A.58)$$

where $[NO_3]$, $[NH_4]$, and $[Si]$ represent the concentrations of nitrate, ammonium, and silicate, respectively.

The first terms in Equations A.56 and A.57 represent the uptake by both small and large phytoplankton. The first term in Equation A.58 represents the uptake by large phyto-

plankton only, assuming an insignificant silicon uptake by small phytoplankton. Similarly to the nitrogen uptake by ice algae, the relative preference index for nitrate uptake is formulated as a function of ammonium concentration following *Denman* [2003]:

$$p_{no3} = \frac{v_n}{v_n + [NH_4]} \quad (\text{A.59})$$

The second terms in Equations A.56 and A.57 represent the nitrification, which is a source for nitrate and a sink for ammonium. The rate of nitrification depends on temperature [*Kawamiya et al.*, 1995] and is assumed to be photo-inhibited [*Aumont et al.*, 2015]:

$$\eta = \frac{r_{nit} \exp(b_{nit}[T])}{1 + [PAR]} \quad (\text{A.60})$$

where the rate constant (r_{nit}) and the temperature sensitivity coefficient (b_{nit}) for nitrification are set to 0.03 d^{-1} and $0.0693 \text{ (}^\circ\text{C)}^{-1}$ following *Kawamiya et al.* [1995].

The third and the fourth terms in Equation A.57 respectively represent the sources for ammonium due to linear mortality of small and large zooplankton. The fifth and the six terms in the same equation represent the sources due to remineralization of small and large detritus, respectively.

The second term in Equation A.58 represents the source for silicate due to remineralization of biogenic silica. The second last terms in Equations A.56, A.57, and A.58 represent the diffusive exchange of nutrients between the uppermost layer of the water column and the ice skeletal layer. The last terms in these equations represent the vertical mixing of dissolved nutrients between the model layers in the water column.

Lastly, for each of the living organisms (IA , $P1$, $P2$, $Z1$, and $Z2$), all the sink terms in the equation are neglected (i.e., set to zero) when its biomass is below its initial concentration in order to maintain its overwintering level.

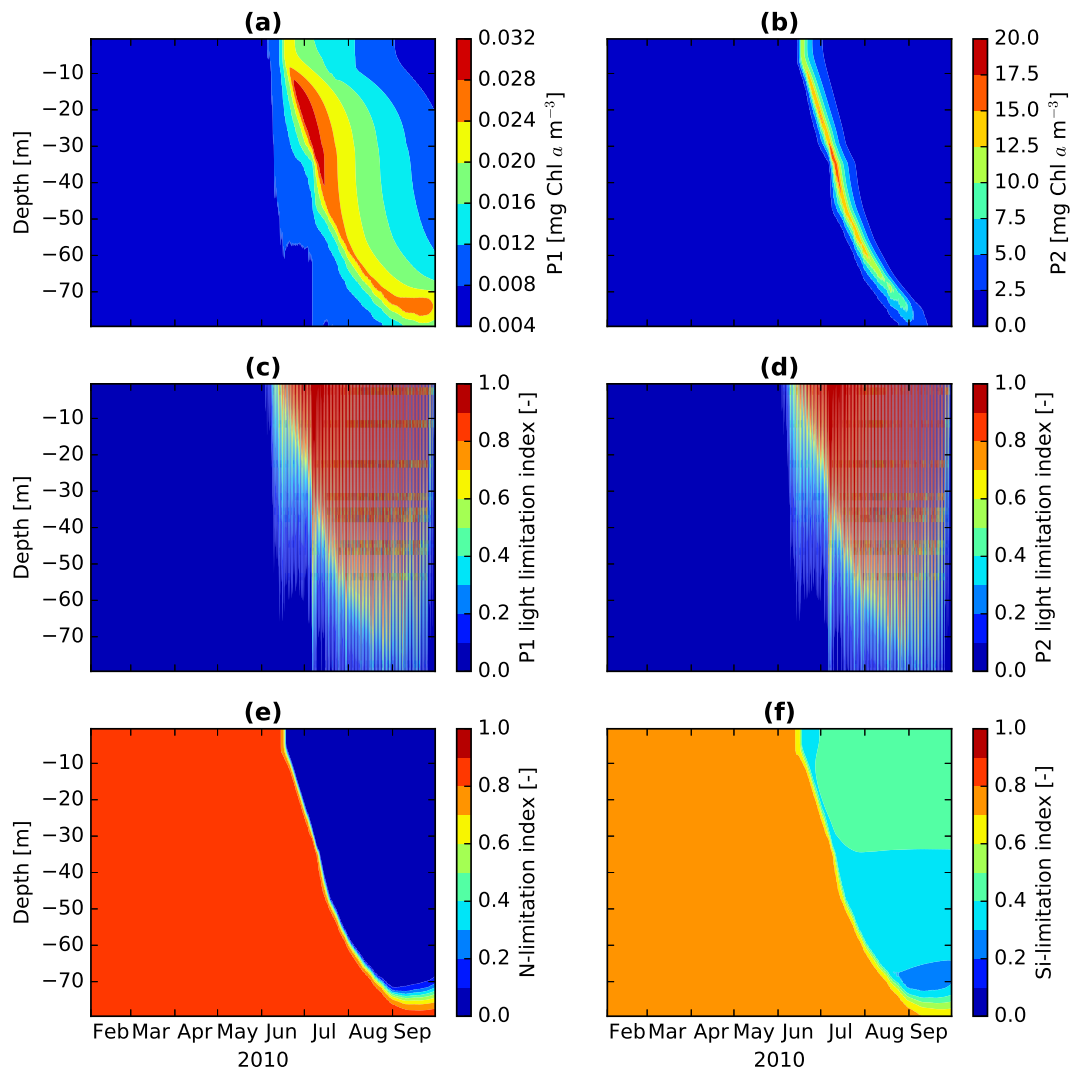


Figure A.1: P1, P2, and their light and nutrient limitations. Time series of simulated biomass of (a) P1 and (b) P2, light limitation index of (c) P1 and (d) P2, (e) nitrogen limitation index of P1 and P2, and (f) silicate limitation index of P2.

Table A.1: List of state variables in the coupled sea ice-ocean biogeochemical model.

Symbol	Description	Unit
$[IA]$	Ice algae in the bottom-ice skeletal layer	mmol N m^{-3}
$[NO_3]_{ia}$	Nitrate in the bottom-ice skeletal layer	mmol N m^{-3}
$[NH_4]_{ia}$	Ammonium in the bottom-ice skeletal layer	mmol N m^{-3}
$[Si]_{ia}$	Silicate in the bottom-ice skeletal layer	mmol Si m^{-3}
$[P1]$	Small phytoplankton in the water column	mmol N m^{-3}
$[P2]$	Large phytoplankton in the water column	mmol N m^{-3}
$[Z1]$	Small zooplankton in the water column	mmol N m^{-3}
$[Z2]$	Large zooplankton in the water column	mmol N m^{-3}
$[D1]$	Small detritus in the water column	mmol N m^{-3}
$[D2]$	Large detritus in the water column	mmol N m^{-3}
$[BSi]$	Biogenic silica in the water column	mmol Si m^{-3}
$[NO_3]$	Nitrate in the water column	mmol N m^{-3}
$[NH_4]$	Ammonium in the water column	mmol N m^{-3}
$[Si]$	Silicate in the water column	mmol Si m^{-3}

Table A.2: Parameters for the sea ice biogeochemical model.

Symbol	Description	Unit	Default value	Reference
α^{ia}/P_m^{ia}	Ratio of photosynthetic parameters (photosynthetic efficiency and maximum photosynthetic rate) for IA	$(\mu\text{mol photons m}^{-2} \text{s}^{-1})^{-1}$	0.44	Within the range of Lavoie et al. [2005a]
b_{ia}	Temperature sensitivity coefficient for ice algal growth	$(^\circ\text{C})^{-1}$	0.0633	Lavoie et al. [2005a]
C_{ice}	Critical ice growth/melt rate	m d^{-1}	0.015	Lavoie et al. [2005a]
C_{io}	Drag coefficient at the ice-ocean interface	-	0.0054	Shirasawa and Ingram [1997]
D	Molecular diffusivity for nutrients at the ice-water interface	$\text{m}^2 \text{s}^{-1}$	0.47×10^{-9}	Rebreanu et al. [2008]
f_{lia}	Fraction of ice algae linear mortality that goes to NH_4	-	0.3	This study
f_{seed}	Fraction of ice algae sloughing that contributes to P2 seeding	-	0.1	Lavoie et al. [2009]
k_n	Half-saturation constant for nitrogen uptake	mmol N m^{-3}	1	Lavoie et al. [2005a]
k_s	Half-saturation constant for silicon uptake	mmol Si m^{-3}	4	Lavoie et al. [2005a]
m_{lia}	Rate constant for ice algae linear mortality	d^{-1}	0.03	This study
m_{qia}	Rate constant of ice algae quadratic mortality	$\text{d}^{-1} (\text{mmol N m}^{-3} \text{d}^{-1})^{-1}$	0.00015	This study
μ_{ia}^{max}	Maximum specific ice algal growth rate	d^{-1}	0.85	Lavoie et al. [2005a]
q_{si2n}	Intracellular silicon-to-nitrogen ratio	$\text{mol Si}:\text{mol N}$	1.7	Mundy et al. [2014a]
r_{pond}	Melt pond drainage rate	m d^{-1}	0.0175	Taylor and Feltham [2004]
r_{nit}	Nitrification rate constant in sea ice	d^{-1}	0.01	This study
v_n	Scale factor for nitrogen preference function	mmol N m^{-3}	0.2	Denman [2003]
ν	Kinematic viscosity of seawater	$\text{m}^2 \text{s}^{-1}$	1.85×10^{-6}	Lavoie et al. [2005a]
z_{ia}	Thickness of the ice skeletal layer	m	0.03	This study
z_{oc}	Thickness of the ocean vertical grid	m	1	This study

Table A.3: Parameters for the ocean biogeochemical model.

Symbol	Description	Unit	Default value	Reference
a_1	Assimilated fraction of grazing by Z1	-	0.7	<i>Lavoie et al.</i> [2009]
a_2	Assimilated fraction of grazing by Z2	-	0.7	<i>Lavoie et al.</i> [2009]
α^{p1}/P_m^{p1}	Ratio of photosynthetic parameters (photosynthetic efficiency and maximum photosynthetic rate) for P1	$(\mu\text{mol photons m}^{-2} \text{ s}^{-1})^{-1}$	0.07	This study
α^{p2}/P_m^{p2}	Ratio of photosynthetic parameters (photosynthetic efficiency and maximum photosynthetic rate) for P2	$(\mu\text{mol photons m}^{-2} \text{ s}^{-1})^{-1}$	0.07	This study
b_{nit}	Temperature sensitivity coefficient for nitrification	$(^\circ\text{C})^{-1}$	0.0693	<i>Kawamiya et al.</i> [1995]
f_{d1}	Grazing preference on D1	-	0.5	<i>Monahan and Denman</i> [2004]
f_{d2}	Grazing preference on D2	-	0.5	<i>Lavoie et al.</i> [2009]
f_{z1}	Grazing preference on Z1	-	0.5	<i>Monahan and Denman</i> [2004]
γ_{z1}	Specific grazing rate of Z1	d^{-1}	1	This study
γ_{z2}	Specific grazing rate of Z2	d^{-1}	1	This study
k_{z1}	Half-saturation constant for Z1 grazing	mmol N m^{-3}	1	This study
k_{z2}	Half-saturation constant for Z2 grazing	mmol N m^{-3}	1	This study
m_{lp1}	Rate constant for P1 linear mortality	d^{-1}	0.03	This study
m_{lp2}	Rate constant for P2 linear mortality	d^{-1}	0.03	This study
m_{lz1}	Rate constant for Z1 linear mortality	d^{-1}	0.03	This study
m_{lz2}	Rate constant for Z2 linear mortality	d^{-1}	0.03	This study
m_{qp2}	Rate constant for P2 quadratic mortality	$\text{d}^{-1} (\text{mmol N m}^{-3} \text{ d}^{-1})^{-1}$	0.05	This study
m_{qz2}	Rate constant for Z2 quadratic mortality	$\text{d}^{-1} (\text{mmol N m}^{-3} \text{ d}^{-1})^{-1}$	0.1	This study
μ_{m1}^{max}	Maximum specific growth rate of P1	d^{-1}	0.5	<i>Steiner et al.</i> [2006a]
μ_{m2}^{max}	Maximum specific growth rate of P2	d^{-1}	2.0	<i>Steiner et al.</i> [2006a]
Q_{10p}	Q10 factor for phytoplankton	-	1.55	<i>Suzuki and Takahashi</i> [1995]
Q_{10z}	Q10 factor for zooplankton	-	2.14	<i>Buitenhuis et al.</i> [2006]
Q_{10b}	Q10 factor for bacteria	-	1.9	<i>Aumont et al.</i> [2015]
r_{d1}	Rate constant for D1 remineralization	d^{-1}	0.03	<i>Steiner et al.</i> [2006a]
r_{d2}	Rate for D2 remineralization	d^{-1}	0.3	<i>Lavoie et al.</i> [2009]
r_{bsi}	Rate constant for BSi remineralization	d^{-1}	0.01	This study
r_{n0}	Nitrification rate at 0 °C in seawater	d^{-1}	0.03	<i>Kawamiya et al.</i> [1995]
w_{d1}	D1 sinking rate	m d^{-1}	1	This study
w_{d2}	D2 sinking rate	m d^{-1}	50	<i>Lavoie et al.</i> [2009]

A.2 Additional information for Chapter 4

A.2.1 CanOE documentation

The following section is a draft of the CanOE documentation:

Christian, J.R., Denman, K.L., Lee, W.G., Riche, O.G.J., Steiner, N.S., and Swart, N. (in prep.): The Canadian Ocean Ecosystem Model (CanOE): a new ocean biogeochemistry model based on the NEMO modelling system.

The documentation is repeated here with permission of the lead author.

The Canadian Ocean Ecosystem Model (CanOE): a new ocean biogeochemistry model based on the NEMO modelling system

James R. Christian¹, Kenneth L. Denman², Warren G. Lee³, Olivier G.J. Riche², Nadja Steiner¹, Neil Swart³

1 Fisheries and Oceans Canada, Canadian Centre for Climate Modelling and Analysis, Victoria, BC, Canada

2 School of Earth and Ocean Sciences, University of Victoria, Victoria, BC, Canada

3 Environment and Climate Change Canada, Canadian Centre for Climate Modelling and Analysis, Victoria, BC, Canada

Introduction

The Canadian Ocean Ecosystem Model (CanOE) is a new ocean biogeochemistry module developed for the Canadian Earth System Model (CanESM, cf. Arora et al., 2011). It differs from the earlier Canadian Model of Ocean Carbon (CMOC; Zahariev et al., 2008) in having multiple functional groups of phytoplankton and zooplankton, flexible elemental ratios, prognostic iron and oxygen cycles, and prognostic calcification and denitrification. The overall computational cost is greater by about a factor of three (19 tracers vs. 6). CanOE has been implemented within the NEMO ocean modelling system, and CMOC has also been adapted to run within NEMO, so that we have several different biogeochemistry models to compare under identical circulation.

Among the more unsatisfactory aspects of CMOC in CanESM1 and CanESM2 was the excessive accumulation of nitrate beneath the Eastern Boundary Currents. This is a common failing of coarse-resolution ocean models (Moore and Doney, 2007). In CMOC it is exacerbated by the denitrification parameterization, which spreads nitrate loss over the ocean basins so that total N is conserved within each vertical column (total N_2 fixation and total denitrification are equal at each grid point where N_2 fixation occurs). CanOE has prognostic denitrification, but like CMOC it uses a parameterization of inputs of 'new' fixed N as function of temperature, irradiance and nutrients rather than an explicit N_2 -fixer functional group.

Another aspect of CMOC that is particularly unsatisfying is the parameterization of iron limitation as a static 'iron mask' based on the distribution of surface nitrate in the current climate. In order to implement a prognostic iron cycle with a minimum of additional tracers, CanOE has fixed C/N/Fe ratios in zooplankton and detritus and variable ratios only in phytoplankton. Detrital particulate iron, iron speciation, and the concentrations of the ligands that keep iron in solution are not explicitly represented. There are only three iron-based tracers: dissolved iron and small and large phytoplankton iron.

CanESM1 and CanESM2 also did not simulate dissolved oxygen. While it is straightforward to include oxygen (the biological sources and sinks are essentially those of DIC multiplied by -1 and solubility is well constrained), it was excluded due to limitations of processing capacity. The new NEMO version of CMOC reproduces exactly the original CanESM1/2 version in most respects, but also includes oxygen, which can be characterized as a 'downstream' tracer with no feedbacks to biology (e.g., effects on denitrification are neglected). Including oxygen further permits us to incorporate prognostic representations of processes like denitrification in CanOE, that were neglected in CMOC.

Model description

The NEMO modelling system is a publicly available archive of codes based on the OPA (Océan PARallelisé) ocean model (Madec and Imbard, 1996; Guilyardi and Madec, 1997). It comes with

two options for biogeochemistry: PISCES (Pelagic Interactions Scheme for Carbon and Ecosystem Studies) and LOBSTER (LODyC Ocean Biogeochemical System for Ecosystem and Resources). CanOE and the NEMO implementation of CMOC are built around the basic code structure of PISCES, using NEMO v3.4.1.

The biology, carbon chemistry, gas exchange and light attenuation have all been modified to various degrees; in a few cases PISCES parameterizations or a slightly modified version of these were adopted. CanOE uses PISCES three-band attenuation while NEMO-CMOC uses broadband (PAR) attenuation for consistency with the published version of CMOC. Carbon chemistry was modified to be consistent with the Best Practices Guide (Dickson et al., 2007). All calculations are done on the total scale and the recommended formulae for the equilibrium constants employed. The PISCES conventions for convergence of carbon chemistry calculations were retained, i.e., a greater number of iterations in the surface layer offers greater accuracy in calculating $p\text{CO}_2$ and gas exchange, while in subsurface layers the number of iterations is fixed at five (in subsurface layers the only function of the carbon chemistry is to calculate burial of calcite in the sediments). NEMO-CMOC uses the same carbon chemistry as CanOE but does not solve the carbon chemistry equations in the subsurface layers.

The biology model is a substantially new model based on the cellular regulation model of Geider et al. (1998). Each phytoplankton functional group has four state variables: carbon, nitrogen, iron and chlorophyll. Photosynthesis is decoupled from cell production and photosynthetic rate is a function of the cell's internal N and Fe quotas. Each functional group has a specified minimum

and maximum N quota and Fe quota, and nutrient uptake ceases when the maximal cell quota is reached. Chlorophyll synthesis is a function of nitrogen uptake and increases at low irradiance. Model parameters and their values are listed in Table 1.

2.1 Photosynthesis and phytoplankton growth

For simplicity and clarity, the equations are shown here for single phytoplankton species, and do not differ structurally for small and large phytoplankton. Some parameter values differ for the two phytoplankton groups; all parameter values are listed in Table 1.

Temperature dependence of photosynthetic activity is expressed by the Arrhenius equation

$$T_f = \exp\left(-\frac{E_a}{R}\left(\frac{1}{T} - \frac{1}{T_{ref}}\right)\right) \quad (1)$$

where E_a is an enzyme activation energy that corresponds approximately to that of RuBisCo (cf. Raven and Geider 1988), R is the gas constant ($8.314 \text{ J mol}^{-1} \text{ K}^{-1}$), and temperature T and reference temperature T_{ref} are in Kelvin. Maximal rates of nutrient uptake are given by

$$V_{\max}^X = V_{ref}^X T_f \left(\frac{Q_{\max}^X - Q^X}{Q_{\max}^X - Q_{\min}^X}\right)^{0.05} \quad (2)$$

where V_{max}^X is the maximal uptake rate in mg of nutrient X per mg of cell C, X can represent N or Fe, Q is the nutrient cell quota and Q_{min} and Q_{max} its minimum and maximum values, and V_{ref}^X is a (specified) basal rate at $T=T_{ref}$ and $Q=Q_{min}$. These maximum rates are then reduced according to the ambient nutrient concentration, i.e.

$$V^N = V_{max}^N (L_{NH4} + (1 - L_{NH4})L_{NO3}) \quad (3a)$$

where $L_{NH4} = \frac{N_a}{K_{NH4} + N_a}$ and $L_{NO3} = \frac{N_i}{K_{NO3} + N_i}$, with N_i and N_a indicating nitrate and ammonium respectively, and

$$V^{Fe} = V_{max}^{Fe} \left(\frac{Fe}{K_{Fe} + Fe} \right) \quad (3b)$$

The maximal carbon based growth rate is given by

$$P_{max}^C = P_{ref}^C T_f \min \left\{ \frac{Q^N - Q_{min}^N}{Q_{max}^N - Q_{min}^N}, \frac{Q^{Fe} - Q_{min}^{Fe}}{Q_{max}^{Fe} - Q_{min}^{Fe}} \right\} \quad (4)$$

where P_{ref}^C is the rate at the reference temperature T_{ref} under nutrient-replete conditions ($Q=Q_{max}$). The light-limited growth rate is then given by

$$P_{phot}^C = P_{max}^C \left(1 - e^{-\alpha_{chl} E \theta / P_{max}^C} \right) \quad (5)$$

where θ is the chlorophyll-to-carbon ratio. The rate of chlorophyll synthesis is

$$\rho_{chl} = \theta_{max}^N \frac{P_{phot}^C}{E \alpha_{chl} \theta} \quad (6)$$

These rates are then used to define a set of state equations for phytoplankton carbon (C_p), nitrogen (N_p), iron (Fe_p), and chlorophyll (M).

$$\frac{dC_p}{dt} = (P^C_{phot} - \zeta V_N) C_p - (G + C_{XS}) - m_1 C_p - m_2 C_p^2 - k_{XU} C_{INTR} \quad (7)$$

where ζ is the respiratory cost of biosynthesis, G is the grazing rate (see Eq. 12), C_{XS} is the excess (above the ratio in grazer biomass) carbon in grazing losses, C_{INTR} is the concentration of intracellular carbohydrate carbon in excess of biosynthetic requirements, and k_{XU} is a rate coefficient for its exudation to the environment.

$$\frac{dN_p}{dt} = \frac{V^N}{Q_N} - (G + m_1 C_p + m_2 C_p^2) R_{NC} - N_{XS} \quad (8)$$

$$\frac{dFe_p}{dt} = \frac{V^{Fe}}{Q_{Fe}} - (G + m_1 C_p + m_2 C_p^2) R_{FeC} - Fe_{XS} \quad (9)$$

$$\frac{dM}{dt} = \frac{\rho_{chi} V^N}{\theta_C} M - (G + m_1 C_p + m_2 C_p^2) \theta_C - k_{dgr} M \quad (10)$$

where k_{dgr} is a rate coefficient for nonspecific losses of chlorophyll e.g., by photooxidation, in addition to losses to grazing and other processes that also affect C_p , N_p , and Fe_p . N_{XS} and Fe_{XS} are remineralization of "excess" (relative to grazer or detritus ratios) N or Fe and are defined below (Eq. 16).

2.2 Grazing and food web interactions

Grazing rate depends on the phytoplankton carbon concentration, which most closely represents the food concentration available to the grazer (Elser and Urabe 1999; Loladze et al. 2000).

Zooplankton biomass is also in carbon units. State equations for small and large zooplankton are

$$\frac{dZ_s}{dt} = \lambda G_s - (R + G_Z + m_1 Z_s + m_2 Z_s^2) \quad (11a)$$

$$\frac{dZ_l}{dt} = \lambda G_l - (R + m_1 Z_l + m_2 Z_l^2) \quad (11b)$$

where

$$G_s = G_{s0} (1 - e^{-a_s C_{ps}}) Z_s \quad (12a)$$

$$G_l = G_{l0} (1 - e^{-a_l (C_{pl} + Z_s)}) Z_l \quad (12b)$$

for small and large zooplankton respectively, G_Z is grazing of small zooplankton by large zooplankton, R is respiration, and m_1 and m_2 are nongrazing mortality rates. Large zooplankton grazing is divided into grazing on large phytoplankton and small zooplankton in proportion to the relative abundances of each

$$G_p = G_l \frac{P_l}{P_l + Z_s} \quad (13a)$$

$$G_z = G_l \frac{Z_s}{P_l + Z_s} \quad (13b)$$

Zooplankton biomass loss to respiration is given by

$$R = \max\{r_2 T_f Z - C_{XS}, 0\} \quad (14)$$

Respiration (R) is assumed to consume only carbon and not result in catabolism of existing biomass when “excess” carbon is available in the prey. In addition, conservation of mass must be maintained by recycling to the dissolved pool grazer consumption in excess of biosynthetic requirements when prey elemental ratios differ from the predator’s. This is very straightforward in the case where the nutrient quota (relative to carbon) exceeds the grazer fixed ratio: the excess nutrient is remineralized to the dissolved inorganic pool. However, in the case where the nutrient quota is less than the grazer ratio, the grazer intake is reduced to what can be supported by the least abundant nutrient (relative to the grazer biomass ratio) and excess carbon is remineralized. For the case of two nutrients (in this case N and Fe) it is necessary to define

$$G' = G \min\left(\frac{N_p}{C_p} R_{CN}, \frac{Fe_p}{C_p} R_{CFe}, 1\right) \quad (15)$$

where G is equal to G_S (equation 12a) for small zooplankton and G_P (equation 13a) for large zooplankton, and R_{XY} indicates the fixed ratio of element X to element Y in grazer biomass. The 'excess' carbon available for respiration is

$$C_{XS} = G' \max\left(\frac{C_p}{N_p} R_{NC} - 1, \frac{C_p}{Fe_p} R_{FeC} - 1, 0\right) \quad (16a)$$

and the excess nutrients remineralized to their inorganic pools are

$$N_{XS} = G' \max\left(\frac{N_p}{C_p} - R_{NC}, 0\right) + G' \max\left(R_{NC} \left(\frac{N_p}{Fe_p} R_{FeN} - 1\right), 0\right) \quad (16b)$$

$$Fe_{XS} = G' \max\left(\frac{Fe_p}{C_p} - R_{FeC}, 0\right) + G' \max\left(R_{FeC} \left(\frac{Fe_p}{N_p} R_{NFe} - 1\right), 0\right) \quad (16c)$$

For three elements there are six (3!) possible cases: for nitrogen greater or less than $C_p R_{NC}$, iron may be either in excess relative to both C and N, deficient relative to both, or in excess relative to one but not the other. The second terms in equations 16b and 16c allow e.g. remineralization of Fe when it is in excess relative to N but deficient relative to C, with the total intake determined by the element least abundant relative to the grazer biomass ratios. In all of these cases the second term in at least one of equations 16b and 16c is nonzero; one or both of the first terms are nonzero except when both N and Fe are deficient relative to carbon (Table 2).

2.3 Organic and inorganic pools

There are two pools of detritus with different sinking rates but the same fixed elemental ratios. Detrital C/N/Fe ratios are the same as zooplankton, so zooplankton mortality or grazing of small zooplankton by large zooplankton produce no 'excess'. Phytoplankton mortality and defecation by zooplankton grazing on phytoplankton produces excess nutrient or excess carbon that needs to be recycled into the inorganic pool in a similar fashion as outlined above for the assimilated fraction of grazing on phytoplankton.

The conservation equations for detrital C are

$$\frac{dD_s}{dt} = m_1(C_{ps} + Z_s) + m_2(C_{ps}^2 + Z_s^2) - r_1 D_s T_g - w_s \frac{dD_s}{dz} \quad (17a)$$

$$\frac{dD_l}{dt} = m_1(C_{pl} + Z_l) + m_2(C_{pl}^2 + Z_l^2) - r_2 D_l T_g - w_l \frac{dD_l}{dz} \quad (17b)$$

where T_g is an Arrhenius function for temperature dependence of remineralization and w is the sinking speed. The conservation equations for inorganic C, N, and Fe are

$$\frac{dC_i}{dt} = (\zeta V^N - P_{phot}^C) C_p + R + C_{XS} + (r_1 D_s + r_2 D_l) T_g \quad (18a)$$

$$\frac{dN_i}{dt} = -\frac{V^N}{Q^N} N_p \left(\frac{L_{NO_3}}{L_{NO_3} + L_{NH_4}} \right) + N_{ox} - N_{dentr} \quad (18b)$$

$$\frac{dN_a}{dt} = -\frac{V^N}{Q^N} N_p \left(\frac{L_{NH_4}}{L_{NO_3} + L_{NH_4}} \right) + \frac{R}{R_{CN}} + N_{XS} + (r_1 D_s + r_2 D_l) R_{NC} T_g - N_{ox} + N_{dnf} \quad (18c)$$

$$\frac{dFe}{dt} = \frac{V^{Fe}}{Q^{Fe}} Fe_p + \frac{R}{R_{CFe}} + Fe_{XS} + (r_1 D_s + r_2 D_l) R_{FeC} T_g \quad (18d)$$

where N_{ox} is microbial oxidation of ammonium to nitrate (nitrification) and N_{dnf} and N_{dentr} are sources and sinks associated with dinitrogen fixation and denitrification. The oxygen equation is essentially the inverse of equation 18a, with additional terms for oxidation and reduction of N, i.e.,

$$\frac{dO_2}{dt} = -\frac{dC_i}{dt} + 2 \frac{V^N}{Q^N} N_p \left(\frac{L_{NO_3}}{L_{NO_3} + L_{NH_4}} \right) - 2N_{ox} \quad (19)$$

Nitrification is given by

$$N_{ox} = k_{NH_4ox} N_a \frac{1}{1 + E(z)} \quad (20)$$

where $E(z)$ is the layer mean irradiance at depth z . Dinitrogen fixation is parameterized as an external input of ammonium dependent on light, temperature and Fe availability, and inhibited by high ambient concentrations of inorganic N.

$$N_{dnf} = k_{dnf} T_{dnf} \left(1 - e^{-aE}\right) \left(\frac{Fe}{K_{Fe} + Fe}\right) \left(\frac{K_{NO3}}{K_{NO3} + N_i + N_a}\right) \quad (21)$$

Denitrification is parameterized as a fraction of total remineralization that increases as a linear function of oxygen concentration for concentrations less than a threshold concentration O_{msd}

$$N_{frxn} = 1 - \frac{\min(O_2, O_{msd})}{O_{msd}} \quad (22)$$

Remineralization is then divided among oxygen ($1 - N_{frxn}$), nitrate ($0.85N_{frxn}$), and ammonium ($0.15N_{frxn}$) assuming an average annamox contribution of 30% (Babbín et al., 2014).

2.4 Calcification, calcite dissolution, and alkalinity

Calcification is represented in a fashion similar to PISCES, with a detrital CaCO_3 state variable but no explicit calcifier groups. Detrital CaCO_3 sinks in the same fashion as POC, with its own sinking rate that is independent of those for both large and small organic detritus. Calcite production is represented as a fixed fraction of POC production from small phytoplankton and small zooplankton mortality. Calcite dissolution occurs throughout the water column as a first order process (i.e., no dependence on temperature or saturation state). Approximately 80% of calcite produced is exported from the euphotic zone. Burial in the sediments is represented as a simple 'on/off' switch dependent on the calcite saturation state (zero when $\Omega_C < 1$ and 1 when $\Omega_C \geq 1$).

For each mole of calcite production two moles of alkalinity equivalent are lost from the dissolved phase; the reverse occurs during calcite dissolution. There are additional sources and sinks for alkalinity associated with phytoplankton nutrient uptake, organic matter remineralization, nitrification, denitrification and dinitrogen fixation (Table 3; see also Wolf-Gladrow et al., 2007). The annamox reaction does not in itself contribute to alkalinity (Jetten et al., 2001); there is a sink associated with ammonium oxidation to nitrite that offsets the gain from dinitrogen fixation (the model does not distinguish between nitrite and nitrate). The sources and sinks offset each other such that there is no net gain or loss as long as the global fixed N pool is conserved. If dinitrogen fixation and denitrification are allowed to vary freely there will generally be a net gain or loss of fixed N and therefore of alkalinity.

References

- Arora, V., J. Scinocca, G. Boer, J. Christian, K. Denman, G. Flato, V. Kharin, W. Lee, and W. Merryfield (2011), Carbon emission limits required to satisfy future representative concentration pathways of greenhouse gases, *Geophysical Research Letters*, 38, doi:10.1029/2010GL046270
- Babbin, A., R. Keil, A. Devol, and B. Ward (2014), Organic Matter Stoichiometry, Flux, and Oxygen Control Nitrogen Loss in the Ocean, *Science*, 344, 406-408.
- Christian, J. (2005), Biogeochemical cycling in the oligotrophic ocean: Redfield and non-Redfield models, *Limnology and Oceanography*, 50, 646-657.
- Christian, J., et al. (2010), The global carbon cycle in the Canadian Earth system model (CanESM1): Preindustrial control simulation, *Journal of Geophysical Research-Biogeosciences*, 115, doi:10.1029/2008JG000920

Elser, J., and J. Urabe (1999), The stoichiometry of consumer-driven nutrient recycling: Theory, observations, and consequences, *Ecology*, 80(3), 735-751.

Geider, R., H. MacIntyre, and T. Kana (1998), A dynamic regulatory model of phytoplanktonic acclimation to light, nutrients, and temperature, *Limnology and Oceanography*, 43, 679-694.

Guilyardi, E., and G. Madec (1997), Performance of the OPA/ARPEGE-T21 global ocean-atmosphere coupled model, *Climate Dynamics*, 13, 149-165.

Jetten, M., M. Wagner, J. Fuerst, M. van Loosdrecht, G. Kuenen, and M. Strous (2001), Microbiology and application of the anaerobic ammonium oxidation ('anammox') process, *Current Opinion in Biotechnology*, 12, 283-288.

Loladze, I., Y. Kuang, and J. Elser (2000), Stoichiometry in producer-grazer systems: Linking energy flow with element cycling, *Bulletin of Mathematical Biology*, 62, 1137-1162.

Madec, G., and M. Imbard (1996), A global ocean mesh to overcome the North Pole singularity, *Climate Dynamics*, 12, 381-388.

Moore, J., and S. Doney (2007), Iron availability limits the ocean nitrogen inventory stabilizing feedbacks between marine denitrification and nitrogen fixation, *Global Biogeochemical Cycles*, 21, doi:10.1029/2006GB002762.

Raven, J., and R. Geider (1988), Temperature and algal growth, *New Phytologist*, 110, 441-461.

Wolf-Gladrow, D., R. Zeebe, C. Klaas, A. Kortzinger, and A. Dickson (2007), Total alkalinity: The explicit conservative expression and its application to biogeochemical processes, *Marine Chemistry*, 106, 287-300.

Zahariev, K., J. Christian, and K. Denman (2008), Preindustrial, historical, and fertilization simulations using a global ocean carbon model with new parameterizations of iron limitation, calcification, and N₂ fixation, *Progress in Oceanography*, 77, 56-82.

Table 1 – Ecosystem model parameters.

Symbol	Description	Unit	
T_{ref}	Reference temperature	K	298.15
E_a	Activation energy for phytoplankton Arrhenius function	kJ mol^{-1}	37.4
Q_{mins}^N	Small phytoplankton minimum N quota	g N g C^{-1}	0.04
Q_{maxs}^N	Small phytoplankton maximum N quota	g N g C^{-1}	0.172
Q_{minl}^N	Large phytoplankton minimum N quota	g N g C^{-1}	0.04
Q_{maxl}^N	Large phytoplankton maximum N quota	g N g C^{-1}	0.172
Q_{mins}^{Fe}	Small phytoplankton minimum Fe quota	$\mu\text{g Fe g C}^{-1}$	4.65
Q_{maxs}^{Fe}	Small phytoplankton maximum Fe quota	$\mu\text{g Fe g C}^{-1}$	93.08
Q_{minl}^{Fe}	Large phytoplankton minimum Fe quota	$\mu\text{g Fe g C}^{-1}$	4.65
Q_{maxl}^{Fe}	Large phytoplankton maximum Fe quota	$\mu\text{g Fe g C}^{-1}$	69.81
V_{ref}^N	Reference rate of N uptake	$\text{g N g C}^{-1} \text{d}^{-1}$	0.6
V_{ref}^{Fe}	Reference rate of Fe uptake	$\mu\text{g Fe g C}^{-1} \text{d}^{-1}$	79.28
P_{ref}^C	Reference rate of photosynthesis	$\text{g C g C}^{-1} \text{d}^{-1}$	3
k_{XU}	Rate coefficient for exhudation	d^{-1}	0.8
k_{dgr}	Rate coefficient for chlorophyll degradation	d^{-1}	0.02
ζ	Respiratory cost of biosynthesis	g C g N^{-1}	2
α_{chl}	Initial slope of P-E curve	$(\text{g C g CHL}^{-1} \text{h}^{-1})$	0.045
K_{NIS}	Half-saturation for small phytoplankton nitrate uptake	$\text{mmol}^{-1} \text{m}^3$	0.1
K_{NaS}	Half-saturation for small phytoplankton ammonium uptake	$\text{mmol}^{-1} \text{m}^3$	0.05
K_{FeS}	Half-saturation for small phytoplankton iron uptake	$\text{nmol}^{-1} \text{m}^3$	100
K_{NiL}	Half-saturation for large phytoplankton nitrate uptake	$\text{mmol}^{-1} \text{m}^3$	0.5
K_{NaL}	Half-saturation for large phytoplankton ammonium uptake	$\text{mmol}^{-1} \text{m}^3$	0.05

K_{FeL}	Half-saturation for large phytoplankton iron uptake	$\text{nmol}^{-1} \text{m}^3$	200
m_{1S}	Small phytoplankton mortality rate (linear)	d^{-1}	0.05
m_{2L}	Small phytoplankton mortality coefficient (quadratic)	$\text{mmol}^{-1} \text{C m}^3 \text{d}^{-1}$	
m_{1L}	Large phytoplankton mortality rate (linear)	d^{-1}	0.05
m_{2L}	Large phytoplankton mortality coefficient (quadratic)	$\text{mmol}^{-1} \text{C m}^3 \text{d}^{-1}$	
a_L	Large zooplankton grazing parameter	$(\text{mmol C m}^{-3})^{-1}$	
G_{L0}	Large zooplankton maximum grazing rate	d^{-1}	
a_S	Small zooplankton grazing parameter	$(\text{mmol C m}^{-3})^{-1}$	
G_{S0}	Small zooplankton maximum grazing rate	d^{-1}	
λ	Assimilation efficiency	n.d.	0.8
r_z	Zooplankton specific respiration rate at T_{ref}	d^{-1}	0.05
r_{DS}	Small detritus remineralization rate at T_{ref}	d^{-1}	0.25
r_{DL}	Large detritus remineralization rate at T_{ref}	d^{-1}	0.25

Table 2 - Cases where the 'excess' terms are nonzero. These terms are always greater than or equal to zero, and always zero when the phytoplankton elemental ratio is equal to the grazer biomass ratio. A + indicates cases where a specific term is positive. N_1 and N_2 and Fe_1 and Fe_2 indicate the first and second terms in equations 15b and 15c. R_{NC} is the grazer N/C (Redfield) ratio.

	Fe in excess relative to both C and N					Fe in excess relative to C or N but not both					Fe deficient relative to both C and N				
	C	N_1	N_2	Fe_1	Fe_2	C	N_1	N_2	Fe_1	Fe_2	C	N_1	N_2	Fe_1	Fe_2
$N/C > R_{NC}$		+		+	+		+	+	+		+	+	+		
$N/C < R_{NC}$	+			+	+	+				+	+		+		

Table 3 - Alkalinity sources and sinks associated with nitrogen cycle processes in moles of alkalinity equivalent per mole of N. Positive value indicates alkalinity source.

Process	Alkalinity source/sink
Phytoplankton NH_4 uptake	-1
Phytoplankton NO_3 uptake	+1
Organic N remineralization	+1
N_2 fixation	+1
Nitrification (NH_4 oxidation to NO_3)	-2
Denitrification	+1
Annamox	0

Table A.4: Prescribed annual-mean river-flow concentrations of biogeochemical variables at the 6 major Arctic rivers in the model simulation.

Variable	Mackenzie	Yukon	Kolyma	Lena	Yenisey	Ob'
DIC (mmol C m ⁻³)	1717	1792	642	817	908	1175
DOC (mmol C m ⁻³)	368	544	592	841	611	785
DIC+DOC (mmol C m ⁻³)	2085	2336	1234	1658	1519	1955
TA (mmol C m ⁻³)	1540	1707	449	788	845	1181
DON (mmol N m ⁻³)	7.1	14.2	7.2	14.4	14.2	7.1
NO ₃ (mmol N m ⁻³)	7.1	7.1	3.6	3.6	7.1	7.1

A.2.2 Meteorological forcing and ocean boundary conditions

All model simulations were forced at the surface using a prescribed meteorology based on the Drakkar Forcing Set 5.2 [DFS; *Dussin et al.*, 2016]. The meteorological variables were precipitation (snow and total), temperature and humidity at 2m above sea surface, short and longwave radiation, and zonal and meridional velocities at 10m. The DFS data are on a 0.7° grid with a time resolution of 3 hours for all meteorological variables except for precipitation and radiation, which had a daily time resolution. For the spinup period (1969 – 1979), precipitation data were not available, so for this period 1979 data was repeated every year over that time period.

Physical oceanographic variables (temperature, salinity, and horizontal currents) were initialized in 1969 based on Ocean Reanalysis System 4 [ORAS4; *Balmaseda and Weaver*, 2013]. The physical oceanographic variables were prescribed for the open ocean boundaries using interannual monthly-mean fields, also based on ORAS4. Relaxation time-scale for all variables was set to 1 day for inflow and 15 days for outflow following *Dupont et al.* [2015]. The fields for biogeochemical variables (NO₃, DIC, and TA) at the boundaries, as well as initialization, are based on climatological GLObal Ocean Data Analysis Project version 2 (GLODAP) data [*Lauvset et al.*, 2016]. Ecosystem functional groups were initialized at arbitrarily low values, as the time of initialization (January 1969) was at a biologically inert time of year.

Lastly, the river flow was prescribed based on the monthly mean annually-varying product of *Dai et al.* [2009] up to 2007. From 2007 – 2015, river flow from the year 2007 is repeated annually. Biogeochemical concentrations for river flow (DIC, TA, and NO₃) are based on *Cooper et al.* [2008]; *Tank et al.* [2012]; *Holmes et al.* [2012]; *McClelland et al.* [2012], for each of the six respective major Arctic rivers (the MacKenzie and Yukon Rivers in North America, and, from east to west, the Kolima, Lena, Yenisey, and Ob' Rivers out of Eurasia). Organic and inorganic nutrients were combined at the time of outflow. For carbon, the organic and inorganic concentrations for each river were prescribed by the

above sources for biogeochemical concentrations. For nitrogen, the organic concentration was assumed based on the DIN:DON ratio prescribed in CanOE. River-flow concentrations for all rivers are given in Table A.4.

A.2.3 Regional trends in carbonate system surface properties/fluxes

This section includes tables highlighting trends in the pan-Arctic mean and six regions with substantial deviations from the pan-Arctic mean for the following variables relevant to sea surface carbon system properties and to air-sea flux of carbon: pH, sea surface pCO₂, mean carbon flux, Ω_{arag} and Ω_{calc} , and ice coverage.

Table A.5: Changes to pH over the standard run. The initial value is the mean of the first half-decade (1981 – 1985), the final value is the mean of the last half-decade (2010 – 2015), the difference, percent difference, and difference/decade are between initial and final decadal means.

Region	Initial	Final	Difference	% Diff.	Diff./decade
pan-Arctic	8.09	8.02	-0.07	-0.89	-0.02
Can. Polar Shelf	8.17	8.07	-0.1	-1.26	-0.03
S. Beaufort	8.04	7.95	-0.09	-1.13	-0.03
N. Beaufort	8.07	7.99	-0.08	-0.94	-0.02
Laptev	7.97	7.92	-0.06	-0.7	-0.02
Barents	8.15	8.08	-0.07	-0.85	-0.02
Norwegian	8.13	8.06	-0.06	-0.8	-0.02

Table A.6: Changes to sea surface pCO₂ (μatm) over the standard run. Headings are the same as in Table A.5

Region	Initial	Final	Difference	% Diff.	Diff./decade
pan-Arctic	299	354	55	17	18
Can. Polar Shelf	263	329	66	22	21
S. Beaufort	318	384	66	19	21
N. Beaufort	296	345	49	15	16
Laptev	368	409	41	11	13
Barents	283	336	54	17	17
Norwegian	299	351	52	16	17

Table A.7: Changes to air-sea flux of CO₂ ($\text{mg C m}^{-2} \text{ year}^{-1}$, positive is into the ocean) over the standard run. Headings are the same as in Table A.5

Region	Initial	Final	Difference	% Diff.	Diff./decade
pan-Arctic	9.25	11.04	1.79	17.7	0.58
Can. Polar Shelf	14.09	13.33	-0.76	-5.56	-0.25
S. Beaufort	3.77	3.49	-0.28	-7.72	-0.09
N. Beaufort	3.11	4.21	1.1	30.03	0.35
Laptev	2.49	2.65	0.17	6.43	0.05
Barents	25.7	29.39	3.69	13.39	1.19
Norwegian	20.53	25.23	4.7	20.55	1.52

Table A.8: Changes to sea surface Ω_{arag} over the standard run. Headings are the same as in Table A.5

Region	Initial	Final	Difference	% Diff.	Diff./decade
pan-Arctic	1.22	1.06	-0.16	-13.81	-0.05
Can. Polar Shelf	1.5	1.18	-0.32	-23.66	-0.1
S. Beaufort	0.91	0.75	-0.16	-19.79	-0.05
N. Beaufort	0.97	0.8	-0.17	-19.01	-0.05
Laptev	0.75	0.68	-0.07	-9.46	-0.02
Barents	1.68	1.51	-0.18	-11.12	-0.06
Norwegian	1.65	1.48	-0.17	-10.64	-0.05

Table A.9: Changes to sea surface Ω_{calc} over the standard run. Headings are the same as in Table A.5

Region	Initial	Final	Difference	% Diff.	Diff./decade
pan-Arctic	1.95	1.7	-0.25	-13.93	-0.08
Can. Polar Shelf	2.41	1.9	-0.51	-23.66	-0.16
S. Beaufort	1.48	1.21	-0.27	-19.91	-0.09
N. Beaufort	1.56	1.29	-0.27	-19.01	-0.09
Laptev	1.22	1.11	-0.11	-9.88	-0.04
Barents	2.68	2.39	-0.28	-11.22	-0.09
Norwegian	2.62	2.36	-0.27	-10.76	-0.09

Table A.10: Changes to ice coverage (% of total area) over the standard run. Headings are the same as in Table A.5

Region	Initial	Final	Difference	% Diff.	Diff./decade
pan-Arctic	0.7	0.63	-0.07	-11.08	-0.02
Can. Polar Shelf	0.59	0.55	-0.03	-5.64	-0.01
S. Beaufort	0.78	0.64	-0.14	-19.3	-0.04
N. Beaufort	0.92	0.87	-0.04	-4.77	-0.01
Laptev	0.82	0.7	-0.12	-16.37	-0.04
Barents	0.32	0.21	-0.1	-38.99	-0.03
Norwegian	0.23	0.17	-0.07	-33.37	-0.02

Bibliography

- Abraham, C., N. S. Steiner, A. Monahan, and C. Michel (2015), Effects of subgrid-scale snow thickness variability on radiative transfer in sea ice, *Journal of Geophysical Research : Oceans*, *120*, 5597–5614, doi:10.1002/2015JC010741.
- Arrigo, K. R. (2014), Sea ice ecosystems, *Annual Review of Marine Science*, *6*(1), 439–467, doi:10.1146/annurev-marine-010213-135103.
- Arrigo, K. R. (2017), Sea ice as a habitat for primary producers, in *Sea Ice*, edited by D. N. Thomas, 3 ed., pp. 352–369, John Wiley, Hoboken, NJ, doi:10.1002/9781118778371.ch14e.
- Arrigo, K. R., and C. W. Sullivan (1994), A high resolution bio-optical model of microalgal growth: Tests using sea-ice algal community time-series data, *Limnology and Oceanography*, *39*(3), 609–631, doi:10.4319/lo.1994.39.3.0609.
- Arrigo, K. R., S. Pabi, G. L. Van Dijken, and W. Maslowski (2010), Air-sea flux of CO₂ in the Arctic Ocean, 1998–2003, *Journal of Geophysical Research: Biogeosciences*, *115*(4), 1998–2003, doi:10.1029/2009JG001224.
- Aumack, C. F., and A. R. Juhl (2015), Light and nutrient effects on the settling characteristics of the sea ice diatom *Nitzschia frigida*, *Limnology and Oceanography*, *60*(3), 765–776, doi:10.1002/lno.10054.
- Aumont, O., C. Ethé, A. Tagliabue, L. Bopp, and M. Gehlen (2015), PISCES-v2: an ocean biogeochemical model for carbon and ecosystem studies, *Geoscientific Model Development*, *8*(8), 2465–2513, doi:10.5194/gmd-8-2465-2015.
- Balmaseda, M. A., and A. T. Weaver (2013), Evaluation of the ECMWF ocean reanalysis system ORAS4, *Quarterly Journal of the Royal Meteorological Society*, *139*(July), 1132–1161, doi:10.1002/qj.2063.
- Barber, D. G., H. Hop, C. J. Mundy, B. Else, I. A. Dmitrenko, J.-E. Tremblay, J. K. Ehn, P. Assmy, M. Daase, L. M. Candlish, and S. Rysgaard (2015), Selected physical,

- biological and biogeochemical implications of a rapidly changing Arctic Marginal Ice Zone, *Progress in Oceanography*, 139, 122–150, doi:10.1016/j.pocean.2015.09.003.
- Bates, N. R., and J. T. Mathis (2009), The Arctic Ocean marine carbon cycle: evaluation of air-sea CO₂ exchanges, ocean acidification impacts and potential feedbacks, *Biogeochemistry*, 6(4), 2433–2459, doi:10.5194/bgd-6-6695-2009.
- Bednaršek, N., G. A. Tarling, D. C. E. Bakker, S. Fielding, and R. A. Feely (2014), Dissolution dominating calcification process in polar pteropods close to the point of aragonite undersaturation, *PLOS ONE*, 9(10), 1–14, doi:10.1371/journal.pone.0109183.
- Bellerby, R., L. G. Anderson, E. Osborne, N. Steiner, I. Pipko, J. Cross, M. Chierici, A. Fransson, K. Azetsu-Scott, J. Ólafsson, and L. A. Miller (2018), *AMAP Assessment 2018: Arctic Ocean Acidification*, chap. 2. Arctic Ocean acidification: an update, pp. 3 – 14, Arctic Monitoring and Assessment Programme (AMAP), Tromsø, Norway.
- Bouillon, S., M. A. M. Maqueda, V. Legat, and T. Fichefet (2009), An elastic–viscous–plastic sea ice model formulated on Arakawa B and C grids, *Ocean Modelling*, 27(3), 174–184, doi:10.1016/j.ocemod.2009.01.004.
- Brown, K. A., L. A. Miller, C. J. Mundy, T. Papakyriakou, R. Francois, M. Gosselin, G. Carnat, K. Swystun, and P. D. Tortell (2015), Inorganic carbon system dynamics in landfast Arctic sea ice during the early-melt period, *Journal of Geophysical Research: Oceans*, 120(5), 3542–3566, doi:10.1002/2014JC010620.
- Brown, K. A., L. A. Miller, C. J. Mundy, T. Papakyriakou, R. Francois, M. Gosselin, G. Carnat, K. Swystun, and P. D. Tortell (2015-1), Inorganic carbon system dynamics in landfast Arctic sea ice during the early-melt period: Spring Sea Ice Inorganic Carbon System, *Journal of Geophysical Research: Oceans*, 120(5), 3542–3566, doi: 10.1002/2014JC010620.
- Brown, Z. W., K. E. Lowry, M. A. Palmer, G. L. van Dijken, M. M. Mills, R. S. Pickart, and K. R. Arrigo (2015-2), Characterizing the subsurface chlorophyll a maximum in the Chukchi Sea and Canada Basin, *Deep Sea Research Part II: Topical Studies in Oceanography*, 118, Part A, 88–104, doi:10.1016/j.dsr2.2015.02.010.
- Bruggeman, J., and K. Bolding (2014), A general framework for aquatic biogeochemical models, *Environmental Modelling & Software*, doi:10.1016/j.envsoft.2014.04.002.
- Buitenhuis, E., C. Le Quéré, O. Aumont, G. Beaugrand, A. Bunker, A. Hirst, T. Ikeda, T. O'Brien, S. Piontkovski, and D. Straile (2006), Biogeochemical fluxes through mesozooplankton, *Global Biogeochemical Cycles*, 20(2), GB2003, doi:10.1029/2005GB002511.

- Burchard, H., K. Bolding, W. Kühn, A. Meister, T. Neumann, and L. Umlauf (2006), Description of a flexible and extendable physical biogeochemical model system for the water column, *Journal of Marine Systems*, 61(3–4), 180–211, doi:10.1016/j.jmarsys.2005.04.011.
- Burgers, T. M., L. A. Miller, H. Thomas, B. G. T. Else, M. Gosselin, and T. Papakyriakou (2017), Surface Water $p\text{CO}_2$ Variations and Sea-Air CO_2 Fluxes During Summer in the Eastern Canadian Arctic, *Journal of Geophysical Research: Oceans*, 122(12), 9663–9678, doi:10.1002/2017JC013250.
- Cai, W.-J., L. Chen, B. Chen, Z. Gao, S. H. Lee, J. Chen, D. Pierrot, K. Sullivan, Y. Wang, X. Hu, W.-J. Huang, Y. Zhang, S. Xu, A. Murata, J. M. Grebmeier, E. P. Jones, and H. Zhang (2010), Decrease in the CO_2 uptake capacity in an ice-free Arctic Ocean basin., *Science*, 329(5991), 556–559, doi:10.1126/science.1189338.
- Campbell, K., C. J. Mundy, D. G. Barber, and M. Gosselin (2015), Characterizing the sea ice algae chlorophyll a–snow depth relationship over Arctic spring melt using transmitted irradiance, *Journal of Marine Systems*, 147, 76–84, doi:10.1016/j.jmarsys.2014.01.008.
- Campbell, K., C. Mundy, M. Gosselin, J. Landy, A. Delaforge, and S. Rysgaard (2017), Net community production in the bottom of first-year sea ice over the arctic spring bloom, *Geophysical Research Letters*, 44, 8971 – 8978, doi:10.1002/2017GL074602.
- Carmack, E., and F. McLaughlin (2011), Towards recognition of physical and geochemical change in Subarctic and Arctic Seas, *Progress in Oceanography*, 90(1–4), 90–104, doi:10.1016/j.pocean.2011.02.007.
- Carmack, E. C., F. A. McLaughlin, S. Vagle, H. Melling, and W. J. Williams (2010), Structures and property distributions in the three oceans surrounding Canada in 2007: A basis for a long-term ocean climate monitoring strategy, *Atmosphere-Ocean*, 48(4), 211–224, doi:10.3137/OC324.2010.
- Carmack, E. C., M. Yamamoto-Kawai, T. W. N. Haine, S. Bacon, B. A. Bluhm, C. Lique, H. Melling, I. V. Polyakov, F. Straneo, M.-L. Timmermans, and W. J. Williams (2016), Freshwater and its role in the Arctic Marine System: Sources, disposition, storage, export, and physical and biogeochemical consequences in the Arctic and global oceans, *Journal of Geophysical Research: Biogeosciences*, 121(3), doi:10.1002/2015JG003140.
- Ciais, P., C. Sabine, G. Bala, L. Bopp, V. Brovkin, J. Canadell, A. Chhabra, R. DeFries, J. Galloway, M. Heimann, C. Jones, C. L. Quéré, R. B. Myneni, S. Piao, and P. Thornton

- (2013), Carbon and Other Biogeochemical Cycles, *Climate Change 2013 - The Physical Science Basis*, pp. 465–570, doi:10.1017/CBO9781107415324.015.
- Comeau, S., S. Alliouane, and J. Gattuso (2012), Effects of ocean acidification on overwintering juvenile arctic pteropods *limacina helicina*, *Marine Ecology Progress Series*, 456, 279–284.
- Cooper, L. W., J. W. McClelland, R. M. Holmes, P. A. Raymond, J. J. Gibson, C. K. Guay, and B. J. Peterson (2008), Flow-weighted values of runoff tracers ($\delta^{18}\text{O}$, DOC, Ba, alkalinity) from the six largest Arctic rivers, *Geophysical Research Letters*, 35(18), 3–7, doi:10.1029/2008GL035007.
- Cota, G. F., S. J. Prinsenberg, E. B. Bennett, J. W. Loder, M. R. Lewis, J. L. Anning, N. H. F. Watson, and L. R. Harris (1987), Nutrient fluxes during extended blooms of Arctic ice algae, *Journal of Geophysical Research: Oceans*, 92(C2), 1951–1962, doi:10.1029/JC092iC02p01951.
- Cross, J. N., J. T. Mathis, R. S. Pickart, and N. R. Bates (2018), Formation and transport of corrosive water in the Pacific Arctic region, *Deep-Sea Research Part II*, 152(June), 67–81, doi:10.1016/j.dsr2.2018.05.020.
- Cubasch, U., D. Wuebbles, D. Chen, M. Facchini, D. Frame, N. Mahowald, and J.-G. Winther (2013), Introduction, in *Climate Change 2013: The Physical Science Basis. Contribution of Working Group I to the Fifth Assessment Report of the Intergovernmental Panel on Climate Change*, edited by T. Stocker, D. Qin, G.-K. Plattner, M. Tignor, S. Allen, J. Boschung, A. Nauels, Y. Xia, V. Bex, and P. Midgley, pp. 119–158, Cambridge University Press, Cambridge, United Kingdom and New York, NY, USA.
- Curry, B., C. M. Lee, B. Petrie, R. E. Moritz, and R. Kwok (2014), Multiyear Volume, Liquid Freshwater, and Sea Ice Transports through Davis Strait, 2004–10, *Journal of Physical Oceanography*, 44(4), 1244–1266, doi:10.1175/JPO-D-13-0177.1.
- Dai, A., T. Qian, and K. E. Trenberth (2009), Changes in Continental Freshwater Discharge from 1948 to 2004, *Journal of Climate*, pp. 2773–2792, doi:10.1175/2008JCLI2592.1.
- Deal, C., M. Jin, S. Elliott, E. Hunke, M. Maltrud, and N. Jeffery (2011), Large-scale modeling of primary production and ice algal biomass within arctic sea ice in 1992, *Journal of Geophysical Research*, 116(C7), doi:10.1029/2010JC006409.
- Delille, B., M. Vancoppenolle, N.-X. Geilfus, B. Tilbrook, D. Lannuzel, V. Schoemann, S. Becquevort, G. Carnat, D. Delille, C. Lancelot, L. Chou, G. S. Dieckmann, and J.-L.

- Tison (2014), Southern Ocean CO₂ sink: The contribution of the sea ice, *Journal of Geophysical Research : Oceans*, 119, 6340–6355, doi:10.1002/2014JC009941.
- Denman, K. L. (2003), Modelling planktonic ecosystems: parameterizing complexity, *Progress in Oceanography*, 57(3–4), 429–452, doi:10.1016/S0079-6611(03)00109-5.
- Dickson, A. G., Sabine, and Christian (2007), *Guide to Best Practices for Ocean CO₂ Measurements*, vol. 3, PICES Special Publication, Sidney, Canada.
- Dieckmann, G. S., G. Nehrke, S. Papadimitriou, J. Göttlicher, R. Steininger, H. Kennedy, D. Wolf-Gladrow, and D. N. Thomas (2008), Calcium carbonate as ikaite crystals in Antarctic sea ice, *Geophysical Research Letters*, 35(8), 35–37, doi:10.1029/2008GL033540.
- Dieckmann, G. S., G. Nehrke, C. Uhlig, J. Göttlicher, S. Gerland, M. A. Granskog, and D. N. Thomas (2010), Brief Communication: Ikaite (CaCO₃ · 6H₂O) discovered in Arctic sea ice, *The Cryosphere*, 4(2), 227–230, doi:10.5194/tc-4-227-2010.
- Dukhovskoy, D. S., P. G. Myers, G. Platov, M.-L. Timmermans, B. Curry, A. Proshutinsky, J. L. Bamber, E. Chassignet, X. Hu, C. M. Lee, and R. Somavilla (2016a), Greenland freshwater pathways in the sub-Arctic Seas from model experiments with passive tracers, *Journal of Geophysical Research: Oceans*, 121(1), 877–907, doi:10.1002/2015JC011290.
- Dukhovskoy, D. S., P. G. Myers, G. Platov, M.-L. Timmermans, B. Curry, A. Proshutinsky, J. L. Bamber, E. Chassignet, X. Hu, C. M. Lee, and R. Somavilla (2016b), Greenland freshwater pathways in the sub-Arctic Seas from model experiments with passive tracers, *Journal of Geophysical Research : Oceans*, pp. 877–907, doi:10.1002/2015JC011290.
- Dupont, F., S. Higginson, R. Bourdallé-Badie, Y. Lu, F. Roy, G. C. Smith, J. F. Lemieux, G. Garric, and F. Davidson (2015), A high-resolution ocean and sea-ice modelling system for the Arctic and North Atlantic oceans, *Geoscientific Model Development*, 8(5), 1577–1594, doi:10.5194/gmd-8-1577-2015.
- Dussin, R., B. Barnier, L. Brodeau, and J. M. Molines (2016), The making of the drakkar forcing set dfs5.
- Else, B. G. T., R. J. Galley, B. Lansard, D. G. Barber, K. Brown, L. A. Miller, A. Mucci, T. N. Papakyriakou, J.-É. Tremblay, and S. Rysgaard (2013), Further observations of a decreasing atmospheric CO₂ uptake capacity in the Canada Basin (Arctic Ocean) due to sea ice loss, *Geophysical Research Letters*, 40(6), 1132–1137, doi:10.1002/grl.50268.

- Eppley, R. W. (1972), Temperature and phytoplankton growth in the sea, *Fish. Bull*, 70(4), 1063–1085.
- Evans, W., J. T. Mathis, J. N. Cross, N. R. Bates, K. E. Frey, B. G. T. Else, T. N. Papkyriakou, M. D. Degrandpre, F. Islam, W.-j. Cai, B. Chen, M. Yamamoto-Kawai, E. Carmack, W. J. Williams, and T. Takahashi (2015), Sea-air CO₂ exchange in the western Arctic coastal ocean, *Global Biogeochemical Cycles RESEARCH*, 29, 1190–1209, doi:10.1002/2015GB005153.
- Fasham, M. J. R., H. W. Ducklow, and S. M. McKelvie (1990), A nitrogen-based model of plankton dynamics in the oceanic mixed layer, *Journal of Marine Research*, 48(3), 591–639.
- Fetterer, F., K. Knowles, W. Meier, M. Savoie, and A. K. Windnagel (2017), Sea ice index, version 3, *Tech. rep.*, NSIDC: National Snow and Ice Data Center, doi: <https://doi.org/10.7265/N5K072F8>.
- Flato, G. M., and R. D. Brown (1996), Variability and climate sensitivity of landfast Arctic sea ice, *Journal of Geophysical Research: Oceans*, 101(C11), 25,767–25,777, doi: 10.1029/96JC02431.
- Fransson, A., M. Chierici, and Y. Nojiri (2009), New insights into the spatial variability of the surface water carbon dioxide in varying sea ice conditions in the Arctic Ocean, *Continental Shelf Research*, 29(10), 1317–1328, doi:10.1016/j.csr.2009.03.008.
- Frey, K. E., D. K. Perovich, and B. Light (2011), The spatial distribution of solar radiation under a melting Arctic sea ice cover, *Geophysical Research Letters*, 38(22), L22,501, doi: 10.1029/2011GL049421.
- Fripiat, F., D. M. Sigman, S. E. Fawcett, P. A. Rafter, M. A. Weigand, and J.-L. Tison (2014), New insights into sea ice nitrogen biogeochemical dynamics from the nitrogen isotopes, *Global Biogeochemical Cycles*, 28(2), 2013GB004,729, doi:10.1002/2013GB004729.
- Gale, M. (2014), On The Biophysical Factors That Control Under-Ice Phytoplankton Bloom Onset in the Central Canadian Archipelago, Ph.D. thesis.
- Galindo, V., M. Levasseur, C. Mundy, M. Gosselin, J.-E. Tremblay, M. Scarratt, Y. Gratton, T. Papakiriakou, M. Poulin, and M. Lizotte (2014), Biological and physical processes influencing sea ice, under-ice algae, and dimethylsulfoniopropionate during spring in the Canadian Arctic Archipelago, *Journal of Geophysical Research: Oceans*, doi: 10.1002/2013JC009497.

- Galley, R. J., D. Babb, M. Ogi, B. G. T. Else, N.-X. Geilfus, O. Crabeck, D. G. Barber, and S. Rysgaard (2016), Replacement of multiyear sea ice and changes in the open water season duration in the Beaufort Sea since 2004, *Journal of Geophysical Research: Oceans*, *121*(3), 1806–1823, doi:10.1002/2015JC011583.
- Geilfus, N.-X., R. J. Galley, O. Crabeck, T. Papakyriakou, J. Landy, J.-L. Tison, and S. Rysgaard (2015), Inorganic carbon dynamics of melt pond-covered first year sea ice in the Canadian Arctic, *Biogeosciences*, *12*, doi:10.5194/bgd-12-2047-2015.
- Geilfus, N.-X., R. J. Galley, O. Crabeck, T. Papakyriakou, J. Landy, J.-L. Tison, and S. Rysgaard (2015a), Inorganic carbon dynamics of melt-pond-covered first-year sea ice in the Canadian Arctic, *Biogeosciences*, *12*(6), 2047–2061, doi:10.5194/bg-12-2047-2015.
- Geilfus, N.-X., R. J. Galley, B. G. T. Else, K. Campbell, T. Papakyriakou, O. Crabeck, M. Lemes, B. Delille, and S. Rysgaard (2016), Estimates of ikaite export from sea ice to the underlying seawater in a sea ice-seawater mesocosm, *The Cryosphere*, *10*(5), 2173–2189, doi:10.5194/tc-10-2173-2016.
- Golden, K. M., S. F. Ackley, and V. I. Lytle (1998), The Percolation Phase Transition in Sea Ice, *Science*, *282*(5397), 2238–2241, doi:10.1126/science.282.5397.2238.
- Goosse, H., and T. Fichefet (1999), Importance of ice-ocean interactions for the global ocean circulation: A model study, *Journal of Geophysical Research: Oceans*, *104*(C10), 23,337–23,355, doi:10.1029/1999JC900215.
- Gosselin, M., L. Legendre, J.-C. Therriault, and S. Demers (1990), Light and nutrient limitation of sea-ice microalgae (Hudson Bay, Canadian Arctic), *Journal of Phycology*, *26*(2), 220–232, doi:10.1111/j.0022-3646.1990.00220.x.
- Gosselin, M., M. Levasseur, P. A. Wheeler, R. A. Horner, and B. C. Booth (1997), New measurements of phytoplankton and ice algal production in the Arctic Ocean, *Deep Sea Research Part II: Topical Studies in Oceanography*, *44*(8), 1623–1644.
- Grenfell, T. C., and G. A. Maykut (1977), The optical properties of ice and snow in the Arctic Basin, *Journal of Glaciology*, *18*, 445–463.
- Grimm, R., D. Notz, R. N. Glud, S. Rysgaard, and K. D. Six (2016), Assessment of the sea-ice carbon pump: Insights from a three-dimensional ocean-sea-ice-biogeochemical model (MPIOM/HAMOCC), *Elementa: Science of the Anthropocene*, *4*(November), 136, doi:10.12952/journal.elementa.000136.

- Harrison, W. G., G. F. Cota, and R. E. H. Smith (1990), Nitrogen utilization in ice algal communities of Barrow Strait, Northwest Territories, Canada., *Marine Ecology Progress Series*, *67*, 275–283.
- Hayashida, H. (2018b), Modelling sea-ice and oceanic dimethylsulfide production and emissions in the arctic, Ph.D. thesis, University of Victoria.
- Hayashida, H., N. Steiner, A. Monahan, V. Galindo, M. Lizotte, and M. Levasseur (2016), Implications of sea-ice biogeochemistry for oceanic production and emissions of dimethylsulfide in the Arctic, *Biogeosciences Discussions*, pp. 1–38, doi:10.5194/bg-2016-399.
- Hayashida, H., N. Steiner, A. Monahan, V. Galindo, M. Lizotte, and M. Levasseur (2017), Implications of sea-ice biogeochemistry for oceanic production and emissions of dimethyl sulfide in the Arctic, *Biogeosciences*, *14*(12), 3129–3155, doi:10.5194/bg-14-3129-2017.
- Hayashida, H., J. Christian, A. Holdsworth, X. Hu, A. Monahan, E. Mortenson, P. Myers, O. Riche, T. Sou, and N. Steiner (2018), Development of a sea-ice biogeochemical module for the Nucleus for European Modelling of the Ocean (NEMO), *Geoscientific Model Development*, doi:10.5194/gmd-2018-191.
- Holmes, R. M., J. W. McClelland, B. J. Peterson, S. E. Tank, E. Bulygina, T. I. Eglinton, V. V. Gordeev, T. Y. Gurtovaya, P. A. Raymond, D. J. Repeta, R. Staples, R. G. Striegl, A. V. Zhulidov, and S. A. Zimov (2012), Seasonal and Annual Fluxes of Nutrients and Organic Matter from Large Rivers to the Arctic Ocean and Surrounding Seas, *Estuaries and Coasts*, *35*(2), 369–382, doi:10.1007/s12237-011-9386-6.
- Jin, M., C. J. Deal, J. Wang, K.-H. Shin, N. Tanaka, T. E. Whitley, S. H. Lee, and R. R. Gradinger (2006), Controls of the landfast ice–ocean ecosystem offshore Barrow, Alaska, *Annals of Glaciology*, *44*(1), 63–72.
- Jin, M., C. Deal, J. Wang, V. Alexander, R. Gradinger, S.-i. Saitoh, T. Iida, Z. Wan, and P. Stabenro (2007), Ice-associated phytoplankton blooms in the southeastern Bering Sea, *Geophysical Research Letters*, *34*(6), L06,612, doi:10.1029/2006GL028849.
- Jin, M., C. Deal, S. H. Lee, S. Elliott, E. Hunke, M. Maltrud, and N. Jeffery (2012), Investigation of Arctic sea ice and ocean primary production for the period 1992–2007 using a 3-D global ice–ocean ecosystem model, *Deep Sea Research Part II: Topical Studies in Oceanography*, *81–84*, 28–35, doi:10.1016/j.dsr2.2011.06.003.
- Jin, M., J. Hutchings, and Y. Kawaguchi (2015), Sensitivity study of subgrid scale ocean mixing under sea ice using a two-column ocean grid in climate model CESM, *Frontiers of Earth Science*, *9*(4), 594–604, doi:10.1007/s11707-014-0489-9.

- Kawamiya, M., M. J. Kishi, Y. Yamanaka, and N. Suginozawa (1995), An ecological-physical coupled model applied to Station Papa, *Journal of Oceanography*, 51(6), 635–664.
- Kirst, G. O., and C. Wiencke (1995), Ecophysiology of polar algae, *Journal of Phycology*, 31(2), 181–199.
- Krembs, C., H. Eicken, and J. W. Deming (2011), Exopolymer alteration of physical properties of sea ice and implications for ice habitability and biogeochemistry in a warmer Arctic, *Proceedings of the National Academy of Sciences*, 108(9), 3653–3658, doi:10.1073/pnas.1100701108.
- Lauvset, S. K., R. M. Key, A. Olsen, S. V. Heuven, A. Velo, X. Lin, C. Schirnick, A. Kozyr, T. Tanhua, M. Hoppema, and S. Jutterström (2016), A new global interior ocean mapped climatology : the 1° X 1° GLODAP version 2, *Earth System Science Data*, pp. 325–340, doi:10.5194/essd-8-325-2016.
- Lavoie, D., K. Denman, and C. Michel (2005a), Modeling ice algal growth and decline in a seasonally ice-covered region of the Arctic (Resolute Passage, Canadian Archipelago), *Journal of Geophysical Research*, 110(C11), doi:10.1029/2005JC002922.
- Lavoie, D., K. Denman, and C. Michel (2005b), Modeling ice algal growth and decline in a seasonally ice-covered region of the Arctic (Resolute Passage, Canadian Archipelago), *Journal of Geophysical Research: Oceans*, 110(11), 1–17, doi:10.1029/2005JC002922.
- Lavoie, D., R. W. Macdonald, and K. L. Denman (2009), Primary productivity and export fluxes on the Canadian shelf of the Beaufort Sea: A modelling study, *Journal of Marine Systems*, 75(1–2), 17–32, doi:10.1016/j.jmarsys.2008.07.007.
- Legendre, L., S. F. Ackley, G. S. Dieckmann, B. Gulliksen, R. Horner, T. Hoshiai, I. A. Melnikov, W. S. Reeburgh, M. Spindler, and C. W. Sullivan (1992), Ecology of sea ice biota, *Polar Biology*, 12(3–4), 429–444, doi:10.1007/BF00243114.
- Leu, E., C. J. Mundy, P. Assmy, K. Campbell, T. M. Gabrielsen, M. Gosselin, T. Juul-Pedersen, and R. Gradinger (2015), Arctic spring awakening - Steering principles behind the phenology of vernal ice algal blooms, *Progress in Oceanography*, 139, 151–170, doi:10.1016/j.pocean.2015.07.012.
- Light, B., T. C. Grenfell, and D. K. Perovich (2008), Transmission and absorption of solar radiation by Arctic sea ice during the melt season, *Journal of Geophysical Research*, 113(C3), doi:10.1029/2006JC003977.

- Lindsay, R., and A. Schweiger (2015), Arctic sea ice thickness loss determined using subsurface, aircraft, and satellite observations, *The Cryosphere*, *9*(1), 269–283, doi:10.5194/tc-9-269-2015.
- Long, M. C., K. Lindsay, and M. M. Holland (2015), Modeling photosynthesis in sea ice-covered waters, *Journal of Advances in Modeling Earth Systems*, doi:10.1002/2015MS000436.
- Lueker, T. J., A. G. Dickson, and C. D. Keeling (2000), Ocean pCO₂ calculated from dissolved inorganic carbon, alkalinity, and equations for K₁ and K₂: validation based on laboratory measurements of CO₂ in gas and seawater at equilibrium, *Marine Chemistry*, *70*(1), 105–119, doi:10.1016/S0304-4203(00)00022-0.
- MacGilchrist, G. A., A. C. Naveira Garabato, T. Tsubouchi, S. Bacon, S. Torres-Valdés, and K. Azetsu-Scott (2014), The Arctic Ocean carbon sink, *Deep-Sea Research Part I: Oceanographic Research Papers*, *86*, 39–55, doi:10.1016/j.dsr.2014.01.002.
- Madec, G., and the NEMO team (2008), Nemo ocean engine, *Note du Pôle de modélisation, Institut Pierre-Simon Laplace (IPSL), France*, *27*, 1288–1619.
- Manizza, M., M. J. Follows, S. Dutkiewicz, D. Menemenlis, C. N. Hill, and R. M. Key (2013), Changes in the Arctic Ocean CO₂ sink (1996-2007): A regional model analysis, *Global Biogeochemical Cycles*, *27*(4), 1108–1118, doi:10.1002/2012GB004491.
- Manizza, M., D. Menemenlis, C. E. Miller, and Hong Zhang (2019), Modeling the recent changes in the Arctic Ocean CO₂ sink (2006 – 2013), *Global Biogeochemical Cycles*, doi:10.1029/2018GB006070.
- McClelland, J. W., R. M. Holmes, K. H. Dunton, and R. W. Macdonald (2012), The Arctic Ocean Estuary, *Estuaries and Coasts*, *35*(2), 353–368, doi:10.1007/s12237-010-9357-3.
- McDonald, S., T. Koulis, J. Ehn, K. Campbell, M. Gosselin, and C. Mundy (2015), A functional regression model for predicting optical depth and estimating attenuation coefficients in sea-ice covers near Resolute Passage, Canada, *Annals of Glaciology*, *56*(69), 147–154, doi:10.3189/2015AoG69A004.
- McLaughlin, F. A., and E. C. Carmack (2010), Deepening of the nutricline and chlorophyll maximum in the Canada Basin interior, 2003–2009, *Geophysical Research Letters*, *37*(24), L24,602, doi:10.1029/2010GL045459.

- Melling, H., and R. M. Moore (1995), Modification of halocline source waters during freezing on the Beaufort Sea shelf: evidence from oxygen isotopes and dissolved nutrients, *Continental Shelf Research*, *15*(1), 89–113, doi:10.1016/0278-4343(94)P1814-R.
- Miller, L. A., G. Carnat, B. G. T. Else, N. Sutherland, and T. N. Papakyriakou (2011a), Carbonate system evolution at the Arctic Ocean surface during autumn freeze-up, *Journal of Geophysical Research*, *116*, C00G04, doi:10.1029/2011JC007143.
- Miller, L. A., T. N. Papakyriakou, R. E. Collins, J. W. Deming, J. K. Ehn, R. W. Macdonald, A. Mucci, O. Owens, M. Raudsepp, and N. Sutherland (2011b), Carbon dynamics in sea ice: A winter flux time series, *Journal of Geophysical Research: Oceans*, *116*(C02028), doi:10.1029/2009JC006058.
- Miller, L. A., R. W. Macdonald, F. McLaughlin, A. Mucci, M. Yamamoto-Kawai, K. E. Giesbrecht, and W. J. Williams (2014), Changes in the marine carbonate system of the western Arctic: Patterns in a rescued data set, *Polar Research*, *33*, 20,577, doi:10.3402/polar.v33.20577.
- Millero, F. J. (1995), Thermodynamics of the carbon dioxide system in the oceans, *Geochimica et Cosmochimica Acta*, *95*(4), 661–677.
- Monahan, A. H., and K. L. Denman (2004), Impacts of atmospheric variability on a coupled upper-ocean/ecosystem model of the subarctic Northeast Pacific, *Global Biogeochemical Cycles*, *18*(2), n/a–n/a, doi:10.1029/2003GB002100.
- Monod, J. (1949), The growth of bacterial cultures, *Annual Review of Microbiology*, *3*(1), 371–394, doi:10.1146/annurev.mi.03.100149.002103.
- Moreau, S., M. Vancoppenolle, L. Bopp, O. Aumont, G. Madec, B. Delille, J.-L. Tison, P.-Y. Barriat, and H. Goosse (2016), Assessment of the sea-ice carbon pump: Insights from a three-dimensional ocean-sea-ice biogeochemical model (NEMO-LIM-PISCES), *Elementa: Science of the Anthropocene*, *4*(1), doi:10.12952/journal.elementa.000122.
- Mortenson, E., H. Hayashida, N. Steiner, A. Monahan, M. Blais, M. A. Gale, V. Galindo, M. Gosselin, X. Hu, D. Lavoie, and C. J. Mundy (2017), A model-based analysis of physical and biological controls on ice algal and pelagic primary production in Resolute Passage, *Elementa: Science of the Anthropocene Sci Anth*, *5*, 39, doi:10.1525/elementa.229.
- Mortenson, E., N. Steiner, A. H. Monahan, L. A. Miller, N.-X. Geilfus, and K. Brown (2018), A model-based analysis of physical and biogeochemical controls on carbon ex-

- change in the upper water column, sea ice, and atmosphere in a seasonally ice-covered arctic strait, *Journal of Geophysical Research : Oceans*, *123*, 7529 – 7549, doi:10.1029/2018JC014376.
- Mucci, A. (1983), The solubility of calcite and aragonite in seawater at various salinities, temperatures, and one atmosphere total pressure, *American Journal of Science*, *283*, 780–799.
- Mundy, C., M. Gosselin, J. Ehn, Y. Gratton, A. Rossnagel, D. G. Barber, J. Martin, J.-\., Tremblay, M. Palmer, K. R. Arrigo, G. Darnis, L. Fortier, B. Else, and T. Papakyriakou (2009), Contribution of under-ice primary production to an ice-edge upwelling phytoplankton bloom in the Canadian Beaufort Sea, *Geophysical Research Letters*, *36*(17), L17,601, doi:10.1029/2009GL038837.
- Mundy, C., M. Gosselin, Y. Gratton, K. Brown, V. Galindo, K. Campbell, M. Levasseur, D. Barber, T. Papakyriakou, and S. Bélanger (2014a), Role of environmental factors on phytoplankton bloom initiation under landfast sea ice in Resolute Passage, Canada, *Marine Ecology Progress Series*, *497*, 39–49, doi:10.3354/meps10587.
- Mundy, C. J., M. Gosselin, Y. Gratton, K. Brown, V. Galindo, K. Campbell, M. Levasseur, D. Barber, T. Papakyriakou, and S. Bélanger (2014b), Role of environmental factors on phytoplankton bloom initiation under landfast sea ice in Resolute Passage, Canada, *Marine Ecology Progress Series*, *497*(2009), 39–49, doi:10.3354/meps10587.
- Niemi, A., and C. Michel (2015), Temporal and spatial variability in sea-ice carbon:nitrogen ratios on Canadian Arctic shelves, *Elementa: Science of the Anthropocene*, *3*, 78, doi:10.12952/journal.elementa.000078.
- Niemi, A., C. Michel, K. Hille, and M. Poulin (2011), Protist assemblages in winter sea ice: setting the stage for the spring ice algal bloom, *Polar Biology*, *34*(12), 1803–1817, doi:10.1007/s00300-011-1059-1.
- Nomura, D., M. A. Granskog, P. Assmy, D. Simizu, and G. Hashida (2013), Arctic and Antarctic sea ice acts as a sink for atmospheric CO₂ during periods of snowmelt and surface flooding, *Journal of Geophysical Research: Oceans*, *118*(12), 6511–6524, doi:10.1002/2013JC009048.
- Nomura, D., M. A. Granskog, A. Fransson, M. Chierici, A. Silyakova, K. I. Ohshima, L. Cohen, B. Delille, S. R. Hudson, and G. S. Dieckmann (2018), CO₂ flux over young and snow-covered Arctic sea ice in winter and spring, *Biogeosciences Discussions*, *15*, 3331–3343, doi:10.5194/bg-15-3331-2018.

- Onodera, J., E. Watanabe, N. Harada, and M. C. Honda (2015), Diatom flux reflects water-mass conditions on the southern Northwind Abyssal Plain, Arctic Ocean, *Biogeosciences*, *12*(5), 1373–1385, doi:10.5194/bg-12-1373-2015.
- Overland, J. E., and M. Wang (2013), When will the summer Arctic be nearly sea ice free?, *Geophysical Research Letters*, *40*(10), 2097–2101, doi:10.1002/grl.50316.
- Palmer, M. A., B. T. Saenz, and K. R. Arrigo (2014a), Impacts of sea ice retreat, thinning, and melt-pond proliferation on the summer phytoplankton bloom in the Chukchi Sea, Arctic Ocean, *Deep Sea Research Part II: Topical Studies in Oceanography*, *105*, 85–104, doi:10.1016/j.dsr2.2014.03.016.
- Palmer, M. A., B. T. Saenz, and K. R. Arrigo (2014b), Impacts of sea ice retreat, thinning, and melt-pond proliferation on the summer phytoplankton bloom in the Chukchi Sea, Arctic Ocean, *Deep Sea Research Part II: Topical Studies in Oceanography*, *105*, 85–104, doi:10.1016/j.dsr2.2014.03.016.
- Papadimitriou, S., H. Kennedy, P. Kennedy, and D. N. Thomas (2014), Kinetics of ikaite precipitation and dissolution in seawater-derived brines at sub-zero temperatures to 265K, *Geochimica et Cosmochimica Acta*, *140*, 199–211, doi:10.1016/j.gca.2014.05.031.
- Papakyriakou, T., and L. Miller (2011), Springtime CO₂ exchange over seasonal sea ice in the Canadian Arctic Archipelago, *Annals of Glaciology*, *52*(57), 215–224.
- Perovich, D. K., T. C. Grenfell, B. Light, and P. V. Hobbs (2002), Seasonal evolution of the albedo of multiyear Arctic sea ice, *Journal of Geophysical Research: Oceans*, *107*(C10), 8044, doi:10.1029/2000JC000438.
- Pogson, L., B. Tremblay, D. Lavoie, C. Michel, and M. Vancoppenolle (2011), Development and validation of a one-dimensional snow-ice algae model against observations in Resolute Passage, Canadian Arctic Archipelago, *Journal of Geophysical Research*, *116*(C4), doi:10.1029/2010JC006119.
- Qi, D., L. Chen, B. Chen, Z. Gao, W. Zhong, R. A. Feely, L. G. Anderson, H. Sun, J. Chen, M. Chen, L. Zhan, Y. Zhang, and W.-J. Cai (2017), Increase in acidifying water in the western arctic ocean, *Nature Climate Change*, *7*, doi:10.1038/NCLIMATE3228.
- Rebreanu, L., J.-P. Vanderborcht, and L. Chou (2008), The diffusion coefficient of dissolved silica revisited, *Marine Chemistry*, *112*(3–4), 230–233, doi:10.1016/j.marchem.2008.08.004.

- Redfield, A. C., B. H. Ketchum, and F. A. Richards (1963a), The influence of organisms on the composition of sea water, in *The Sea*, edited by M. N. Hill, Wiley-Interscience, New York.
- Redfield, A. C., B. Ketchum, and F. Richards (1963b), The influence of organisms on the composition of sea-water, in *The composition of sea-water: comparative and descriptive oceanography, The sea, ideas and observations on progress in the study of the seas*, vol. 2, pp. 26–77, Interscience Pub, New York.
- Riedel, A., C. Michel, and M. Gosselin (2006), Seasonal study of sea-ice exopolymeric substances on the Mackenzie shelf: implications for transport of sea-ice bacteria and algae, *Aquatic Microbial Ecology*, *45*, 195–206, doi:10.3354/ame045195.
- Roulet, G., and G. Madec (2000), Salt conservation, free surface and varying levels: a new formulation for ocean general circulation models, *Journal of Geophysical Research*, *105(C10)*, 23,923–927,942.
- Róžańska, M., M. Poulin, and M. Gosselin (2008), Protist entrapment in newly formed sea ice in the Coastal Arctic Ocean, *Journal of Marine Systems*, *74*(3-4), 887–901, doi: 10.1016/j.jmarsys.2007.11.009.
- Rysgaard, S., J. Bendtsen, B. Delille, G. S. Dieckmann, R. N. Glud, H. Kennedy, J. Mortensen, S. Papadimitriou, D. N. Thomas, and J. L. Tison (2011), Sea ice contribution to the air-sea CO₂ exchange in the Arctic and Southern Oceans, *Tellus, Series B: Chemical and Physical Meteorology*, *63*(5), 823–830, doi:10.1111/j.1600-0889.2011.00571.x.
- Rysgaard, S., D. H. Søgaard, M. Cooper, M. Pućko, K. Lennert, T. N. Papakyriakou, F. Wang, N. X. Geilfus, R. N. Glud, J. Ehn, D. F. McGinnis, K. Attard, J. Sievers, J. W. Deming, and D. Barber (2013), Ikaite crystal distribution in winter sea ice and implications for CO₂ system dynamics, *The Cryosphere*, *7*, 707–718, doi:10.5194/tc-7-707-2013.
- Rysgaard, S., F. Wang, R. J. Galley, R. Grimm, D. Notz, M. Lemes, N.-X. Geilfus, A. Chaulk, A. A. Hare, O. Crabeck, B. G. T. Else, K. Campbell, L. L. Sørensen, J. Sievers, and T. Papakyriakou (2014), Temporal dynamics of ikaite in experimental sea ice, *The Cryosphere*, *8*(4), 1469–1478, doi:10.5194/tc-8-1469-2014.
- Sarmiento, J. L., and N. Gruber (2006), *Ocean biogeochemical dynamics*, Princeton University Press.
- Schuster, U., G. A. McKinley, N. Bates, F. Chevallier, S. C. Doney, A. R. Fay, M. González-Dávila, N. Gruber, S. Jones, J. Krijnen, P. Landschützer, N. Lefèvre, M. Manizza,

- J. Mathis, N. Metzl, A. Olsen, A. F. Rios, C. Rödenbeck, J. M. Santana-Casiano, T. Takahashi, R. Wanninkhof, and A. J. Watson (2013), An assessment of the Atlantic and Arctic sea–air CO₂ fluxes, 1990–2009, *Biogeosciences*, *10*(1), 607–627, doi:10.5194/bg-10-607-2013.
- Sejr, M. K., D. Krause-Jensen, S. Rysgaard, L. L. Sørensen, P. B. Christensen, and R. N. Glud (2011), Air-sea flux of CO₂ in arctic coastal waters influenced by glacial melt water and sea ice, *Tellus, Series B: Chemical and Physical Meteorology*, *63*(5), 815–822, doi:10.1111/j.1600-0889.2011.00540.x.
- Semiletov, I., I. Pipko, Ö. Gustafsson, L. G. Anderson, V. Sergienko, S. Pugach, O. Dudarev, A. Charkin, A. Gukov, L. Bröder, A. Andersson, E. Spivak, and N. Shakhova (2016), Acidification of East Siberian Arctic Shelf waters through addition of freshwater and terrestrial carbon, *Nature Geoscience*, *9*(May), doi:10.1038/NEGO2695.
- Shirasawa, K., and R. G. Ingram (1997), Currents and turbulent fluxes under the first-year sea ice in Resolute Passage, Northwest Territories, Canada, *Journal of Marine Systems*, *11*(1–2), 21–32, doi:10.1016/S0924-7963(96)00024-3.
- Sibert, V., B. Zakardjian, F. Saucier, M. Gosselin, M. Starr, and S. Senneville (2010), Spatial and temporal variability of ice algal production in a 3d ice-ocean model of the Hudson Bay, Hudson Strait and Foxe Basin system: Modelling ice algal production in the Hudson Bay system, *Polar Research*, *29*(3), 353–378, doi:10.1111/j.1751-8369.2010.00184.x.
- Smith, R. E., W. G. Harrison, L. R. Harris, and A. W. Herman (1990), Vertical fine structure of particulate matter and nutrients in sea ice of the high Arctic, *Canadian Journal of Fisheries and Aquatic Sciences*, *47*(7), 1348–1355.
- Smith, R. E. H. (1988), Abundance and production of ice algae in Resolute Passage, Canadian Arctic, *Mar. Ecol. Prog. Ser.*, *48*, 251–263.
- Steele, M., R. Morley, and W. Ermold (2001), PHC: A global ocean hydrography with a high-quality Arctic Ocean, *Journal of Climate*, *14*(9), 2079–2087.
- Steiner, N., and K. Denman (2008), Parameter sensitivities in a 1-D model for DMS and sulphur cycling in the upper ocean, *Deep-Sea Research Part I: Oceanographic Research Papers*, *55*(7), 847–865, doi:10.1016/j.dsr.2008.02.010.
- Steiner, N., K. Denman, N. McFarlane, and L. Solheim (2006a), Simulating the coupling between atmosphere–ocean processes and the planktonic ecosystem during SERIES,

Deep Sea Research Part II: Topical Studies in Oceanography, 53(20-22), 2434–2454, doi:10.1016/j.dsr2.2006.05.030.

Steiner, N., K. Denman, N. McFarlane, and L. Solheim (2006b), Simulating the coupling between atmosphere-ocean processes and the planktonic ecosystem during SERIES, *Deep-Sea Research Part II: Topical Studies in Oceanography*, 53(20-22), 2434–2454, doi: 10.1016/j.dsr2.2006.05.030.

Steiner, N., K. Azetsu-Scott, J. Hamilton, K. Hedges, X. Hu, M. Y. Janjua, D. Lavoie, J. Loder, H. Melling, A. Merzouk, W. Perrie, I. Peterson, M. Scarratt, T. Sou, and R. Tallmann (2015a), Observed trends and climate projections affecting marine ecosystems in the Canadian Arctic, *Environmental Reviews*, 23(2), 191–239, doi: 10.1139/er-2014-0066.

Steiner, N., C. Deal, D. Lannuzel, D. Lavoie, F. Massonnet, L. A. Miller, S. Moreau, E. Popova, J. Stefels, and L. Tedesco (2016a), What sea-ice biogeochemical modellers need from observers, *Elementa: Science of the Anthropocene*, 4, 000,084, doi:10.12952/journal.elementa.000084.

Steiner, N., C. Deal, D. Lannuzel, D. Lavoie, F. Massonnet, L. A. Miller, S. Moreau, E. Popova, J. Stefels, and L. Tedesco (2016b), What sea-ice biogeochemical modellers need from observers, *Elementa: Science of the Anthropocene*, 4, 84, doi:10.12952/journal.elementa.000084.

Steiner, N. S., M. Robert, M. Arychuk, M. L. Levasseur, A. Merzouk, M. A. Peña, W. A. Richardson, and P. D. Tortell (2012), Evaluating DMS measurements and model results in the Northeast subarctic Pacific from 1996-2010, *Biogeochemistry*, 110(1-3), 269–285, doi:10.1007/s10533-011-9669-9.

Steiner, N. S., W. G. Lee, and J. R. Christian (2013), Enhanced gas fluxes in small sea ice leads and cracks: Effects on CO₂ exchange and ocean acidification, *Journal of Geophysical Research: Oceans*, 118(3), 1195–1205, doi:10.1002/jgrc.20100.

Steiner, N. S., T. Sou, C. Deal, J. M. Jackson, M. Jin, E. Popova, W. Williams, and A. Yool (2015b), The future of the subsurface chlorophyll-a maximum in the Canada Basin - a model intercomparison, *Journal of Geophysical Research: Oceans*, pp. n/a–n/a, doi:10.1002/2015JC011232.

Stroeve, J. C., V. Kattsov, A. Barrett, M. Serreze, T. Pavlova, M. Holland, and W. N. Meier (2012), Trends in Arctic sea ice extent from CMIP5, CMIP3 and observations:

ARCTIC SEA ICE EXTENT FROM CMIP5, *Geophysical Research Letters*, 39(16), doi:10.1029/2012GL052676.

Suzuki, Y., and M. Takahashi (1995), Growth responses of several diatom species isolated from various environments to temperature, *Journal of Phycology*, 31(6), 880–888, doi:10.1111/j.0022-3646.1995.00880.x.

Takahashi, T., J. Olafson, J. G. Goddard, D. W. Chipman, and S. C. Sutherland (1993), Seasonal variation of CO₂ and nutrients in the high-latitude surface oceans: a comparative study, *Global Biogeochemical Cycles*, 7(4), 834–878.

Tank, S. E., P. A. Raymond, R. G. Striegl, J. W. McClelland, R. M. Holmes, G. J. Fiske, and B. J. Peterson (2012), A land-to-ocean perspective on the magnitude, source and implication of DIC flux from major Arctic rivers to the Arctic Ocean, *Global Biogeochemical Cycles*, 26(4), 1–15, doi:10.1029/2011GB004192.

Taylor, P. D., and D. L. Feltham (2004), A model of melt pond evolution on sea ice, *Journal of Geophysical Research: Oceans*, 109(C12), C12,007, doi:10.1029/2004JC002361.

Tedesco, L., M. Vichi, and D. N. Thomas (2012), Process studies on the ecological coupling between sea ice algae and phytoplankton, *Ecological Modelling*, 226, 120–138, doi:10.1016/j.ecolmodel.2011.11.011.

Tremblay, J.-É., K. Simpson, J. Martin, L. Miller, Y. Gratton, D. Barber, and N. M. Price (2008), Vertical stability and the annual dynamics of nutrients and chlorophyll fluorescence in the coastal, southeast Beaufort Sea, *Journal of Geophysical Research: Oceans*, 113(C7), C07S90, doi:10.1029/2007JC004547.

Vancoppenolle, M., H. Goosse, A. de Montety, T. Fichefet, B. Tremblay, and J.-L. Tison (2010), Modeling brine and nutrient dynamics in Antarctic sea ice: The case of dissolved silica, *Journal of Geophysical Research*, 115(C2), doi:10.1029/2009JC005369.

Vancoppenolle, M., K. M. Meiners, C. Michel, L. Bopp, F. Brabant, G. Carnat, B. Delille, D. Lannuzel, G. Madec, S. Moreau, J.-L. Tison, and P. van der Merwe (2013a), Role of sea ice in global biogeochemical cycles: emerging views and challenges, *Quaternary Science Reviews*, 79, 207–230, doi:10.1016/j.quascirev.2013.04.011.

Vancoppenolle, M., K. M. Meiners, C. Michel, L. Bopp, F. Brabant, G. Carnat, B. Delille, D. Lannuzel, G. Madec, S. Moreau, J.-L. Tison, and P. van der Merwe (2013b), Role of sea ice in global biogeochemical cycles: emerging views and challenges, *Quaternary Science Reviews*, 79, 207–230, doi:10.1016/j.quascirev.2013.04.011.

- Vaughan, D., J. Comiso, I. Allison, J. Carrasco, G. Kaser, R. Kwok, P. Mote, T. Murray, F. Paul, J. Ren, E. Rignot, O. Solomina, K. Steffen, and T. Zhang (2013), IPCC 13 Observations: Cryosphere, *Climate Change 2013: The Physical Science Basis. Contribution of Working Group I to the Fifth Assessment Report of the Intergovernmental Panel on Climate Change*, pp. 317–382, doi:10.1017/CBO9781107415324.012.
- Wallhead, P. J., R. G. J. Bellerby, A. Silyakova, D. Slagstad, and A. A. Polushkin (2017), Bottom Water Acidification and Warming on the Western Eurasian Arctic Shelves: Dynamical Downscaling Projections, *Journal of Geophysical Research : Oceans*, *122*, 8126–8144, doi:10.1002/2017JC013231.
- Wanninkhof, R. H. (1992), Relationship between wind speed and gas exchange, *Journal of Geophysical Research*, *97*(C5), 7373–7382, doi:10.1029/92JC00188.
- Weiss, R. F. (1974), Carbon dioxide in water and seawater: the solubility of a non-ideal gas, *Marine Chemistry*, *2*, 203–215, doi:10.1016/0304-4203(74)90015-2.
- Wolf-Gladrow, D. A., R. E. Zeebe, C. Klaas, A. Körtzinger, and A. G. Dickson (2007), Total alkalinity: The explicit conservative expression and its application to biogeochemical processes, *Marine Chemistry*, *106*(1-2 SPEC. ISS.), 287–300, doi:10.1016/j.marchem.2007.01.006.
- Yasunaka, S., A. Murata, E. Watanabe, M. Chierici, A. Fransson, S. van Heuven, M. Hoppema, M. Ishii, T. Johannessen, N. Kosugi, S. K. Lauvset, J. T. Mathis, S. Nishino, A. M. Omar, A. Olsen, D. Sasano, T. Takahashi, and R. Wanninkhof (2016), Mapping of the air–sea CO₂ flux in the Arctic Ocean and its adjacent seas: Basin-wide distribution and seasonal to interannual variability, *Polar Science*, *10*(3), 323–334, doi:10.1016/j.polar.2016.03.006.
- Zeebe, R. E., H. Eicken, D. H. Robinson, D. Wolf-Gladrow, and G. S. Dieckmann (1996), Modeling the heating and melting of sea ice through light absorption by microalgae, *Journal of Geophysical Research: Oceans*, *101*(C1), 1163–1181, doi:10.1029/95JC02687.
- Zhang, J., and D. A. Rothrock (2003), Modeling global sea ice with a thickness and enthalpy distribution model in generalized curvilinear coordinates, *Monthly Weather Review*, *131*(5), 845–861, doi:10.1175/1520-0493(2003)131<0845:MGSIWA>2.0.CO;2.